# LATERAL CAPACITY OF PILES AND CAISSONS IN COHESIVE SOILS

A Dissertation

by

FRANCISCO JAVIER GRAJALES SAAVEDRA

Submitted to the Office of Graduate and Professional Studies of
Texas A&M University
in partial fulfillment of the requirement for the degree of

DOCTOR OF PHILOSOPHY

| | |
|---|---|
| Chair of Committee, | Charles P. Aubeny |
| Co-Chair of Committee, | Giovanna Biscontin |
| Committee Members, | Marcelo Sánchez-Castilla |
| | Alan Palazzolo |
| Head of Department, | Robin Autenrieth |

May 2017

Major Subject: Civil Engineering

# ABSTRACT

Upper bound plastic limit analysis (PLA) solutions have been widely used to assess maximum capacity of laterally loaded piles and caissons. However, for the specific case of short piles and caissons with aspect ratios generally ranging from one to three, the current solutions tend to over-estimate capacities. Furthermore, these over predictions seem to be significantly influenced by eccentricity of loading. This dissertation presents a unified upper bound plastic limit analysis solution aiming to improve predictions of capacity for the aforementioned cases. In addition, a simplified upper bound method is proposed for cases in which computational efficiency is needed. Both solutions are compared to results from three dimensional finite element studies.

Towards this end, most of the existing simplified predictive methods typically apply to idealized soil strength profiles that are either constant or linearly increasing with depth. However, site investigations often reveal complex strength profiles that deviate significantly from simple linear profiles. One example is the case in which a superficial stiff layer overlays a thicker layer of very soft soil. The work herein presented also includes analyses of pile and caisson performance in stratified soils based on a three dimensional upper bound PLA with a collapse mechanism comprising a surface failure wedge, a flow-around region and a spherical base failure surface. An introductory discussion on the influence of soil stratigraphy and geology for design purposes is included. Selected strength distributions are representative from field data obtained through cone penetration testing.

Finally, the installation of driven piles and suction caissons in clayey soils generates

excess pore pressures that temporarily reduce load capacity due to side resistance. Time dependent dissipation of these excess pore pressures leads to recovery of side resistance, a process known as ‘setup’. Since many facilities cannot be put into operation until sufficient pile load capacity has been mobilized, realistic predictions of setup time can be important. A simplified method of analysis for calculation of the setup time following open ended pile penetration is also presented.

To my beloved wife Melisabel

and to my parents Teresa and Aurelio

Having you in my life truly a blessing.

Thank you!

*"Love and do that you will."*

*Augustine of Hippo (354-430).*

# ACKNOWLEDGMENTS

It has been truly a privilege working under the supervision of Dr. Charles Aubeny. I would like to thank him for the patience, guidance and mentoring that he kindly provided to me. Dr. Aubeny, thank you for all the motivation that kept me learning all of these years. I would like to thank you for introducing me to the field of offshore geotechnics and helping me grow up as a researcher, as a professional and as a person.

Also, I would like to express my deep appreciation and gratitude to my co-chair, Dr. Giovanna Biscontin. She has been a stepping stone throughout my academic life. Dr. Biscontin, thank you for all the words of motivation and encouragement that you had for me during difficult times.

Thanks to Dr. Marcelo Sanchez, Dr. Alan Palazzolo and Dr. Philippe Jeanjean for contributing as members of my committee.

Special thanks to Dr. Robin Autenrieth and Dr. Sharath Girimaji, for the mentorship and help provided throughout my time here at Texas A&M University.

I would like to thank my research partners Dr. Maddy Murali and Dr. Ryan Beemer, for all the interesting conversations and support provided during my doctoral studies. Doing research with you two as a team was a tremendously unique experience. Thank you!

To my fellow classmates and coworkers at both Texas A&M University and University of Cambridge: Dane Drew, Kirstyn Hein, Rebecca Cummins, Noe Morales, Chuhao Liu, Kristen Ewert, Nicholas Boardman and Elliese Shaughnessy. Thank you for all the hours spent working together with me, but mostly for the cheerful conversations.

I would like to thank the staff at the Zachry Department of Civil Engineering at Texas A&M University, very specially to Mrs. Laura Byrd, Mr. Chris Grunkenmeyer, Ms. Sarah Curylo and Mrs. Terry Taeger, for all the help and support during my time as a graduate student.

Thank you to the Texas A&M High Performance Research Computing facility for providing resources needed to perform numerical simulations.

To my mentors from Panama: Dr. Casilda Saavedra, Dr. Ramiro Vargas, Dr. Dario Solis, Dr. Humberto Alvarez, Dr. Martin Candanedo and Dr. Oscar Ramirez. Thank you for the help and guidance provided to me during the initial stages of my graduate studies. In the same way, I deeply appreciate the constant support of all my friends, mostly those who kept encouraging me at all times. Also, a very special thank you goes to Dr. Isabel Riano, M.D. for all the help she has provided me.

I would like to extend a big thank you to all my family, especially Javi, Mr. Lucho, Mrs. Alma, Almis, Luchito and Juancho. I am blessed by having you in my life. Thank you for all your visits to College Station and encouragement during my graduate studies.

To my parents Teresa and Aurelio, thank you for bringing me to this world and supporting me throughout my life. It is because your love, care and life examples that I have had the motivation and inspiration to set and reach for every goal in my life.

Finally I would like to thank my wife Melisabel and my daughter Melisita. You girls have been the sunshine of my life and without your sacrifice, encouragement and happiness during this journey, I wouldn't have been able to cross the finish line. I love you.

# CONTRIBUTORS AND FUNDING SOURCES

## Contributors

This work was supervised by a dissertation committee consisting of the following persons:

- Dr. Charles P. Aubeny, P.E., Professor, Zachry Department of Civil Engineering, Texas A&M University, College Station, Texas, USA [Chair]
- Dr. Giovanna Biscontin, Lecturer, Department of Engineering, University of Cambridge, Cambridge, UK [Co-Chair]
- Dr. Marcelo Sanchez Castilla, Associate Professor, Zachry Department of Civil Engineering, Texas A&M University, College Station, Texas, USA [Member]
- Dr. Alan Palazzolo, P.E., Professor, Department of Mechanical Engineering, Texas A&M University, College Station, Texas, USA [Member]
- Dr. Philippe Jeanjean, P.E., Technical Authority, Geotechnics, Global Upstream Projects, BP America Inc., Houston, Texas, USA [Special Appointment]

All the work for this dissertation was completed by the student, in collaboration with colleagues from the Zachry Department of Civil Engineering at Texas A&M University, namely: Mr. Dane Drew, Ms. Rebecca Cummins, Dr. Ryan Beemer and Dr. Madhuri Murali.

## Funding Sources

Graduate studies were supported through a five year Scholarship for Doctoral Studies sponsored the National Secretary of Science, Technology and Innovation (SENACYT) of

the Republic of Panama.

Additional support has been provided by the Graduate Teaching Fellows Program of the Dwight Look College of Engineering at Texas A&M University.

Parts of this work were made possible by the National Science Foundation under Grant Number 1041604. Cone Penetration Test datasets were provided by BP America, Inc.

# TABLE OF CONTENTS

# LIST OF FIGURES

# LIST OF TABLES

# 1 INTRODUCTION

## 1.1 The Offshore Environment

The ocean environment is composed by a series of factors that drive not only the design stage but also the installation and construction of any structural system intended to be at an offshore location. Some of these environmental factors are Gerwick (2007): (1) Ocean waves, currents and tides; (2) Wind, wind gusts and storms and (3) earthquakes and tsunamis.

Environmental events translate into forces that are applied to the structural system. Environmental loading conditions for an offshore structure can be classified into steady and oscillating forces Chakrabarti (2005). Examples of steady forces are those generated by steady winds and ocean currents. On the other hand, oscillating forces often arise from wind gusts and water wave forces.

## 1.2 Offshore Structures

Traditionally offshore structures have been related to the exploration and production of oil and gas Randall (2010). These structures range from the very common fixed structures to several more recent systems such as tension leg platforms (TLP's) and SPAR platforms, as shown in Figure 1.1. In addition to oil and gas applications, in recent years interest has been focused on wind energy as an alternative to fossil fuels. Offshore wind farms offer the benefit of more sustained and stronger winds at lower heights, and also they

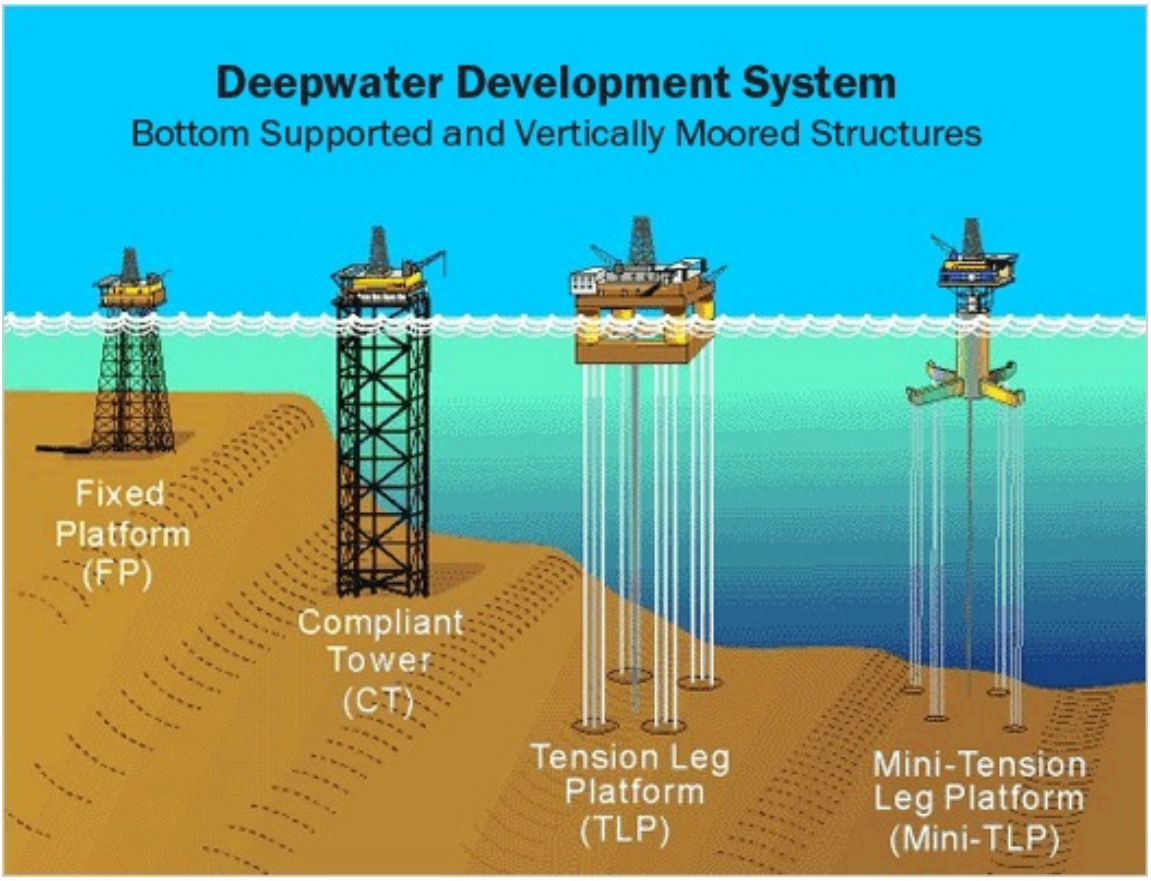


Figure 1.1: Bottom supported and vertically moored structures

avoid the aesthetic issues common for onshore developments of such a type.

Oil and gas structures typically have very large vertical loads and smaller horizontal loads, which is why horizontal loading is not the controlling factor in the design process. However, wind turbines, are purportedly subject to large horizontal and moment loads (compared to the vertical load). These loading characteristics have significant implications on design, because design criteria for oil and gas structures are not entirely applicable for wind towers.

The loads applied on the structure are transferred to the soil, thus, configuration of

those loads and the properties of the soil govern the size and type of foundation required to support an offshore structure Schneider and Senders (2010). Also, the type of foundation depends on the conceptual design of the superstructure. Figure 1.2 shows the variation of the type of foundation depending on the type of superstructure for the case of offshore wind turbines. In the case of monopile foundations (i.e. foundation consisting on a single pile) the lateral and moment loads are transmitted directly to the foundation, creating a relatively high moment demand. On the other hand, for multi-leg systems the moment loading is largely resisted by push-pull axial loading in the piles, with a relatively small bending moment loading in the piles themselves.

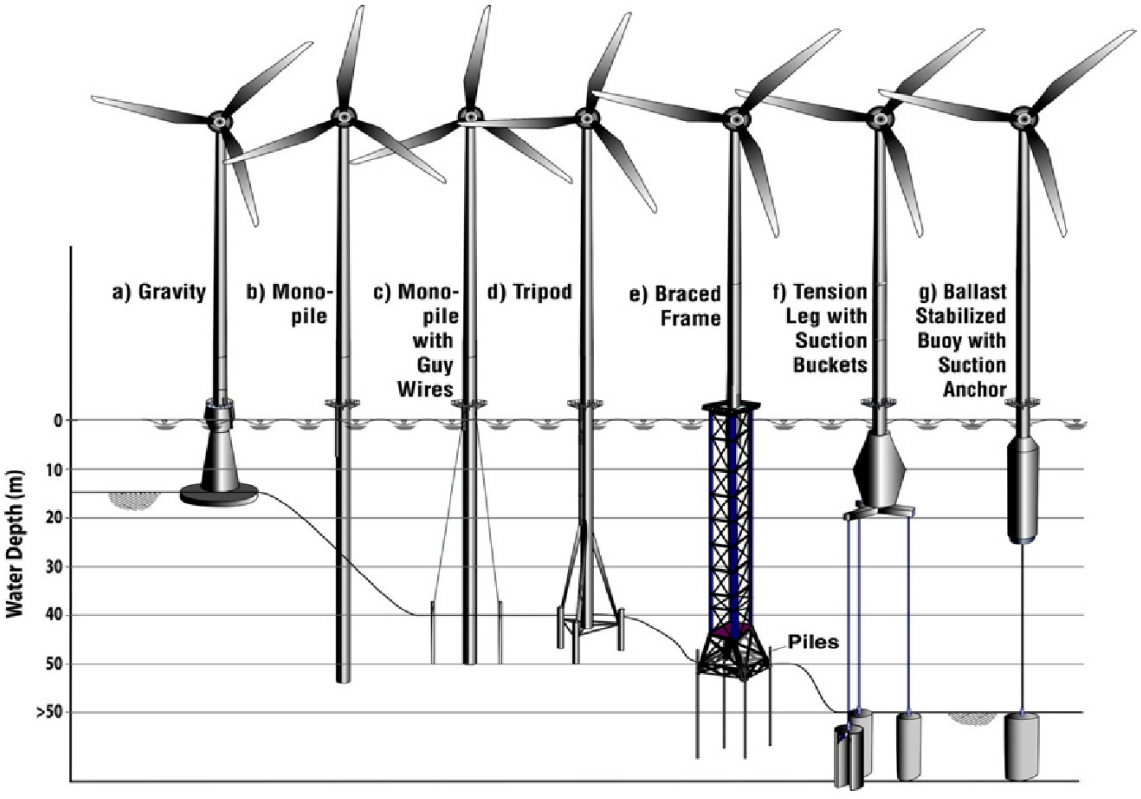


Figure 1.2: Variation of the type of foundation depending on the conceptual design of several support structures Maholtra (2009)

## 1.3 Pile Foundations

Pile foundations are the most commonly used type of foundation for several offshore applications. Offshore piles vary widely in both diameter and length, however typically they have an aspect ratio ($L_f/D$) on the order of 20 to 70 Schneider and Senders (2010) and diameter to wall thickness ratios ($D/t_w$) of 25 to 100. Most of the oil and gas structures are

Figure 1.3: Offshore piles with installation hammer (white). (Courtesy of Dr. James D. Murff)

massive and large, therefore the foundation is designed as an arrangement of piles. On the other hand, monopiles are the most common foundation type for offshore wind turbines. Monopile foundations for offshore wind towers require large diameter piles (usually 3 to 6 m) with $L_f/D$ ratios of 4 to 20.

In the offshore industry two types of piles are commonly used: driven piles and grouted piles. Open ended driven piles are the most prevalent choice (Randolph and Gour-

venec, 2011). The installation process of this piles involves the usage of a submersible hydraulic hammer that literally pushes the pile into the soil. Typically a barge or jack-up platform (Figure 1.4) is required in order to make the installation. Very long piles might need to be spliced during installation. All these facts add cost and lengthen the construction time.

Figure 1.4: Jack-up platform. (Courtesy of Dr. Aubeny)

Drilled and grouted piles are used as an alternative to driven piles when the soil conditions comprise rock or calcareous sediments. They are composed of a tubular steel pipe that is inserted into a previously drilled oversized hole, which finally is grouted. The procedure is very similar to onshore grouted piles, with the slight difference that instead

of a reinforcement cage a steel pipe is used. This procedure is quite expensive because it requires more time than driven piles.

## 1.4 Suction Caissons

The concept of using vacuum pressure (i.e. suction) in order to install bucket-type foundations was initially introduced by Goodman et al. (1961). They encountered that suction penetration is particularly well suited for clayey soils with moisture content close to the plastic limit were. Poorer results were obtained for sandy soils.

Suction caissons have a cylindrical shape (Fig. 1.5): they are hollow at the bottom and closed at the top Andersen et al. (2005). The length to diameter ratio ($L_f/D$) normally oscillates between 3 and 8; therefore they are short structures, unlike conventional inland piles that are rather slender ($L_f/D$ of 30 for example).

The main characteristic of suction caissons is that, as their name implies, the installation process is performed through a combination of self-weight and suction Clukey et al. (2004). As presented in Figure 1.6, initial penetration of the structure in the seabed is done by gravity, dropping the structure from certain height. The top of the caisson is equipped with a valve to which a remote operated vehicle (ROV) carrying a water pump is connected. Pumping the water outside the caisson creates an under-pressure (negative pressure) that allows the caisson to penetrate in the seabed.

Caissons have been used in the last years as a less expensive alternative to conventional piles. They have several advantages over the latter:


Figure 1.5: Suction caisson ready to be installed. Source: Colliat et al. (2011)

1. The installation time is shorter and less equipment is required
2. Because of caissons are smaller than piles, the manufacturing process normally requires less material and, therefore, it is less expensive
3. Transportation to the installation site is more efficient than conventional piles; several caissons can fit in the same transportation vessel. (Fig.1.7).
4. Regarding their functionality, caissons can be used widely as anchor system for floating structures (such as TLP's and SPAR's); however they can also work as a foundation system for vertically supported offshore structures as is the case of offshore wind turbines.

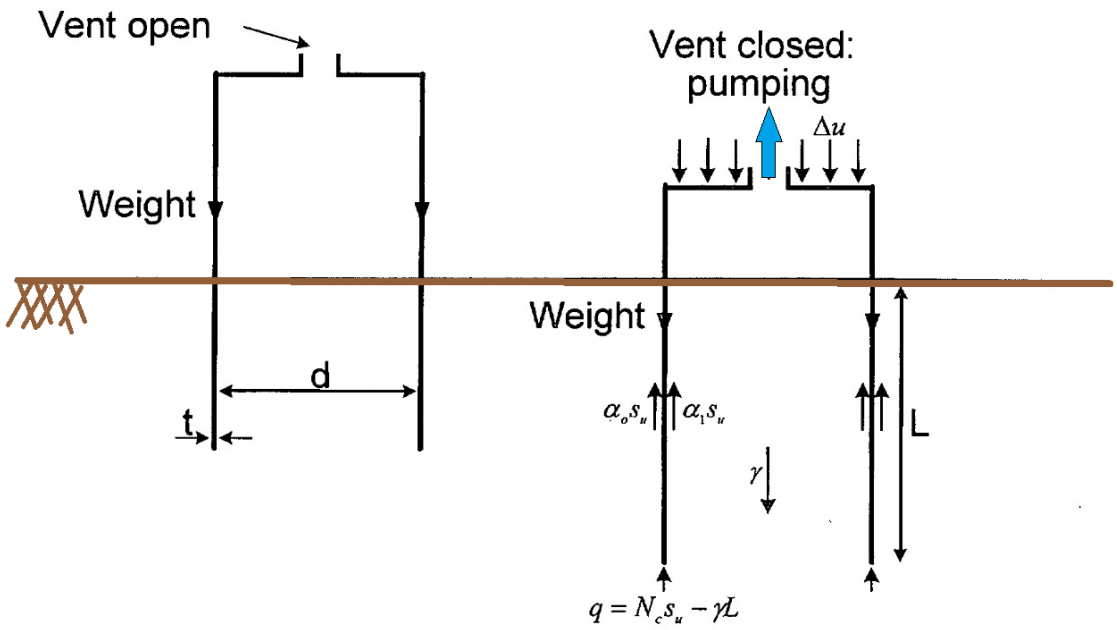


Figure 1.6: Schematic of installation of a suction caisson. Source: Aubeny et al. (2001b)

## 1.5 Finite Element Analysis for Offshore Structures

Despite the fact that, until recent years, hand calculations and plasticity methods have been widely used in the offshore industry, finite element analyses (FEA) are becoming a very common approach in order to assess with main geotechnical issues that are common to these structures, such as Andresen et al. (2011):

1. Bearing capacity
2. Stiffness of the structure-foundation system
3. Consolidation
4. Soil-structure interaction

Finite element analyses have several advantages over conventional methods such as the possibility of including complicated geometries, varying soil properties and material

Figure 1.7: Transportation of suction caissons to installation site. Source: Colliat et al. (2011)

laws that account for soil non-linearities and contact behavior between the structure and the soil surrounding it.

## 1.6 Problem of Study

### 1.6.1 Undrained capacity of short piles and caissons in clays

Figure 1.8 intends to aid on the definition of the scope of this investigation. As it has been mentioned previously, long and flexible piles have been for long time the foundation system of choice due to their high capacity and reliability. Thus, plenty of solutions exist in order to characterize their behavior and performance. On the other extreme, there are those

| METHOD | ADVANTAGES | DISADVANTAGES |
|---|---|---|
| **FINITE ELEMENT** | • Complex geometries<br>• Complex material config. | • High computational effort for refined mesh.<br>• Over-estimation of capacities |
| **PLASTIC LIMIT ANALYSIS** | • Complex geometries<br>• Complex material config.<br>• Accurate – Long Piles | • Optimization time high depending on complexity<br>• Method not intended for short and stubby piles: over-estimates capacity |
| **EMPIRICAL** | • Simple solution<br>• Easy to implement in Excel spreadsheet<br>• Running time - fast | • Can not accommodate complex material properties. |
| **EXACT SOLUTIONS** | • Give exact answer without need of approximation or optimization methods | • Feasible for idealized situations with well defined boundary cond. |

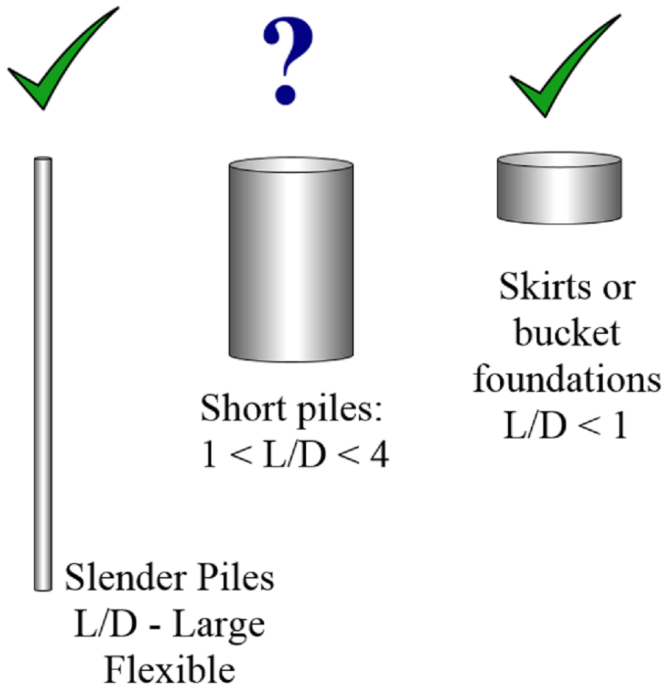


Figure 1.8: Definition of the problem of study: capacity of short piles

foundations of short aspect ratio ($L_f/D$ less than one), which have been widely studied in recent years at University of Western Australia. Although more research is needed in order to refine solutions and come up with formal design criteria, there is plenty of information on how to handle these types of foundations.

Contrary to this, to date there is limited ways to estimate behavior of intermediate (or transitional) foundations: piles and caissons with aspect ratios which typically range from 1 to 4. Methods used for long piles (i.e. Murff and Hamilton (1993)) have been used to analyze these type of foundations, however, it is known that these techniques do over-estimate capacities.

This part of research will employ several techniques (included also in Fig.1.8), namely: finite element method, upper bound plastic limit analysis and empirical upper bound solutions. Each of the three methods has its advantages and limitations.

Upper bound plastic limit analysis (PLA) provides a strong and sound theoretical framework for the computation of ultimate capacity. Both complex geometries and material properties can be incorporated into such type of solutions. They however rely on optimization procedures which, depending on the complexity of the problem, could take significant computing resources. Plastic limit analysis has been widely used to assess maximum capacity of laterally loaded piles and caissons. However, for the specific case of short and squat piles and caissons with aspect ratios generally ranging from one to three, the current solutions tend to over-estimate capacities. Furthermore, these over predictions seem to be significantly influenced by eccentricity of loading. This study presents a unified

upper bound plastic limit analysis solution aiming to improve predictions of capacity for the aforementioned cases.

Results from 3D upper bound PLA are compared to predictions from three dimensional finite element studies. Finite element studies are going to be developed using the software ABAQUS. They consist on displacement controlled analyses of piles with different aspect ratios, friction coefficients and velocity fields. The comparisons are to be performed both terms of the total resistance that is exerted by the soil on the pile and in terms of the equivalent soil resistance distribution along the length of the pile. FE studies allow to model capacity for different displacement fields and also to compute interactions between different loading modes.

Simplified upper bound solutions based on empirically fitted soil resistance functions (Aubeny et al., 2001a, 2003) provide a more relaxed computational framework for estimating capacities. Such type of methodologies are relatively easy to implement in traditional spreadsheets and analyses tend to be performed very fast. However, existing solutions have been calibrated only for idealized soil strength conditions: constand and linearly increasing shear strength profiles. Furthermore, current empirical functions were calibrated based on three dimensional upper bound PLA methods, which brings as a consequence over-estimation of capacities for short piles and caissons. This study aims to provide a modified soil resistance functions which could be adequate to model the behavior of short piles.

### 1.6.2 Capacity of piles and caissons in soils with crust

Presence of "crust zones" in offshore clay deposits has been documented in the last 10 years (Ehlers et al., 2005; Kuo and Bolton, 2009; Kuo, 2011; Kuo and Bolton, 2013; Yetniger et al., 2012; Peuchen, 2000; Palix et al., 2013) and Low et al. (2008). This crusts usually translate into a highly non-linear undrained shear strength profile, as indicated in figure 1.9, where the case of as stiff layer over a soft clay layer is presented. Although no definitive agreement seems to exist on a specific reason why these crusts form, many authors converge to causes such as overconsolidation, presence of bacteria and presence of invertebrate organisms. A significantly important issue lies in the fact that current method-

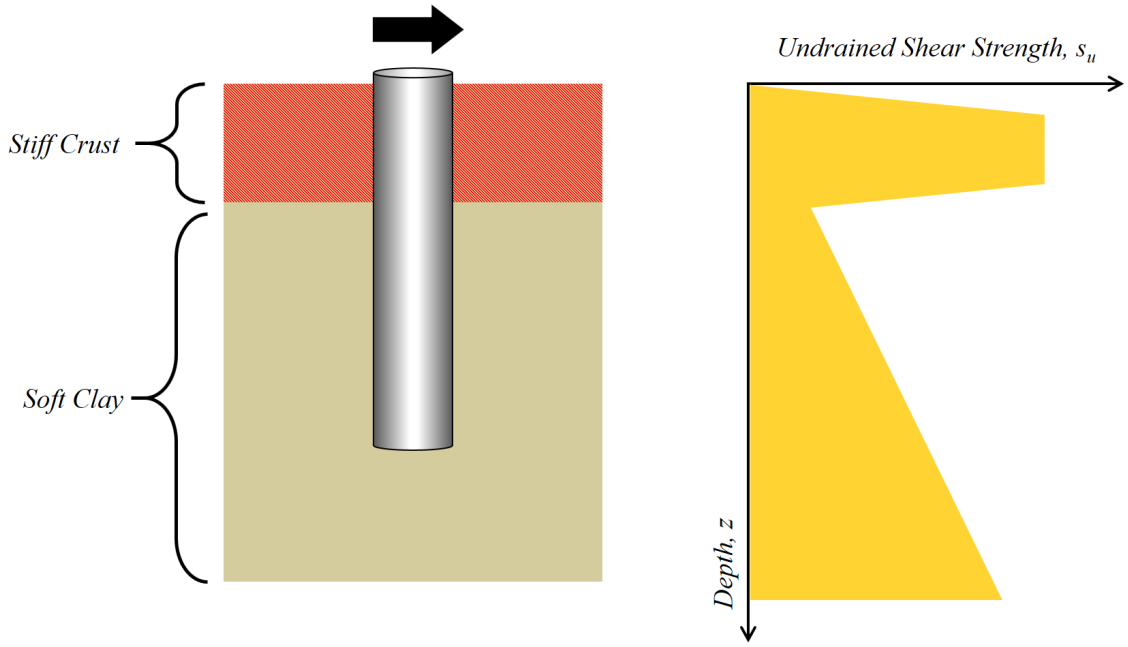


Figure 1.9: Illustrative diagram of soils with crust.

ologies for prediction of lateral bearing capacity of piles and caissons are based on idealized strength profiles. For cases of very long and slender piles, neglecting the crust might

be a conservative approach, however, things could change drastically if the foundation in question is a short caisson with aspect ratio less than 3.

The previously mentioned upper bound method (Murff and Hamilton, 1993) will be modified by incorporating several non-linear strength profiles. Results will be interpreted from the stand point of total capacity, but primarily as equivalent soil pressures. One question to answer is whether free surface effects are affected or not by the existence of the crust.

Parametric studies will be presented showing the effect of load attachment depth (i.e. directly associated with moment-horizontal load interaction) and aspect ratio. Finally, preliminary design recommendations will be made based on obtained results.

### 1.6.3 Dissipation of excess pore pressures after installation

Piles and suction caissons are widely used as foundations and anchors for offshore structures (e.g. tension leg platforms, spars, wind turbines). Installation of deep foundations (piles or caissons) in fine grained soils generally occurs under undrained conditions, generating excess pore pressures (EPPs) that reduce effective stress in the soil near the pile shaft with a corresponding reduction in load capacity. At the end of installation, these pore pressures slowly dissipate over time (i.e. radial consolidation), producing an increase in effective stress. This process is known as 'setup'. The process is illustrated in figure 1.10 Initial excess pore pressures due to installation disturbance will be predicted based on a strain path analysis based on a ring source moving at constant velocity in an incompressible medium. It is assumed that the setup occurs primarily due to dissipation of excess

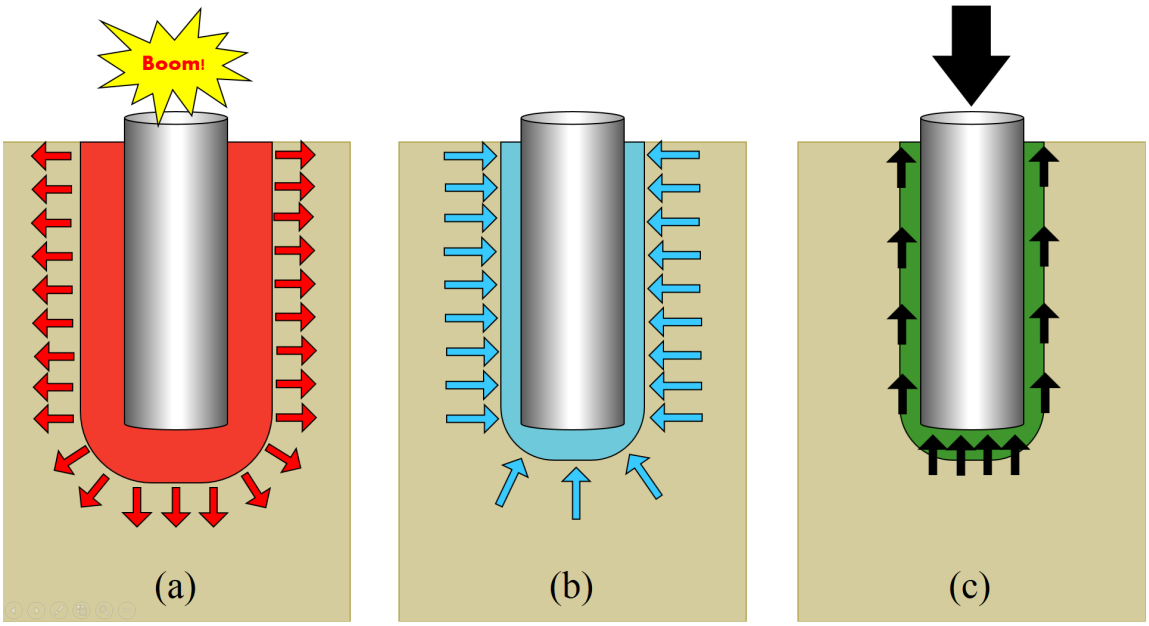


Figure 1.10: Typical stages of a pile foundation: (a) Installation, (b) Setup (or equilibration) and (c) loading. (After Randolph (2003))

pore pressures generated during the installation process; thixotropic effects are neglected. The analysis employs an elastic perfectly plastic model of soil behavior and an uncoupled analysis of consolidation to simulate conditions on the pile shaft outside of the influence of tip effects.

Parametric studies will be presented in order to asses the effects that wall thickness and soil rigidity index cold exert on setup times. Strain path solutions will be compared to both laboratory, centrifuge and field measurements of pore pressure dissipation around thin-walled piles typical of suction caissons.

# 2 THEORETICAL BACKGROUND

## 2.1 Fundamentals of Plasticity

Theory of plasticity is a topic that has been addressed in several bibliographic sources, which include textbooks (Prager, 1959; Hill, 1950; Calladine, 2000; Chen, 2008; Yu, 2006), doctoral dissertations (Han, 2002; Yang, 2008; Chi, 2010) and numerous journal articles.

Theory of plasticity has been a central element through the development of several solutions related to the field of geotechnical engineering (Murff, 2002). Major classes of solutions include upper bound analyses based on a kinematically admissible failure mechanism, lower bound solutions satisfying equilibrium, and limit equilibrium solutions based on intuitively plausible systems of forces or stresses.

Plasticity theory deals with situations where inelastic (i.e. permanent) deformations occur, which is termed "yielding". One branch of plasticity theory, plastic limit analysis (PLA), focuses on ultimate or collapse load of a structure or soil mass, with no information sought on behavior prior to the ultimate state. The work presented in Chapters 4 and 5 of this dissertation focuses exclusively on collapse loads, so a PLA framework is extensively used. The focus of the finite element analyses in Chapter 3 is also extensively on determining collapse loads. Although sub-yield behavior is not of interest in this study, the FE formulation requires an elastoplastic description of soil behavior. An elastoplastic soil model is therefore employed to permit implementation of the FE analysis, but the elastic

parameters have no influence on computed collapse loads.

Normally, elastoplastic behavior is idealized as presented follows: a straight inclined line indicates the elastic range and extents up to a yielding point after which there is increase of deformation without producing an increase in stress. Recognizing that such an idealization rarely represents true behavior of real materials, the reason behind it success is that analyses are significantly simplified while providing a reliable insight of the real material behavior (Murff, 2002).

Four are the fundamental elements required in order to define any plasticity model:

1. Yield criterion
2. Flow rule
3. Hardening Law, and
4. Elastic behavior beneath yield

Understanding of elements 1 and 2 is fundamental for the subject in study, thus a discussion on both topics is presented in the following sections.

### 2.1.1 Yield criterion and yield surface

The yield criterion or yield condition can be defined as the point (stress state) at which a material stops behaving elastically and starts exhibiting plastic deformations (Yu, 2006). In other words, the stress level at which the elastic limit is attained.

The simplest example of this is the yielding point presented in Figure 2.1, which represents the yield criterion for an idealized element under one-dimensional loading. For cases of two-dimensional loading, the yield criterion is defined as a curve (i.e. a series of

points) in a stress space. Finally, for three-dimensional loading the yield condition becomes a surface (i.e. a series of curves) also plotted in a stress space (Yu, 2006) .

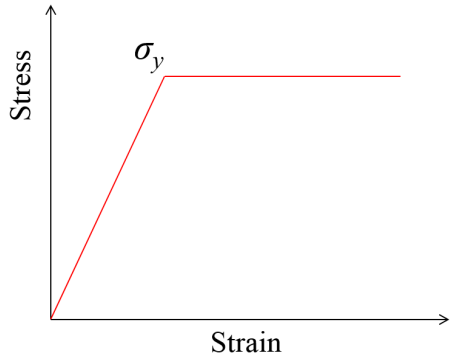


Figure 2.1: Linear-Elastic Perfectly-Plastic behavior

In soil analyses, yield surfaces typically are presented as function of stress states for different shearing modes. As Figure 2.2 illustrates, some of the soil under a spread footing will be under triaxial shearing, however, there is a section that has combined stress states. In these cases, stress state would fall at some point on or below the yield surface. There are several yield criteria that can be used to model different situations and yet, the yield surface of a given model does not necessarily match experimental data. Indeed, the form of a yield surface is very often driven by mathematical convenience (Aubeny, 2012 - Notes Adv Num Meth Geotech Engr).

In an isotropic material, the yield criterion is defined mathematically as:

$$f\left(\sigma_{ij}\right) = f\left(I_1, I_2, I_3\right) = 0 \tag{2.1}$$

Where variables $I_1$, $I_2$ and $I_3$ are the invariants of the stress tensor.

Some of the most common yield criteria are the Tresca and von Mises yield criterion.

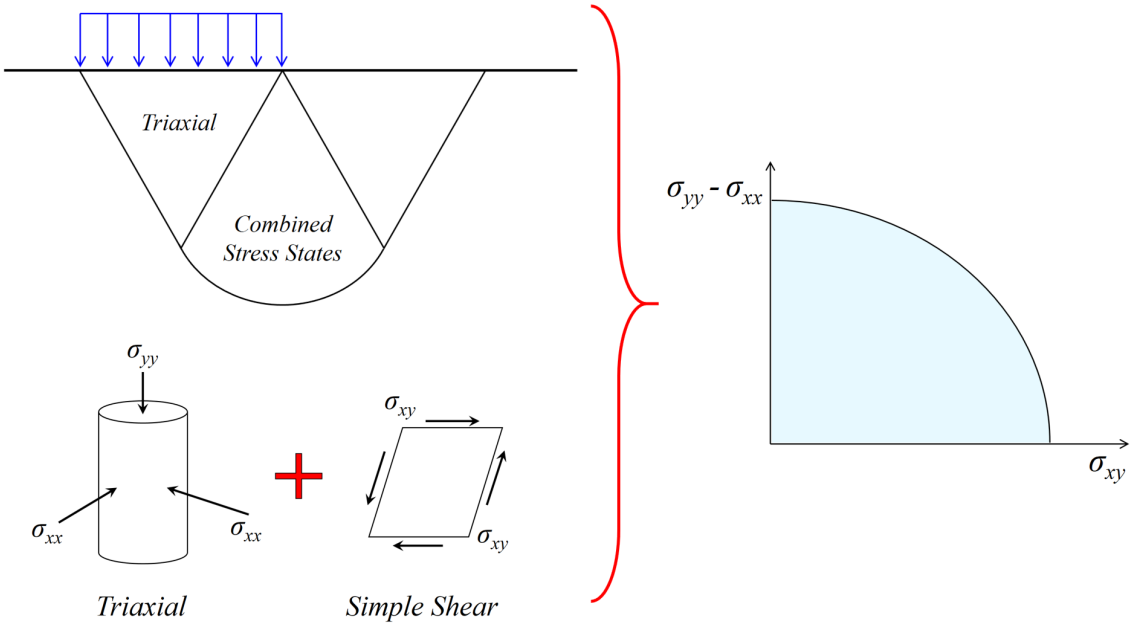


Figure 2.2: Soil analyses typically involve combined shearing modes. Triaxial and Simple shear diagrams are presented. Interaction diagram of both stress states is shown.

Tresca's criterion is expressed mathematically by as follows:

$$\frac{(\sigma_1 - \sigma_3)}{2} = s_u \tag{2.2}$$

And thus,

$$f = \sigma_1 - \sigma_3 - 2 \cdot s_u = 0 \tag{2.3}$$

Also, for computational efficiency, it becomes useful to express it as function of the second invariant of deviatoric stress tensor, $J_2$:

$$f = \sqrt{J_2}\cos\theta_l - s_u \tag{2.4}$$

Where $\theta_l$ is Lode's angle and is defined according to Eq.2.5 below (Yu, 2012):

$$\theta_l = \tan^{-1}\left[\frac{1}{\sqrt{3}} \cdot \left(\frac{2\sigma_3 - \sigma_1 - \sigma_2}{\sigma_1 - \sigma_2}\right)\right] \tag{2.5}$$

And the second invariant of the deviatoric stress tensor is given in term of principal stresses

as described in Eq.2.6 :

$$J_2 = \frac{1}{6}\left[(\sigma_1 - \sigma_2)^2 + (\sigma_2 - \sigma_3)^2 + (\sigma_3 - \sigma_1)^2\right] \tag{2.6}$$

or in terms of x-y-z stress components as presented in Eq.2.7:

$$J_2 = \frac{1}{6}\left[(\sigma_{xx} - \sigma_{yy})^2 + (\sigma_{yy} - \sigma_{zz})^2 + (\sigma_{zz} - \sigma_{xx})^2\right] + \sigma_{xy}^2 + \sigma_{yz}^2 + \sigma_{xz}^2 \tag{2.7}$$

Von Mises yield criterion is expressed in Eq. 2.8 as a function of the second invariant of the deviatoric stress tensor as well. The parameter $k$ present in the equation represents the undrained shear strength in a simple shear mode.

$$f = \sqrt{J_2} - k = 0 \tag{2.8}$$

Both von Mises and Tresca yield criteria are well suited to model the undrained behavior of saturated cohesive soils. Figure 2.3 presents a comparison between both failure surfaces. Tresca criterion plots like a hexagon whilst von Mises plots like a circle. This in general means that von Mises assumes slightly higher undrained strength than Tresca, asumming that the parameter $k$ is equal to the strength in a simple shear mode. However, one clear disadvantage of Tresca's yield criterion is that it is not differentiable at the corners, which tends to produce singularities that must be treated with care.

### 2.1.2 Flow rule

When the state of stress reaches the yield criterion ($f$) the material undergoes plastic deformations; this is also called plastic flow. The flow rule can be used to determine what portion of the strain increment is recoverable (elastic) and what portion is permanent. Flow rule is related to the plastic potential function $g(\sigma_{ij})$, and it is defined by the equation

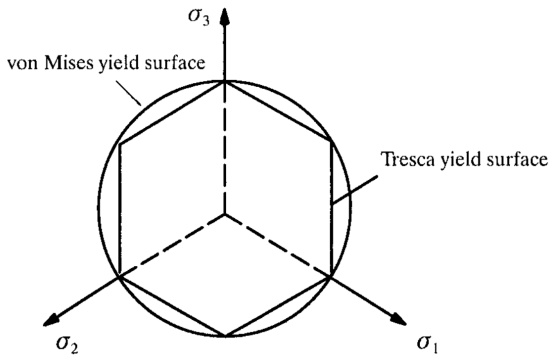


Figure 2.3: Comparison of Tresca and von Mises yield surfaces in a stress space.

presented below (2.9). This is also illustrated in Figure 2.4.

$$\dot{\varepsilon}_{ij}^{P} = \lambda \frac{\partial g(\sigma_{ij})}{\partial \sigma_{ij}} \tag{2.9}$$

Where $\lambda$ is a scalar multiplier and $\dot{\varepsilon}_{ij}^{P}$ is the plastic strain rate.

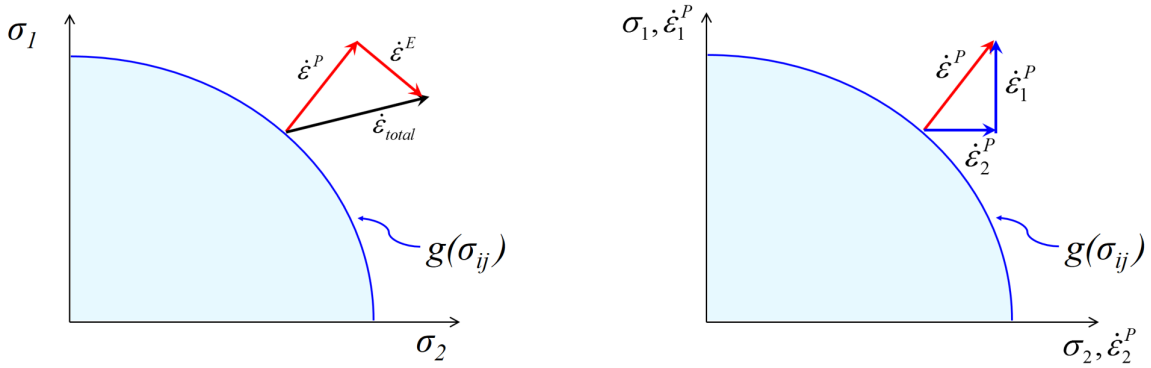


(a) (b)

Figure 2.4: Illustration of plastic potential functions.

The direction of plastic strain vectors is defined through a flow rule by assuming the existence of a plastic potential function to which the incremental strain vectors are orthogonal. For some materials, the plastic potential function $g$ and the yield function $f$

can be assumed to be the same. Such materials are considered to follow the associative flow rule of plasticity. However, for many geologic materials, the yield function $f$ and the plastic potential function $Q$ are often different. These materials are considered to follow non-associative flow rules of plasticity.

Typically, for the purpose of mathematical simplicity, an associated flow rule is assumed: this implies that plastic strains occur perpendicularly to the failure surface. However this assumption is not necessarily valid.

## 2.2 Bound Theorems

There are two principal bound theorems in plasticity. The lower bound theorem involves guessing a stress field that leads to a lower bound estimate of the collapse load. On the other hand, the upper bound theorem involves guessing a velocity (or displacement) field that allows computation of upper bound estimate of collapse load. Formal definitions of both theorems are presented below:

- ***Lower Bound Theorem***: If any stress distribution throughout the structure can be found which is everywhere in equilibrium internally and balances certain external loads and at the same time does not violate the yield criterion, those loads will be carried safely by the structure.
- ***Upper Bound Theorem***: If an estimate of the plastic collapse load of a body is made by equating internal rate of dissipation of energy to the rate at which external forces do work in any postulated mechanism of deformation of the body, the estimate will

be either high or correct.

The upper bond method is in general much easier to implement. It allows for incorporation of soil strength non-homogeneity and even anisotropic properties. This theorem (upper bound) is a major building block of the research contained in this dissertation. For that reason the following two sections will be devoted to explaining formulation and application of upper bound methods to problems of interest.

## 2.3 Upper Bound Theorem

There is a well defined series of steps needed in order to apply the upper bound method. They are described below:

1. Establish a yield criterion. An associated flow rule must be assumed.
2. Postulate a kinematically admissible collapse mechanism. Within the mechanism, the unknown load $F$ should be defined and it is assumed to move at a virtual velocity, $v_0$
3. Derive strain rate fields. They need to be associated with the virtual velocity ($v_0$) and ensured to satisfy strain compatibility at any point.
4. Determine of internal energy dissipation rate as a function of the strain rate.
5. Compute rate of external work
6. Solve for the unknown force by equating external virtual work to virtual energy dissipation rates.
7. Optimize collapse mechanism. The solution must be optimized with respect to ge-

ometrical parameters that define the mechanism in order to obtain the configuration that produces the minimum force.

In order to use it a collapse mechanism needs to be guessed. This is typically the most delicate step of the analysis. It requires intuition or usage of known solutions with slight modifications. The mechanism considered must be continuous (i.e. no gaps can open up within the body) but can contain slip surfaces where all the motion is tangential to the surface.

The mechanism must be kinematically admissible. This is: it must satisfy kinematic constraints. For example: if a boundary is rigid (or fixed) the mechanism cannot violate this condition. If a footing or pipe is rigid and is pushed into the deforming material, the deforming material must be compatible, which usually means that the normal velocity of the footing and the deforming material at the interface are equal (Murff, 2002).

By equating external work to internal energy dissipation one can solve for the unknown load or load scale factor. The answer is guaranteed to be greater or equal than the actual collapse load or load scale factor.

Step 4 outlined above is one that requires special attention, since it involves working out mathematical expressions for virtual energy dissipations of stresses based on strains. The following section presents a detailed overview of this step.

### 2.3.1 Calculation of energy dissipations

Two main cases need to be reviewed in order to continue ahead on this work:

1. Energy dissipation rates in continuously deforming regions, and

2. Energy dissipation rates in slip surfaces

Mathematical expressions needed for these procedures have been widely explained by Dr. James D. Murff on his Geomechanics course notes (Murff, 2002) and summarized by several authors (Han, 2002; Shi, 2005; Yang, 2008; Chi, 2010; Sharma, 2004). However, skipping explanation of these concepts would make this document incomplete. For this reason the following section is devoted to this topic.

### 2.3.2 Energy dissipation rates in continuously deforming regions

Consider an element similar to the one presented in Figure 2.5, which is under a plane strain state. If the material is assumed to be under yielding conditions, then the criterion presented in Eq.2.10 applies (Murff, 2002).

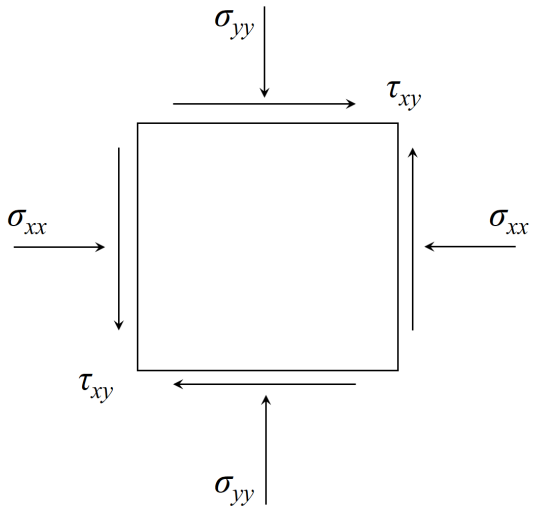


Figure 2.5: Element under study

$$f = \left[ \frac{(\sigma_{xx} - \sigma_{yy})^2}{4} + \frac{1}{2}\tau_{xy}^2 + \frac{1}{2}\tau_{yx}^2 \right]^{1/2} - s_u = 0 \tag{2.10}$$

And, thus, re-arranging the equation, the undrained shear strength ($s_u$) is expressed as presented below (Eq.2.11):

$$s_u = \left[ \frac{(\sigma_{xx} - \sigma_{yy})^2}{4} + \frac{1}{2}\tau_{xy}^2 + \frac{1}{2}\tau_{yx}^2 \right]^{1/2} \tag{2.11}$$

Where:

- $\sigma_{xx}, \sigma_{yy}$ are the normal stresses and $\tau_{xy}, \tau_{yx}$ are shear stresses.
- $s_u$ is the undrained shear strength
- $f$ is the yield function, equaled to zero when the element reaches plastic flow.

By assuming an associated flow rule, plastic strains in 2 dimensions can be expressed as indicated in Eq.2.12, 2.13 and 2.14. The variable $\lambda$ is a scalar parameter (proportionality constant) which depends on the constraints near the point in study.

$$\dot{\varepsilon}_{xx} = \lambda \frac{\partial f}{\partial \sigma_{xx}} = \frac{1}{2}\lambda \left[ \frac{(\sigma_{xx} - \sigma_{yy})^2}{4} + \frac{1}{2}\tau_{xy}^2 + \frac{1}{2}\tau_{yx}^2 \right]^{-1/2} \cdot \frac{2(\sigma_{xx} - \sigma_{yy})}{4} \tag{2.12}$$

$$\dot{\varepsilon}_{yy} = \lambda \frac{\partial f}{\partial \sigma_{yy}} = \frac{1}{2}\lambda \left[ \frac{(\sigma_{xx} - \sigma_{yy})^2}{4} + \frac{1}{2}\tau_{xy}^2 + \frac{1}{2}\tau_{yx}^2 \right]^{-1/2} \cdot \frac{2(\sigma_{yy} - \sigma_{xx})}{4} \tag{2.13}$$

$$\dot{\varepsilon}_{xy} = \lambda \frac{\partial f}{\partial \tau_{xy}} = \frac{1}{2}\lambda \left[ \frac{(\sigma_{xx} - \sigma_{yy})^2}{4} + \frac{1}{2}\tau_{xy}^2 + \frac{1}{2}\tau_{yx}^2 \right]^{-1/2} \tau_{xy} \tag{2.14}$$

Equations 2.12 through 2.14 can be significantly simplified by combining them with Eq. 2.11, as presented below:

$$\dot{\varepsilon}_{xx} = \frac{\lambda}{4 s_u} \cdot (\sigma_{xx} - \sigma_{yy}) \tag{2.15}$$

$$\dot{\varepsilon}_{yy} = \frac{\lambda}{4 s_u} \cdot (\sigma_{yy} - \sigma_{xx}) \tag{2.16}$$

$$\dot{\varepsilon}_{xy} = \dot{\varepsilon}_{yx} = \frac{\lambda}{2 s_u} \cdot \tau_{xy} \tag{2.17}$$

At this point, it is useful to recall the expression describing volumetric strain rate of cohesive undrained media (Eq. 2.18), which has to be equal to zero, basically stating that the material is incompressible. The failure mechanism also needs to comply with these constraints.

$$\dot{\varepsilon}_v = \dot{\varepsilon}_{xx} + \dot{\varepsilon}_{yy} = \frac{\partial \dot{u}}{\partial x} + \frac{\partial \dot{v}}{\partial y} = 0 \tag{2.18}$$

Energy dissipation rate can be computed as presented in Eq. 2.19:

$$\dot{D} = \sigma_{ij} \dot{\varepsilon}_{ij}^{P} \tag{2.19}$$

This equation expresses dissipation rate as the inner product of both the stress tensor $\sigma_{ij}$ and the plastic strains tensor $\dot{\varepsilon}_{ij}^{P}$, which could have either 4 or 9 components depending on whether the problem is 2 or 3-dimensional.

The plastic strain rates are given by equation 2.20

$$\dot{\varepsilon}_{ij}^{P} = \lambda \frac{\partial f}{\partial \sigma_{ij}} \tag{2.20}$$

Therefore, substituting Eq.2.20 back into Eq. 2.19 produces the expression shown in Eq. 2.21

$$\dot{D} = \lambda \sigma_{ij} \frac{\partial f}{\partial \sigma_{ij}} \tag{2.21}$$

The mathematical operation indicated in Eq. 2.21 can be completed by using definitions previously presented in Eq. 2.10, Eq.2.11 and Eqs.2.15 through 2.17. The procedure is described below in Eqs.2.22 through 2.25. The dissipation rate is finally given by Eq. 2.25.

$$\dot{D} = \lambda \left\{ \left[ \sigma_{xx} \frac{(\sigma_{xx} - \sigma_{yy})}{4 s_u} \right] + \left[ \sigma_{yy} \frac{(\sigma_{yy} - \sigma_{xx})}{4 s_u} \right] + \tau_{xy} \frac{\tau_{xy}}{2 s_u} + \tau_{yx} \frac{\tau_{yx}}{2 s_u} \right\} \tag{2.22}$$

$$\dot{D} = \frac{\lambda}{4 s_u} \left\{ (\sigma_{xx} - \sigma_{yy})^2 + 2\tau_{xy}^2 + 2\tau_{yx}^2 \right\} \tag{2.23}$$

$$\dot{D} = \frac{\lambda}{s_u} \left\{ \frac{(\sigma_{xx} - \sigma_{yy})^2}{4} + \frac{\tau_{xy}^2}{2} \tau + \frac{\tau_{yx}^2}{2} \right\} \tag{2.24}$$

$$\dot{D} = \frac{\lambda}{s_u} s_u^2 = \lambda s_u \tag{2.25}$$

It becomes now necessary to compute an expression for the scalar multiplier $\lambda$. Equations 2.15 through 2.17 can be inverted in order to obtain expresions for deviatoric stress and shear stress as a function of $\lambda$.

$$(\sigma_{xx} - \sigma_{yy}) = \frac{4 s_u}{\lambda} \dot{\varepsilon}_{xx}^P \tag{2.26}$$

$$(\sigma_{yy} - \sigma_{xx}) = \frac{4 s_u}{\lambda} \dot{\varepsilon}_{yy}^P \tag{2.27}$$

$$\tau_{xy} = \frac{2 s_u}{\lambda} \dot{\varepsilon}_{xy}^P \tag{2.28}$$

These three equations (2.26 through 2.28) can be substituted into the yield criterion in order to obtain an expression for $\lambda$. Notice that in Eq.2.29 below, the variable $\dot{\varepsilon}_{xy}^P$ has been temporarily replaced by $\underline{\dot{\varepsilon}}_{xx}$.

$$\lambda = \left( 2\underline{\dot{\varepsilon}}_{xx}^2 + 2\underline{\dot{\varepsilon}}_{yy}^2 + 2\underline{\dot{\varepsilon}}_{xy}^2 + 2\underline{\dot{\varepsilon}}_{yx}^2 \right)^{1/2} \quad where \quad \underline{\dot{\varepsilon}}_{xx}^2 \equiv \left( \dot{\varepsilon}_{xx}^P \right)^2 \tag{2.29}$$

Using Equations 2.25 and 2.29, and taking into account that $\dot{\varepsilon}^P_{xx} = -\dot{\varepsilon}^P_{yy}$ and $\dot{\varepsilon}^P_{xy} = \dot{\varepsilon}^P_{yx}$, the dissipation can be re-written as:

$$\dot{D} = 2s_u\left(\underline{\dot{\varepsilon}}^2_{xx} + \underline{\dot{\varepsilon}}^2_{xy}\right)^{1/2} \tag{2.30}$$

Which is the energy dissipation rate for the 2-dimensional problem in study. For general 3-dimensional problems (as is the case of the collapse mechanism to be considered in this study) the following expressions can be derived for both von Mises and Tresca's criteria respectively:

$$\dot{D} = s_u\left(2\dot{\varepsilon}^P_{ij}\dot{\varepsilon}^P_{ij}\right)^{1/2} \tag{2.31}$$

$$\dot{D} = 2s_u\left|\dot{\varepsilon}^P\right|_{\max} \tag{2.32}$$

### 2.3.3 Energy dissipation rates in slip surfaces

A somewhat similar relationship can be derived for the case of slip surfaces. The derivation is based on equations used in the previous section. Figure 2.6 presents a system of two rigid blocks in which the bottom block is static while the upper block moves horizontally at a velocity $v_0$. In between the rigid blocks there is a region of unit width and thickness $t$. Velocities for the deforming region are also given in Fig. 2.6.

In this case, the only strain components that take a value (non-zero) are $\dot{\varepsilon}^P_{xy}$ and $\dot{\varepsilon}^P_{yx}$, thus, the maximum shear strain can be described as presented in Eq.2.33.

$$\dot{\varepsilon}^P_{\max} = \dot{\varepsilon}^P_{xy} = \dot{\varepsilon}^P_{yx} = \frac{1}{2}\left(\frac{\partial v_x}{\partial y} + \frac{\partial v_y}{\partial x}\right) = \frac{1}{2}\frac{v_0}{t} \tag{2.33}$$

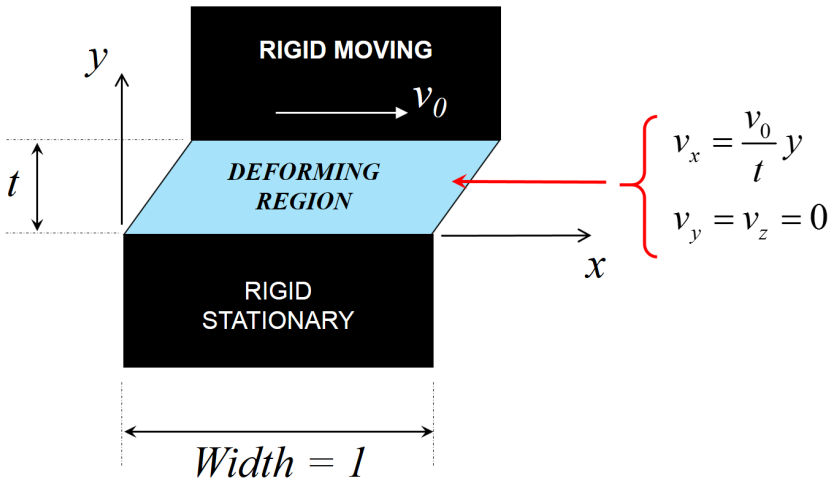


Figure 2.6: System of two rigid blocks with a deforming region in between.

Assuming a von Mises yield criterion, the dissipation rate can be then expressed as function of the velocity field (Eq. 2.34)using the postulate presented in Eq.2.31. Note that the dissipation rate becomes a function of the undrained shear strength and the thickness of the deforming region.

$$\dot{D} = 2s_u \left[ \left( \frac{1}{2} \frac{v_0}{t} \right)^2 \right]^{1/2} = s_u \frac{v_0}{t} \tag{2.34}$$

Finally, the total energy dissipation rate is obtained by calculation a volumetric integral, presented in Eq. 2.35. It is observed that as the thickness ($t$) vanishes, the dissipation rate is simpli the product of the undrained shear strength and the velocity ($v0$).

$$\dot{D}_{Total} = \int_V \dot{D} dV = \dot{D} \cdot V = s_u \frac{v_0}{t} (1 \cdot t) = s_u v_0 \tag{2.35}$$

Both approaches: dissipation on continuously deforming regions and dissipation oc-

curring in slip surfaces will be extensively used in the next chapters.

## 2.4 Capacity of Laterally Loaded Piles and Caissons

Broms (1964) carried out some of the earliest studies dealing with laterally loaded piles. The ultimate resisting force acting along a vertical distance $\Delta z$ was defined as function of the net horizontal force per projected unit area of the pile ($P$) and the diameter of the pile ($D$):

$$\Delta H = PD\Delta z \tag{2.36}$$

Assuming a purely cohesive soil, the side resistance $P$ and the undrained shear strength $s_u$ can be related by introducing a dimensionless bearing factor $N_{ps}$, in such a way that $P = N_{ps}s_u$. Subsequent works made by Matlock (1970) and Reese et al. (1975) used empirical estimates of $N_{ps}$.

Randolph and Houlsby (1984) introduced a solution for predicting the lateral load capacity of piles by using classical plasticity theory. The solution considers the idealized situation of a rigid cylinder translating under plane strain conditions. Although several adhesions (i.e. friction between the cylinder and surrounding soil) are considered, the two limiting conditions are the most important ones: (1) full adhesion between the pile and the surrounding soil and (2) no adhesion between soil and pile (Fig.2.7). The results of these investigations showed that for those two cases, the bearing factor $N_{ps}$ are equal to 11.94 and 9.14 respectively. In recent years, Martin and Randolph (2006) revised the bearing factor for no-adhesion and corrected this number to be 9.2 instead of 9.14. It is important

to remark that, given the aforementioned idealization, this solution can only predict the lateral resistance at a depth sufficiently large so that the free surface effects can be ignored.

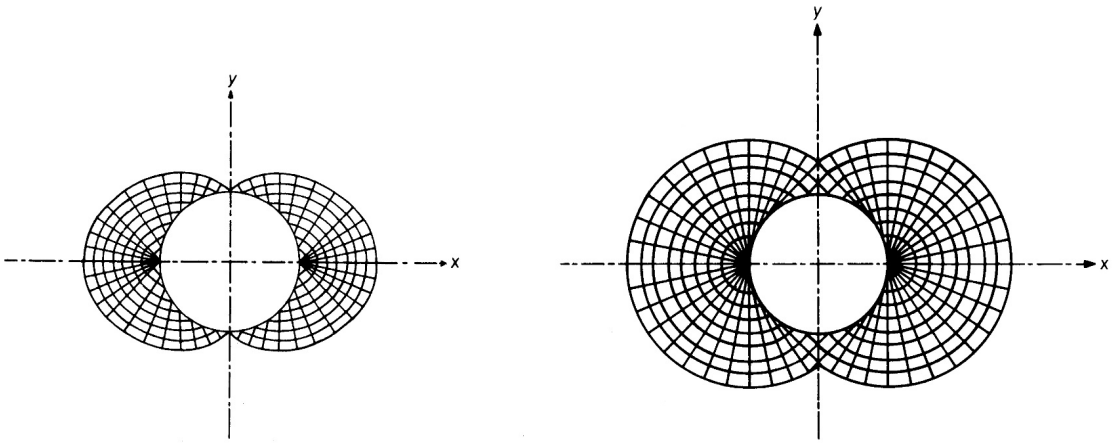


Figure 2.7: Randolph and Houlsby (1984) slip lines analyses: (left) no adhesion and (right) Full Adhesion.

Later, Murff and Hamilton (1993) proposed a three-dimensional upper bound plastic limit formulation for the analysis of the ultimate capacity of laterally loaded piles under undrained conditions. They extended the analysis in order to account for the strength reduction effects produced by the free surface condition (at the top of the pile) and for the tip resistance (at the bottom of the pile).

The behavior of piles and caissons subject to combined loading has been widely studied by a number of authors Tan (1990); Murff (1994); Houlsby and Martin (1992); Bransby and Randolph (1998). Plasticity methods have been used to formulate yield loci for combined loading response. Empirically fitted yield loci based on centrifuge or 1 g model tests have also been proposed Martin (1994); Murff (1994); Dean et al. (1992).

Caisson (Aspect ratio, $L_f/D = 1$) and spudcan response in normally consolidated clay was studied by Cassidy and Byrne (2001) and Cassidy (2012) using the drum centrifuge at the University of Western Australia. Martin (2001) investigated the vertical bearing capacity of shallow skirted foundations using lower and upper bounds of plasticity and presented results of a parametric study in the form of dimensionless charts which compared well with findings by Villalobos et al. (2009).

Failure envelopes have been studied in detail for caissons with aspect ratios ($L_f$/D) of one (Gourvenec, 2007, 2008) and five (Zhang et al., 2011; Lau, 2015) based on finite element results and centrifuge tests. The ultimate capacity under monotonic load for aspect ratio of 5 was found to be comparable to calculations based on existing design methods, including theoretical plasticity solutions and empirical methods Zhang et al. (2011).

The complex interaction of vertical, horizontal and moment loads is further influenced by a dependence on soil strength profile. The analysis by Randolph is also relevant to the vertical insertion or extraction of a T-bar penetrometer (Stewart and Randolph, 1991) which was used to characterize strength in these experiments.

### 2.4.1 Upper bound analysis of laterally loaded piles

Murff and Hamilton (1993) presented a three dimensional upper bound plastic limit analysis method for the computation of the ultimate undrained capacity of laterally loaded long piles (Grajales et al., 2015). The collapse mechanism comprises three regions (Figure 2.8): a surface failure wedge, a plane strain flow around zone and a spherical failure surface. Expressions for internal energy dissipation were derived based on kinematically

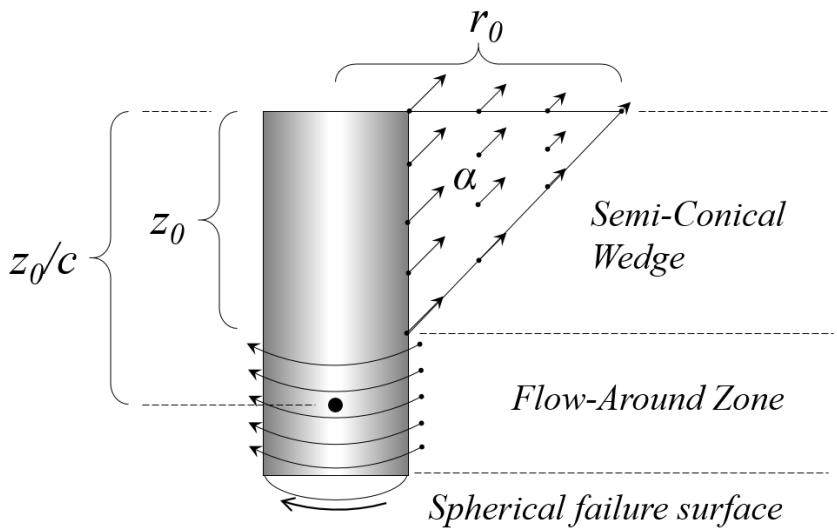


Figure 2.8: Three dimensional collapse mechanism proposed by Murff and Hamilton (1993)

admissible velocity fields in the surface failure wedge and in the spherical failure surface at the tip. Meanwhile, the energy dissipation occurring in the flow around zone was computed using the Randolph and Houlsby (1984) approach.

Since compatibility is not enforced between the three regions of the collapse mechanism and since the flow around zone does not behave purely in a plane strain mode (except for the case of a fully translated pile or caisson, with no rotation), the Murff and Hamilton (1993) solution is not strictly speaking a rigorous upper bound solution. However the model has been used extensively in the industry and also several authors (Randolph et al., 1998; Sukumaran and McCarron, 1999; Aubeny et al., 2001a) have validated the model using both numerical approximations and experimental results.

Some of the additional features of the Murff and Hamilton (1993) formulation are (Aubeny and Murff, 2005):

1. It considers rotation of the pile or caisson about a point located at a depth $L_0$
2. The model can accommodate the development of a plastic hinge in the pile. This is useful when long piles are the subjects of study, however it is not relevant for short piles or caissons.
3. It can model various conditions such as soil-pile interface adhesion, suction on the windward side of the pile and soil stratification.
4. The model considers four optimization parameters: (1) the depth of the center of rotation, (2) the depth of the wedge, (3) the radial extent of the top of the wedge and (4) the radial variation of velocity along the wedge.

After performing a parametric study two main conclusions yielded: (1) the equivalent soil resistance distribution $N_{ps}$ is independent of the depth of the center of rotation and (2) $N_{ps}$ is a function of the depth z.

The original analysis was performed by doing optimization of several variable parameters. Finally, a simplified expression for equivalent lateral bearing factors was proposed as shown in Eq.2.37:

$$N_p = \frac{\Delta F}{s_u D \Delta L_f} \tag{2.37}$$

where $s_u$ is the undrained shear strength at the depth in question, $D$ is the caisson diameter, $\Delta L_f$ is an increment in length (depth) of the caisson, and $\Delta F$ is the increase in lateral capacity for pure translation of the caisson corresponding to the increment in length. Their study also showed that predicted lateral resistance profiles for translating and rotating caissons are similar (i.e. the resistance is independent of the location of the center of rotation). This

is consistent with methods based on equivalent p-y curves or semi empirical models Matlock (1970); Reese et al. (1975). Murff and Hamilton (1993) also compared their bearing factors to centrifuge data carried out by Hamilton et al. (1991) and found good agreement.

### 2.4.2 Simplified virtual work analysis

Based on Murff and Hamilton (1993) upper bound formulation, Aubeny et al. (2001a) presented a simplified approach to predict lateral capacity (Figure 2.9). This simplified model considers the usage of one optimization parameter (the depth to the center of rotation) instead of the four used by the original Murff and Hamilton model.

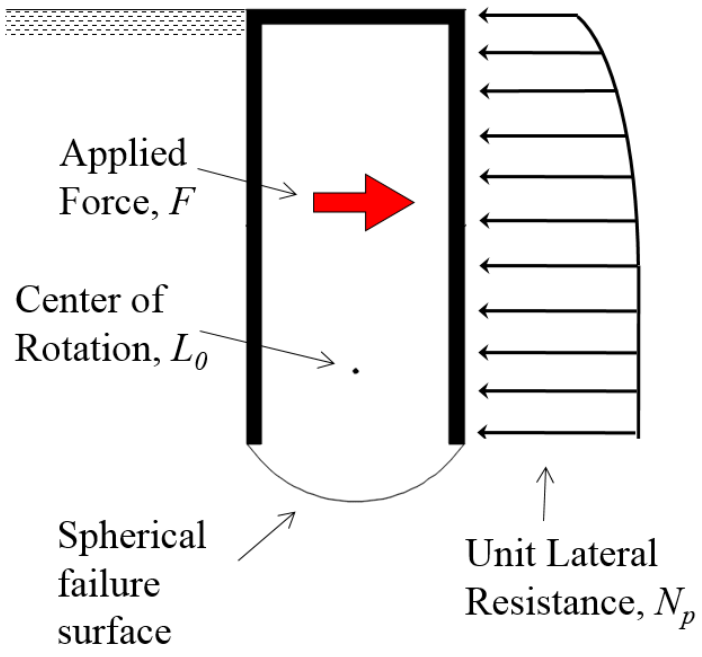


Figure 2.9: Simplified failure mechanism for analysis by Aubeny et al. (2001a)

A virtual velocity field is assumed (Figure 2.10(a)), in which the velocity varies linearly with the depth. The internal rate of energy dissipation is computed by integrating the product of the mobilized pressure multiplied by the velocity and the elemental area

along the projected side area of the caisson.

The virtual work analysis assumes the pile rotates as a rigid body about a center of rotation ($L_0$). The energy dissipation rate from side resistance can be calculated in terms of (1) a linear distribution in velocity about a depth to the center of rotation $L_0$, (2) the Murff-Hamilton soil resistance function $N_{ps}(z)$, and (3) the undrained shear strength profile $s_u(z)$. The depth $L_0$ to the center of rotation is an optimization variable to be determined. The bearing resistance function is assumed to apply to both forward and reverse motions of the caisson. Although the analysis can proceed in terms of an arbitrary strength profile $s_u(z)$, evaluation of the $N_{ps}(z)$ profile requires an approximate linearization of the profile to obtain the $\eta$ factor. The energy dissipation rate due to side resistance is computed using the following integral (Eq. 2.38):

$$\dot{D}_s = \int \dot{\beta}\, N_{ps}(z)\, |L_0 - z|\, s_u(z) D\, dz \tag{2.38}$$

Where $\dot{\beta}$ is an angular velocity at the center of rotation and is directly related to the velocity $v_0$ previously mentioned for Murff and Hamilton (1993).

### 2.4.3 Inclined loading

Aubeny et al. (2003) extended this lateral load capacity analysis: in order to consider inclined loading the velocity field used in the previous formulation (Aubeny et al., 2001a) was modified to incorporate vertical velocities (Figure 2.10(b)). This approach can evaluate for load orientations ranging from vertical to horizontal. Also, the load attachment depth can be at any point along the center or wall of the caisson.

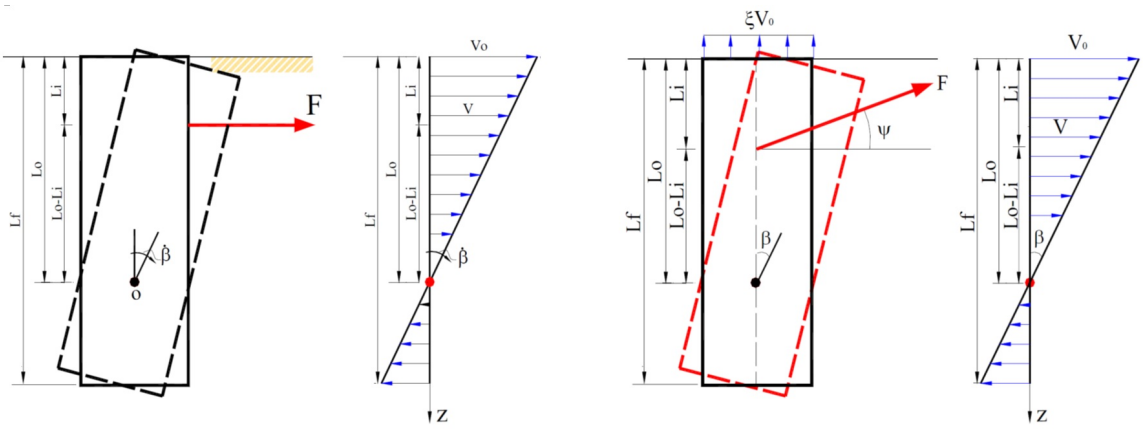


Figure 2.10: Failure mechanisms for simplified methods: (a)Aubeny et al. (2001a) and (b)Aubeny et al. (2003). Source: Han (2002)

In order to validate the predicted capacities for axial and lateral capacities three-dimensional finite element studies were conducted. From interpretation of those studies an interaction diagram was developed for axial and lateral resistance bearing factors, with values of around 3 for pure axial loading and 12 for horizontal loading. The FEM solutions showed reasonable results when relatively slender caissons were considered ($6 < L_f/D < 10$). However, for short caissons ($L_f/D \approx 2$) are considered, the FEM predictions suggest that the limit formulations become less reliable, since it over predicts the capacity (Aubeny et al., 2003). This is illustrated in Figure 2.11.

### 2.4.4 Tip resistance

The tip resistance contribution is also a relatively important aspect to consider, more significantly when dealing with short stubby caissons. When larger caissons are considered, the tip resistance becomes less important. As it was previously pointed, Murff and

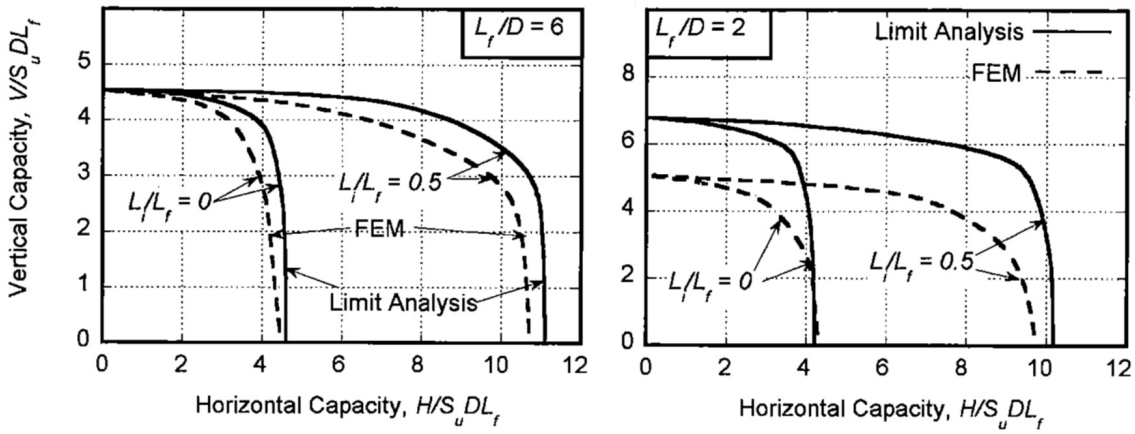


Figure 2.11: Plastic limit analyses and FEM solutions for uniform soil strength profiles. Source: Aubeny et al. (2003)

Hamilton Murff and Hamilton (1993) suggested a spherical failure surface at the tip, which assumes a rotating spherical mass of soil located at the bottom of the caisson. This solution considers by default the interaction between the horizontal and the moment resistance.

Aubeny et al. (2001a) introduced a simplified equation in order to account for the interaction between the vertical load and the moment load. This empirical function was originally introduced by Bransby and Randolph (1998) and it accounts for the interaction between horizontal, vertical and moment loads.

In 2002, Randolph and House (2002) published an analysis technique (AGSPANC) with the purpose of predicting capacity of suction caissons under combined loading conditions (vertical and horizontal). Their program is based on a 3-dimensional collapse mechanism somewhat similar to that presented by Murff and Hamilton (1993). This mechanism is shown in Fig. 2.12 main difference between both is the way in which Randolph and House (2002) compute end resistance for cases of forward rotation (e.g. load attached at

the mudline, caisson tilts forward). The collapse mechanism comprised active and pas-

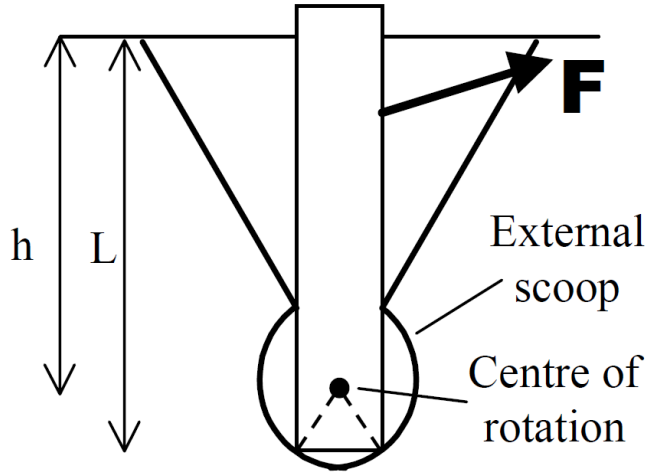


Figure 2.12: Elements of collapse mechanism proposed by Randolph and House (2002)

sive failure wedges (similar to those by Murff-Hamilton) and a failure mechanism in the form of a scoop. On the other hand, the mechanism for backward rotation is similar to the one used by Murff and Hamilton (1993). Nevertheless, dissipation equations for the scoop mechanism and internal deformation of wedges were not provided. Their method has been througly validated by comparisons to both finite element predictions and geotechnical centrifuge experiments.

## 2.5 Capacity of Laterally Loaded Piles in Stratified Soils

Layered soil profiles are regularly found in offshore areas. Several researchers have developed predictive models to simulate the behavior of laterally loaded piles in such soils including those of Davisson and Gill (1963); Khadilkar et al. (1973); Naik and Peyrot (1976) and Georgiadis (1983).

Murff and Hamilton (1993) developed analyses and presented a validation of the current $N_{ps}$ function for a two-layered soil system with different uniform strengths by using the approach presented by Georgiadis (1983). A comparison of lateral resistance calculated by the formal upper bound method and the empirical equation was developed. Caution was recommended, since relatively large errors seemed to occur to cases with high variations in strength from one layer to another one.

In recent years, several researchers have proposed methods to approach the problem by using analytical tools (Yang and Jeremic, 2005; Rani and Prashant, 2015; Zhang et al., 2015) and upper bound methods (Yu et al., 2015).

## 2.6 Undrained Shear Strength of Marine Clay Deposits

### 2.6.1 Common practice: linearly increasing strength profiles

Different types of cohesive soil strength profiles will be used as reference for this study. It is very common to idealize strength profiles as linearly increasing relationships which are depth dependent. However, such characterizations need to be based on actual data measured with either field or laboratory equipment.

Soils representing different regions around the world are considered. Gulf of Mexico clays have been widely studied by several researchers (Aubeny et al., 2001b; Bogard, 2001; Jeanjean, 2006; Murali, 2011). A sample profile obtained from Liedtke et al. (2006) is shown below (Fig.2.13). West Africa marine clays have also been the focus of a significant amount of research during the last ten years (Colliat et al., 2011).

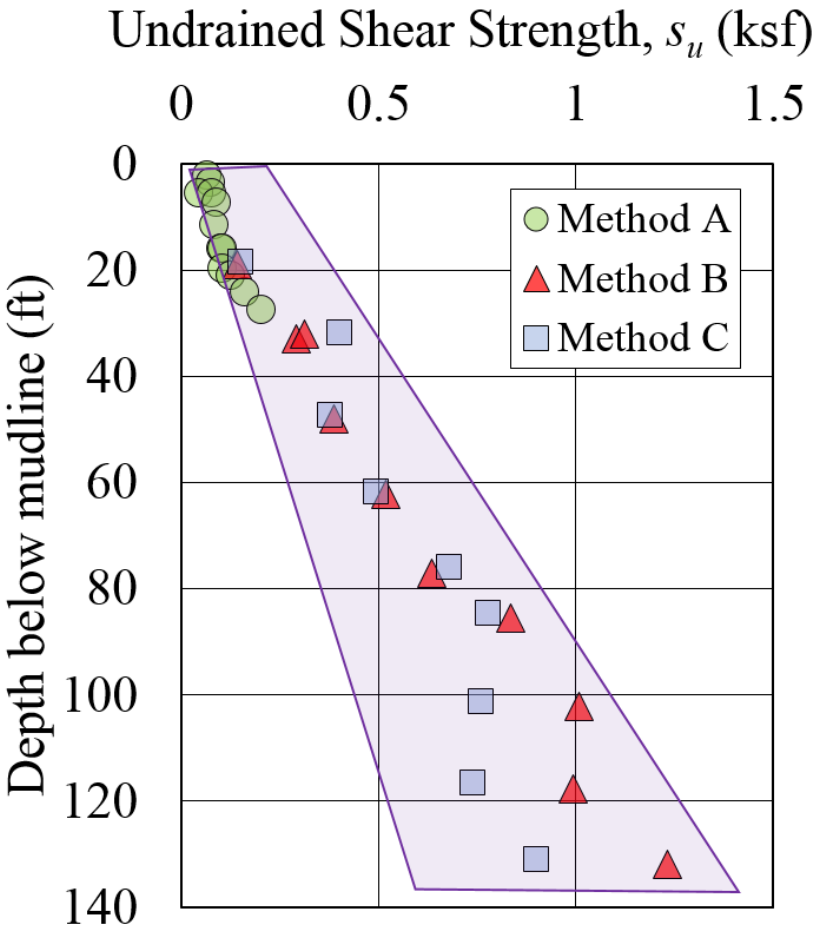


Figure 2.13: Undrained shear strength profiles from cone penetration test, seabed vane, torvane and miniature vane. After Liedtke et al. (2006)

Table 2.1, presents a summary of strength parameters as reported by different researchers. Along the next chapters, strength profiles in accordance with the ones presented in Table 2.1 will be assumed, in order to make computations based on realistic data.

In Table 2.1, $s_{u0}$ is the undrained shear strength at the mudline level; $k$ is the strength gradient; $\gamma'$ is the submerged unit weight and the following locations are included: Gulf of Mexico (GoM), West Africa (WA), North Sea (NS) and Bothkennar, Scotland (BS).

Table 2.1: Some examples of undrained shear strength profiles based on measured data

| Source | $s_{u0}$ (kPa) | $k$ (kPa/m) | $\gamma'$ (kN/m$^3$) | Location* |
|---|---|---|---|---|
| Aubeny et al. (2001b) | 0 to 6.97 | 1.2 to 1.4 | | GoM |
| Schroeder et al. (2006)<br>Schroeder and Resseguier (2015) | $\approx$ 3.3 | 0.8 to 1.7 | 4 to 7 | GoM |
| Schroeder and Resseguier (2015)<br>Puech et al. (2005) | $\approx$ 2.4 | $\approx$ 1.6 | $\approx$ 3.5 | WA |
| Aubeny et al. (2001b)<br>Schroeder and Resseguier (2015) | $\approx$ 4.0 | 2.1 to 2.4 | 6.3 to 7 | NS |
| Boylan et al. (2007) | 5 to 15 | 1 to 2.3 | 5.2 to 7.2 | BS |

Density (i.e. unit weight) is another important element for this study. Although it is recognized that soil density is a property highly influenced by factors such as stress history, confinement and water content. The ratio of the buoyant unit weight and the strength gradient ($\gamma_b/k$) is a non-dimensional parameter that controls behavior in several upper bound models.

### 2.6.2 Stratification in deep-water soil deposits: soils with crust

Existing simplified methods for the prediction of the behavior of laterally loaded piles typically apply to idealized soil strength profiles that are either constant or linearly increasing with depth. However, site investigations often reveal complex strength profiles that deviate significantly from simple linear profiles, for example, a common setup consists on a superficial stiff layer overlying a thicker layer of very soft soil, setup that is commonly named 'crust zones'.

Existence of crust zones in offshore deepwater soils around the world has been documented by numerous authors such as Bohlke and Bennett (1980); Peuchen (2000); Ehlers et al. (2005); Kuo and Bolton (2009); Kuo (2011); Yetniger et al. (2012); Kuo and Bolton

(2013); Palix et al. (2013) and Low et al. (2008). Such crusts have been located all around the world such as the Mississippi River Delta, Gulf of Mexico, Gulf of Guinea, South China Sea and gas fields at Norway. Although it seems to be a relatively common soil setup, to date there is limited knowledge on how to assess lateral capacity of piles installed in these soils. The origin of the crust seems to be site specific and strongly dependent on the geologic setting. Thus, no definitive agreement seems to exist on the exact reason why these crusts form. Many authors point to causes such as differential consolidation, presence of silt, presence of bacteria and existence of invertebrate organisms.

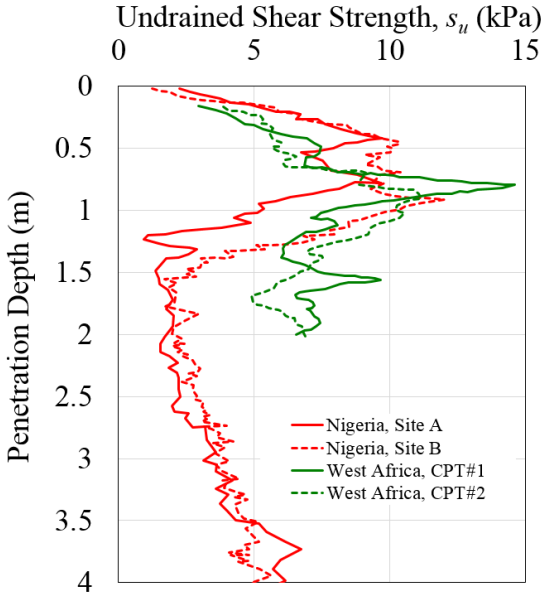


Figure 2.14: Undrained shear strength profiles showing presence of crusts. Modified after Kuo and Bolton (2009); Ehlers et al. (2005)

Sedimentation, erosion and downslope movement of sedimentary deposits (such as mudflows and slumps) have been pointed out as possible reasons for the presence of over-consolidated soil layers in marine environments (McCave, 1984; Bennett et al., 1999;

Doyle et al., 1971). Some researchers believe that the formation of crusts could also be influenced by the presence of silt within the soil (Doyle, 1973; Roberts et al., 1976; Hopper, 1980). For some locations, it has been determined that the soil forming the crustal zone has a somewhat greater percentage of silt particles than the surrounding soft soils (Hopper, 1980). As a matter of fact, the silt seems to be encountered in the zone of peak strength.

Experiments in a wave tank developed by Doyle (1973) demonstrated that marine clays strengthened with time due to remolding and re-consolidation. It was noted that the relatively rapid densification of the clay produced small cracks and fractures which allowed dissipation of excess pore pressures. Furthermore, Doyle (1973) found that such fractures were mostly filled with silt particles. The presence of silt implies that there are zones with higher permeability and rapid drainage compared to the surrounding clay. Hopper (1980) hypothesized that the origin of crusts can be explained on the basis of a consolidation process, assuming that a drainage surface forms inside a mudflow deposit, allowing for rapid dewatering.

This hypothesis is largely supported by Bohlke and Bennett (1980). In an extensive review on the formation of crusts in the Mississippi Delta, they concluded that these are formed probably by the remolding and shearing that takes place on surficial soils during mass movements such as mudflows and slumps. They also encountered slightly higher concentration of silts within the crust.

A different explanation was presented by Ehlers et al. (2005), for the case of crusts located in Gulf of Guinea and West Africa. They concluded that formation of crust zones

might be linked to several biochemical processes:

1. Shear strength of the surface is largely a result of biological activities coupled with biologically mediated chemical changes;
2. High shear strengths within the crust are the result of significant burrowing and tube-building by invertebrate organisms;
3. The presence of organic carbon (in seabed sediments) creates anaerobic conditions for nitrate, manganese, iron and sulfate reduction to occur, and the mobilization and re-precipitation of these and other oxidants may result in chemical bonding with clay platelets that would lead to higher shear strengths (Ehlers et al., 2005).

Results by Ehlers et al. (2005) have been extensively studied and validated by Kuo (2011). The presence of a crust has been confirmed through penetrometer testing and Cam-shear testing (Kuo et al., 2011). In addition, significant evidence abundant mucus-covered fecal pellets (likely from invertebrate species) was found within crusts, suggesting that high amounts of bacteria may be present within it. Kuo (2011) postulated a sound hypothesis which aims to explain the origin of crusts. This hypothesis is summarized in Figure 2.15 (Original source: Kuo (2011)). Sediments from water onto the soil includes either degrading biological components (organics) and clay sediments (inorganics). Once in the soil, these sediments are ingested by invertebrate organisms which extrude them as feces in the form of pellets. Most of invertebrates burrow within the top 0.5 (and possibly up to 2) meters of seabed, which corresponds to the typical crust zone.

Finally, for some regions in the Gulf of Mexico, it is believed that the high shear

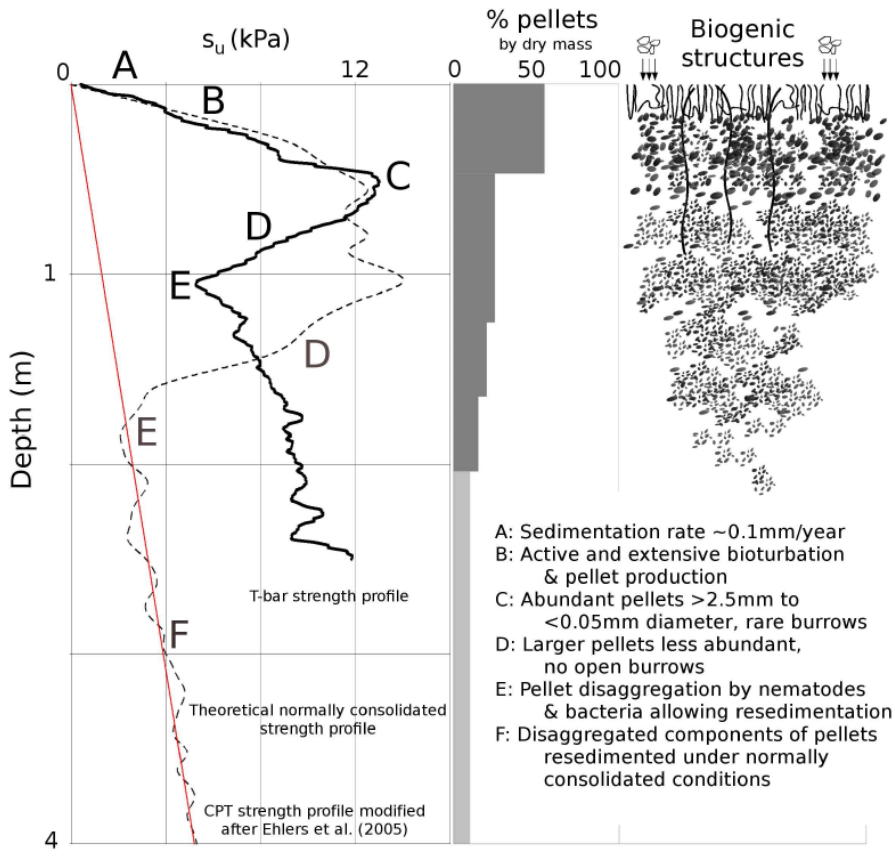


Figure 2.15: Kuo's Hypothesis about origin of crusts in Gulf of Guinea Soils. Credit: Kuo (2011)

strength in the crust zones is produced due to either bioturbation (benthic fauna) and to the presence of high amounts of silt and sand-size foraminifera or forams, as they are commonly named (Jeanjean et al., 1998; Young et al., 2003; Jeanjean, 2017). Foraminifera are single-celled organisms with external shells that cover the cell. These shells can be made of either organic matter, sand grains and other particles that are cemented together. It is assumed that the crushing strength of some of these shells could be greater than the shear strength of the soil close to the surface. Figure 2.16 presents an example of typical sand-size forams from a coral reef.


Figure 2.16: Photo with different species of foraminifera. Credit: Dr Pamela Hallock/University of South Florida; Smithsonian (2016)

## 2.7 Deep Penetration Problems

Deep penetration problems (such as pile installation or soil sampling) are regularly simulated as the expansion of a cylindrical or spherical cavity in an undrained medium. However, Baligh (1985) points out that cavity expansion methods (CEM) might be too simplistic in order to describe the two-dimensional nature of the deep penetration problems. Baligh (1985) presented the Strain Path Method (SPM). The method provides a rational framework for describing mechanics of quasi-static, steady, undrained deep penetration in saturated clay (Aubeny, 1992).

## 2.8 The Strain Path Method

The strain path method (SPM) consists on an analytical technique to predict soil disturbances produced by the penetration of rigid objects (in general piles, in situ testing devices, soil samplers or suction caissons), in the soil (Baligh, 1985). The method provides an integrated and systematic framework for the solution of problems involving deep

penetration. It has been throughly explained by Baligh (1985) and Aubeny (1992). Thus, in this work only the basic steps to use the method will be presented. Should the reader need to understand and learn the method, it is highly recommended to review the mentioned references, since much of the content of the current section is a summarized review of Baligh (1985). Steps to obtain solutions by using the strain path method. These steps are presented as a diagram in Figure 2.17:

1. Calculate an estimate of the initial stress state and pore water pressure in the soil prior to installation.
2. Postulate a velocity field that satisfies conservation laws (volume or mass) and boundary conditions. This velocity field defines the deformation rate of individual soil particles as they move around the penetrating element.
3. From the velocity field, compute soil deformations by integrating along streamlines.
4. By differentiation of velocities with respect to the spatial coordinates it is possible to compute the strain rates, $\dot{\varepsilon}_{ij}$
5. Strain rates must be now integrated along streamlines in order to obtain the strain path $\varepsilon_{ij}$ for all soil elements
6. Determine effective stresses. Procedure is detailed in Baligh (1985)
7. Having effective stresses, pore pressures can be computed from equilibrium considerations
8. Compute total stress

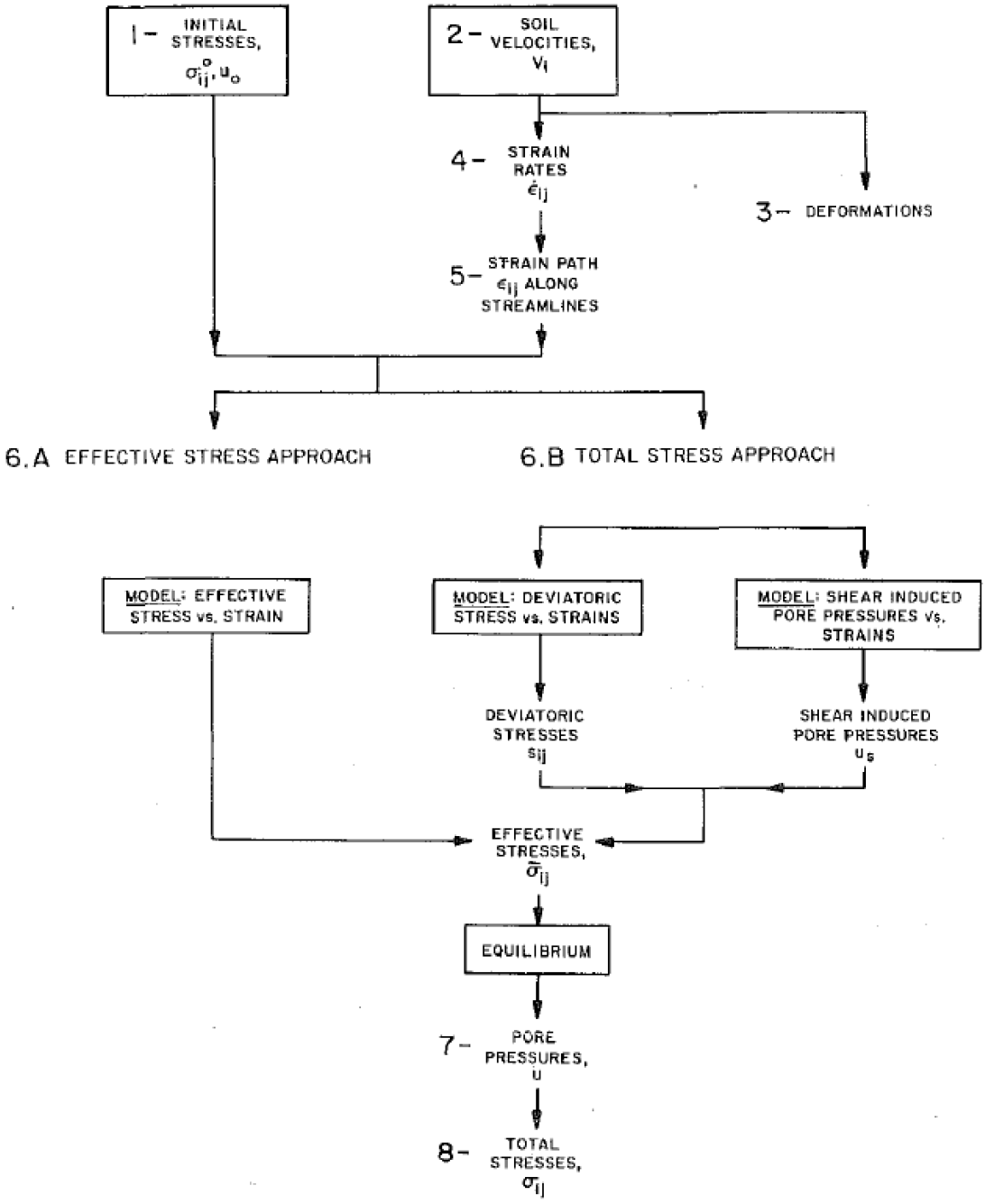


Figure 2.17: Flow diagram of steps required to implement the Strain Path Method. (Baligh, 1985).

## 2.9 Prediction of Setup Time for Piles and Caissons

Following installation stage, decay of excess pore pressure occurs over time, producing an increase in the inter-granular pressure (i.e. effective stress) and, thus, an increase in capacity (Soderberg, 1962), a process termed 'setup' or soil reconsolidation. The process is visually illustrated in Figure 2.18. Predicting the dissipation time of the EPPs (or 'setup' time) is an important consideration in the design of piles and suction caissons, since side friction can be a major component of total capacity. Even though much analytical and experimental studies have been conducted on this topic (Randolph and Wroth, 1979; Carter et al., 1979; Jeanjean, 2006; Cao et al., 2002b; Vasquez et al., 2010; Olson et al., 2003), this process is a complex phenomenon and is not yet fully understood.

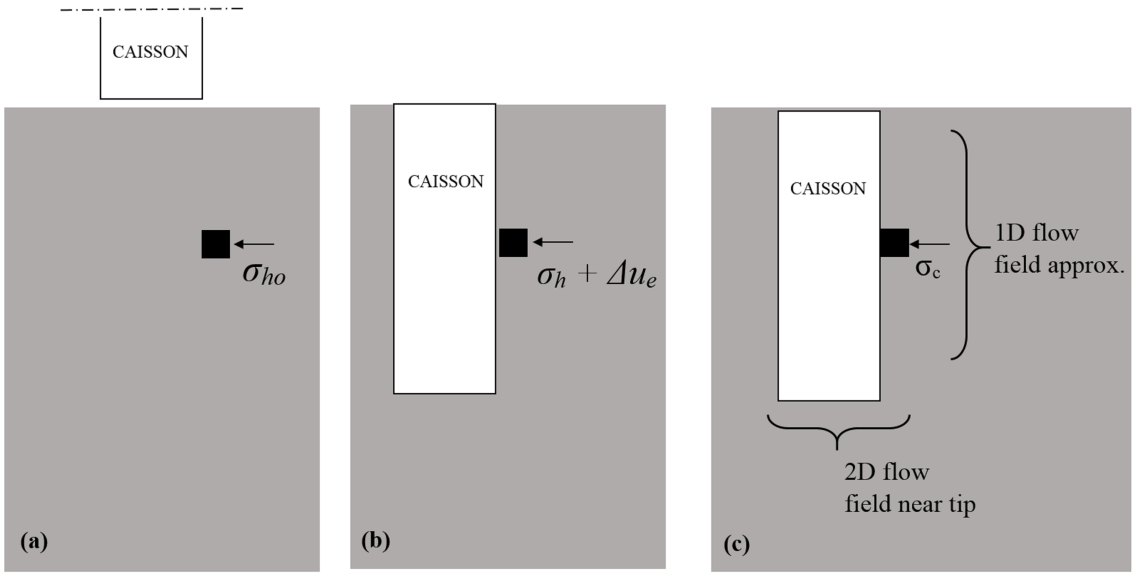


Figure 2.18: Diagram of setup process: (a) Pile installation, (b) immediatelly after installation and (c) after re-equilibration of pore pressures

Since dissipation times are strongly influenced by the spatial extent of the zone of dis-

turbance containing excess pore pressures, analysis of setup time first requires prediction of the stress and pore pressure fields surrounding the pile due to installation disturbance. A widely adopted approach to predict pile installation disturbance is based on expansion of a cylindrical cavity (Yu, 2000) . For solid piles the cylindrical cavity is expanded from zero to the outer radius of the pile. The cavity expansion method (CEM) can also be applied to open-ended piles, although some ambiguity exists with regard to the relative proportions of soil flowing into and outside of the pile. While the CEM in either case cannot fully simulate the complex distortions and resultant soil disturbance occurring during pile penetrations, it does provide useful first order analyses of the setup process.

The strain path method (SPM) is based on the assumption that, due to the severe kinematic constraints occurring during deep penetration, soil deformation during undrained penetration is essentially independent of soil properties. The SPM thus retains the relative simplicity of the cavity expansion approach, while providing much more realistic analysis of the effects of penetrator geometry. The SPM has been successfully applied to the analysis of sampling disturbance (Baligh et al., 1987), in situ testing (Aubeny, 1992) and pile shaft resistance in clays (Azzouz et al., 1990). In these examples, soil effective stresses were a prime concern, so a sophisticated soil constitutive model was used in conjunction with the strain path analysis. The present study, for which setup time (i.e. time of dissipation of excess pore pressures) is the prime focus, utilizes a simple linearly elastic model with perfect plasticity upon yield.

Once the zone of disturbance and distribution of excess pore pressures have been

estimated dissipation of excess pore pressures can be analyzed within the framework of consolidation. Strictly speaking, the process involves two-dimensional axisymmetric consolidation in a coupled hydro-mechanical system (Aubeny et al., 2000) . However, where the prime concern is dissipation of excess pore pressures on the sides of the pile far above the tip, a one-dimensional radial consolidation analysis may reasonably be employed, as described by Kavvadas (1982). The analysis may be further simplified by considering a decoupled consolidation analysis in which the rate of dissipation is driven by a single soil parameter, the coefficient of consolidation $c$. A successful application of this approach is given by Levadeux and Baligh (1986).

In summary, the analytical framework used in this study for estimating setup time following pile installation comprises:

1. A strain path analysis utilizing a linearly elastic-perfectly plastic model of soil behavior to predict the field of excess pore pressures due to installation disturbance.
2. A one-dimensional radial uncoupled consolidation analysis to predict the rate of dissipation of disturbance pore pressures.

The installation analysis will require a single soil material parameter, the soil rigidity index $I_r = G/s_u$, where $G$ is shear modulus and $s_u$ is undrained shear strength. The consolidation analysis requires a second parameter, the coefficient of consolidation $c$.

Vesic (1972) recommends rigidity indices $I_r$ ranging from 10 to 300 for soft to very stiff clays. Foott and Ladd (1981) presented correlations of normalized secant modulus ($E_u/S_u$) against the shear stress ratio ($\tau_u/s_u$) for a variety of clays. Considering their data

for marine clays at $\tau_u/s_u$ = 50% indicates a range of normalized secant moduli $E_{50}/s_u$ = 300-600. Assuming a Poisson ratio of 0.5 for undrained loading produces an estimated range rigidity indices $I_r$ = 100-200 for normally consolidated marine clays. This range turns out to be roughly consistent with the range recommended by Cao et al. (2002b) and Hjortnaes-Pedersen and Bezuijen (1992) for interpreting pile setup data in kaolin test beds. In the research herein presented, general parametric studies will be presented in terms of a rigidity index $I_r$ ranging from 50 to 500, with a range $I_r$ = 100 to 200 tentatively accepted as appropriate for normally consolidated clays.

The coefficient of consolidation $c$ is a well-known soil parameter in soil mechanics and needs no further elaboration here. However, this parameter is far from uniform at a given site and will vary according to whether the soil is intact versus remolded as well as normal consolidation versus recompression (NAVFAC, 1986) as presented in 2.19. Levadeux and Baligh (1986) argue that, since setup around driven piles is primarily involves recompression, the coefficient of consolidation corresponding to an over-consolidated stress state ($c_{oc}$) is most appropriate.

Arguably, a coefficient of consolidation derived from piezo-cone holding test data would be ideally suited to estimating setup due to the similarity in the two processes. Recognizing that more work is needed in this area, this research does not focus on this issue.

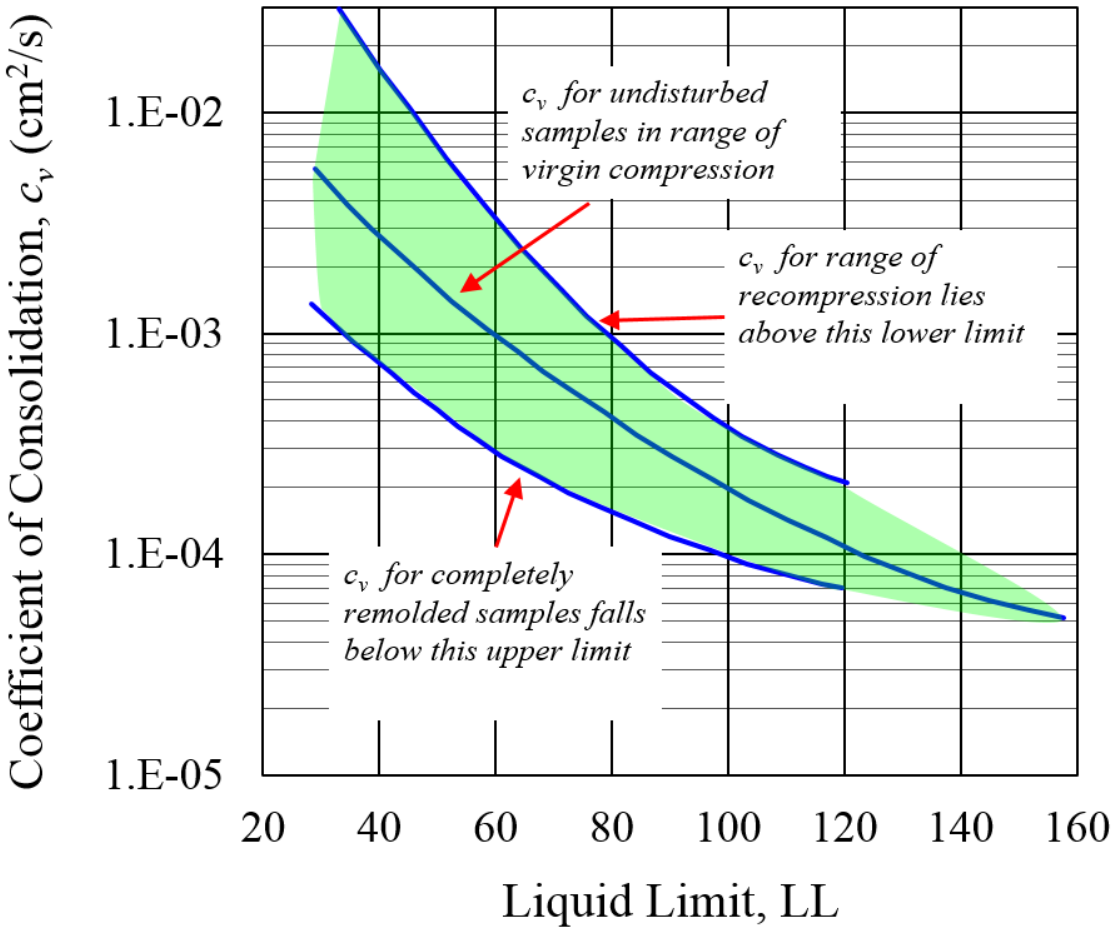


Figure 2.19: Approximate correlations for consolidation coefficients of soft soils. Adapted from NAVFAC (1986).

# 3 FINITE ELEMENT MODEL

This chapter describes fundamental aspects needed to understand the finite element (FE) model. A brief tutorial describing how to use the mesh generator is included.

## 3.1 Model Properties

### 3.1.1 Mesh geometry

The mesh consists on a cylinder of soil and a pile embedded in the middle, as shown in Figure 3.1. A Matlab (Mathworks, 2013) based mesh generation code was developed in order to be able to produce different models in a systematic and straight forward way, its usage will be addressed later in this chapter. Several geometrical configurations have been evaluated in order maximize effectiveness of the model. The radial extent (i.e. distance from the center line to the far end of the cylinder) of the mesh is set to be equal to 5 diameters and the soil depth was set as 3 times the length of the pile (i.e. minimum depth of 2 Lf below the pile tip). Such an assumption presents the advantage that, when short piles are simulated, no unnecessary elements are included.

Elements adjacent to the pile were configured in such a way that the ratio of the circular segment to the radial increment is equal to one, as this has been proven to increase accuracy of results (Han, 2002) . The shape of elements located inside the caisson has been modified in order to avoid six-node wedge elements at the center, since these type of element tend to produce singularities when considering soil resistance inside the caisson.

A close-up to the central part of the mesh is presented in Figure 3.2.

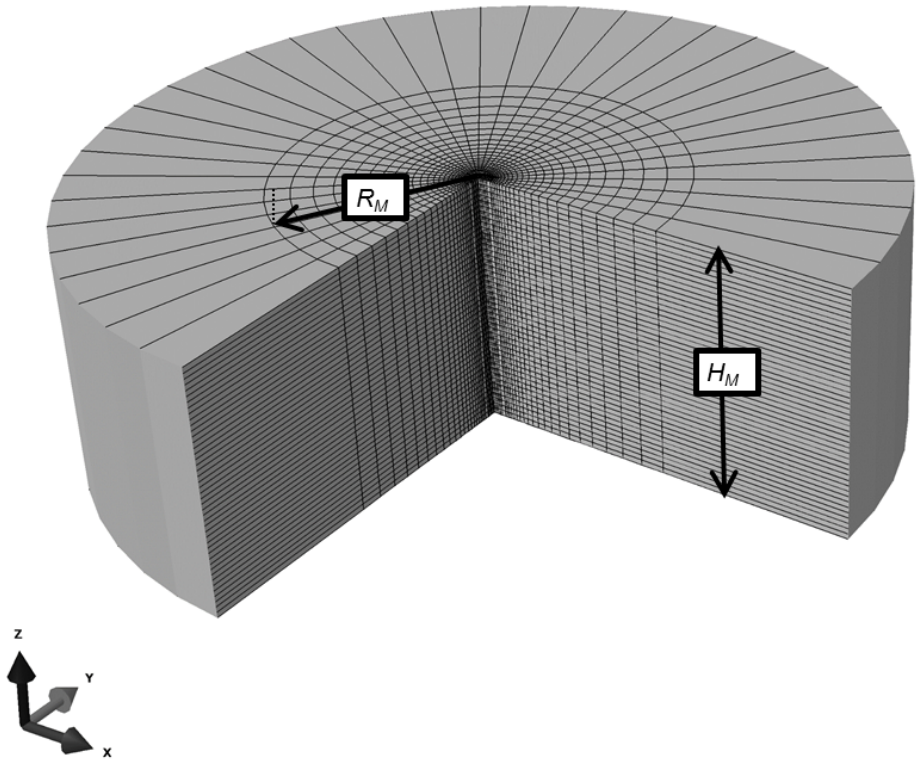


Figure 3.1: Finite Element Mesh

### 3.1.2 Material properties

The soil is assumed to be isotropic (i.e. the undrained shear strength is independent of the type of load or shearing mode applied), the soil is modeled as a continuum. Although a saturated soil is actually a two-phase material the zero volume change undrained constraint permits it to be effectively modeled as a single phase material and is assumed to be rate independent. Elements of the type C3D8 (Continuum 8-node linear elements) were utilized to model the soil medium. The material model was assumed to be linear-elastic with Mohr-

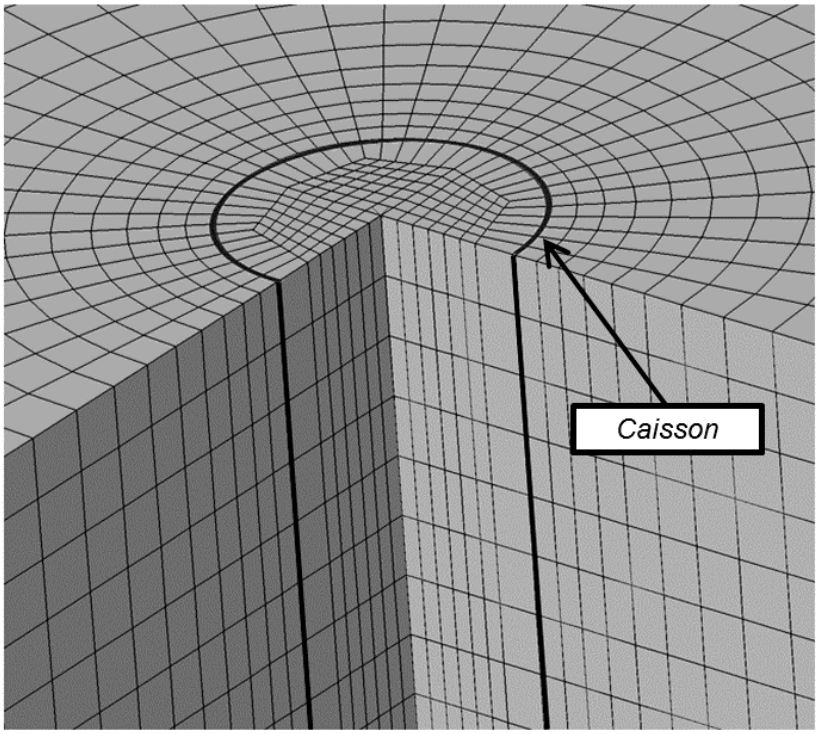


Figure 3.2: Modified elements inside the caisson

Coulomb plasticity. The Mohr-Coulomb plasticity model assumes a Mohr-Coulomb yield criterion and an associated flow rule. For this specific case, since the friction angle is set equal to zero ($\phi$= 0), the yield criteria becomes the pressure independent Tresca model.

Undrained shear is assumed to increase with depth. This allows the user to introduce either a constant undrained shear strength or a linearly increasing one. For this study, several strength gradients will be considered. These are described in the table presented in (either chapter 2 or the table presented below).

Young's modulus was defined in terms of the rigidity index ($I_r$) is defined in this study as the ratio between the shear modulus ($G$) and the undrained shear strength ($s_u$).

Vesic (1972) has recommended rigidity indices ranging from 100 to 300 for soft to very stiff clays respectively. Foott and Ladd (1981) presented correlations of normalized secant modulus ($E_u/s_u$) against shear stress ratio ($\tau_u/s_u$) for a variety of clays. Considering their data for marine clays at $\tau_u/s_u$ = 50% indicates a range of normalized secant moduli $E_{50}/s_u$ values of 300 to 600. Assuming a Poisson's ratio of 0.5, which is a reasonable number for undrained conditions, estimate values of rigidity indices $I_r$ ranging from 100 to 200 can be obtained for normally consolidated marine clays (Aubeny and Grajales, 2015) . The finite element model herein presented has been configured with a rigidity index of 100. However, depending on the needs of the user, different values can be easily introduced to account for soil stiffness effects. Recommended values based on the aforementioned authors are presented in the table below.

Finally, the model offers capability to account for soil stratification, that is, different strength profiles and material properties can be introduced for as many soil layers as needed. However, a word of caution on this: setting abrupt changes in soil strength might lead to significant stress concentrations in the interface between soil layers, which at the same time are likely to produce overestimated results, which must be accounted by the user during the data processing.

### 3.1.3 Kinematic constraints and boundary conditions

Simulations are displacement-controlled. A horizontal displacement is applied in order to produce failure of the pile. For cases in which translational displacement fields are needed the pile is restricted to move only in the direction on loading (i.e. rotation or

torsion are not allowed). If rotations need to be included in the analysis, then no kinematic constraints are applied to the pile itself.

It has been reported that finite element analyses tend to overestimate capacity when compared to either exact solutions or good field or laboratory data. One of the reasons of this phenomenon is that FE models create high stress concentrations around the pile tip (Aubeny et al, 2001), due to the abrupt discontinuity that occurs in that region. In order to account for this, reduced strength elements have been included exclusively at the tip of the pile. Some investigators have utilized slip elements on these stress concentration zones, however this adds up a significant amount of computation time to each run. Thus, this study employed a simpler approach involving reduction of the strength of soil element adjacent to the pile tip.

### 3.1.4 Formation of gaps

Formation of gaps is a phenomenon that has been observed on laterally loaded piles in cohesive soils (mostly on relatively stiff over-consolidated clays). However, gapping will not be considered as a default option in the finite element model (i.e. no contact pairs will be defined using commands and options available in Abaqus library). One of the reasons is that assuming full contact at the soil-pile interface allows to compare predicted values against exact solutions, such as the one developed by Randolph and Houlsby (1984). Secondly it has been observed that for reasons not yet fully determined, many FE models seem to predict gapping depths that extend all the way to the bottom of the caisson when a translational displacement field is applied. Meanwhile, if rotation of the pile is modeled,

gap depths tend to extend to the location of the center of rotation of the pile. In the author's opinion this is not the most adequate representation of the real behavior.

## 3.2 Results Post-processing

In order to obtain load capacity, a horizontal displacement is applied at a reference node which is attached to the pile. The node can be located at any depth along either the centerline or the wall of the pile, therefore it is possible to change load application points according the conditions of the case in study. Once resisted load is obtained results will be processed using two principal approaches:

1. Total load resisted
2. Equivalent soil resistance profiles

The first approach (i.e. total load) is the most intuitive one and consists on obtaining the reactions occurring at the load application node. For the present study, the most important reactions are the horizontal force in the positive $X$ direction and the moment reaction in the $Y$ direction. Loads are presnted as bearing capacities. Normalization of lateral and moment loads is done by dividing over the product of the average undrained shear strength, pile length and diameter, as described in Equations 3.1 and 3.2 presented below.

$$N_h = \frac{H}{s_{u_{avg}} D L_f} \tag{3.1}$$

$$N_m = \frac{M}{s_{u_{avg}} D L_f^2} \tag{3.2}$$

Where:

- $N_h$ is the horizontal bearing capacity
- $N_m$ is the moment bearing capacity
- $H$ is the horizontal load
- $M$ is the moment load
- $s_{u_{avg}}$ is the average undrained shear strength along the depth of the pile
- $D$ is the diameter
- $L_f$ is the pile length

The second approach consists on computing equivalent soil resistance (or soil pressure) profiles which are dependent on depth $z$. Figure 3.3 presents an illustrative sketch of steps needed to compute soil resistance profiles. For finite element studies, computation is done by selecting nodal stresses at a certain depth $z(i)$. These nodal stresses represent the effect of all the soil surrounding the region delimited by $\Delta z$. Integration of nodal stresses gives a horizontal force $\Delta F$ that is being resisted by the segment of pile in question. This horizontal force is then normalized by the product of the undrained shear strength at the corresponding depth and the projected area of the pile, as presented in Equation 3.3.

$$N_{ps} = \frac{\Delta F}{s_u D \Delta z} \tag{3.3}$$

Where:

- $N_{ps_{(z)}}$ is the equivalent lateral soil pressure at a depth $z$.
- $s_{u_{(z)}}$ is the undrained shear strength at the depth $z$

- $D$ is the diameter
- $\Delta z$ is the length of the corresponding pile segment.

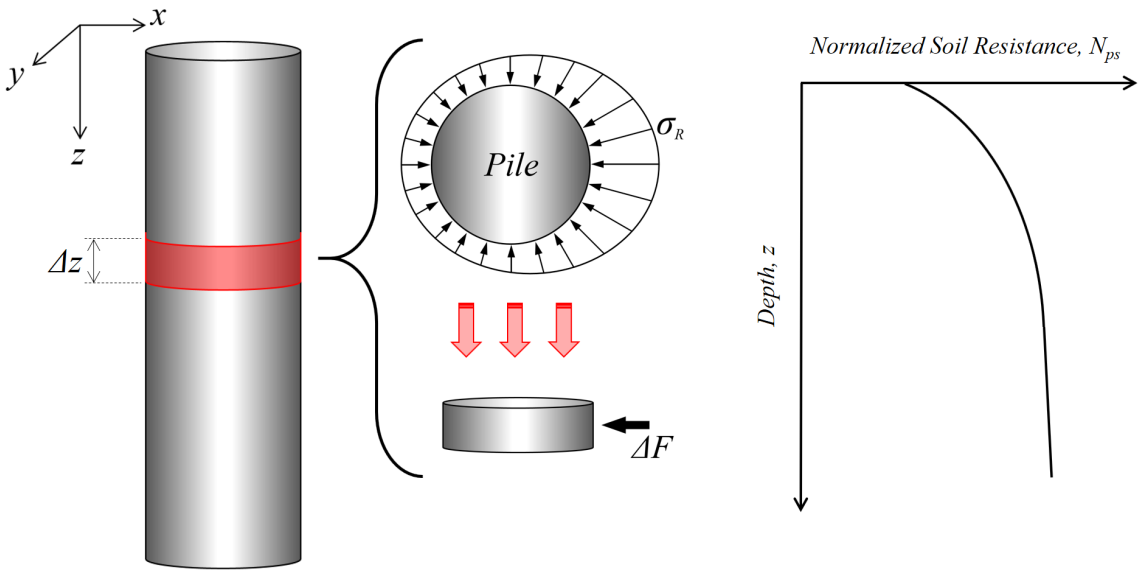


Figure 3.3: Illustrative sketch showing the physical interpretation of a soil resistance profile

This procedure can be repeated for different depths, obtaining a curve like the one presented in Figure 3.3. In general, equivalent soil pressures at the top of the pile should be significantly less than at the bottom, since the soil surface is unconstrained.

## 3.3 Model Calibration

The model was calibrated using the solution presented by Randolph and Houlsby (1984). Randolph-Houlsby's solution applies for the specific case in which a solid cylinder translates in a continuum. Thus, for the case of a translating pile, values of soil resistance ($N_{ps_{(z)}}$) at depths great enough for surface effects to be neglected should at least approximate the numbers provided by Randolph and Houlsby (1984). Figure 3.4a presents

a comparison of soil resistance profiles obtained from FE and the empirical function proposed by Murff and Hamilton (1993), which also uses Randolph-Houlsby solution as a limiting lateral bearing pressure for deep locations. Finite element results are presented for the case of a translating pile (no rotations allowed) with aspect ratios ($L_f/D$) ranging from 1 to 5. Complete soil-pile adhesion is assumed ($\alpha = 1$) and the soil is assumed to have a constant strength.

It can be observed that (Fig. 3.4a) that Finite Element over-estimate plasticity solutions for the flow-around zone. In order to match the exact value ($N_{ps} = 11.94$ for an interface adhesion of 1), a very refined mesh needs to be developed. An example of this was presented by Shi (2005). While this kind of refinement is an acceptable option for two-dimensional studies, three dimensional models become difficult to handle if such a refinement is attempted, mostly because of the run time required. Thus, in this study, a uniform correction factor of 7% is being applied to results obtained from the FE model. This reduction can be observed in Figure 3.4b. By reducing results by 7%, equivalent soil pressures at great depths look much more in agreement with the aforementioned solution. It can also be observed that FE studies seem to show lower estimates of soil resistance for shallow depths (normalized depth, $z/D$ less than 2).

## 3.4 Additional Results

In addition to the aforementioned post-processing methods, the software ABAQUS (SIMULIA, 2012), also allows extraction of contours and vector diagrams. These are very

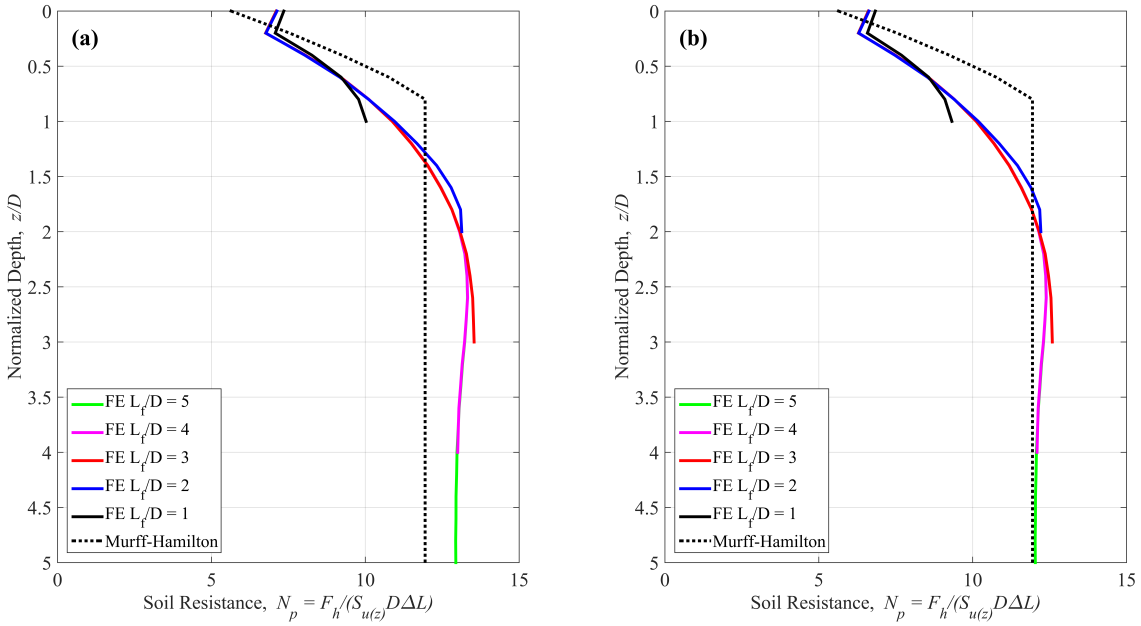


Figure 3.4: Soil Resistance profiles from finite element simulations

helpful in order to develop a insight of what is the code doing when processing results.

Some of the most common contours are stress (or strain) contours and displacement diagrams. An example of a stress contour is shown in 3.5. It can be observed that regions under the highest stresses (or strains) are presented in red color. Displacement plots are also useful in order to make sure that the pile is moving in a desired mode and they help visualize possible failure mechanisms that could be occurring. Figure 3.6 displays an example of a displacement contour for a caisson with an aspect ratio of 2.5.

## 3.5 Comparison to Previous Finite Element Studies

Finite element predictions have been compared against results published by several authors.

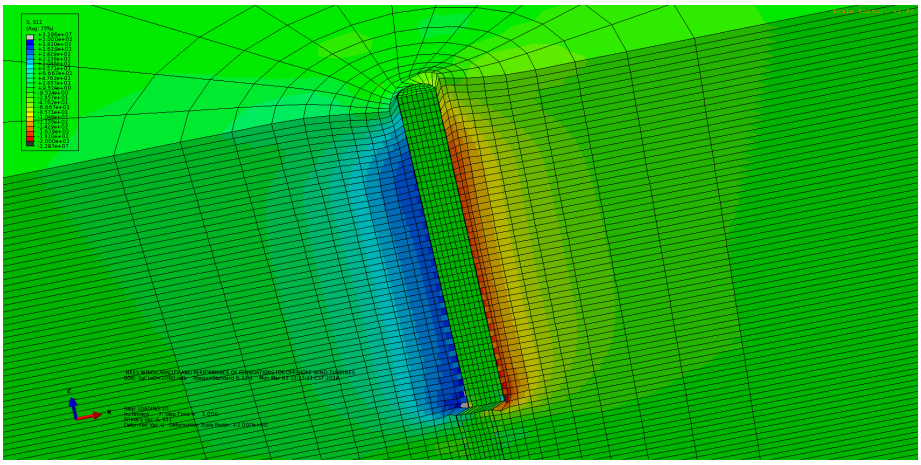

Figure 3.5: Stress Contour plot for X direction. Aspect ratio of 2.5

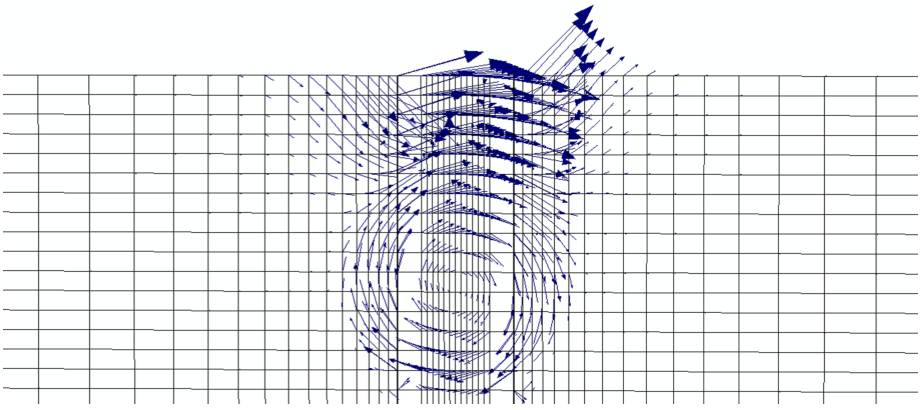

Figure 3.6: Displacement vector plots from FE analyses. Aspect ratio of 2.5

### 3.5.1 Finite element model by Han (2003)

Han (2002) developed a three dimensional FE mesh using Abaqus. In that model, the bottom boundary extended approximately 2 times the length of the caisson whereas the radial extent of the mesh was about 16 diameters. During translational simulations, an equivalent soil pressure factor ($N_{ps}$) of 13.19 was obtained for the flow-around zone. This result was found to be approximately 10% higher than the benchmark plasticity solution (Randolph and Houlsby, 1984).

In comparison, the FE model herein developed provides us with a 7% overestimation of soil resistance ($N_{ps}$) with respect to Randolph-Houlsby solution for the flow-around zone.

Since results from our model are being scaled in order to match the aforementioned exact solution for the flow around zone, it can be expected that, when computing total capacity, results will be significantly improved. This is shown in Figure 3.7. It can be observed that for different aspect ratios ($L_f/D$) the model predicts lower estimates of horizontal load capacity.

Finally, the mesh developed in this study presents several advantages over its predecessor. Some of them are:

1. Offers capability to model the caisson as a hollow structure. This means that effects of structural flexibility can potentially be included into future analyses. It also opens many possibilities regarding studies on behavior of stresses in the soil plug, dissipations of pore pressures after installation, etc.
2. Formation of gaps can be accounted for. Although, care is recommended when including gaps, specifically for the case of a fully translating pile (e.g. a suction anchor with padeye located at the optimal point).

### 3.5.2 Finite element model by Kay and Palix (2012)

Kay and Palix (2011) presented a three dimensional FE model developed using the software Plaxis. They compared their results to predictions done using a limit analysis softwares.

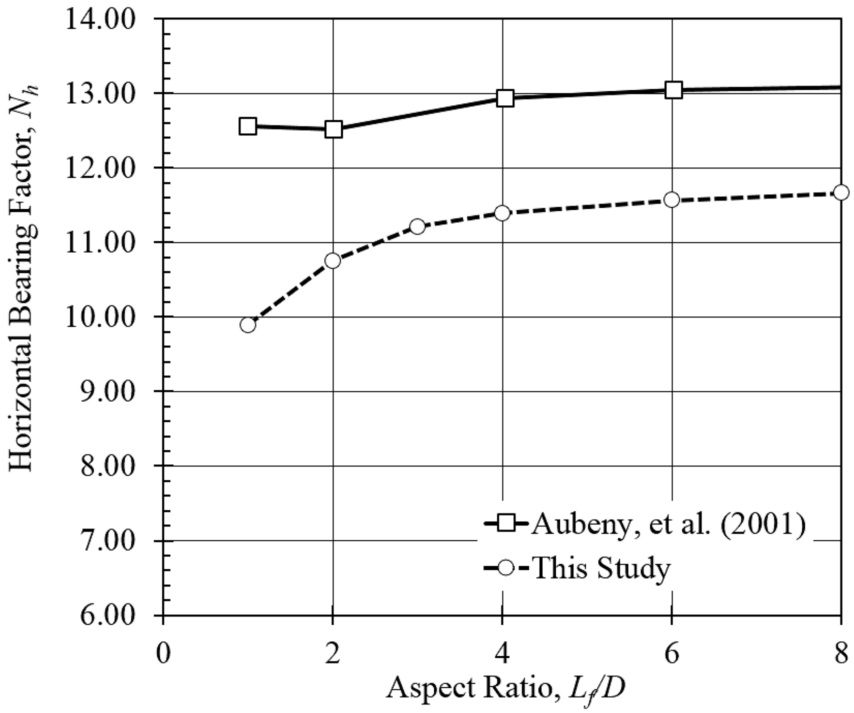


Figure 3.7: Comparison to studies by Han

Figure 3.8 presents comparison between this study and results published by Kay and Palix (2011) for an aspect ratio of 2. It is important to comment here that Kay and Palix (2011) model was developed for an adhesion of 0.7. The finite element results herein presented correspond to full adhesion (i.e. $\alpha$ = 1). Results plot relatively close, with data points from this study being a little bit higher. This is expected due to the difference in adhesions.

### 3.6 Comparison to Centrifuge Tests

Geotechnical centrifuge tests were developed by Murali (2015) and Beemer (2015). This section presents a brief summary the experiment and how obtained results compare

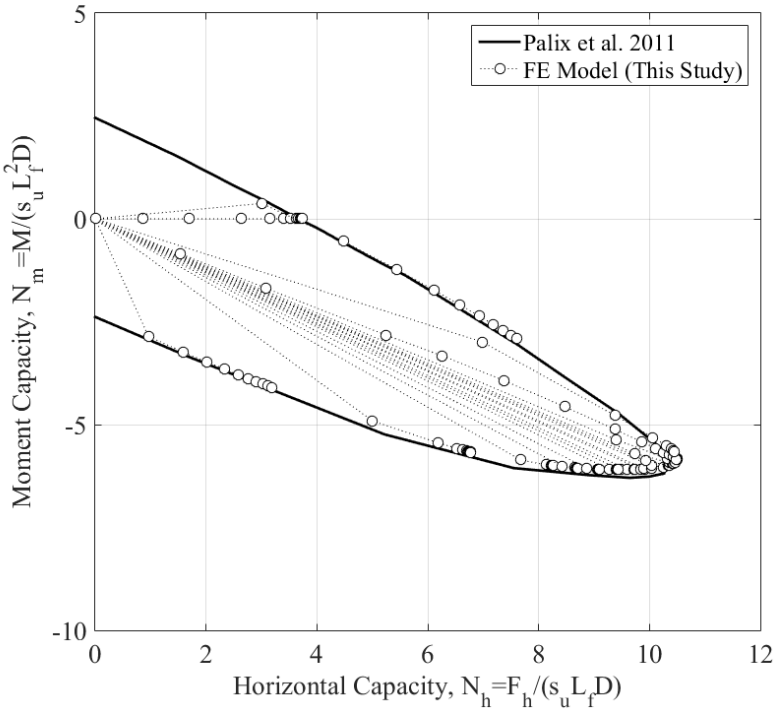


Figure 3.8: Comparison between to FE results by Kay and Palix

to finite element predictions. Should the reader need to know more details on the testing program, please refer to the aforementioned references. In addition, details of the experiment have been presented in several conference papers available in the literature (Murali et al., 2015; Grajales et al., 2015; Beemer et al., 2016).

### 3.6.1 Experimental setup

Tests were carried out in the 150 g-ton, 2.7 m nominal radius centrifuge at the Center for Earthquake Engineering Simulations at Rensselaer Polytechnic Institute (Elgamal et al., 1991). Additionally, the center's four degrees of freedom (DOF) in-flight robot (Ubilla et al., 2006) was utilized for load application and in-situ testing. For application of load a custom cup adaptor was 3-D printed in a stainless steel-bronze alloy. As shown in Figure

3.9a, the cup allowed the rotational motion of the model piles when coupled with the stem.

The model piles consisted of three components: the caisson, the stem, and the sensors platform, as presented in Figure 3.9b Caissons were constructed from aluminum tubing turned down to a diameter of 4.96 cm with a wall thickness of 0.61 mm. All monopiles had a plug length of 10.16 cm with an additional 1.27 cm cap welded to the tubing. Resulting in an aspect ratio ($L_f/D$) of approximately two. Caps were tapped with a vent hole to assist installation and plugged with a small cork while testing. Strain gages were mounted around the circumference of caissons 1.27 cm from the bottom. Strain gage wires were restrained with wrapping and the assembly was coated in rubber

Stems are rotational in nature with a ball at their end (Figure 3.9b). They were constructed from either 9.53 mm diameter steel or aluminum rod and were instrumented with strain gauges to measure applied load. Strain gauge wires were restrained with wrapping thread and paint on rubber. Stems where bolted to the aluminum cap allowing them to be interchanged. Stems varied in height from allowing for diameter normalized load eccentricities of approximately 1.25, 2.5, and 3.5 from the pile cap.

The sensor platforms were fabricated from plastic. They were designed to hold accelerometers above the model water level and the LVDT target flags. Strain gage wires were also tied to the platforms in order to distribute weight and minimize pulling on the gages themselves. LVDT flags were 3D printed in ABS plastic and fastened to the platform. Two single-axis 10g accelerometers were mounted to each platform. These sensors allow measurement of rotation independent of displacement.

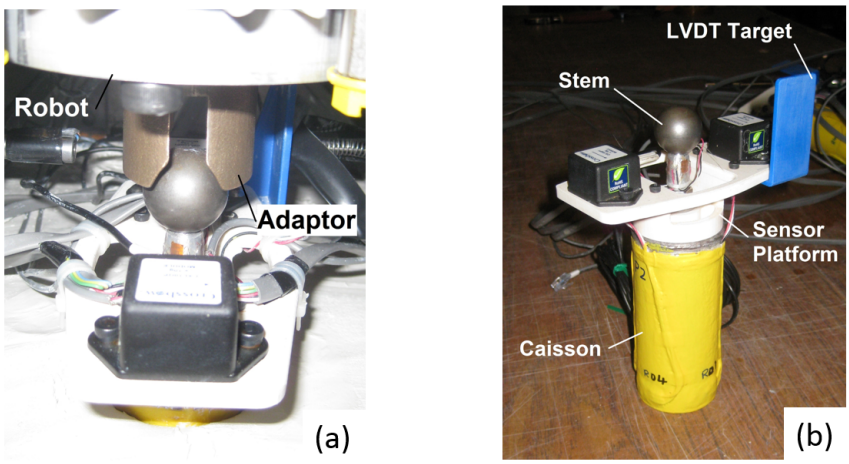


Figure 3.9: (a) Robot adaptor coupling with rotational stem and (b) example of a pile with labeled components (Grajales et al., 2015)

Both soil beds were constructed in the RPI Large Rigid Boxes, 88cm by 39 cm. Kaolinite clay was placed at a water content of 80% to a height of 32 cm. The model was then consolidated at 100g to an average water content of 62.2%. After consolidation the models were excavated to a depth of 23 cm. After an expected recompression of 3 cm the expected in-flight depth was 20 cm. Soil undrained shear strength was determined, by water content correlation (Tessari, 2012), Stress History and Normalized Soil Engineering Properties (SHANSEP) (Ladd, C. C., and Foott, R., 1974), and inflight T-Bar penetrometer tests (Dejong, et al. 2011). Penetrometer runs were conducted before and after each monopile test.

Each experiment had three monopiles spaced 18.5cm on center and in the center of the large box. An example layout is presented in Figure 3.10. They were installed to an approximate depth of 10.16 cm (assuming no or minimal plug heave).

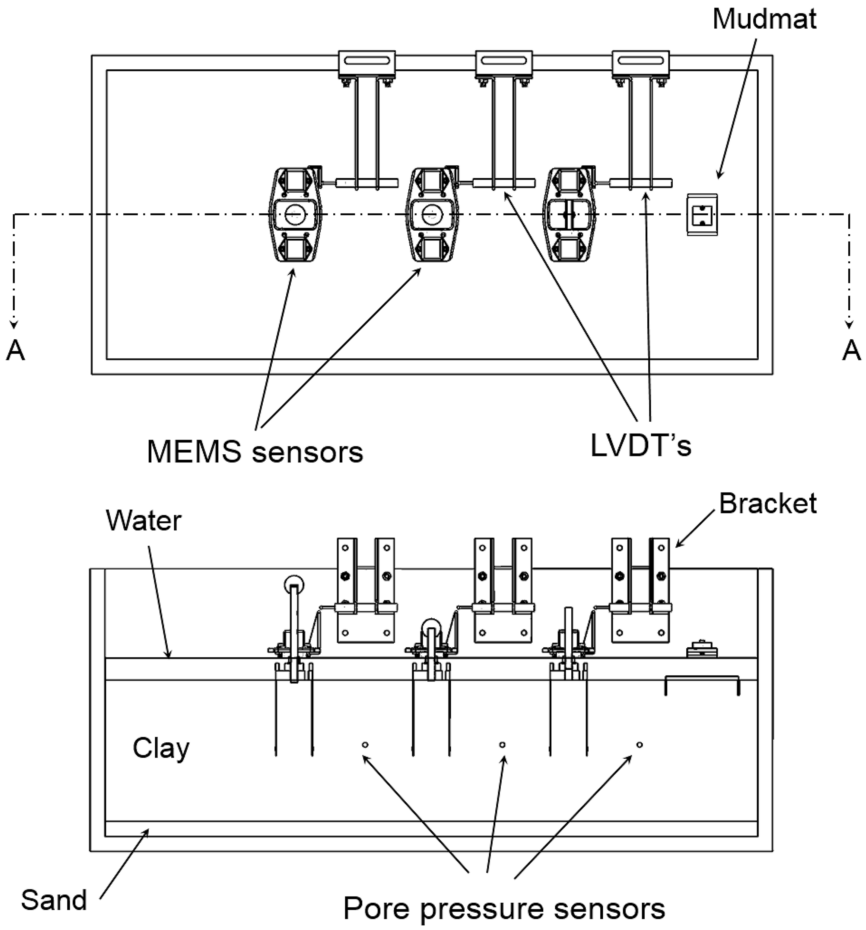


Figure 3.10: Top and side views of a characteristic testbed. Drawing courtesy of Dr. Ryan Beemer

### 3.6.2 Translational response

The load-deflection curve for the pile tested in pure translation is presented in Figure 3.11 along with the calculated ultimate lateral capacity using methods proposed by Murff and Hamilton (1993) and finite element results obtained in this study. The lateral head load, $H$, is presented as a lateral bearing factor $N_h$, which is obtained normalizing load by the product of the projected vertical area, $L_f \cdot D$, and the average shear strength $s_{u,avg}$ over the depth of pile embedded in soil. For experimental data, ultimate capacity is defined as

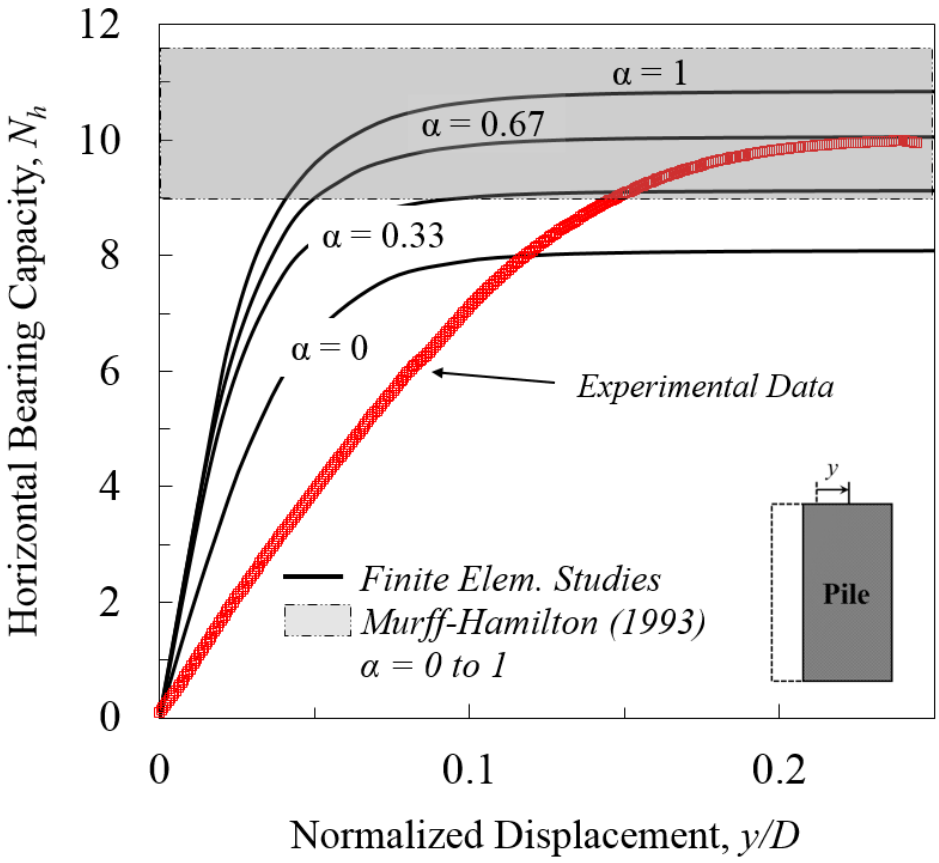


Figure 3.11: Comparison of experimental results against finite element predictions and upper bound solutions (Murali et al., 2015; Grajales et al., 2015; Murff and Hamilton, 1993).

the peak value measured.

The pile was displaced horizontally to an amplitude equal to 30% of the pile diameter, to maintain a suitable distance between adjacent piles during testing. This was not a limitation to compute the ultimate capacity, as 30% of pile diameter is considered to be well above failure. The pile appears to reach its peak value at approximately 24% displacement amplitude, with the computed horizontal bearing capacity factor ($N_h$) being approximately equal to 10 approximately.

Ultimate capacity of the pile tested in translation is found to fall within the range of values predicted by Murff and Hamilton (1993) upper bound solution for no gapping (horizontal gray shaded band in 3.11). For the case of a smooth pile ($\alpha = 0$) a bearing factor of 8.85 was obtained while for the case of a rough pile ($\alpha = 1$) a bearing factor of 11.3 is reported. Although it has been noticed that Murff and Hamilton (1993) tends to over-predict capacity for short piles, this result suggest that there was a significantly low adhesion coefficient ($\alpha$) between the model pile and the soil.

Finite element results are presented for different adhesion factors $\alpha$ ranging from 0 to 1 obtaining lateral bearing factors $N_h$ of 8.08 and 10.8 respectively. Results are plotted as continuous black lines. The first noticeable difference in the plots is that the stiffness exhibited by the experimental data is significantly lower than the one predicted by the finite element model. One reason for this might be that the finite element models the pile as a rigid body due to the fact that it will be used calibrate future upper bound solutions which assume completely rigid structure. In contrast, during the experiment, compliance of the model pile is likely causing a reduction in stiffness.

As it was previously mentioned, maximum capacity ($N_h \approx 10$) seems to occur at a displacement $y/D$ of approximately 24%. These results seem to fall between finite element predictions for a smooth pile ($\alpha = 0.33$) and for an adhesion factor $\alpha = 0.67$ (Lateral bearing factors $N_h$ from 9.12 to 10.05 respectively). The most probable cause for this behavior is the fact that model piles were rubber coated in order to protect strain gages and wires from water and soil particles.

The formation of gaps behind laterally loaded piles is a phenomenon that has been observed by several researchers (Zhang et al., 2011). However, the arrangement using during testing did not allow a high speed camera to be mounted inside the bucket during the spin. Therefore, it was not possible to check for evidence of gapping. In addition, after the application of monotonic load, piles were loaded cyclically in the opposite direction (Beemer et al., 2016), which would create uncertainty on whether a gap occurred during the monotonic loading or after the cyclic load was applied.

### 3.6.3 Rotational response

The monotonic response of the pile subject to rotation was examined for four different eccentricities ($e$): 1.25D, 1.5D, 2.5D and 3.5D. As it was previously mentioned the lateral load, $H$, was normalized by the product of the projected vertical area, $L_f D$, and the average shear strength profile over the depth of pile embedment, $s_{u,avg}$. The lateral displacement, $y$, was computed at the mudline using the tilt and displacement measurements and normalized by the pile diameter, $D$. All the piles were pushed laterally at the top of the ball and socket connector to a displacement amplitude equal to 30% of the pile diameter. Thus the pile displacement amplitude at the mudline varied depending on the eccentricity. Results for these tests are presented in Figure 3.12 (a) through (d). Force displacement curves are plotted for both cases of primary loading (red circles) and post-cyclic loading (blue squares). Finite element predictions for adhesion factors ranging from 0 (smooth interface) to 1 (rough interface) are plotted along experimental results for each of the eccentricities studied.

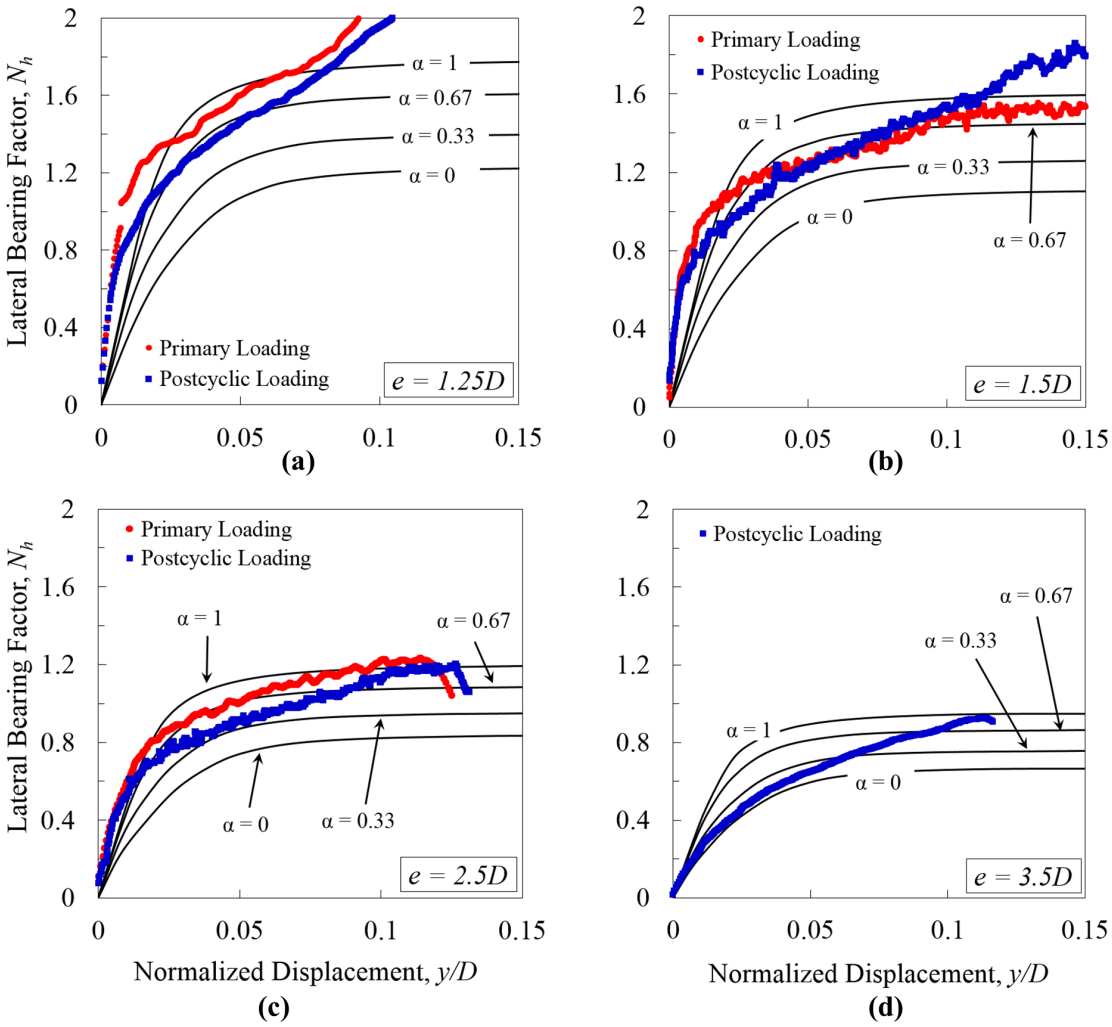


Figure 3.12: Comparison of measured data against finite element predictions: (a) $e$ = 1.25D; (b) $e$ = 1.5D; (c) $e$ = 2.5D; (d) $e$ = 3.5D

As might be expected, lateral capacity decreases with increasing eccentricity for both primary and post-cyclic monotonic loading. Another important observation is what appears to be a work hardening behavior in all of the rotation tests indicating that the piles mobilize increasing strength with increasing displacements due to the rotational failure mechanism of short aspect ratio piles. This type of behavior has been previously reported by several authors Lau (2015); Zhu et al. (2015).

One of the discrepancies between finite element results and experimental data is the slope of the load-displacement curves. However, while for the case of translation (Fig. 3.11) finite element results appeared to be much stiffer, in the case of rotational displacement fields the opposite is observed, except for Fig. 3.12 (d), in which the experimental data seems to fall within the predicted range.

Particular responses are observed for each different eccentricity. For the case of eccentricity, $e = 1.25$ (Fig. 3.12a), experimental data shows that capacity keeps increasing even after a displacement of 0.1 diameters (at the top of the pile). However, if a serviceability limit of 5% is assumed, results for both primary and post-cyclic loading tests seem to fall into the range predicted by finite element simulations. From experimental data, lateral bearing factors $N_h$ of approximately 1.6 and 1.46 are obtained for primary and post-cyclic loading respectively, while finite element predictions for an adhesion factor ($\alpha$) of 0.67 seem to be around 1.5.

For the cases of eccentricities, $e = 1.5D$ and $e = 2.5D$, both experimental and numerical results are in reasonable agreement up to a normalized displacement of 10%. From

Fig. 3.12(b) it is observed that, at 5% displacement, experimental results seem to be within the range of values encompassed by finite element predictions for adhesions $\alpha = 0.33$ and $\alpha = 0.67$ (i.e. horizontal bearing factors, $N_h$ ranging between 1.1 and 1.35). On the other hand, for eccentricity, $e = 2.5D$ (Fig.3.12c), it appears to be that primary loading data matches finite element results for an adhesion of 0.67 while post-cyclic is approximately equal those of $\alpha = 0.33$. Experimental results are presented in tabular form at Table 3.1.

Finally, for eccentricity ($e$) of 3.5 (Fig. 3.12d) it looks like experimental data is in agreement with low adhesion finite element predictions. Also, work hardening effect seems to be less of an issue for this specific case.

The slight discrepancies in bearing factors between the experimental and the upper bound plastic limit analysis results are thought to be due to a combination of reasons. A major contributing factor is thought to be due to the combined effect of vertical and moment loading. There was also uncertainty on whether or not a gap develop at the back of the pile.

Another observation made during the testing was settlement of the piles during loading. The connectors that were fabricated did not vertically constrain the pile, thus as each pile was horizontally loaded there was a corresponding vertical settlement. The influence of this vertical settlement on the failure mechanism is explained briefly in Murali (2015). This paper does not examine the vertical settlement in detail due to a insufficient measured experimental data.

Another possible source of error is the plastic coating applied on the piles to prevent corrosion of the strain gages. It was not possible to quantify the adhesion on the sides of

Table 3.1: Normalized lateral load bearing factors

| Pile test | e | $N_h$ experimental | $N_h$ - no gap Aubeny et al. (2003) |
|---|---|---|---|
| Test 2 | 1.25 | 1.6 | 1.58 |
| Test 3 | 1.25 | 1.46 | 1.58 |
| Test 4 | 1.5 | 1.22 | 1.45 |
| Test 5 | 1.5 | 1.235 | 1.45 |
| Test 6 | 2.5 | 0.99 | 1.09 |
| Test 7 | 2.5 | 0.90 | 1.09 |
| Test 8 | 3.5 | 0.65 | 0.87 |

the pile.

## 3.7 Comparison to 1-g Laboratory Experiments

Beemer (2015) developed a series of 1-g laboratory experiments conducted on squat caissons (aspect ratio, $L_f/D$=2). Results from a total of four experiments were presented. Loading was applied by using a cartesian robot constructed at Texas A&M University. The robot (CARMEn - Cartesian Robot for Marine Engineering) permits application of load in both vertical and horizontal directions. Technical information about this tool was presented by Beemer (2015). Several transducers were utilized in order to measure inclination, bending, vertical and horizontal load. The soil test bed was constructed from EPK kaolinite clay. A general sketch with dimensions is presented in Figure 3.13. The piles utilized were the same as in the previously presented centrifuge testing program. Two different eccentricities were considered.

A comparison between results from this experiment and FE predictions is presented in Figure 3.14. Comparison is done in terms of a normalized load-displacement curve for

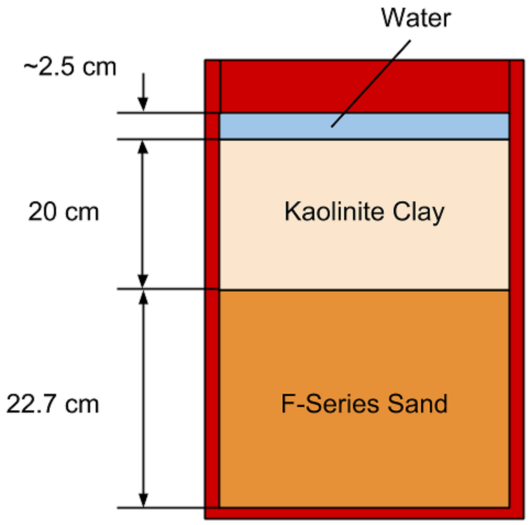


Figure 3.13: Testing soil bed used for 1-g experiments (Beemer, 2015)

the specific case of an eccentricity of 1.2 diameters.

A note of caution here. Beemer (2015) and Murali (2015) define eccentricity as the distance between the load application point and the pile cap. For the purpose of the FE model, eccentricity comes defined as the distance between the mudline and load application depth. This needs to be taken into account when setting up a reference node in the FEM. Measured capacity is bounded by results obtained running FE models for cases of adhesion, $\alpha$ equal to 1 and 0. Indeed, assuming an adhesion coefficient of 0.5 seems to produce agreement between results. It can be observed that the stiffness exhibited by the FE curve is significantly steeper than the measured values. This could be due to the fact that the caisson has been set as a rigid body in the FE model. It has been demonstrated that changing the pile material produces softer curves (Zhang, 2015) , however the final capacity should be

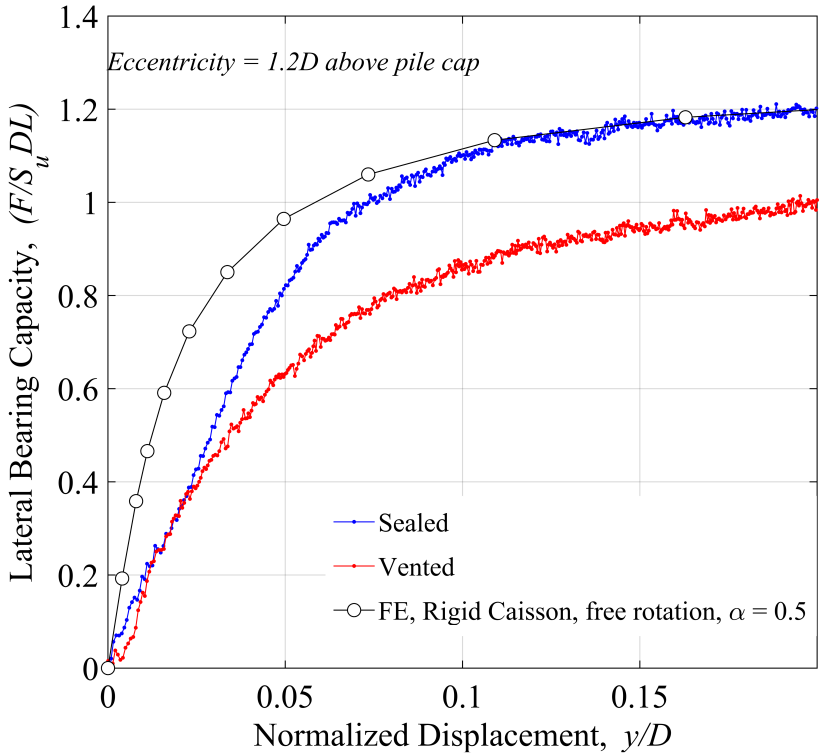


Figure 3.14: Comparison of FE predictions and 1-g laboratory results. Eccentricity, $e$ = 1.2

the same independently of the material.

Beemer (2015) presented curves for caissons tested under vented conditions and sealed conditions. FE predictions seem to match results for sealed conditions. This is consistent with the fact that, during centrifuge tests, all caissons were sealed.

# 4 CAPACITY OF PILES AND CAISSONS IN CLAY

## 4.1 Plastic Limit Analysis of Laterally Loaded Piles

The model herein proposed combines two different three dimensional failure mechanisms. The first one is the PLA developed by Murff and Hamilton (1993) . The second mechanism is similar to the one proposed by Randolph and House (2002); however mathematical expressions for dissipation functions are based on those presented by Murff and Hamilton (1993). It comprises two failure wedges (passive and active) located in front and behind the caisson and also a scoop mechanism, in order to account for interactions due to tip resistance for the case of short caissons.

Formulation of any upper bound solution is characterized by three main steps (Aubeny and Murff, 2005). First a kinematically admissible failure mechanism has to be postulated. Second, internal energy dissipation rates associated with that mechanism need to be computed. This step by itself entails:

1. Calculating strain rates at any point in the deformed soil around the pile by using spatial derivatives of velocity fields,
2. Computation of stresses by invoking an associated flow rule,
3. Computation of rate of energy dissipation per unit volume (i.e. the product of strain rates and stresses) and
4. Numerical integration over the whole volume to obtain total rate of internal energy dissipation.

Third the rate of internal energy dissipation has to be equated to the external work in order to obtain an upper bound estimate of capacity. In the analyses presented forces and moments are considered to be ‘generalized stresses’, while both linear and angular velocities are considered work conjugate ‘generalized strains’ (Prager, 1959).

### 4.1.1 Murff-Hamilton failure mechanism

Murff and Hamilton (1993) failure mechanism (from now on referred to as 'flow-around' mechanism) is presented in Figure 4.1 (a and b). It idealizes the pile as a laterally loaded rigid cylinder embedded in the soil with a radius $R$ and length $L_f$ (Han, 2002). It is assumed that the pile rotates about a point conveniently located on the centerline. Horizontal loading can be applied at any depth along the centerline of the pile (above or below the mudline). The failure mechanism comprises three different regions:

1. Conical failure wedges. Passive and active wedges with conoidal shape are considered to exist in the front and back of the pile respectively. The two wedges configuration corresponds to the assumption that the soil behind the caisson is able to stick to the walls (i.e. a gap does not exists). Gaps can be considered in the model. When doing so, only a passive failure wedge is included into the optimization scheme.
2. A flow-around zone (i.e. plane strain zone). In this zone the soil is assumed to "flow around" the circumference of the pile. Equations utilized for this region are the plasticity solutions developed by Randolph and Houlsby (1984) for the case of a translating cylinder.
3. A hemispherical failure surface at the tip, in order to account for energy dissipation

when rotational displacement fields are applied.

Strictly speaking, this solution does not enforce strain compatibility between the three regions, which is a requirement of upper bound solutions. Nevertheless, the solution is widely used as a benchmark through the offshore geotechnical engineering industry and has been compared numerous times with experimental and field data (Clukey et al., 2004; Randolph et al., 1998; Sukumaran and McCarron, 1999; Aubeny et al., 2001a).

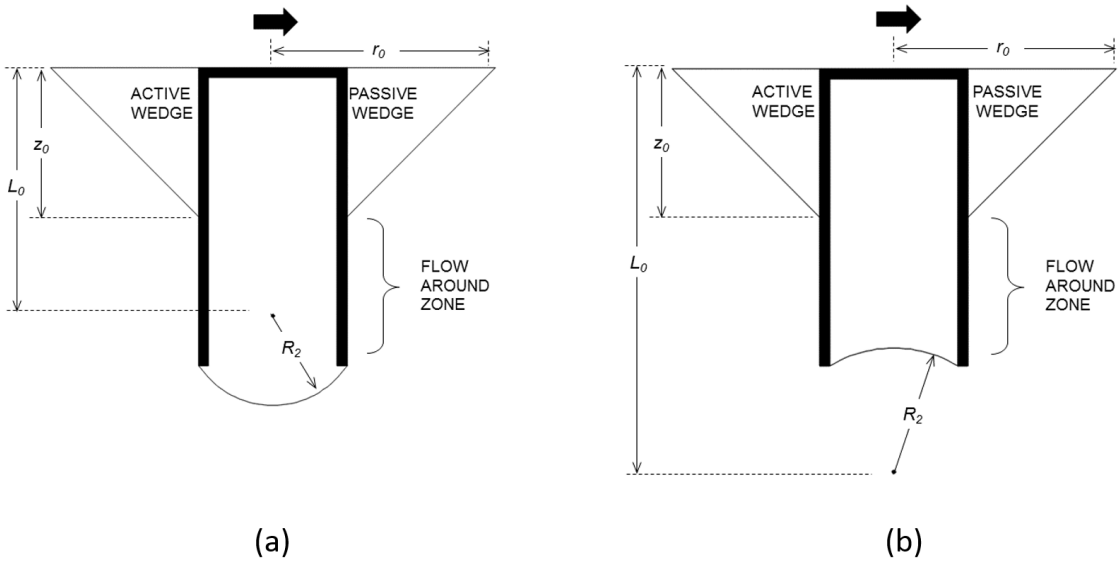


Figure 4.1: Murff-Hamilton failure mechanism for cases of (a) forward rotation and (b) backward rotation

Four optimization parameters define the geometry of the failure mechanism (Fig. 4.1):

1. The vertical extent of the failure wedge, $z_0$ measured from the mudline;
2. The depth to the center of rotation ($L_0$), which is represented by Murff and Hamilton (1993) as the variable $c$, in such a way that $L_0 = z_0/c$. However, in this study it is denoted $c_R$ in order to distinguish it from the coefficient of consolidation ($c$);

3. The radial extent of the failure wedge, $r_0$ measured from the caisson centerline;
4. The optimization parameter $\alpha_{opt}$, which is included in an equation characterizing the radial velocity field inside the wedge.

Internal energy dissipation rate is expressed as the summation of several terms that describe the virtual velocity fields occurring within the failure mechanism. These terms are presented in Figure 4.2, and described below:

**Term $\dot{D}_1$**

- Term $\dot{D}_1$ accounts for the energy dissipation rate (power) occurring due to volumetric deformation of the wedge itself.

$$\dot{D}_1 = 2\int_{r=R}^{r=r_0}\int_{z=0}^{z=z_0[(r_0-r)/(r_0-R)\,]}\int_{\theta=0}^{\theta=(\pi/2\,)}\dot{E}_1 r d\theta dz dr \tag{4.1}$$

- $\dot{D}_2$ is the dissipation rate due to friction between static soil (i.e. soil outside the wedge) and moving soil (i.e. soil within the wedge). Thus it occurs along the surface area in contact.

$$\dot{D}_2 = 2v_0\sqrt{1+\left(\frac{z_0}{r_0-R}\right)^2}\sqrt{1+\left(\frac{R-r_0}{z_0}\right)^2}\cdot\int_{z=0}^{z=z_0} s_u \frac{R^{\alpha_{opt}}\left(1-c_R\frac{z}{z_0}\right)}{\left[r_0-\frac{z}{z_0}(r_0-R)\right]^{\alpha_{opt}-1}}dz \tag{4.2}$$

- The term $\dot{D}_3$ considers dissipation rate occurring in the pile-soil boundary due to total or partial adherence of the soil to the pile wall.

$$\dot{D}_3 = 2\int_{z=0}^{z=z_0}\int_{\theta=0}^{\theta=\pi/2}\eta s_u\sqrt{v_z^2+v_c^2}Rd\theta dz \tag{4.3}$$

- Terms $\dot{D}_4$ and $\dot{D}_5$ compute energy dissipation occurring in the plane strain (flow-around) zone located right below the wedges, in which the velocity is assumed to be in a horizontal plane. The term $\dot{D}_5$ is only activated for the case of a rotational displacement field in which the center of rotation ($L_0$) falls within the length of the caisson.

$$\dot{D}_4 = \int_{z'=0}^{z'=(z_0/c_R)-z_0} 2v_0 z'\left(\frac{c_R}{z_0}\right)s_u N_p R dz' \quad for \quad (z_0/c_R\,) \leq L_f \tag{4.4}$$

or

$$\dot{D}_4 = \int_{z'=(z_0/c_R)-L_f}^{z'=(z_0/c_R)-z_0} 2v_0 z'\left(\frac{c_R}{z_0}\right)s_u N_p R dz' \quad for \quad (z_0/c_R\,) > L_f \tag{4.5}$$

Where $z'$ is computed as: $z' = (z_0/c_R) - z$. And, when needed, term $\dot{D}_5$ takes the form presented below:

$$\dot{D}_5 = \int_{z'=0}^{z'=L_f-(z_0/c_R\,)} 2v_0 z'\left(\frac{c_R}{z_0}\right)s_u N_p R dz' \tag{4.6}$$

Where $z'$ is computed as: $z' = z - (z_0/c_R)$.

- Finally, the term $\dot{D}_6$ takes care of energy dissipation occurring at the pile tip, which is mostly important for piles with a low aspect ratio.

$$\dot{D}_6 = \frac{v_0 R_2^3 c_R}{z_0} \int_{\phi=0}^{\phi=2\pi} \int_{\omega=0}^{\omega=\sin^{-1}\left(R/\sqrt{R_1^2+R^2}\right)} s_u \sin\omega \sqrt{\cos^2\omega + \sin^2\omega \sin^2\phi}\, d\omega d\phi \tag{4.7}$$

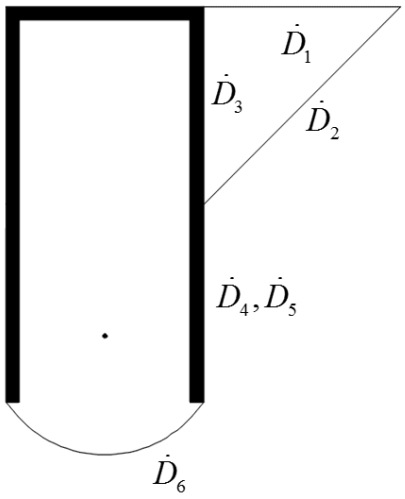


Figure 4.2: Region(s) corresponding to each energy dissipation rate. (Murff and Hamilton, 1993)

The failure surface was idealized as a spherical segment attached to the pile tip centered at the point of rotation ($L_0$) and radius ($R_2$) limited by the end of the caisson wall. This was achieved by using a spherical coordinate system with its origin located at the center of rotation of the pile. The dissipation is computed by integration over the spherical surface, limited by its intersection to the caisson wall. A graphical description of this surface is provided in Figure 4.3. $R_1$ is calculated as the difference between the pile length ($L_f$) minus the depth of the center of rotation ($L_0$); in that way the radius of the spherical segment can be computed using the Pythagorean theorem: $R_2^2 = R_1^2 + R^2$. Equations for dissipation rate terms have been previously presented in several sources (Murff and Hamilton, 1993;

Han, 2002; Sharma, 2005).

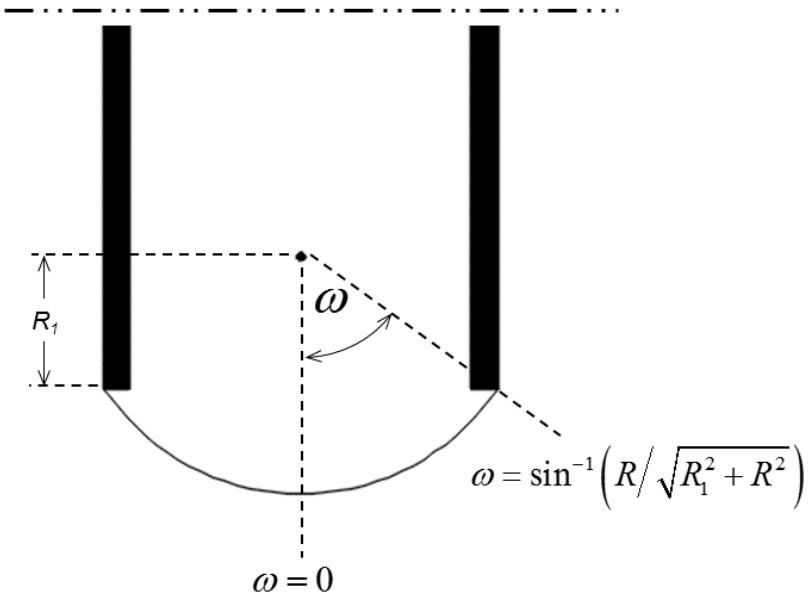


Figure 4.3: Hemispherical failure mechanism for computation of energy dissipation rates at the pile tip. (Murff and Hamilton, 1993)

Plastic hinges forming in long piles can be accommodated. However, for stubby squat piles and caissons this condition is neglected, since the deformation mode is believed to be a different one.

External work needs to be computed from both the self-weight of the wedges and the applied horizontal load. For the case of gapping (i.e. an opening form behind the pile as it moves in the direction of loading), external work by the passive wedge self-weight does play an important role in the equation (Eq. 4.8). However, for cases in which no gaps are considered, both passive and active wedges are assumed to be equal in size thus external work from both wedges is assumed to be equal and opposite (i.e. zero).

$$\dot{W}_1 = 2\int_{r=R}^{r=r_0}\int_{z=0}^{z=z_0[(r_0-r)/(r_0-R)\,]}\int_{\theta=0}^{\theta=(\pi/2\,)} v_z\gamma' r d\theta dz dr \tag{4.8}$$

Finally, the lateral load ($H$) is computing by equating external and internal work, as described by eq. 4.9 presented below:

$$H \cdot v_0 = \left(\sum_{i=1}^{n} \dot{D}_i\right) \cdot v_0 - \dot{W} \cdot v_0 \tag{4.9}$$

Where $H$ is the lateral collapse load, $v_0$ is the virtual velocity (which is canceled), $\dot{D}_i$ denotes the internal energy dissipation rate terms and represents the external work rate. The code is implemented numerically by using a Matlab based function entitled *fminsearchbnd.m*. This function utilizes the simplex algorithm in order to perform an optimization and get a bounded minimum for $H$.

### 4.1.2 Scoop failure mechanism

Inspired by a failure mechanism published by Randolph and House (2002), a second failure mechanism has been developed. This mechanism seems to be more suited for the case of short piles or caissons (aspect ratios less than 3) sustaining large moment loading. The mechanism is presented on Figure 4.4 and comprises two regions: conical failure wedges and spherical scoop failure surface. In this case only three optimization parameters are required: the radial extent of the failure wedge, $r_0$ which is measured from the pile's centerline; the vertical extent of the failure wedge, $z_0$ measured from the mudline and the optimization parameter $\alpha_{opt}$, which was explained in the previous section. The center of

rotation ($L_0$) is defined as a function of the wedge depth ($z_0$) and therefore is not anymore an independent optimization parameter, this is described in Eq. 4.10.

$$L_0 = z_0 + \frac{L_f - z_0}{2} \tag{4.10}$$

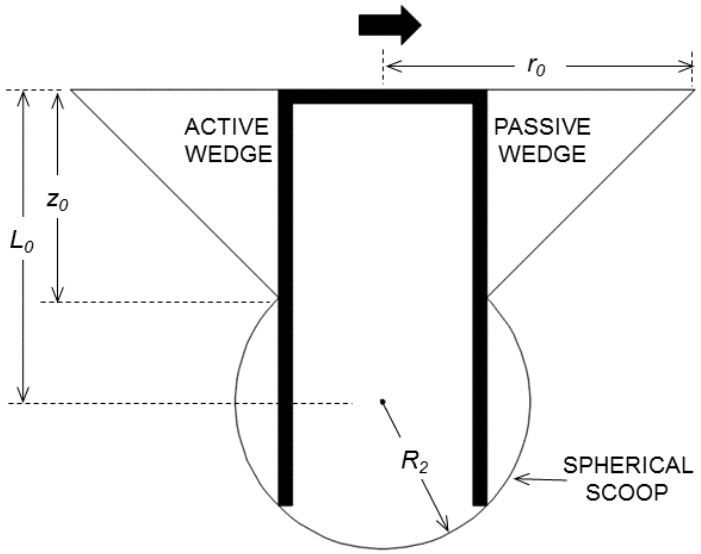


Figure 4.4: Failure mechanism based on proposed method by Randolph and House (2002)

First, active and passive wedges are considered at the back and front of the caisson respectively. In the same way as the flow-around mechanism, if a gap forms behind the pile, only a passive wedge is considered. Dissipation rates for these wedges are calculated using the same equations published by Murff and Hamilton (1993). The energy dissipation rate terms corresponding to both wedges can be expressed mathematically as follows (Eq. 4.11):

$$\dot{D}_{Wedges} = 2 \cdot \left(\dot{D}_1 + \dot{D}_2 + \dot{D}_3\right) \tag{4.11}$$

Where:

- $\dot{D}_1$ is the internal energy dissipation in the wedges,
- $\dot{D}_2$ is the energy dissipation due to friction between static soil and moving soil, and
- $\dot{D}_3$ is the energy dissipated by contact between soil and pile.

The resistance at the base of the pile is accounted by considering a spherical failure surface (or scoop) at the bottom of the pile. This equation is similar to the one utilized by the flow-around mechanism, in which a hemispherical failure surface was defined at the base of the pile and its angular extent was delimited by the circumference of the pile walls at the bottom. By changing the integration limits it is possible to extend this surface to the next point of contact with the pile surface, which forms an almost complete sphere, herein denominated "scoop". The energy dissipation rate term at the caisson tip can be expressed using spherical coordinates by Equation 4.12. A sketch of this failure surface is also provided in Figure 4.5.

$$\dot{D}_{tip} = \frac{v_0 R_2^3 c_R}{z_0} \int_{\phi=0}^{\phi=2\pi} \int_{\omega=0}^{\omega=\sin^{-1}\left(R/\sqrt{R_1^2+R^2}\right)+\pi/2} s_u \sin\omega \sqrt{\cos^2\omega + \sin^2\omega \sin^2\phi}\, d\omega d\phi \tag{4.12}$$

Where:

- $\dot{D}_{tip}$ is the energy dissipation at the tip,
- $v_0$ is the virtual velocity,

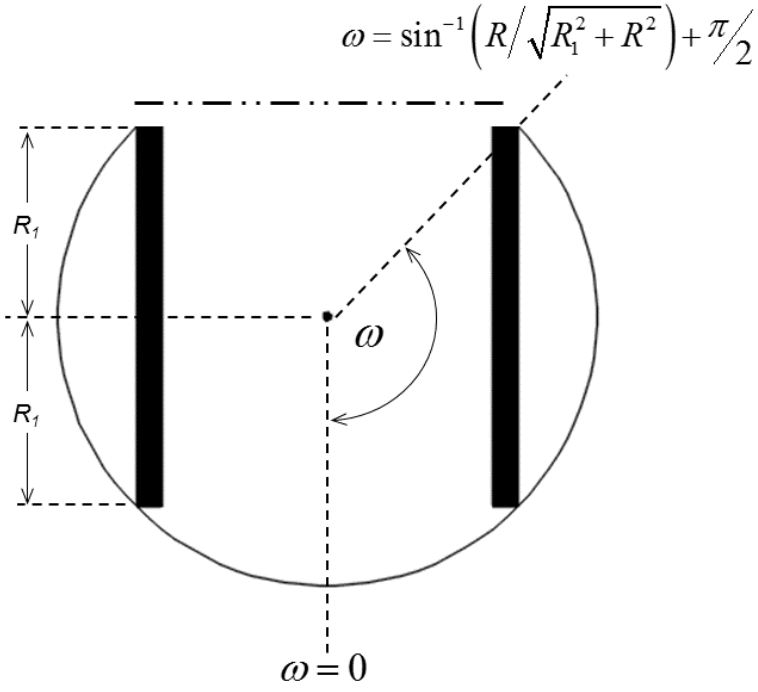


Figure 4.5: Details of integration limits in scoop failure surface

- $R_2$ is the radius of the sphere,
- $s_u$ is the undrained shear strength at each corresponding integration point,
- $\phi$ represents the angle around the pile circumference (varied from 0 to $2\pi$),
- $\omega$ is the angle measured from the pile centerline to the intersection of the scoop with the upper wall of the caisson, as presented in Fig. 4.5.
- $R$ and $R_1$ were previously defined.
- The $c_R$ parameter included in Eq. 4.12. As it was previously mentioned, the original Murff-Hamilton PLA expressed the center of rotation as a function of the wedge depth and the variable $c_R$, which was the optimization parameter. For this scoop mechanism, the center of rotation has been defined as shown in Eq. 4.10. However, from a computational standpoint it is convenient to retain $c_R$ in the equation, but

re-defining it as follow (Eq. 4.13):

$$c_R = \frac{z_0}{L_0} \tag{4.13}$$

Finally, external energy dissipation rate is computed in the exact same way as in the flow-around failure mechanism previously explained. Throughout the remainder of this chapter, this failure mechanism (Randolph and House, 2002) will be denoted as "Scoop" failure mechanism. The original Murff-Hamilton will be named as the "Flow-Around" mechanism to describe the nature of the assumed failure mechanism just above the pile tip.

## 4.2 Comparisons in Terms of Lateral Bearing Capacity

A simple comparative evaluation of the two failure mechanisms is to compute capacities for different aspect ratios (having previously selected a soil strength profile). Figure 4.6 presents a comparison between both approaches. The case corresponds to a laterally loaded caisson. Full adhesion ($\alpha$=1) and no gapping allowed at the back of the pile. The soil strength is uniform and the load is applied at the mudline level. The caisson is allowed to rotate freely.

A notable observation is that, for this specific case of eccentric loading (i.e. the load is applied above the center of rotation, producing a forward rotation motion), the scoop mechanism predicts lower capacities for a limited range of aspect ratios ($L_f/D$) ranging from 1.5 to 5 approximately. For aspect ratios ($L_f/D$) greater than 5, the flow-around mechanism becomes the controlling mechanism. This observation is in agreement with the initial notion that the Flow-Around mechanism (Murff and Hamilton, 1993) applies to

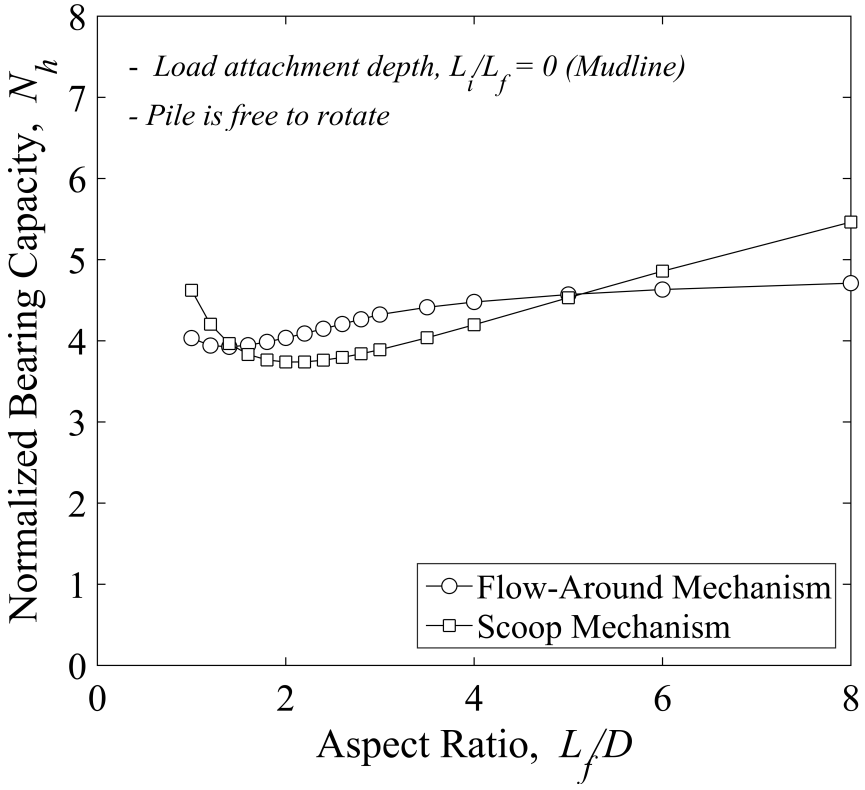


Figure 4.6: Horizontal bearing capacities predicted with both Flow-Around and Scoop models. Aspect ratio, $L_f/D = 2$, load attached at the top of the caisson

long and slender piles but is less accurate for short piles and caissons.

If a pure translation motion is considered (as it is presented in Figure 4.7), the flow-Around mechanism does a significantly better job predicting capacities for both short and long caissons. The only region at which the scoop mechanism performs better corresponds to caissons of aspect ratios less than 1.75 approximately. For greater values of aspect ratio, the scoop mechanism becomes inappropriate as it seems to indicate that capacity keeps increasing, while the flow-around maintains a bearing capacity of around 12. This suggests that the main difference between both approaches is related to the horizontal-moment load

interaction (i.e. eccentric loading).

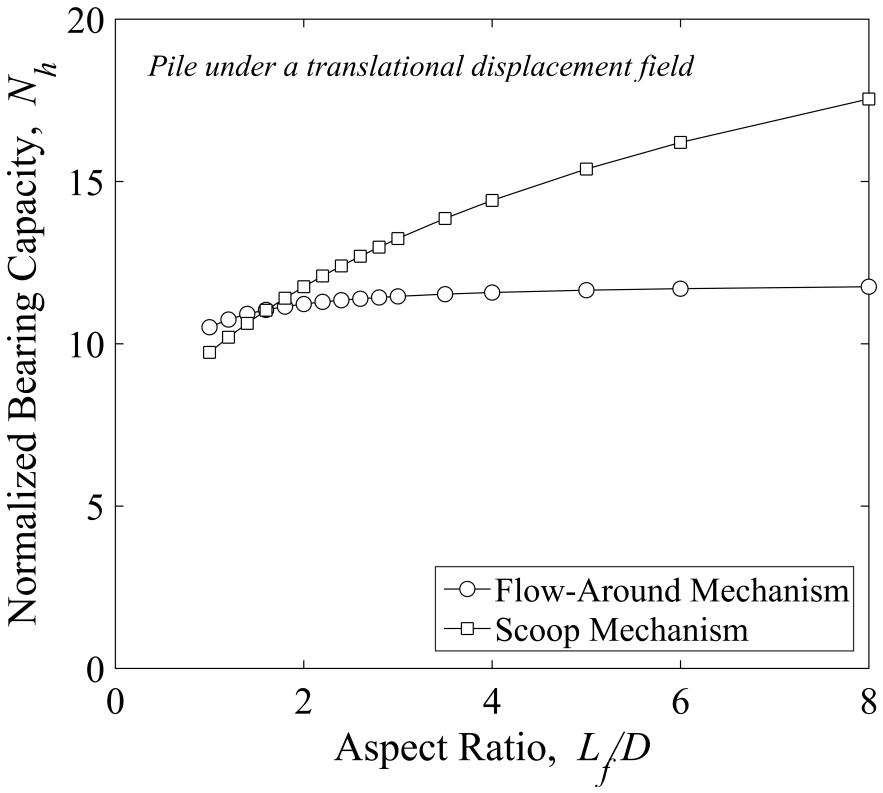


Figure 4.7: Horizontal bearing capacities predicted with both Flow-Around and Scoop models. Aspect ratio, $L_f/D = 2$, pile is under translation

Although it might seem that a translational displacement field is highly unlikely, in many cases suction anchors are designed to as nearly as possible fail in a translational mode. This is done by attaching the chain around the middle of the caisson, region which is very close to the optimal center of rotation, producing thus a translational failure.

### 4.3 Moment-Horizontal Load Interaction

A more sophisticated way to evaluate the two collapse mechanisms is by creating a moment-horizontal load interaction diagram (Fig. 4.8) in order to capture effect of mo-

ment loading. In order to do this, an estimate of the location of the center of rotation is needed. From both these analyses and previous studies (Aubeny et al., 2001a), the optimal center of rotation is located at about 0.5 times the pile length. Several combinations of moment and horizontal loads (or also rotations and displacements) are applied to the pile according to the convention presented also in Fig. 4.8. One of the advantages of this format is that the yield locus becomes symmetric around the $N_h - N_m$ axes, so the effect of moment loading can be more clearly visualized. Results are presented only for the case of a constant strength profile with forward rotation (i.e. the load application point varies from the center of rotation and upwards). Variable strength profiles will be considered in forthcoming sections. In the interaction diagram, moment load is presented in terms of a moment bearing capacity, previously defined in Chapter 3.

For the case of forward rotation (i.e. moment bearing factor plots positive), the flow-around PLA seems to over-predict moment loads by approximately 15% (i.e. flow-around mechanism predicts $N_m$ = 2.65 while scoop mechanism shows $N_m$ = 2.31). Also, for moment bearing capacities exceeding $N_m \approx 1.4$, the scoop mechanism predicts lower numbers for horizontal bearing capacity ($N_h$) compared to flow-around PLA method. On the other hand, for regions where translation dominates (i.e. moment bearing capacity greater than 1.4), the envelope predicted by the flow-around mechanism shows lower estimates and therefore would control the design. As moment loads increase (with corresponding increases in eccentricity, either positive or negative), the scoop mechanism seems to control since it provide lower results for both moment and horizontal load capacities. For exam-

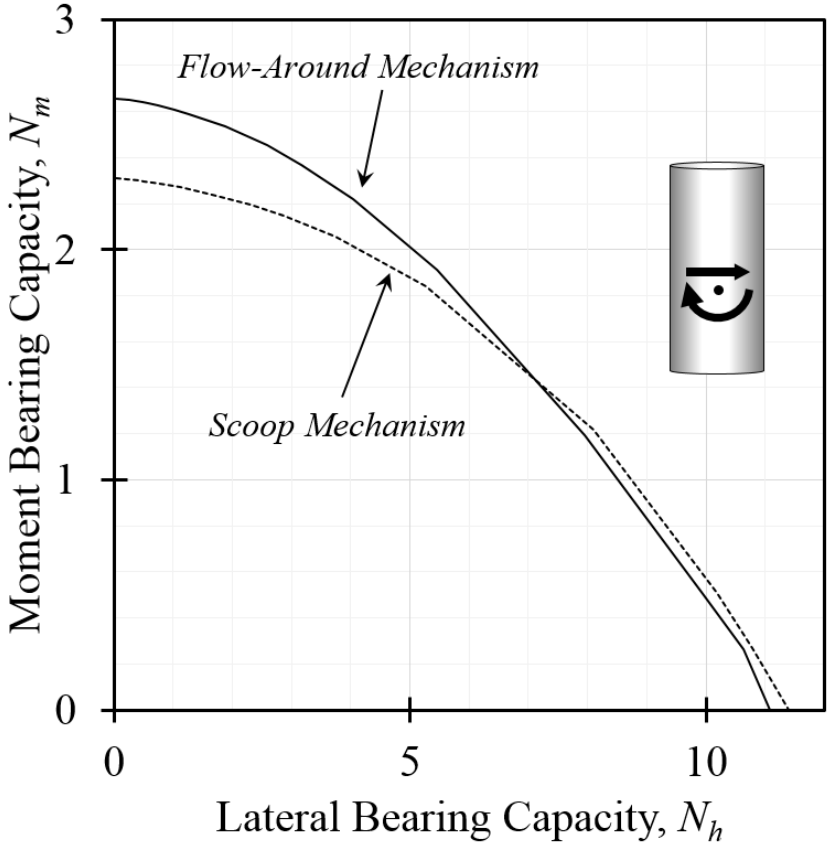


Figure 4.8: Moment-Horizontal loading interaction diagram predicted with both Flow-Around and Scoop models. Aspect ratio, $L_f/D = 2$, load attached at the top of the caisson

ple, if we assume that $N_m$ is fixed to be equal to 2, the flow-around PLA predicts $N_h \approx 5.2$ while the scoop mechanism predicts $N_h \approx = 4.2$. This represents roughly a 25% difference between both methods. This result implies that Murff-Hamilton PLA needs to be updated in order to accommodate horizontal loads applied at relatively high eccentricities.

Another very common way to illustrate moment-horizontal load interaction consists in varying the depth of the load application point from -∞ to ∞ with respect to the mud-line level and plotting capacity as a function of load attachment depth. Figure 4.9 presents the variation of the horizontal capacity as the load attachment depth (or in this case, ec-

centricity) is increased from below the pile to 2 lengths above the mudline. Similar plots have been already presented for depths below the mudline (Aubeny et al, 2001; Aubeny et al, 2003). Horizontal capacity is given in terms of a lateral bearing factor ($N_h$) defined in Chapter 3.

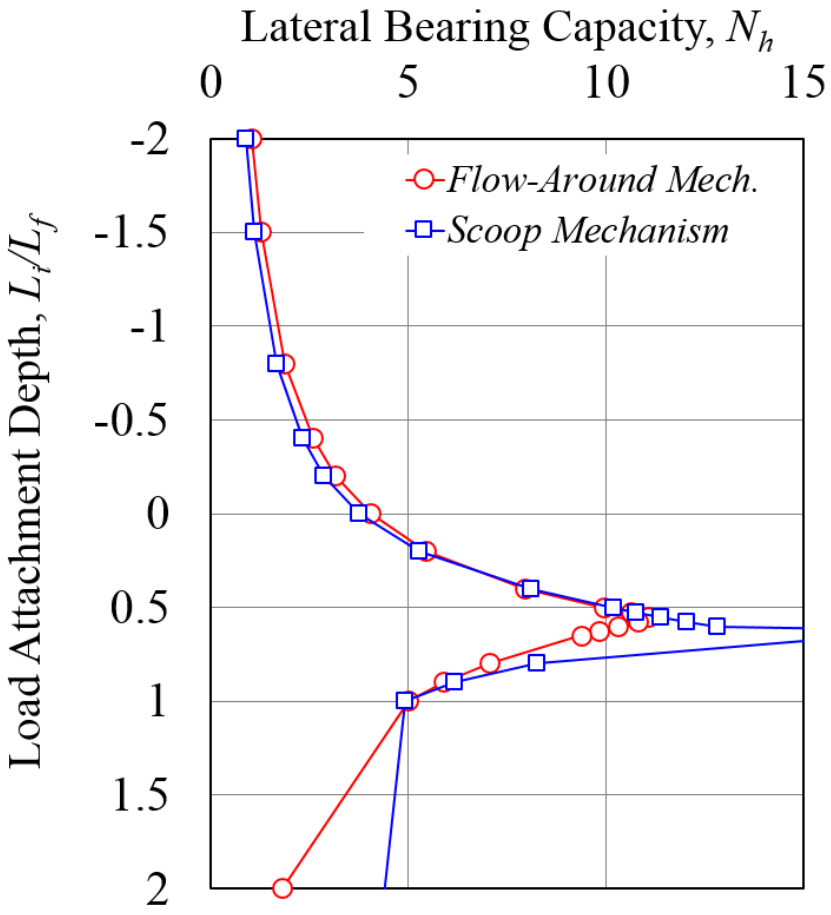


Figure 4.9: Horizontal bearing capacities predicted with both Flow-Around and Scoop models. Aspect ratio, $L_f/D$ = 2, load attached at several points along the length of the caisson

Results are presented for both the case of a constant strength profile. The flow-around mechanism (plotted in red line) seems to over-predict results for load attachment depths above the mudline (i.e. greater than 0) when compared with the scoop mechanism

(blue). Notice that as the load attachment depth approaches the middle of the caisson, both failure mechanisms approach their maximum values, however, in this region the flow-around mechanism preforms significantly better.

Both failure mechanisms have been configured in such a way that a linearly increasing undrained strength profile can be accommodated. The effect of soil strength is accounted by introducing the non-dimensional parameter $\rho$, which is analog to strength gradient and is defined in eq. 4.14. This same parameter will be used throughout the rest of this study.

$$\rho = \frac{s_{u0}}{s_{u1} D} \tag{4.14}$$

Where $s_{u0}$ is the soil strength at the mudline, $s_{u1}$ is the strength gradient assuming a linear increase and $D$ is pile diameter.

## 4.4 Modifications for Short Piles Based on Finite Element Analyses

A first approach is to superimpose FE solution for several aspect ratios over the plot presented in Figure 4.7. This is presented in Figure 4.10. Notice that Fig.4.10 presents the vertical axis starting from $N_h$=8 in order to fully appreciate the behavior. It can be observed that FE predictions approximate the flow-around PLA solution for cases of relatively long piles ($L_f/D > 4$). On the other hand, for the case of aspect ratio equal to 1, FE predictions seem to be in agreement with the value computed with the scoop PLA.

It becomes evident then that lateral capacity is being a bit over-estimated by both PLA methods for piles and caissons with aspect ratios ranging from approximately 1.5 to

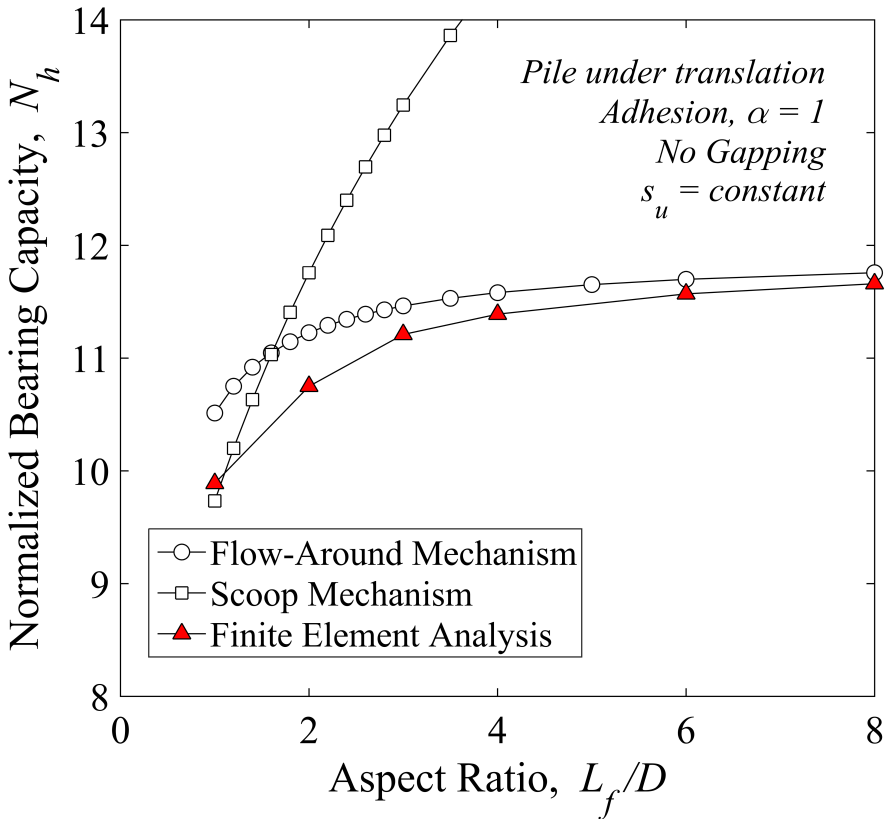


Figure 4.10: Horizontal bearing capacities predicted with both PLA models and compared to FE predictions. Aspect ratio, $L_f/D = 2$, caisson under translation, constant shear strength

3. Which corresponds to the range mentioned in previous chapters.

From Figure 4.10 calculations have been performed in order to compute the difference between both failure mechanisms (i.e. flow-around and scoop), and the predicted horizontal bearing capacities from the finite element study. A power-law correction factor is introduced in equation 4.15 below.

$$\xi = 0.93 \cdot \left(\frac{L_f}{D}\right)^{0.04} \quad for \quad 1 \le \left(\frac{L_f}{D}\right) \le 6 \tag{4.15}$$

Usage of this reduction factor is limited for piles and caissons of short aspect ratios

ranging between 2 and 6. For the rest of the cases it should be set to be equal to one ($\xi = 1$). Implementation of this reduction coefficient is presented figure 4.11, in terms of moment-horizontal load interaction.

If an aspect ratio of 2 is selected, moment-horizontal load interaction diagrams can be computed using both the failure mechanisms and compared against interaction diagrams obtained through FE predictions. Figure 4.11 (a and b) presents the complete envelope, this is, the load attachment point is varied from well above the mudline (positive part of the plot) to well below the tip of the pile (negative part of the plot).

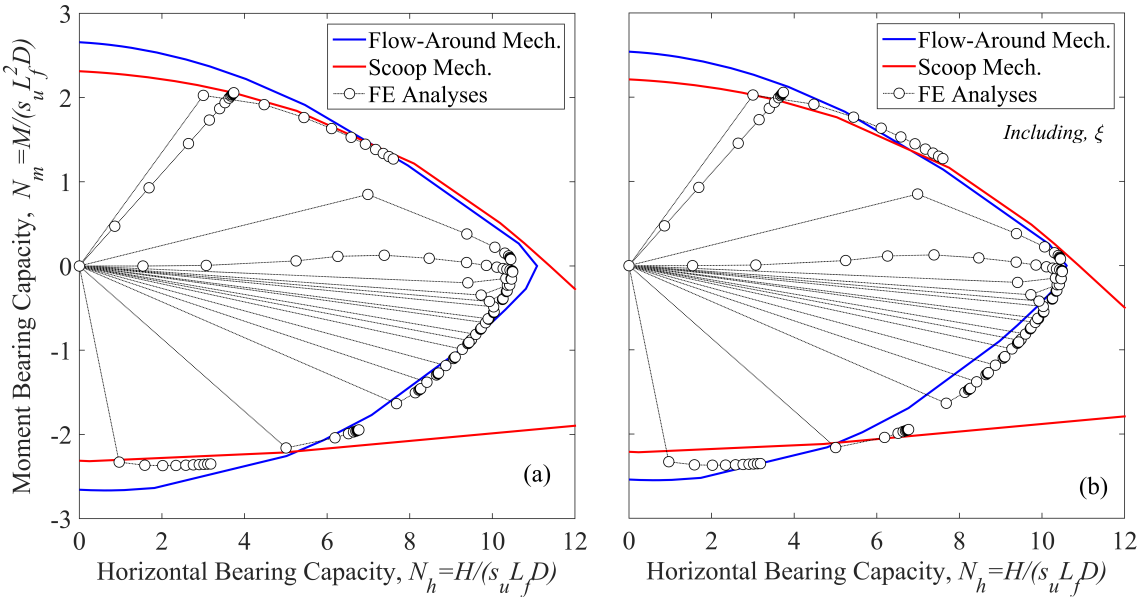


Figure 4.11: Moment-Horizontal load interaction diagram. FE solutions are superimposed together with Flow-Around Mechanism and Scoop Mechanism

In Fig.4.11(a), results from plastic limit analyses are shown without applying any type of reduction. It is possible to notice that FE predictions and scoop mechanism seem to be in very good agreement when it comes to predicting moment capacities. However,

for the case of pure translation (i.e. $N_m = 0$), the flow-around PLA (which controls this part of the envelope) predicts numbers that are roughly 5% higher than FE results.

On the other hand, Fig. 4.11(b) presents reduced PLA calculations compared with the same FE results as in Fig.4.11(a). Horizontal bearing capacities match perfectly ($N_h \approx 10.75$), whilst moment capacities are barely affected. Moment capacities for the cases of forward rotation (load attached above the mudline), still show acceptable agreement with FE solutions. Minor discrepancies can be observed for cases of backward rotation (load is attached well below the pile tip), however, these cases are highly unlikely to occur and are in general included for completeness.

## 4.5 Simplified Upper Bound PLA

Having presented improvements to traditional upper bound PLA methods, it is important to mention that they are in general tedious to code. Also, since their usage relies on the selection of adequate optimization parameters, the user would be required to have developed some insight on how to select appropriate initial and boundary values for these parameters.

For this reason it becomes useful to recall the simplified upper bound PLA explained previously in Chapter 2. The simplified PLA has the advantage of simplicity. It is a tool that can be coded in research oriented programming languages, such as c++, Fortran and Matlab, and yet it can be programmed in a simple spreadsheet. The other advantage that the simplified method presents over its full PLA counterpart is the running time. While

computation of capacity using the full PLA method could take from 5 to 30 depending on complexities, the simplified PLA produces results in just seconds. Due to these reasons, the simplified method has been widely used in industry by consulting firms and engineers in order to generate benchmark solutions for design.

Since empirical functions initially introduced in this method were calculated only based on Murff and Hamilton (1993) PLA code, it is expected that predictions will also over-estimate results for cases of short piles and caissons. The most straight forward way to improve predictions is to introduce modifications in the empirical function originally developed by Murff and Hamilton (1993) based on soil resistance profiles ($N_{ps}$) computed from FE analyses using the approach presented in Section 3.2 of this document.

### 4.5.1 Modified soil resistance function

Figure 4.12 shows FE predictions of the distribution of side resistance $N_{ps}$ versus depth for aspect ratios $L_f/D$ varying from 1 to 5 in a uniform soil strength profile. As it was mentioned in Chapter 3, $N_{ps}$ was computed at a given depth by integrating the resultant of computed FE stresses around the circumference of the caisson.

As a note of caution. The soil resistance profiles shown in Fig.4.12 ignore the severe singularities and spikes that finite element typically produces at the base of the pile. As it was mentioned in Chapter 3, this noisy behavior is very common and mainly due to the abrupt change in stiffness from the last element of the pile to the next element, which is only soil. The main purpose of extracting soil resistance profiles from FE analyses is to re-calibrate the upper part of the diagram, which reflects influence of free surface.

Nevertheless, it is very probable that once re-calibrated, the new soil resistance function will produce conservative results when compared to FE analyses in terms of total capacity. The reader should keep this in mind when checking results to be presented on this section.

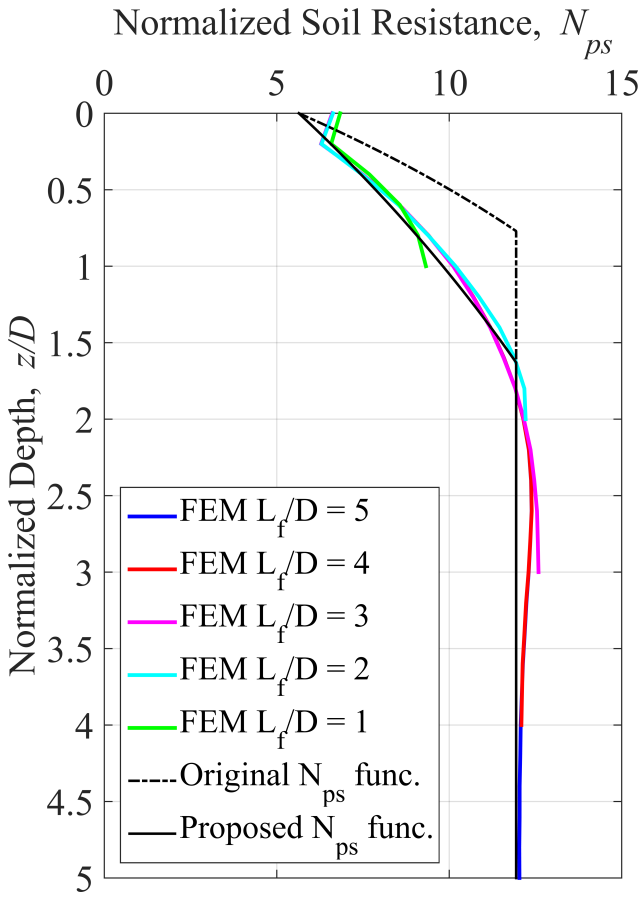


Figure 4.12: Distribution of side resistance compared to empirical function by Murff and Hamilton (1993) and the one proposed in this study.

With the exception of very short caissons ($L_f/D = 1$), the finite element calculations generally support the assumption that $N_{ps}$ is essentially independent of aspect ratio (at least this is true for cases in which no gapping is allowed). Below a normalized depth, $z/D > 3$,

$N_{ps}$ is essentially uniform, indicating that a flow-around collapse mechanism prevails in this region.

Comparison of the soil resistance profile ($N_{ps}$) obtained from FE analyses to the profile from the Murff and Hamilton (1993) mechanism for a uniform soil strength with no gap shows the Murff and Hamilton (1993) empirical $N_{ps}$ profile to exceed the finite element calculations at shallow depths (i.e. $z/D < 2$).

It is important to note here that the Murff and Hamilton (1993) profile shown here is not directly derived from the full upper bound collapse mechanism for a no-gap failure mechanism; i.e. surface failure wedges at the passive and active sides of the caisson (Fig. 4.1). Rather, it is based on a single-wedge collapse mechanism with the bearing factor $N_{ps}$ doubled – but capped so as not to exceed the flow-around value – to account for the added resistance provided by an active wedge. This suggests that the accuracy of the side resistance functions $N_{ps}$ can be improved by developing completely independent empirical relationships.

Murff and Hamilton (1993) proposed the following exponential form for the side resistance bearing factor:

$$N_{ps} = N_1 - N_2 \exp(-\eta z/D) \tag{4.16}$$

The parameter $N_1$ is the flow-around zone bearing resistance ranging from 9.43-11.94, and $N_2$ is the near-surface bearing resistance ranging from 2 to 2.82 when no gapping occurs. The lower and upper bounds cited here relate to surface roughness range, $\alpha$. The parameter $\eta$ controls the rate at which bearing resistance transitions from its near-surface

value to the flow-around condition, which depends on the soil strength profile. For the case of no-gapping, the method assumes that an active wedge forms behind the pile, reason why the soil resistance ($N_{ps}$) for these cases is doubled, but capped in such a way that the maximum is given by $N_1$.

Fitting of Equation 4.16 to the finite element profiles produced the $\eta$ values which closely follows a parabolic form, characterized by Eqs.4.17 and 4.18 presented below.

$$\eta = 0.129 + 0.03\rho - 0.002\rho^2 \quad for \quad \rho \leq 9 \tag{4.17}$$

$$\eta = 0.27 \quad for \quad \rho > 9 \tag{4.18}$$

The equation has been validated for different strength gradient through comparison to soil resistance distributions from FE analyses under similar conditions. Results are presented in Figure 4.13

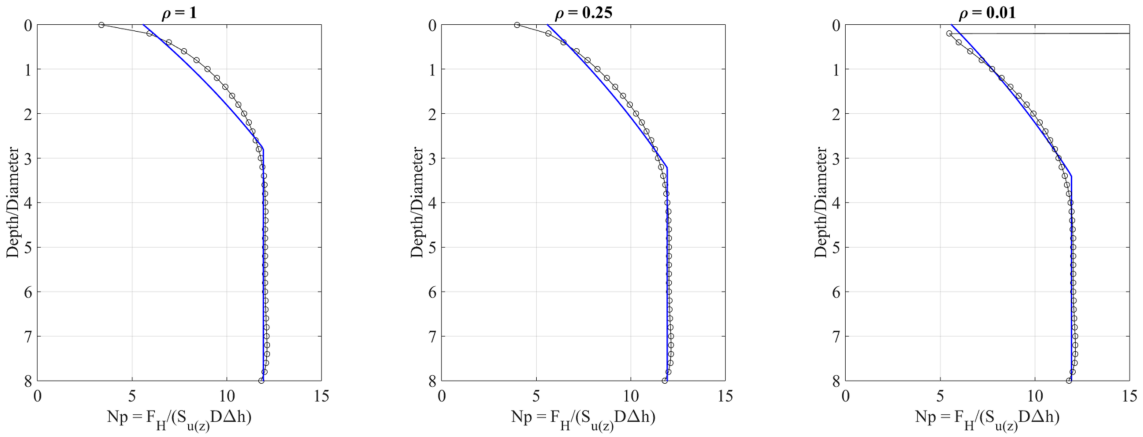


Figure 4.13: Distribution of side resistance compared to new empirical function for different strength gradients.

Having validated a new $\eta$ function, the next step involves incorporating the modi-

fied equations into the existing simplified PLA code, developed by Aubeny et al. (2001a). The method was briefly introduced in Chapter 2 of this document. However, it has been extensively explained by Han (2002) and Aubeny et al. (2003).

Comparisons are presented in Figure 4.14. First observation would be that the simplified solution predicts lower capacities than both the upper bound PLA and the FE method. This is likely due to the fact that when fitting was done to obtain the updated function, high stress concentrations at the pile tip were not considered. Data points corresponding to FE analysis (plotted in red triangles) do include base resistance. As aspect ratio increases, the proposed simplified function approaches capacities predicted by the two other methods.

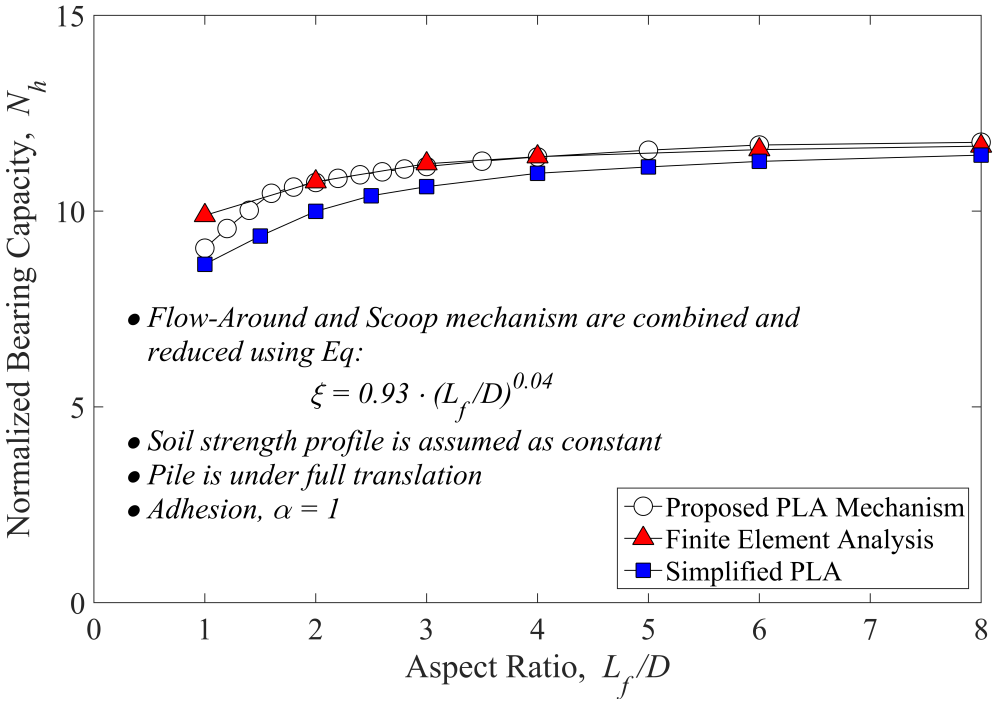


Figure 4.14: Comparison of normalized capacities from different methods.

## 4.6 Formation of Gaps

If gapping occurs, the reduction in horizontal load capacity due to loss of shearing resistance in the active surface wedge is offset somewhat by the removal of the driving stresses that occur when the active wedge separates from the caisson. Thus, modeling of the gapped condition requires the following modifications to the formulation described above for no-gapping:

1. The equivalent soil pressure $N_{ps}$ must not be doubled, since only a passive wedge is assumed to form.
2. The net bearing resistance must be increased to account for the removal of the active driving stresses from the surface wedge. Aubeny et al. (2001a) give the form of the revised equation for the case of gap formation:

$$P = N_{ps} s_u D + \gamma' z D \leq N_1 s_u D \tag{4.19}$$

The inequality in Eq. 4.19 ensures that P will not exceed the flow-around resistance value. However, care must be taken when using the simplified method, especially the region where free surface effects still dominate behavior. Cases with extremely high buoyant unit weights ($\gamma'$) could to produce soil resistance factors ($N_{ps}$) higher than those where no gapping is allowed. Whenever this happens, it is necessary to prevent the 'gapping' values to go beyond the 'no-gapping' values. Figure 4.15 presents a comparison of soil resistance distributions for different buoyant unit weights (designated as B.U.Wt. in the graph), ranging from zero density to the case of no gapping, in which density plays no role at all.

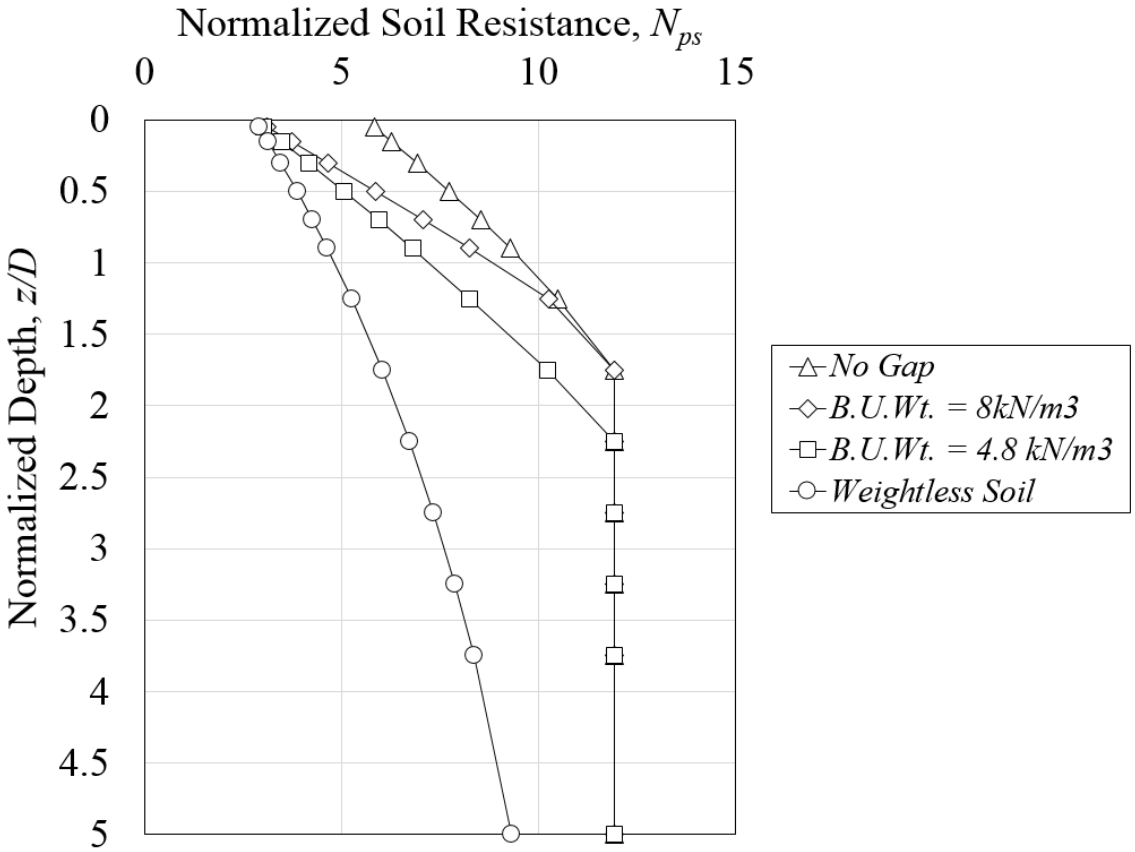


Figure 4.15: Distribution of side resistance compared to empirical function for strength gradient of one.

# 5 CAPACITY OF PILES AND CAISSONS IN SOILS WITH CRUST

## 5.1 Preliminaries

As it has been pointed out in Chapter 2, presence of crust zones in marine soils is a problem that is becoming increasingly common in several locations around the globe. Said this, most of the available tools for analyzing laterally loaded piles have been initially developed for uniform soil profiles.

One of the tools that is readily available on these cases are finite element (FE) analyses. A non-linear soil strength profile can be easily incorporated into the material properties of the soil. After running the model, stresses around the pile can be transformed into equivalent springs (i.e. p-y curves) that can at the same time be used for performing simpler load-deflection analyses.

A limitation of this approach is the fact that FE models need significant computational resources that might not be available to all users in industry. In this sense, plastic limit analyses (PLA) such as the one proposed by Murff and Hamilton (1993) present the advantage of simplicity. Complex soil strength profiles can be incorporated into the code and running time is relatively short ($\approx$ 15min per case) compared to most FE analyses. Still, the Murff-Hamilton upper bound code is available as a Matlab-based application, and learning to use the code adequately can become a time-consuming task.

Given this fact, it would be ideal to be able to incorporate non-linear soil profiles into the simplified PLA approach by Aubeny et al. (2001a) (also explained in Chapter 2).

However, as it stands right now, this approach is limited to either constant or linearly increasing strength profiles. The reason for this is that the empirical soil resistance function (which resembles response obtained with Murff-Hamilton code) depends on the dimensionless strength gradient ($\rho$), which at the same time is function of the soil strength at the mudline and the strength gradient of a linearly increasing strength configuration.

One of the main questions that needs to be answered is whether the presence of a crust affects the equivalent soil resistance ($N_{ps}$) profile of the soil in question. If that is the case, then modifications need to be introduced to the empirical function in order to account for crust effects. In addition, the effect of a crust on capacity is also uncertain at this point. Thus, there is a need to develop a rational basis in order to select an equivalent linear profile given a certain non-linear soil profile. This is the main purpose of this chapter.

## 5.2 Methodology

Ten different pile diameters have been selected for this segment of the study. Diameters and corresponding notations are presented in Table 5.1. Most of the selected sizes are relevant either to pile foundations or wells conductors. Piles 7 through 10 could also be applicable to suction caissons. An aspect ratio (length to diameter, $L_f/D$) of 5 was selected in order to ensure that even small-diameter piles span through the crust and reach the underlying weak layer. An example is the case of Pile No.1 having diameter is $D$ = 0.92 meters. Considering a crust that spans a total depth of 2.5 meters from the mudline, the minimum required aspect ratio such that Pile 1 could span the entire crust would be

around $L_f/D \approx 2.71$. Thus, strictly speaking, an aspect ratio of 3 should suffice for this purpose. However, prior to developing the analyses there was uncertainty on whether the presence of a crust could affect soil resistance distributions for depths located below the stiff layer. For this reason, aspect ratio was selected to be 5.

Although a revised version of the original Murff-Hamilton function has been proposed in Chapter 4 of this dissertation, results obtained through PLA analysis will be compared to the original function, because it was calibrated to match that solution.

Table 5.1: Selected pile diameters

| Pile No. | Diameter (inches) | Diameter (m) |
|---|---|---|
| 1 | 36 | 0.92 |
| 2 | 48 | 1.22 |
| 3 | 60 | 1.52 |
| 4 | 72 | 1.83 |
| 5 | 84 | 2.14 |
| 6 | 96 | 2.44 |
| 7 | 108 | 2.74 |
| 8 | 144 | 3.66 |
| 9 | 180 | 4.57 |
| 10 | 216 | 5.49 |

In order to develop this part of the research, the following steps were followed:

1. Definition of idealized soil strength profiles
2. Incorporation of nonlinear strength profiles into upper bound PLA program
3. Computation of capacities from PLA code
4. Computation of equivalent soil resistance distributions ($N_{ps}$), using procedures previously outlined in Chapter 2 of this dissertation.
5. Comparison to FE analyses in terms of total capacity

6. Comparison to the original $N_{ps}$ function.

Since comparisons are to be presented both in terms of total capacity and, most importantly, lateral bearing capacity along depth, a significantly fine discretization in the vertical ($z$) direction has been selected. In total approximately 1000 optimizations have been executed per crust case for the pile diameters listed in table 5.1.

## 5.3 Idealized Soil Strength Profiles

Determination of both the strength and vertical extent of the crust is possible with the use of cone penetrometer testing (CPT) and box core samplers. Fig. 5.1 presents CPT data obtained from three locations around the world.

A total of 80 CPT records are presented: 46 from Site A, 33 from Site B and one from Site C. The crust can be clearly observed at the top of the soil, with a linear increasing profile occurring below the crust. For the data herein presented, the high shear strength in the crust zone is believed to be either due to bioturbation or to the presence of high amounts of silt and sand-size foraminifera.

A representative soil profile has been developed (Fig. 5.2) to bracket the range of measured data. Parameters required to define geometry of the soil profile are also defined in figure 5.2. Three benchmark cases have been chosen: the case of a high-strength, average-strength and low-strength crust. Geometries for these cases are presented in Table 5.2. However, arguably the case of a high crust is the simplest and easier to model.

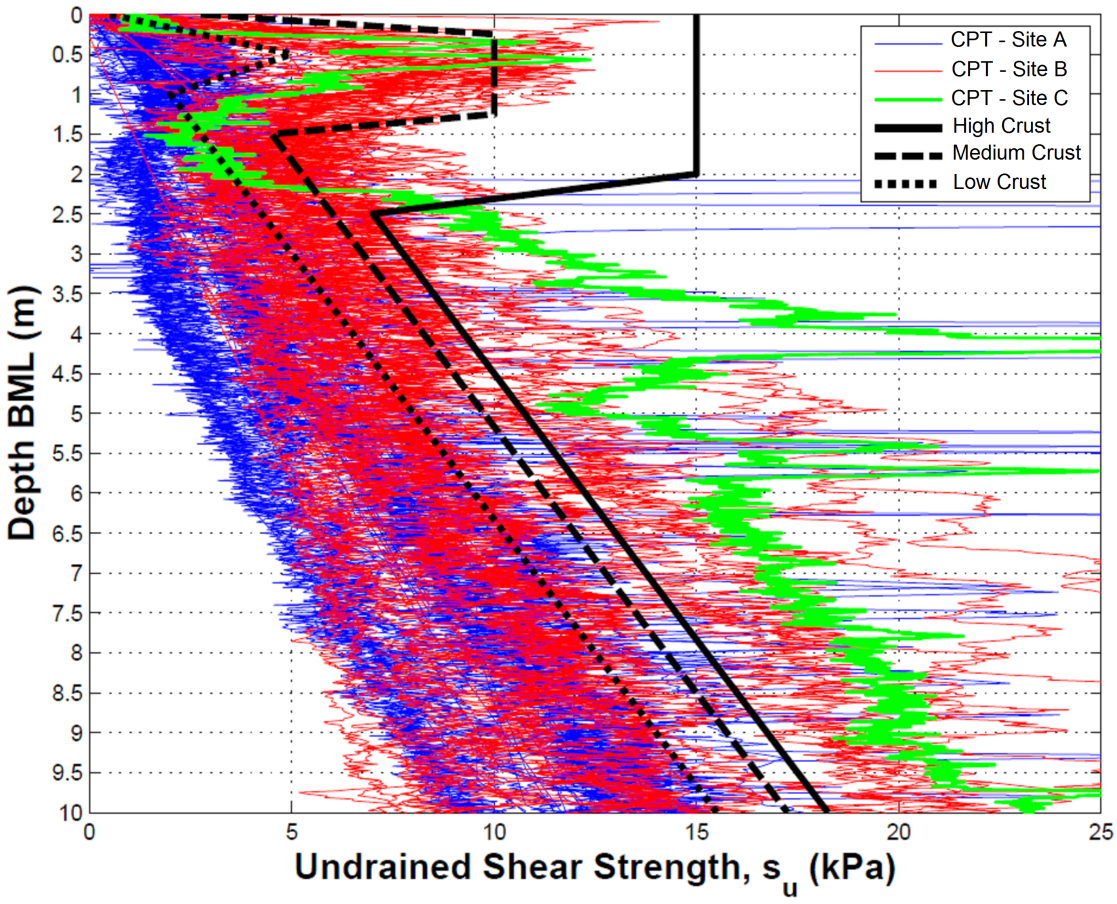


Figure 5.1: Undrained shear strength from CPT data at different locations (Courtesy of Dr. Philippe Jeanjean)

### 5.3.1 Incorporation of non-linear strength profiles into upper bound PLA

The upper bound code has been adapted in order to accommodate nonlinear strength profiles like the ones shown in Fig.5.2. This was done simply incorporating a Matlab based subroutine with the pertinent geometry and strengths into the original Murff-Hamilton code.

The code computes energy dissipation rates for each integration point. For example: within the active wedge, there are one hundred integration points. Each of those points

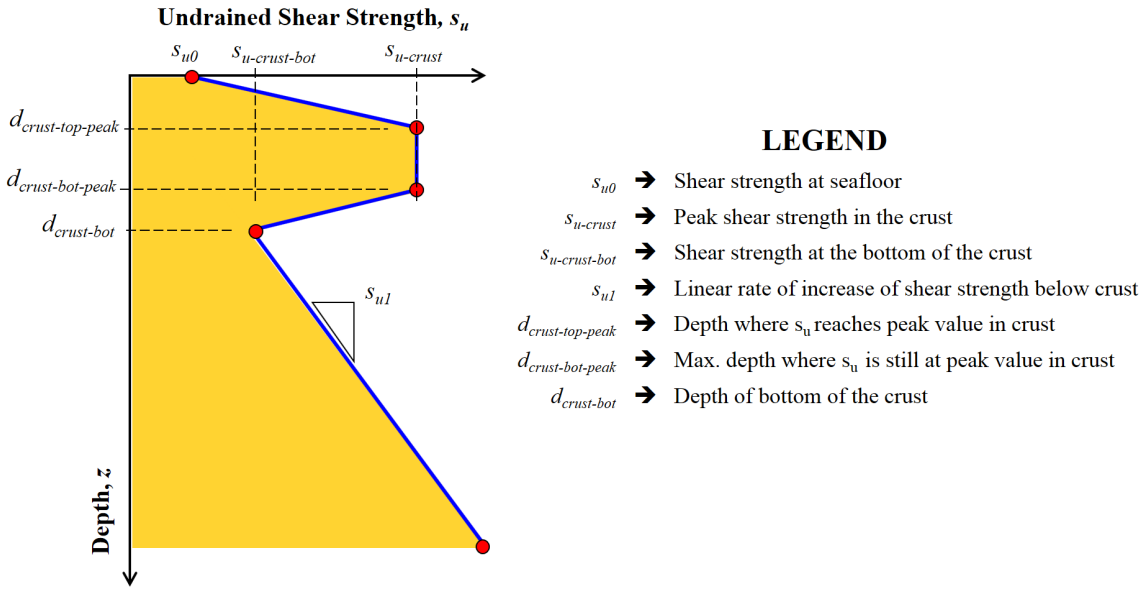


Figure 5.2: Schematic of idealized soil strength profile for stratified analyses

Table 5.2: Soil strength profiles to be considered

| Parameter | Soil 1 | Soil 2 | Soil 3 |
|---|---|---|---|
| $s_{u0}$ (kPa) | 5.00 | 2.75 | 0.5 |
| $s_{u-crust}$ (kPa) | 15.00 | 10.00 | 5.00 |
| $s_{u-crust-bot}$ (kPa) | 7.00 | 4.50 | 2.00 |
| $s_{u1}$ (kPa/m) | 1.5 | 1.5 | 1.5 |
| $d_{crust-top-peak}$ (m) | 0 | 0.25 | 0.50 |
| $d_{crust-bot-peak}$ (m) | 2.00 | 1.25 | 0.50 |
| $d_{crust-bot}$ (m) | 2.50 | 1.50 | 1.00 |

has its properties well defined: position (r, $\theta$,z) and undrained shear strength ($s_u$). Thus, by defining a depth dependent non-linear shear strength profile, one can ensure that every single point along the depth of the pile is assigned different strength properties.

This small fact is one of the major advantages of the upper bound PLA method (Mentioned in Chapter 1). It is very versatile and allows incorporation of highly complex geometries and material properties. The downside of this is that running time triplicates (and sometimes quadruplicates) compared to uniform soils: from 5 minutes to more than 15 min

per optimization. However, it is still less time than most three dimensional finite element simulations would take.

## 5.4 Case 1: High Strength Crust

### 5.4.1 Normalized capacities

Figures 5.3(a and b) and 5.4(a and b) present comparisons in terms of capacity for the case of a high-strength crust (Soil No. 1).

Capacity is indeed affected by the depth of the crust, however, there does not seems to be a consistent pattern in how the curves behave. For small diameters, the presence of a crust seems to produce a rapid increase in capacity with aspect ratio. As diameter increases, the curves resemble more those obtained for linearly increasing strength profiles.

Figures 5.3(a and b) present result of analyses including base resistance. As a consequence, for short caissons in which the diameter is more than the actual length (i.e. $L_f/D < 1$) the normalized capacity seems to increase asymptotically, basically because the contribution from base resistance represents a large percentage of the total capacity. This behavior is unrealistic and is one of the many reasons why the flow-around mechanism (i.e. Murff and Hamilton, 1993) is not suitable for these range of diameters. Nevertheless, when computing capacity of a pile under lateral load, base resistance definitely represents a percentage of the load, thus, for longer piles and caissons it was pertinent to present results this way. The figure has been divided into part a and part b. Figure 5.3a presents capacity curves for those piles which diameter ($D$) is less than the crustal depth whilst Fig.5.3b plots

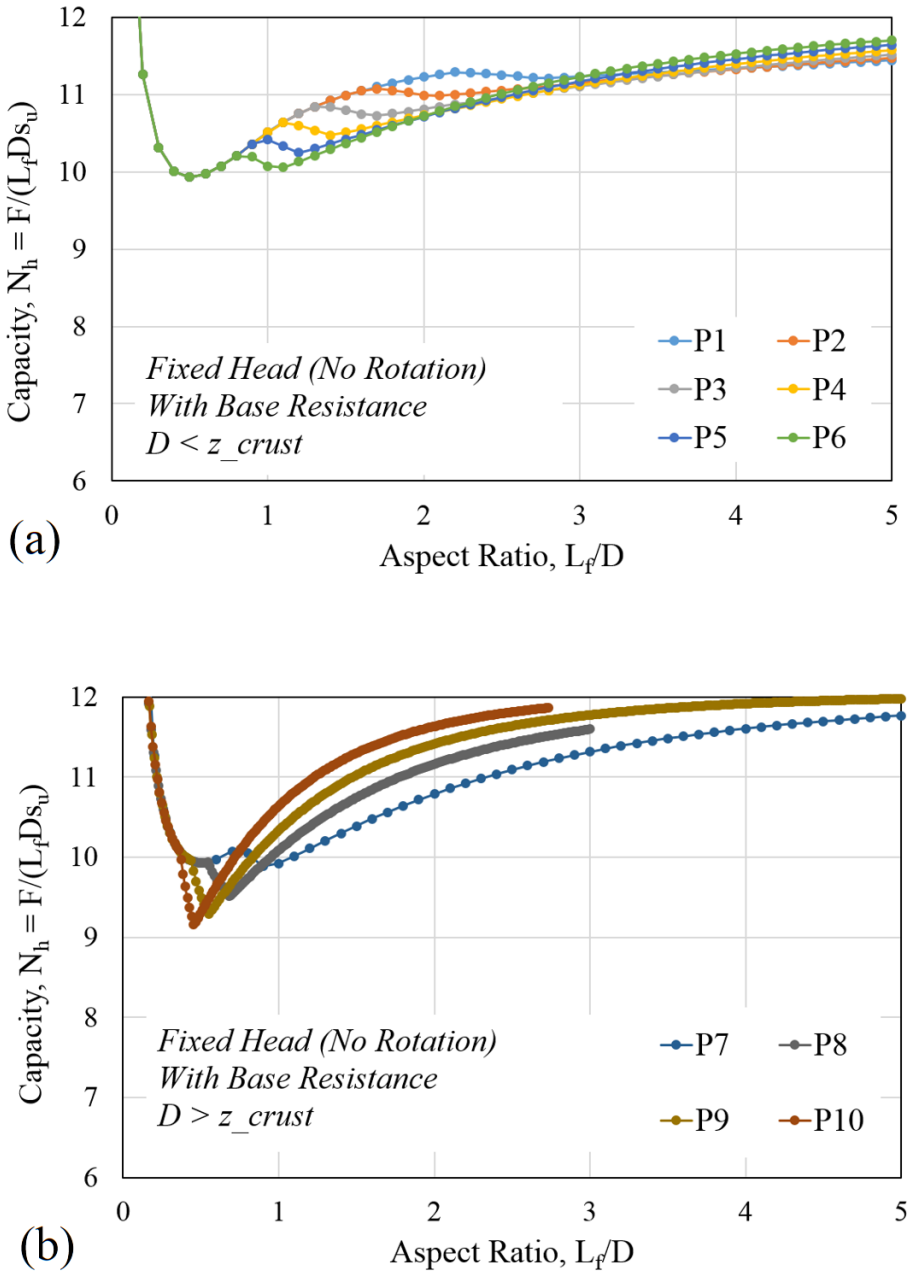


Figure 5.3: Horizontal bearing capacity for different aspect ratios. Base resistance included. Piles under translation

capacity curves for diameters larger than the crustal depth.

As it was mentioned in previous paragraphs, there is no consistent pattern in how the

curves behave. What is a fact is that the thickness of the crust does play a very important role regarding behavior of the pile. For diameters shorter than the crust depth, it can be observed that curves corresponding to smaller diameters (for example, P1, with diameter of 0.92) tend to peak earlier than those from larger diameters (example, P6, with diameter of ), which reach their peak in a more gradual way.

The opposite is observed for cases in which diameter is larger than the crust thickness (Fig.5.3b). The smallest diameter in this picture (P7, $D$ = 2.74m) reaches its maximum resistance gradually at around aspect ratios of 5. On the other hand, the largest diameter pile (P10, $D$ = 5.49m) reaches higher capacities than pile No. 7 for much shorter aspect ratios.

A similar but less severe behavioral pattern can be observed in figures 5.4(a and b), which show results with base resistance subtracted from capacity. A first observation is the fact that small aspect ratios do not reach their maximum as early as larger ones. This reassures our previously mentioned hypothesis. Still there are slight differences between diameters.

This newly observed behavior is in contrast with previous bearing capacity plots, where the strength was considered either constant or linearly increasing with depth. For those cases, normalization does bring all the curves together to the same values, which is not the case for crusted soil profiles.

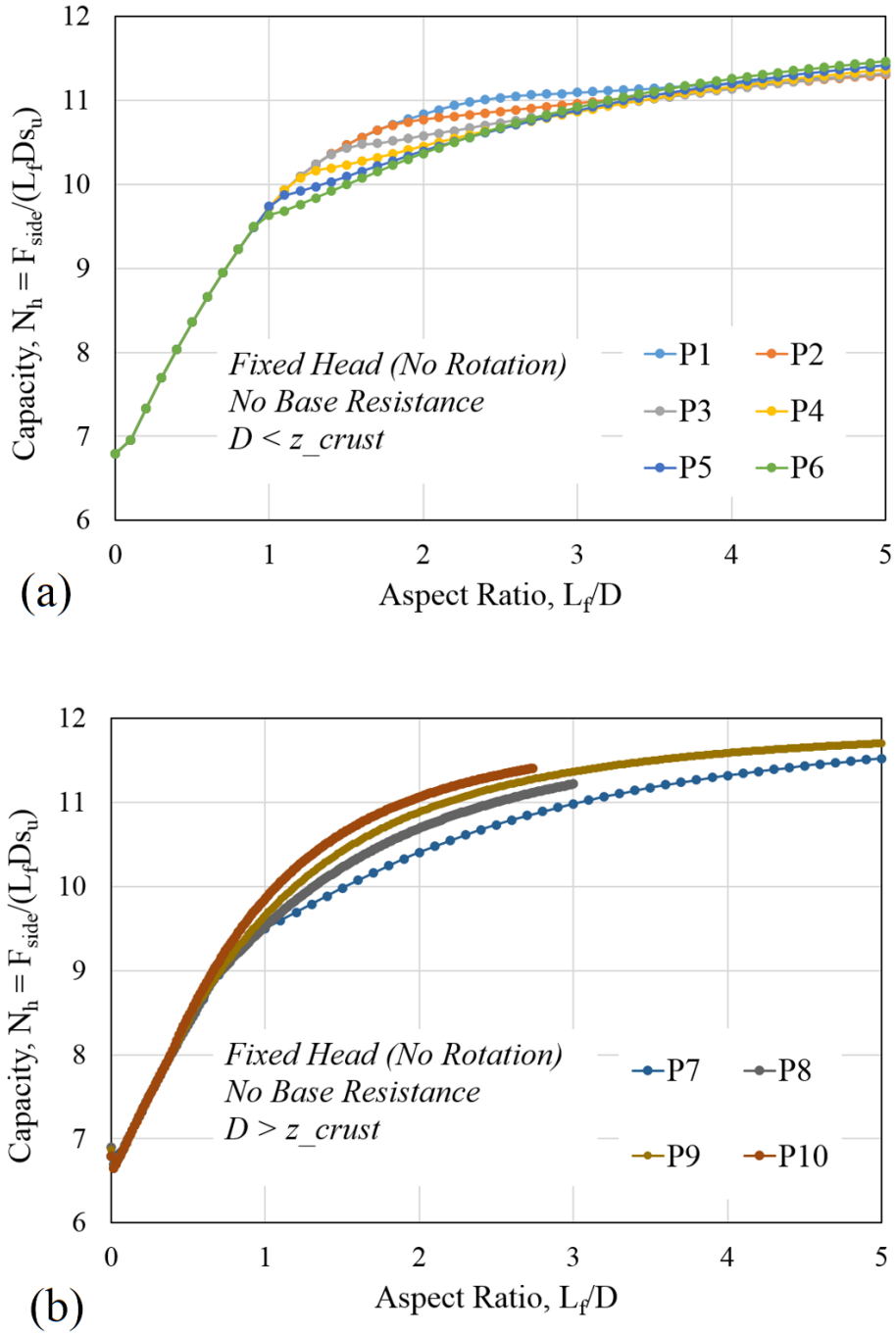


Figure 5.4: Horizontal bearing capacity for different aspect ratios. Without base resistance. Piles under translation.

### 5.4.2 Soil bearing capacity distributions

Soil resistance distributions profiles for all the piles are plotted in Figure 5.5. It can be observed in that there is an evident influence of the crust on the equivalent soil resistance which is particularly noticeable for piles with diameters larger than the assumed crust depth (i.e. Piles 7 through 10). The rest of the piles to converge to the solution of a pile loaded in a linearly increasing soil profile. This observation reinforces the hypothesis that capacities of piles of larger diameters increase in a more significant way by the presence of a crust.

Figure 5.5 is the typical diagram that is utilized in order to generate equivalent p-y curves. However, for the purpose of interpretation and analysis, it could be perhaps a bit misleading. It becomes useful to plot soil pressure distributions versus actual depth (in meters) instead of normalized depth. This is presented in Figure 5.6, which is a lot easier to interpret. The upper zone (red-shaded) corresponds to the peak strength of the crust. Then there is an intermediate region (yellow) named 'transition zone' which is basically the zone in which the crust strength starts decreasing down to the strength of the underlying soil.

An interesting observation here is that soil resistance profiles for small diameter piles seem to be relatively independent of whether there is a crust or not in the seabed. This is very noticeable in plots corresponding to Pile 1 up to Pile 5. Piles 6 and 7 seem to be somewhat affected by the transition zone. This is, the curved portion of their $N_{ps}$ profiles do not end within the crust, but seem to try to kick back to the top of the transition zone.

Probably the most interesting fact to highlight is the behavior of large-diameter piles (8 through 10) with diameters ranging from 3.65 to 5.48 meters. First, these three diameters

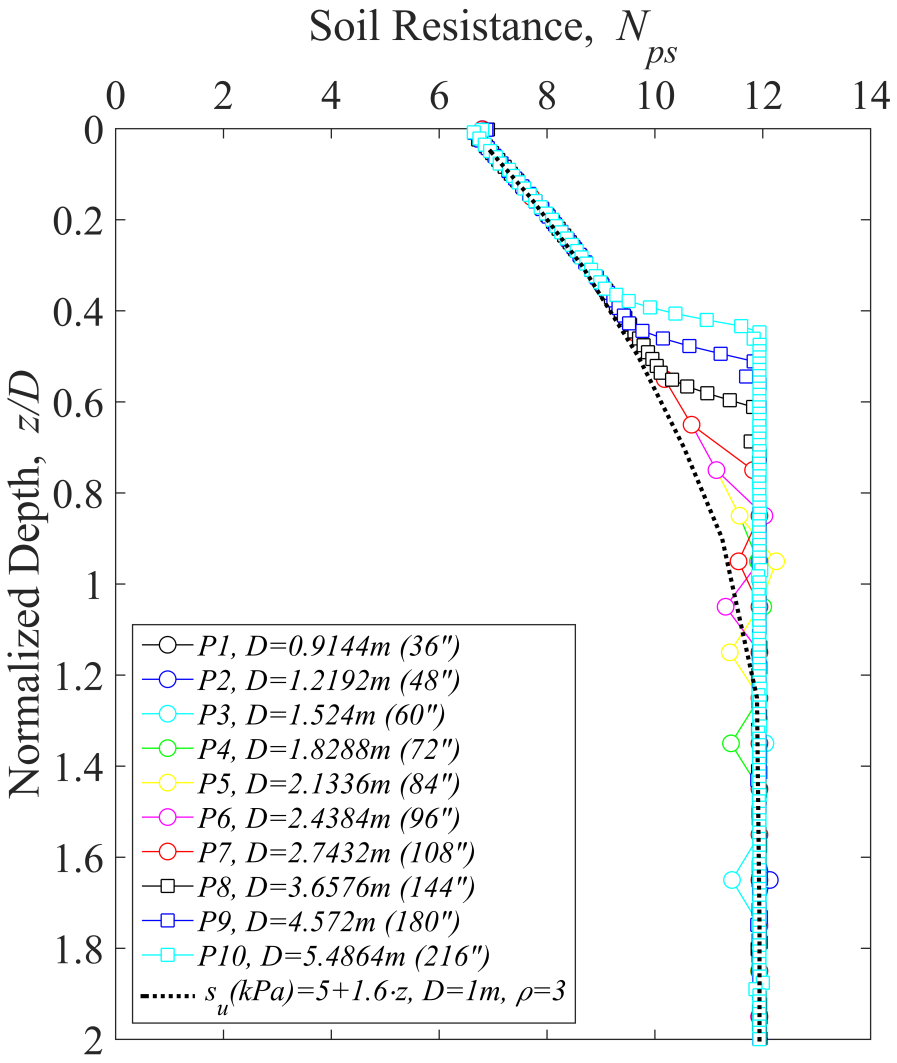


Figure 5.5: Lateral bearing capacity profiles. Case of High-Crust

exceed the crustal depth, and yet, behavior of soil distribution is definitely controlled by the crust. For these three piles, it can be observed that there are three stages. Within the crust, they seem to follow an exponential path (coherent with empirical $N_{ps}$ functions previously mentioned). However, as soon as they hit the transition zone (yellow), they seem to experience a 'kick-back" and rapidly go to the flow-around limit.

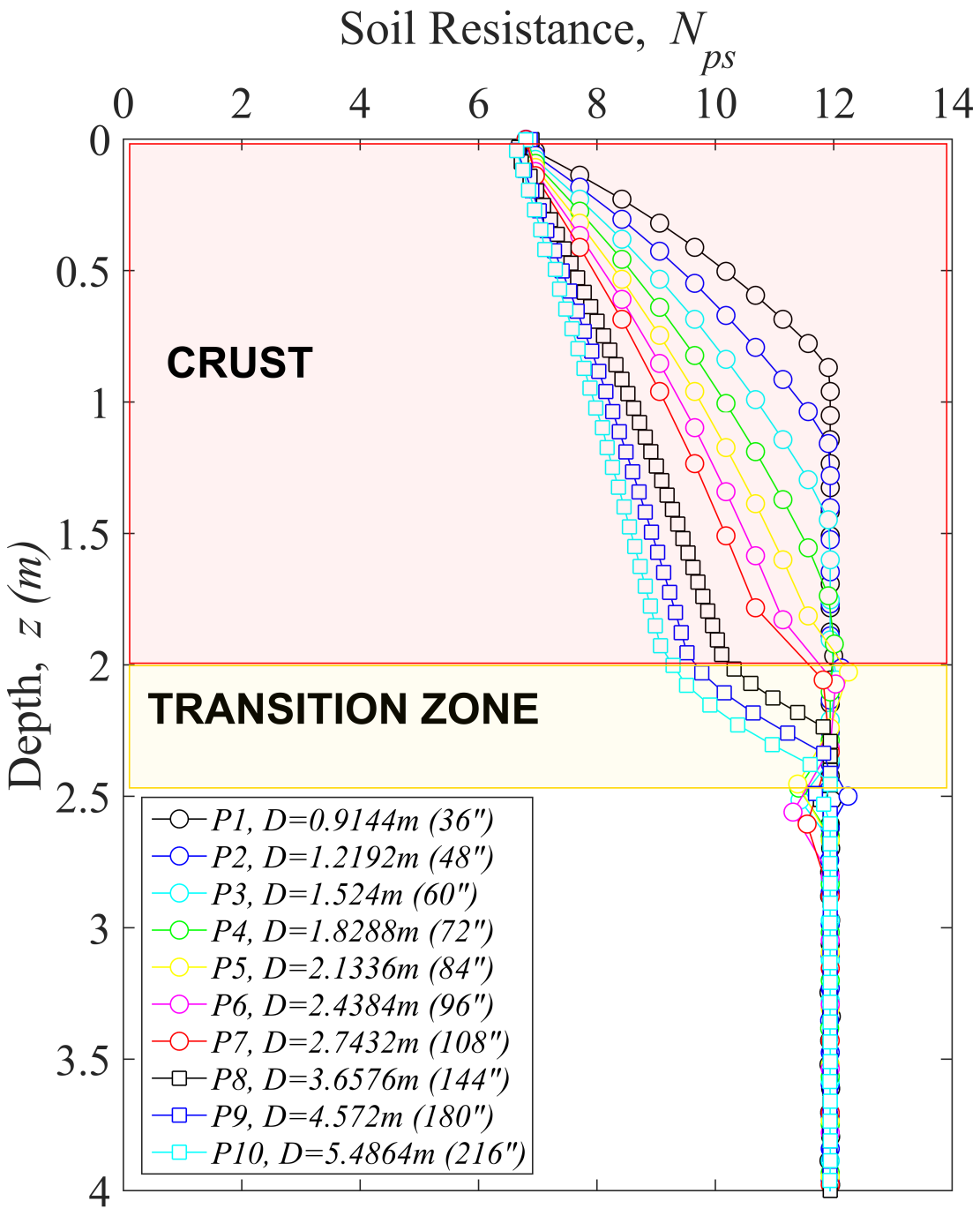


Figure 5.6: Lateral bearing capacity plotted against depth. Case of High-Crust.

## 5.5 Cases 2 and 3: Average and Low Strength Crusts

Data for cases 2 and 3 have been computed and extracted. Results for piles embedded in average and low crusts are presented in Fig.5.7 and 5.8. Interpretation of these is somewhat more complicated. Nevertheless, there is a clear influence of the crust, which can be noticed in Fig. 5.7 at a depth of 1.5m and Fig. 5.8 at a depth of 1m below the mudline.

It is believed that due to the number of different layers (4 layers in the average crust), the formal upper bound method becomes relatively unstable, and this can be observed as random dots that plot outside of the general trend. This resonates with the recommendation initially given by Murff and Hamilton (1993) about the failure mechanism loosing its validity for cases with severe changes in strength.

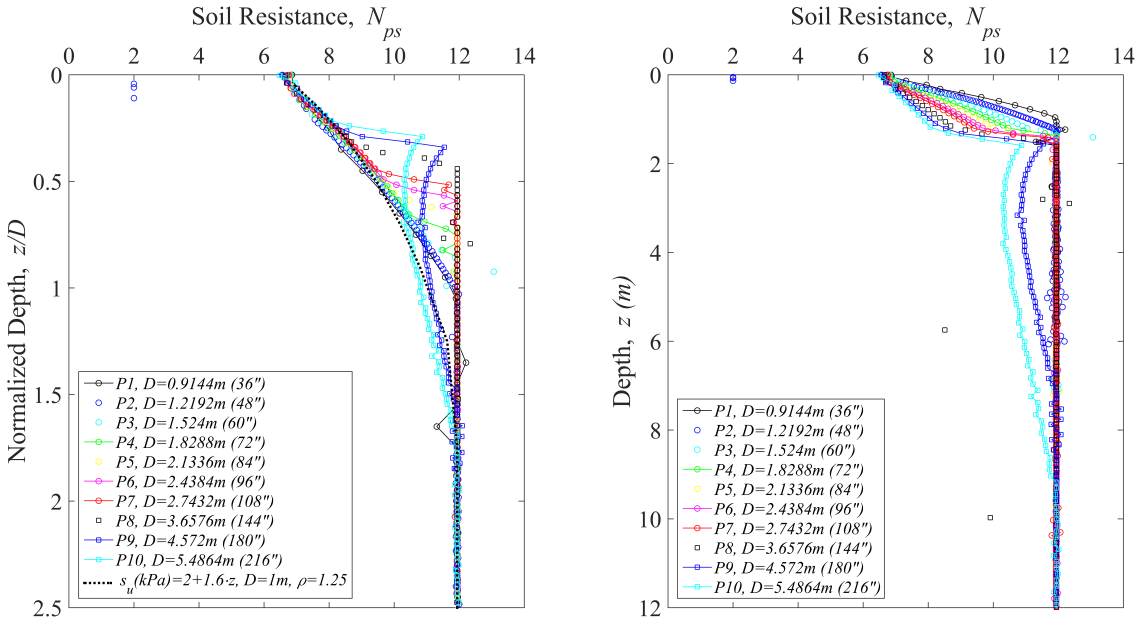


Figure 5.7: Lateral bearing capacity profiles for Average-Crust

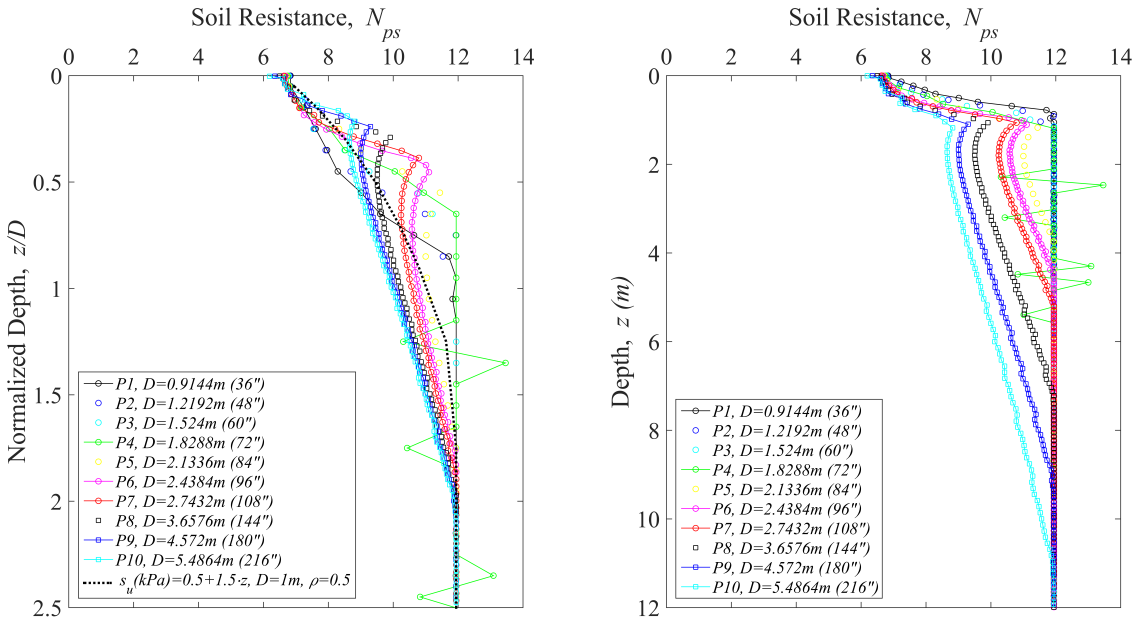


Figure 5.8: Lateral bearing capacity profiles for Low-Crust

## 5.6 Simplified Approach to Calculate Bearing Capacities

An objective of this study was to compare the original $N_{ps}$ empirical function for a linearly increasing strength, to the newly calculated $N_{ps}$ profiles for soils with crust. Two different approaches have been selected. Figures 5.9 through 5.11 present a graphical representation (not to scale) of the studied soil profiles (plotted in black) together with the two approaches.

The first approach consists of applying the empirical $N_{ps}$ function for each soil type by using the equation of the linearly increasing profile corresponding to the soil at the bottom of the crust. This approach has been denominated as 'Empirical-A' and is presented as green dashed lines in Figures 5.9 through 5.11. Utilized numbers are presented as well in the figures. Notice that in this case the intercept with the mudline is a dummy variable

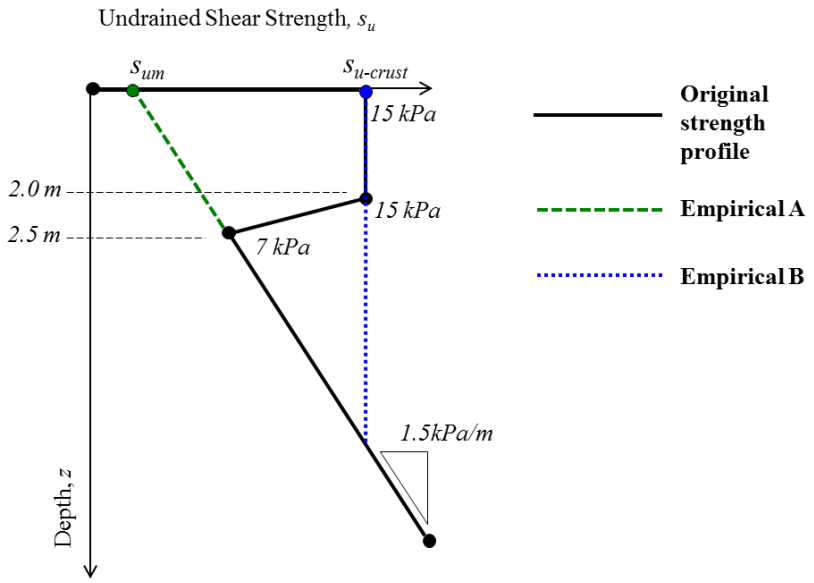


Figure 5.9: Original soil profile for a high-strength crust overlayed with approaches A and B.

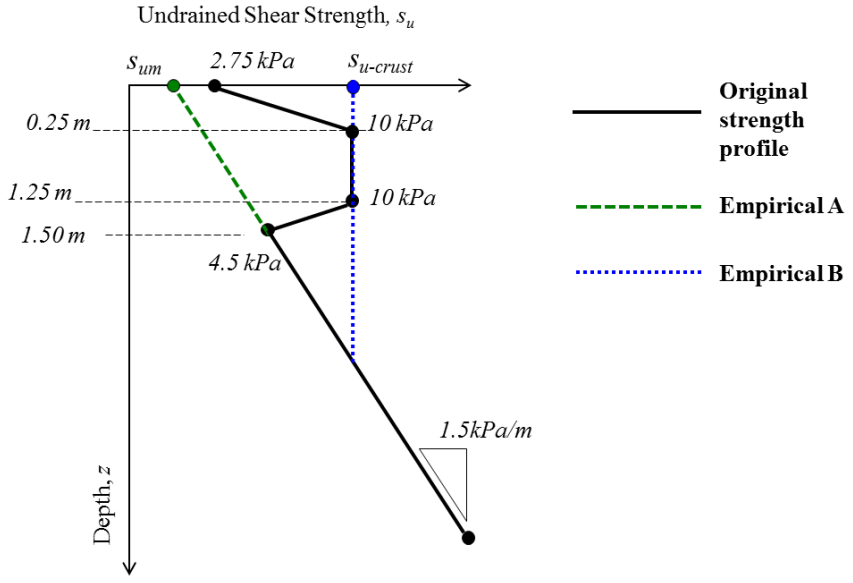


Figure 5.10: Original soil profile for an average-strength crust overlayed with approaches A and B.

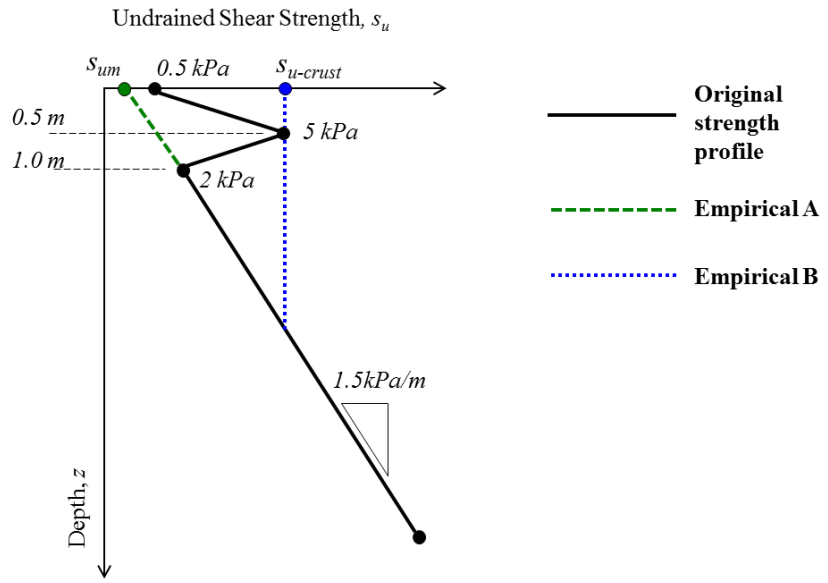


Figure 5.11: Original soil profile for a low-strength crust overlayed with approaches A and B.

that is needed merely for the purpose of using the $N_{ps}$ function.

In the second approach ('Empirical-B'), the $N_{ps}$ empirical function has also been evaluated using the maximum crust strength which is assumed to be a constant strength number and is indicated as blue dotted lines in the figures. This was done based on the observation that for relatively small diameters (i.e. piles 1 to 6) the vertical extent of the failure wedge seems to occur within the crust, which implies that the bearing capacity would not affected by the linearly increasing profile corresponding to the soft soil. Values for su-crust are presented in Fig. 5.9 through 5.11.

Figures 5.12 through 5.19 present comparisons of soil profiles calculated using the formal upper bound PLA method (i.e. Murff-Hamilton) together with the empirical function. PLA results are plotted as squares and the empirical function is presented as a con-

tinuous black line (Empirical-A) and dashed black line (Empirical-B).

Figure 5.12 presents results for a diameter of 36 in (0.9144 m). From Fig. 5.12a it can be concluded that the crust's strength seems to be more appropriate to model behavior of soils with a high-crust. Nevertheless, for the other two crusts (Fig. 5.12b and c), utilizing the crust's depth could lead to an over-estimation of the actual capacity.

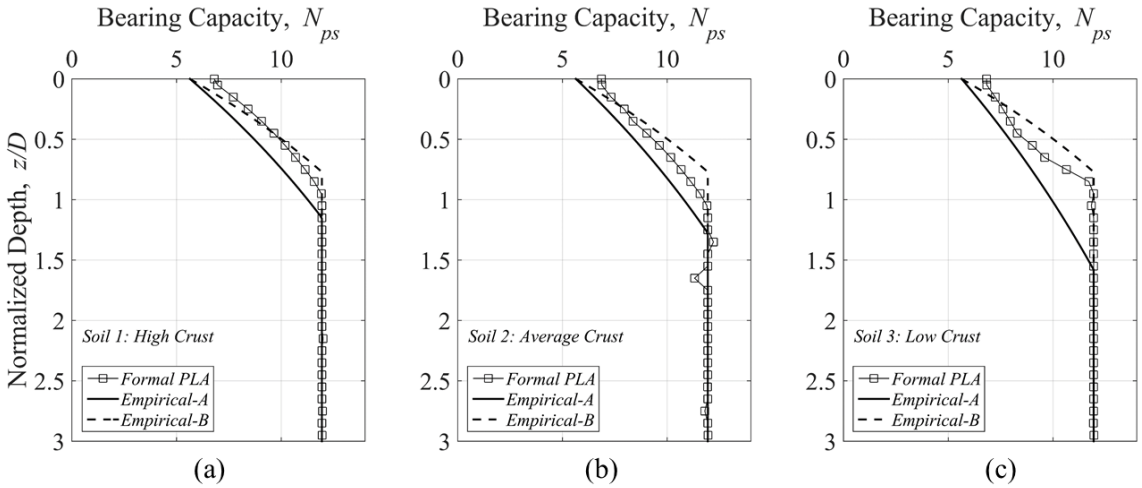


Figure 5.12: Formal PLA vs empirical approaches for Pile 1, Diameter = 36in.

Results for Pile 10, with diameter $D$ = 216 in (5.49 m) are presented in Fig. 5.13 (a, b and c). Contrary to Pile 1, for which predicted bearing capacities were encompassed between the dashed and continuous lines, for this case the PLA predictions indicate that there seems to be a spike, which occurs around the location of the crust ($H_{crust}$ /$D$). For example: for Soil 1 (Fig.5.13a) the spike occurs at a normalized depth of 0.5 whilst for Soil 3 (Fig.5.13c) it occurs at a normalized depth of around 0.2. After a thorough process of trial and error, there was no simple modification that could be applied to the original empirical $N_{ps}$ function to produce a trend similar to that predicted by the upper bound method for

Pile 10.

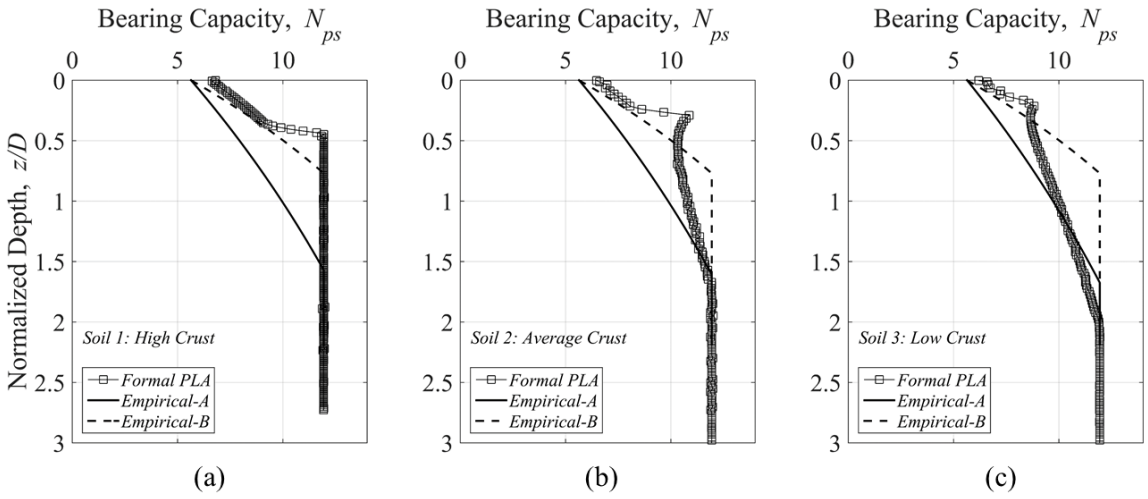


Figure 5.13: Formal PLA vs empirical approaches for Pile 10, Diameter = 216in.

An intermediate diameter (Pile 4, $D$ = 1.83m) is presented in Fig. 5.14(a, b and c). The solution 'Empirical-B', seems to be able to produce an acceptable fit for both the high crust ($H_{crust}$ = 2.5) and average crust ($H_{crust}$ = 1.5). This can be observed in Figs.5.14(a and b). For the low crust (Fig.5.14c), a somewhat less accurate approximation is observed, however it still looks acceptable.

While the approach 'Empirical-A' clearly does not model the increased bearing capacity due to the crust, the approach 'Empirical-B' seems to produce an acceptable fit to the formal upper bound method, at least for small diameters. In order to determine the range of diameters for which this approximation stands valid, the same exercise was repeated for piles P5 through P9. Results are shown in Figs. 5.15 to 5.19.

Upon examination of these figures, it is possible to conclude that for a high crust soil profile the simplification (i.e. 'Empirical-B'), is in very good agreement with upper bound

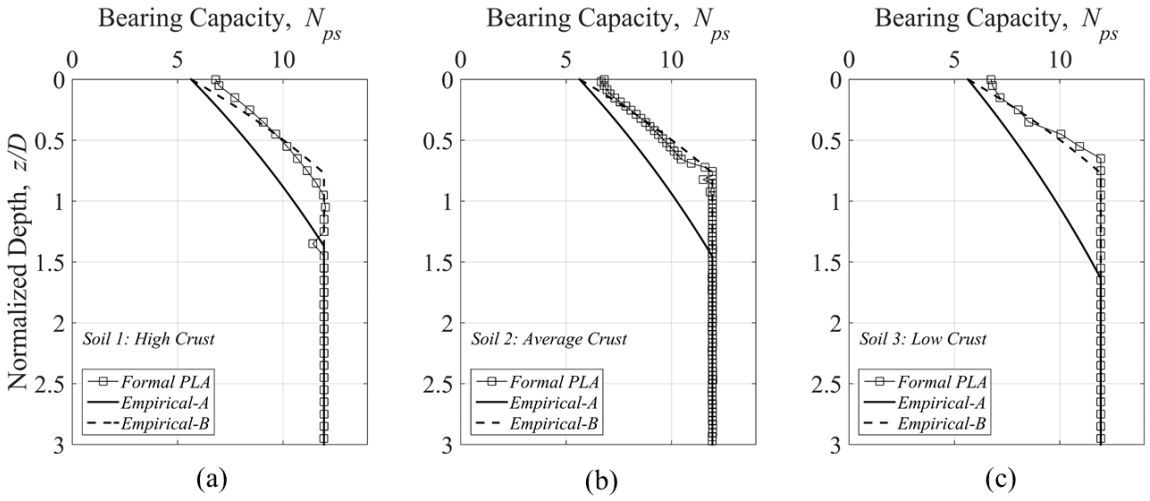


Figure 5.14: Formal PLA vs empirical approaches for Pile 4, Diameter = 72in.

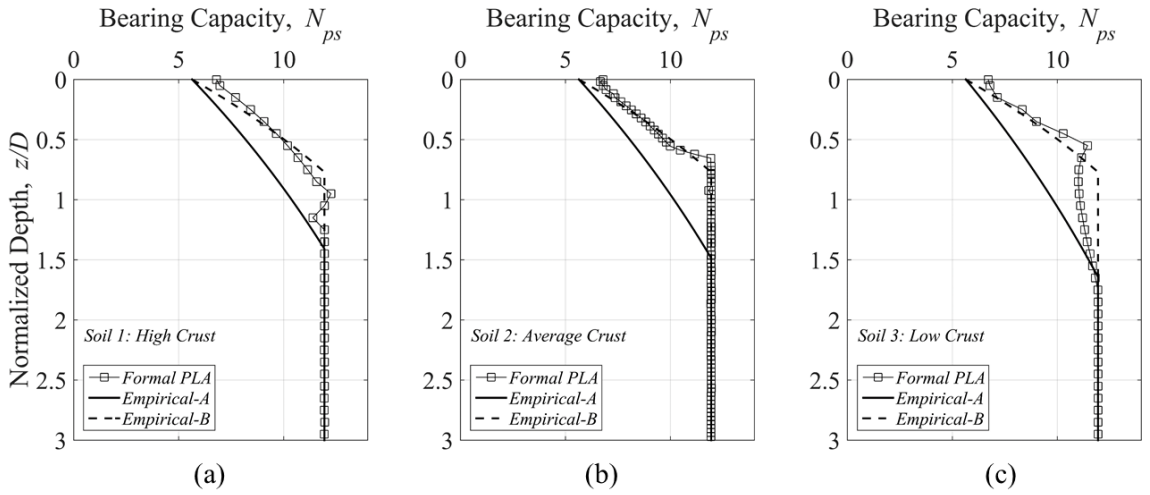


Figure 5.15: Formal PLA vs empirical approaches for Pile 5, Diameter = 84in.

predictions up to a diameter of 108 in (Pile 7), as shown in Fig. 5.17. Also, this diameter is very close to the actual crust thickness ($H_{crust}$), which has a depth of 2.5 m for this soil.

For the case of an average crust, excellent agreement is observed up to a diameter of 72 inches (Fig. 5.14b). For larger diameters, the simplified approach starts departing from upper bound predictions. However, piles P5 and P6, depict a relatively acceptable fit

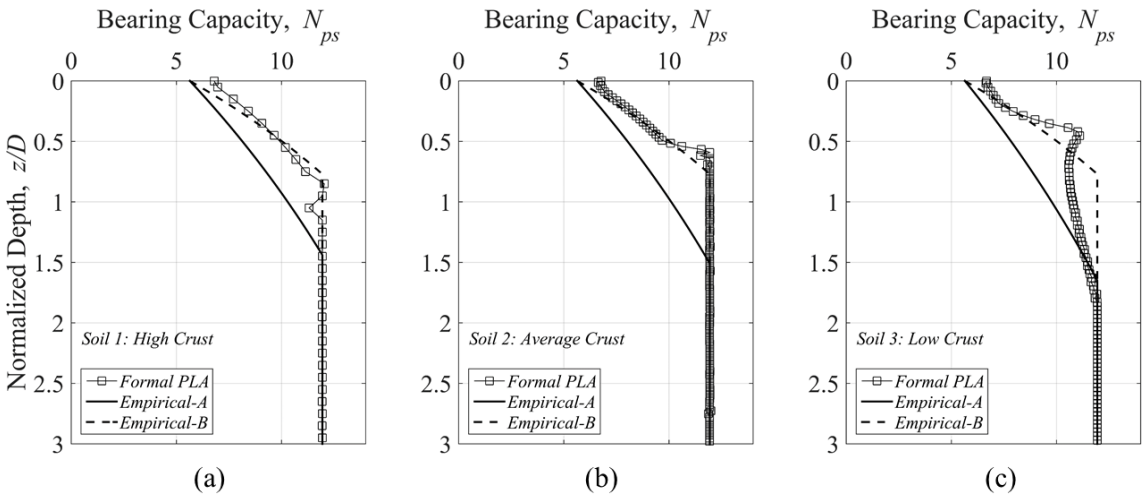


Figure 5.16: Formal PLA vs empirical approaches for Pile 6, Diameter = 96in.

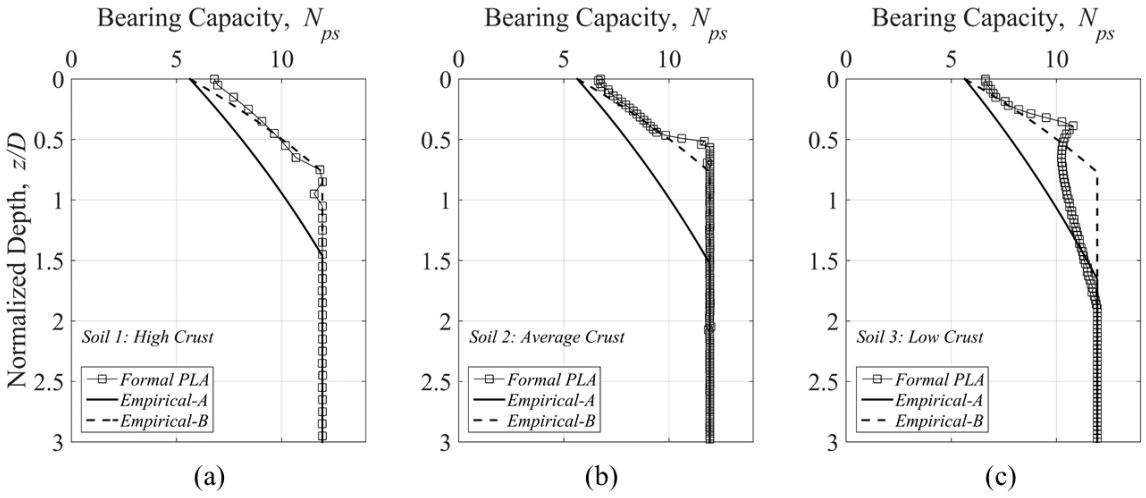


Figure 5.17: Formal PLA vs empirical approaches for Pile 7, Diameter = 108in.

is observed (Figs. 5.15b and 5.16b ).

Finally, almost no agreement between empirical and PLA solutions is observed for the case of piles embedded in a low crust soil. Upper bound predictions for small diameters (i.e. P1 to P4) seem to fall in between the lines described by approaches 'Empirical-A' and 'Empirical-B'. For larger diameters (i.e. P5 to P10) a completely different pattern is

observed in which a relatively concave curve increases up to a peak (presumably at the location of the triangular crust) and then decreases slightly and approximates the flow-around solution.

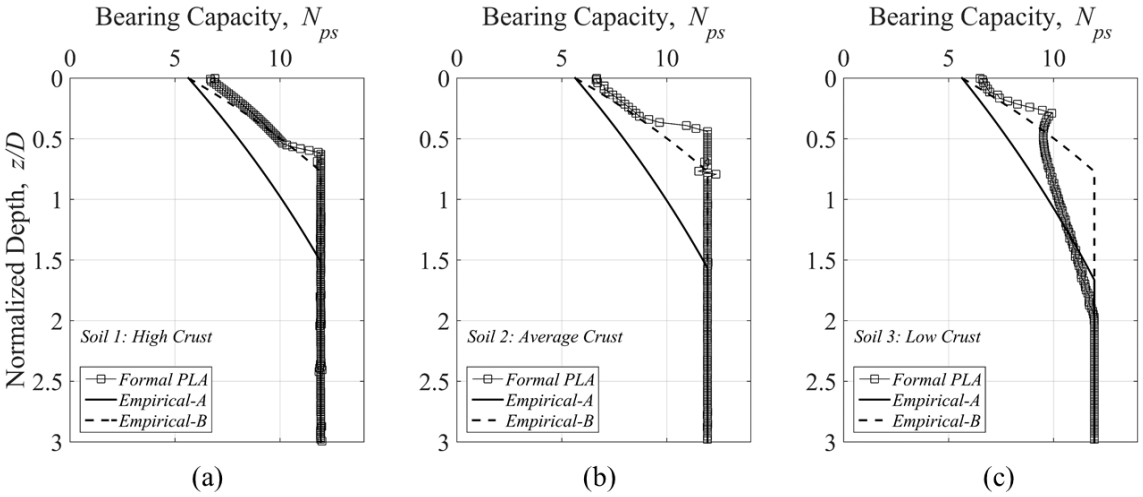


Figure 5.18: Formal PLA vs empirical approaches for Pile 8, Diameter = 144in.

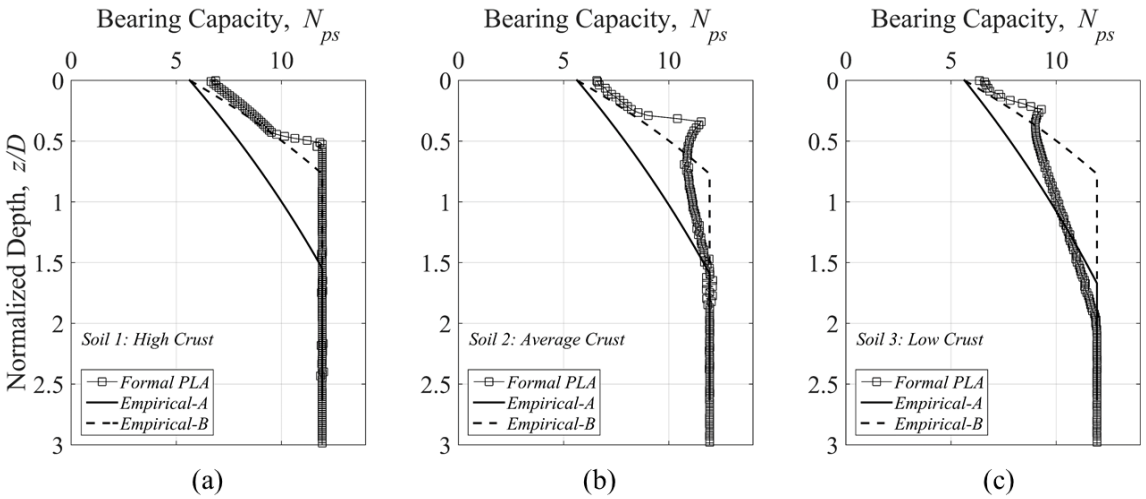


Figure 5.19: Formal PLA vs empirical approaches for Pile 9, Diameter = 180in.

A simple modification to the original $N_{ps}$ function can successfully approximate the

behavior of relatively small diameter piles in a high crusted soil. This is considered a positive outcome of this study, because these diameters, 36 to 96 inches, encompass the dimensions of most offshore wells conductors and piles used today.

For cases where pile diameter is greater than 96 inches (as it is the case of suction caissons) it seems preferable to use the empirical function $N_{ps}$ with the strength gradient corresponding to the soft soil at the bottom of the crust (i.e. approach 'Empirical-A'). However, this would likely underestimate the capacity of the soil-foundation system. Towards this end, a new more complex function would be required for such cases.

# 6 STRAIN PATH ANALYSIS OF PORE PRESSURE DISSIPATION TIMES

## 6.1 Strain Path Solution

Chin (1986) approximated the displacement fields surrounding a penetrating open-ended pile by adapting the analytical solution for a ring source expanding in an incompressible medium (Kuchemann and Weber, 1953) in order to. Equations 6.1 and 6.2 describe the horizontal and vertical velocity ($v_r$ and $v_z$ respectively) components of an infinitesimal soil particle with respect to the vertically advancing pipe. It is assumed that the ring source is made of incompressible material and has a radius $R_r$ and a vertical penetration velocity $U$.

$$v_r = \frac{V}{4\pi^2}\frac{1}{r\sqrt{(r+R_r)^2+z^2}}\left[K(k)\left\{1-\frac{2r(r-R_r)}{z^2+(r-R_r)^2}\right\}E(k)\right] \tag{6.1}$$

$$v_z = U+\frac{V}{4\pi^2}\frac{2z}{(z^2+(r-R_r)^2)\sqrt{(r+R_r)^2+z^2}}E(k) \tag{6.2}$$

Where $z$ is vertical and $r$ is radial coordinate. The functions $K(k)$ and $E(k)$ are elliptic integrals (first and second kind, respectively), which can be defined in terms of infinite series as follows (Eq.6.3 and 6.4):

$$K = \frac{\pi}{2}\left[1+\left(\frac{1}{2}\right)^2 k+\left(\frac{1\cdot 3}{2\cdot 4}\right)^2 k^2+\left(\frac{1\cdot 3\cdot 5}{2\cdot 4\cdot 6}\right)^2 k^3+\left(\frac{1\cdot 3\cdot 5\cdot 7}{2\cdot 4\cdot 6\cdot 8}\right)^2 k^4+...\right] \tag{6.3}$$

$$E = \frac{\pi}{2}\left[1 - \left(\frac{1}{2}\right)^2 \frac{k}{1} - \left(\frac{1\cdot 3}{2\cdot 4}\right)^2 \frac{k^2}{3} - \left(\frac{1\cdot 3\cdot 5}{2\cdot 4\cdot 6}\right)^2 \frac{k^3}{5} - \left(\frac{1\cdot 3\cdot 5\cdot 7}{2\cdot 4\cdot 6\cdot 8}\right)^2 \frac{k^4}{7} + \ldots\right] \quad (6.4)$$

where $k$ is a position parameter defined by Eq. 6.5:

$$k = \frac{4rR_r}{(r+R_r)^2 + z^2} \quad (6.5)$$

The source strength $V$ must be given in units of flow rate, and it must be set equal to the rate at which soil is displaced by the pile as it moves downward, which can computed as the cross-sectional area of the pile multiplied by its penetration rate, as described in Eq. (6.6):

$$V = \pi\left[R^2 - (R - t_w)^2\right] U \approx \pi D t_w U \quad (6.6)$$

where $R$ is the outer radius of the pile and $t_w$ is its wall thickness. This approximation typically applies for thin-walled piles in which second order terms can be treated as negligible. If a rate-independent constitutive model is introduced, a penetration rate $U$ can be arbitrarily selected which is usually assumed to be equal to one.

A careful analysis of this solution shows that the stagnation streamline tends to occurs at an original radial coordinate $r_0$ located approximately three-quarters inside the outer wall of the pile. Therefore, the target pile radius can be achieved by setting the radius of the ring source at a distance $0.75 \cdot t_w$ inside the outer pile wall, or: $R_r = R - 0.75 \cdot t_w$.

The path (i.e. trajectory) of any single soil particle located near the advancing pile is then calculated by integrating Equations 6.1 and 6.2 with respect to time, as described in

Eqs. 6.7 and 6.8:

$$r = r_0 + \int_t v_r \, dt \tag{6.7}$$

$$z = z_0 + \int_t v_z \, dt \tag{6.8}$$

The initial vertical coordinate $z_0$ should always assumed as the distance below the tip of the pile or caisson, because at this point the effects of penetration are negligible. A series of initial radial coordinates $r_0$ and the time range $t$ over which the integration is conducted are selected according to the respective horizontal and vertical ranges of interest (Aubeny and Grajales, 2015). An example of a deformation grid is shown in Fig. 6.1 for the specific case of an open-ended pile with thickness ratio (or normalized thickness) of $D/t_w = 40$. Notice that only half of the pile is shown, and the pile wall is presented as an empty-white space in between the grid.

Strains at any point are usually calculated by taking the spatial derivatives of the velocity of equations 6.1 and 6.2 to obtain strain rates and then integration of these strain rates along each streamline with respect to time allows to obtain strain. However, these calculations can be significantly simplified by recognizing that, if the penetration rate $U$ in the vertical direction is assumed to be a steady velocity, then the derivatives with respect to time are going to be proportional to the spatial derivatives with respect to the vertical dimension. As a result, the following simplifications are possible for calculating the respective strain components (i.e.vertical, tangential, radial and meridianal):

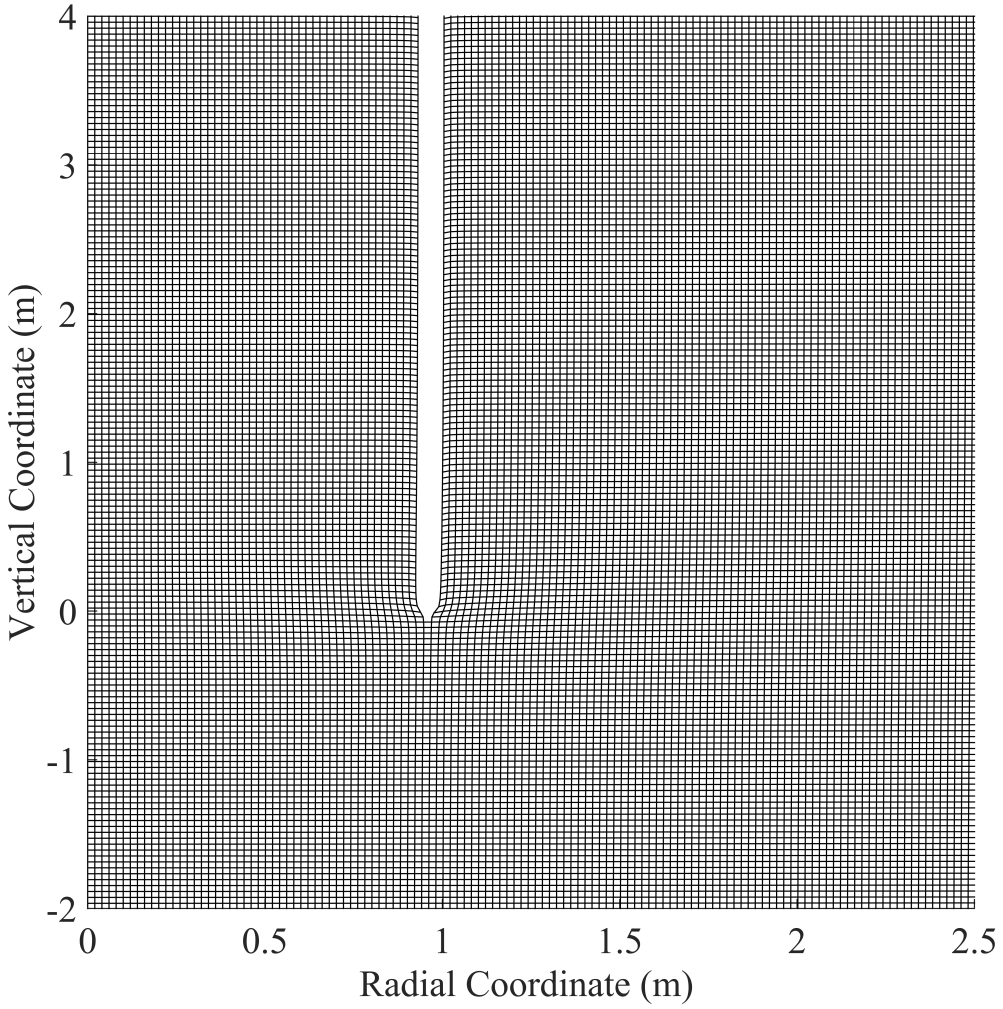


Figure 6.1: Deformation Grid for a thickness ratio of $D/t_w$ = 40. Caisson wall removed from figure.

$$\varepsilon_{zz} = \quad -\int_t \frac{\partial v_z}{\partial z} dt = -\int_t \frac{1}{U}\frac{\partial v_z}{\partial t} dt = 1 - \frac{v_z}{U} \tag{6.9}$$

$$\varepsilon_{\theta\theta} = \quad -\int_t \frac{v_r}{r} dt = -\int_r \frac{dr}{r} = -\ln(r/r_0) \tag{6.10}$$

$$\varepsilon_{rr} = \quad -\varepsilon_{zz} - \varepsilon_{\theta\theta} \tag{6.11}$$

$$\varepsilon_{rz} = \quad -\int_t \frac{\partial v_r}{\partial z} dt = -\int_t \frac{1}{U} \frac{\partial v_r}{\partial t} dt = -\frac{v_r}{U} \tag{6.12}$$

The strain rates in Eqs. 6.9 to 6.12 have been expressed utilizing a soil mechanics sign convention where compression is assumed as positive and tension is negative. The simplified expression for the meridianal strain term $\varepsilon_{rz}$ can be derived by recognizing the velocity field in this case is irrotational and Eq. 6.11 embodies the incompressibility constraint (Aubeny and Grajales, 2015). As a result, the strain at any location can be accurately computed from relatively simple expressions in terms of the current position and velocity of each soil element in question, which simplifies significantly the computational effort.

An example of strains obtained through usage of these equations is presented in Fig. 6.2. Since the system is symmetric, contours are presented only for the right-half of the system. The penetrator had a normalized thickness $D/t_w$ = 40. It can be observed that severe strain concentrations occur at the tip of the penetrator (i.e. 5% and 10% strain).

Once strain histories are defined at all points, deviatoric stresses ($s_{ij}$) can be computed using a constitutive model. For this dissertation, a Prandtl-Reuss model has been used. The model has linearly elastic behavior beneath the yield surface, a von Mises yield criterion, an associated flow rule, and perfectly plastic behavior upon yielding (Aubeny and Grajales, 2015). The constitutive law is then expressed as presented in Eq. 6.13:

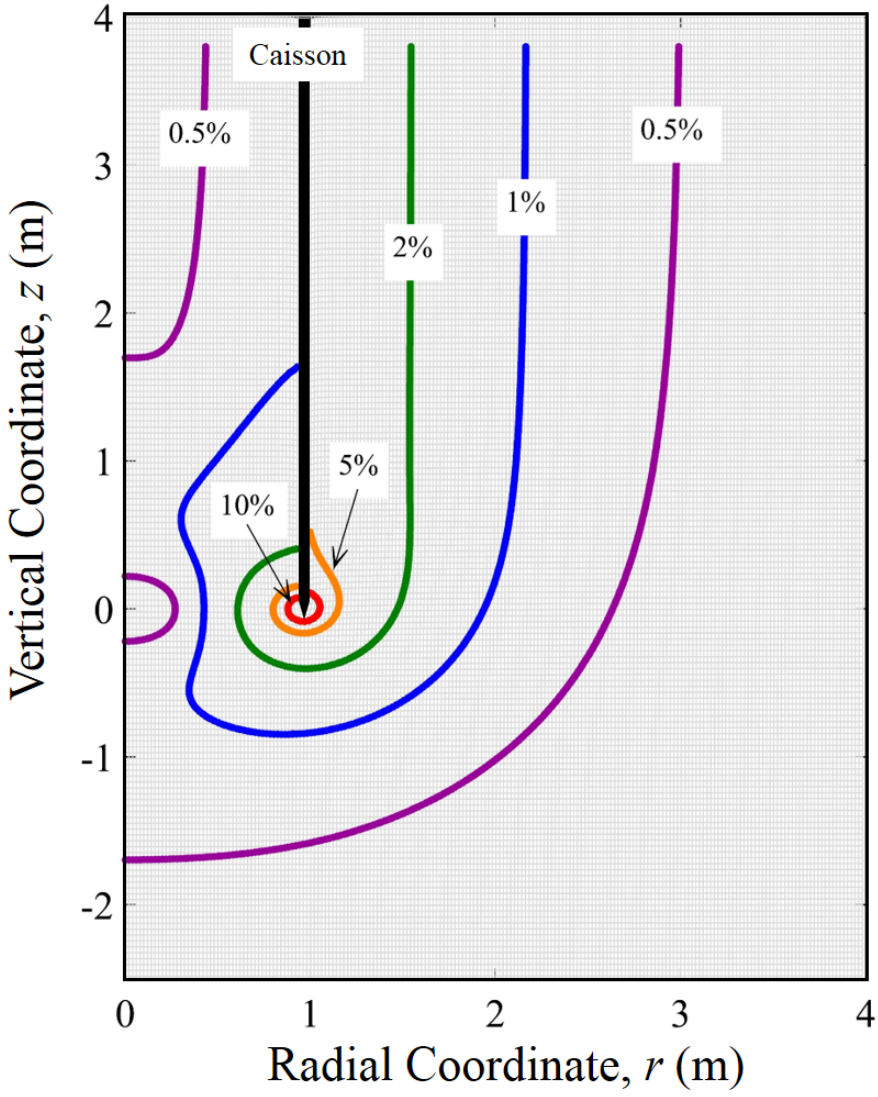


Figure 6.2: Contours of maximum shear strain for open-ended penetration. Normalized thickness $D/t_w = 40$

$$[\delta s] = [C_d][\delta \varepsilon] \tag{6.13}$$

where $\delta_s$ are the increments of deviatoric stress and $\delta_\varepsilon$ are the increments of strain calculated by integrating Eqs. 6.9 to 6.12.

The constitutive matrix needed to relate deviatoric stresses to strains $[C_d]$ for a Prandtl-Reuss model under axisymmetric conditions can be defined as follows:

$$[C_d] = \begin{bmatrix} 4G/3 & -2G/3 & -2G/3 & 0 \\ -2G/3 & 4G/3 & -2G/3 & 0 \\ -2G/3 & -2G/3 & 4G/3 & 0 \\ 0 & 0 & 0 & 2G \end{bmatrix} - \frac{\chi G}{2s_u^2} \begin{bmatrix} s_{rr}s_{rr} & s_{rr}s_{zz} & s_{rr}s_{\theta\theta} & s_{rr}s_{rz} \\ s_{zz}s_{rr} & s_{zz}s_{zz} & s_{zz}s_{\theta\theta} & s_{zz}s_{rz} \\ s_{\theta\theta}s_{rr} & s_{\theta\theta}s_{zz} & s_{\theta\theta}s_{\theta\theta} & s_{\theta\theta}s_{rz} \\ s_{rz}s_{rr} & s_{rz}s_{zz} & s_{rz}s_{\theta\theta} & s_{rz}s_{rz} \end{bmatrix} \tag{6.14}$$

In Equation 6.14, $G$ is shear modulus and $s_u$ is undrained shear strength in a simple shear mode. The parameter $\chi$ is a dummy variable that activates the plastic response. For stress states beneath yield or for unloading from the yield surface it is equal to zero and otherwise set to unity. Deviatoric stress histories are computed by performing numerical integration of Eq. 6.13 along each streamline.

Changes in mean stress ($\Delta\sigma$) are indeterminate from Eqs. 6.13 and 6.14; nevertheless, they can be evaluated from considerations of force equilibrium (Baligh, 1986, 1985; Aubeny and Grajales, 2015). If horizontal equilibrium is assumed, the relevant equation becomes:

$$\frac{\partial(\Delta\sigma)}{\partial r} = -\left(\frac{\partial s_{rr}}{\partial r} + \frac{s_{rr} - s_{\theta\theta}}{r} + \frac{\partial s_{rz}}{\partial z}\right) \tag{6.15}$$

Changes in mean stress ($\Delta\sigma$) during penetration are computed by performing numerical integration of Eq. 6.15 starting from a point located at a sufficiently large radial distance from the pile outer wall, in such a way that disturbance effects can be considered

negligible. If the shear-induced pore pressures are neglected, then the changes in mean stress ($\Delta\sigma$) can be assumed to be the excess pore pressure $u_e$ induced by pile installation. Distributions of excess pore pressures are presented in Fig. 6.3, for a vertical distance of $40{\cdot}t_w$ above the pile tip. They have been calculated by using Eqs. 6.6 to 6.15 for several normalized wall thicknesses ranging from $D/t_w$ = 10 to 160 and a soil rigidity index $I_r = G/s_u = 100$, which is typical for NC clays.

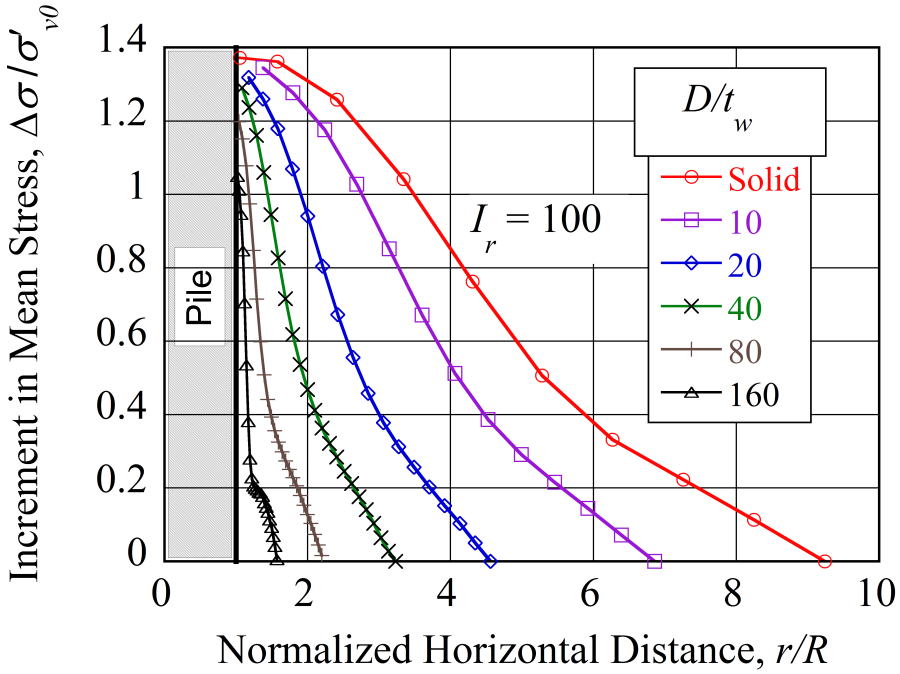


Figure 6.3: Mean stress component of initial excess pore pressure distribution

Also shown in Fig. 6.3 is the excess pore pressure distribution for a solid (or plugged) pile, which is included as a reference for comparisons to be developed later in this chapter. Velocity fields for the solid case (plotted in red circles) are calculated based on the solution for simple pile penetration presented by Baligh (1985):

$$v_r = UR^2/(4\rho^2 \sin\varphi) \tag{6.16}$$

$$v_z = U + UR^2/(4\rho^2 \cos\varphi) \tag{6.17}$$

where $R$ is the radius, $\varphi$ is the polar angle defined as $tan^{-1}(r/z)$, and $\rho$ is the polar radius $(r^2+z^2)^{1/2}$. Except for the modified velocity fields, the rest of the calculations for solid pile penetration are identical to those for open pile penetration, which were previously described in Eqs. 6.7 to 6.15. From Fig.6.3, it can be observed that disturbance is significantly higher as the thickness ratio ($D/t_w$) increases, with minimal increases in mean stress observed for thin piles (i.e.$D/t_w$ = 160)

## 6.2 Pore Pressure Dissipation

The study presented in this dissertation consists on prediction dissipation of excess pore pressures along the pile shaft without considering the influence of tip effects. This problem can be easily characterized in terms of a one-dimensional consolidation process in a homogeneous, semi-finite soil mass. For these conditions an uncoupled analysis is valid (Aubeny and Grajales, 2015), as explained by Levadeux and Baligh (1986) and Sills (1975). Therefore, the time required for excess pore pressures to dissipate of may be computed from a relatively simple one-dimensional diffusion equation. The governing differential equation in polar coordinates is given as:

$$c\left(\frac{\partial^2 u_e}{\partial r^2} + \frac{1}{r}\frac{\partial u_e}{\partial r}\right) = \frac{\partial u_e}{\partial t} \tag{6.18}$$

where the variable $c$ is the coefficient of consolidation. Initial conditions (i.e. pore pressures) are given as presented in Figure 6.3. Several alternatives are feasible for solution of Eq. 6.18. An implicit Euler backward difference approach has been adopted. Computa-

tions of normalized pore pressured decay from Eq.6.18 are shown in Fig. 6.4 for the initial conditions presented in Fig. 6.3. The non-dimensional time (or time factor) in Fig. 6.4 is defined in terms of the coefficient of consolidation $c$, real time $t$, and radius $R$ as described below:

$$T = c \cdot t / R^2 \tag{6.19}$$

Based on the initial excess pore pressure distributions presented in Figure 6.3 for $I_r$ =100, strain path (SPM) solutions were computed for relative wall thicknesses $D/t_w$ ranging from 2 to 160. These results are presented in Fig. 6.4. These wall thicknesses encompasses the range commonly used in practice. These results are also compared with dissipation times computed based on cavity expansion (CEM) calculation of disturbed pore pressures. By looking at Fig. 6.4, it is possible to compare the two-dimensional SPM analyses to the 1-D CEM ones. This result highlights the importance of accounting for the two dimensional nature of the pile penetration process. SPM pore pressure predictions seem to show much more spreaded results.

Normalized times for degrees of consolidation of 50 and 90 percent, $T_{50}$ and $T_{90}$, are presented in Figs. 6.5 and 6.6 respectively. These figures can be used as design guides. Predictions are presented for wall thicknesses $D/t_w$ = 2 to 160 and rigidity indices $I_r$ = 50 to 500, which encompass typical stiffnesses of very soft to stiff clays.

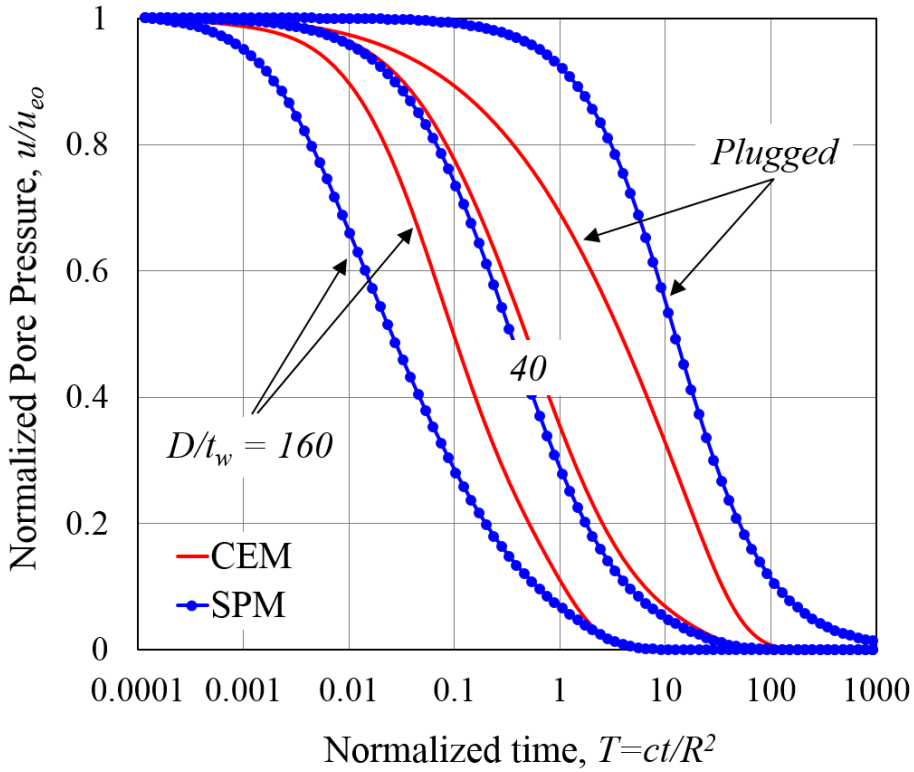


Figure 6.4: Predicted pore pressure dissipation after installation

### 6.3 Normalized Time Scale

With the purpose of unifying the predictions, normalizations of the time scale have been considered. A rational basis for such type of normalization is provided by cylindrical cavity expansion theory. A useful approach could be to define a modified time factor $T_p$ in terms of the radius of zone of plastic yielding during penetration ($R_p$). This radius is related to the actual radius of the pile by the following equation:

$$R_p = R\sqrt{I_r A_r} \tag{6.20}$$

where $I_r$ is rigidity index ($G/s_u$) and $A_r = 4t_w/D$ is the ratio of gross pile cross-sectional area to the annular area of the tip. A modified time factor (i.e. normalized time) can now

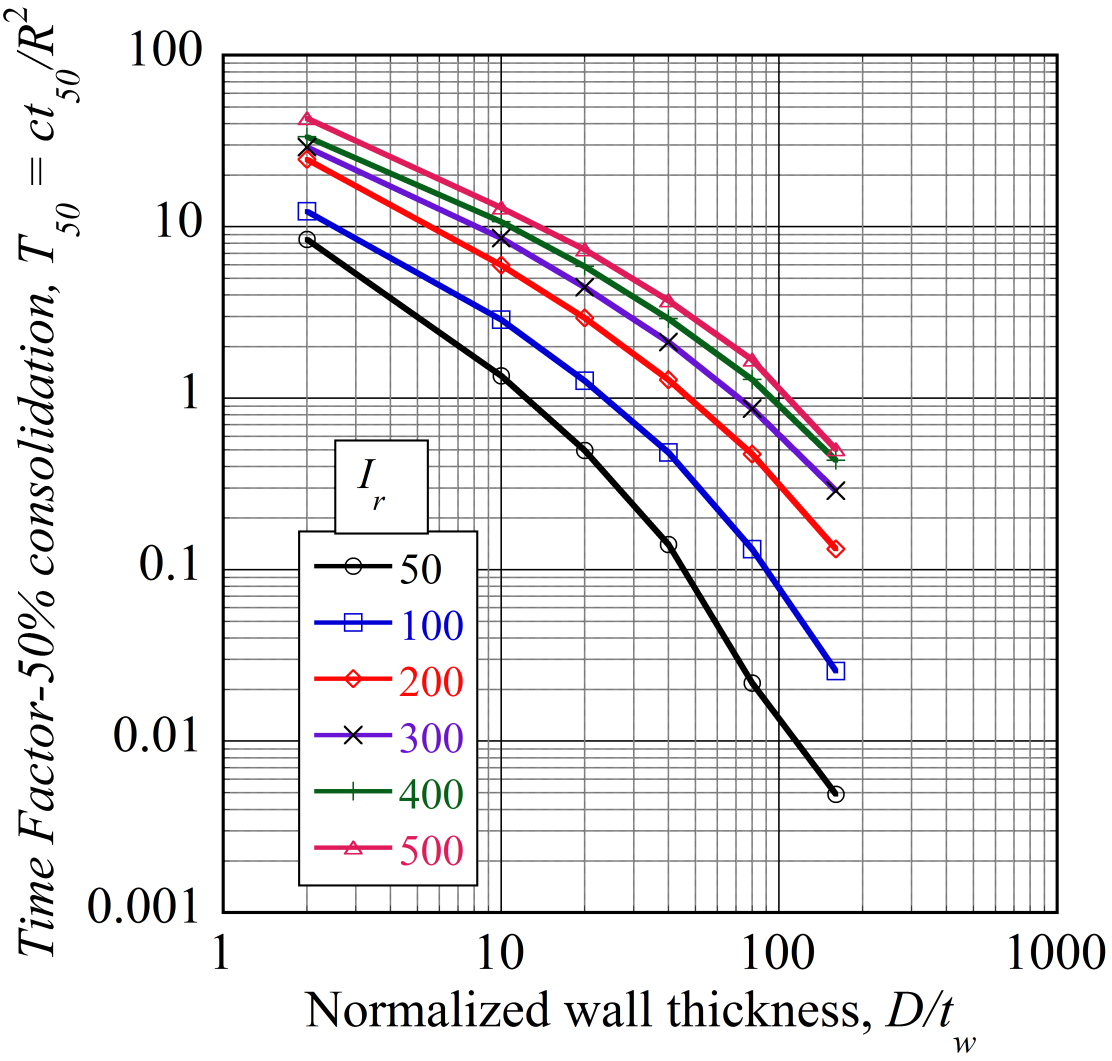


Figure 6.5: Design Guide: Predicted times to 50% consolidation

be defined in terms of the radius of the plastic zone during penetration ($R_p$) as follows:

$$T_p = ct/\left(I_r A_r R^2\right) \tag{6.21}$$

A series of comparisons is shown in Fig. 6.7. In them, the relative wall thickness has been kept constant ($D/t_w$ = 40), whilst rigidity index has been varied from $I_r$ = 50 to 500. The curves indicate that the normalization (i.e. Eq. 6.21) clearly narrows the band of

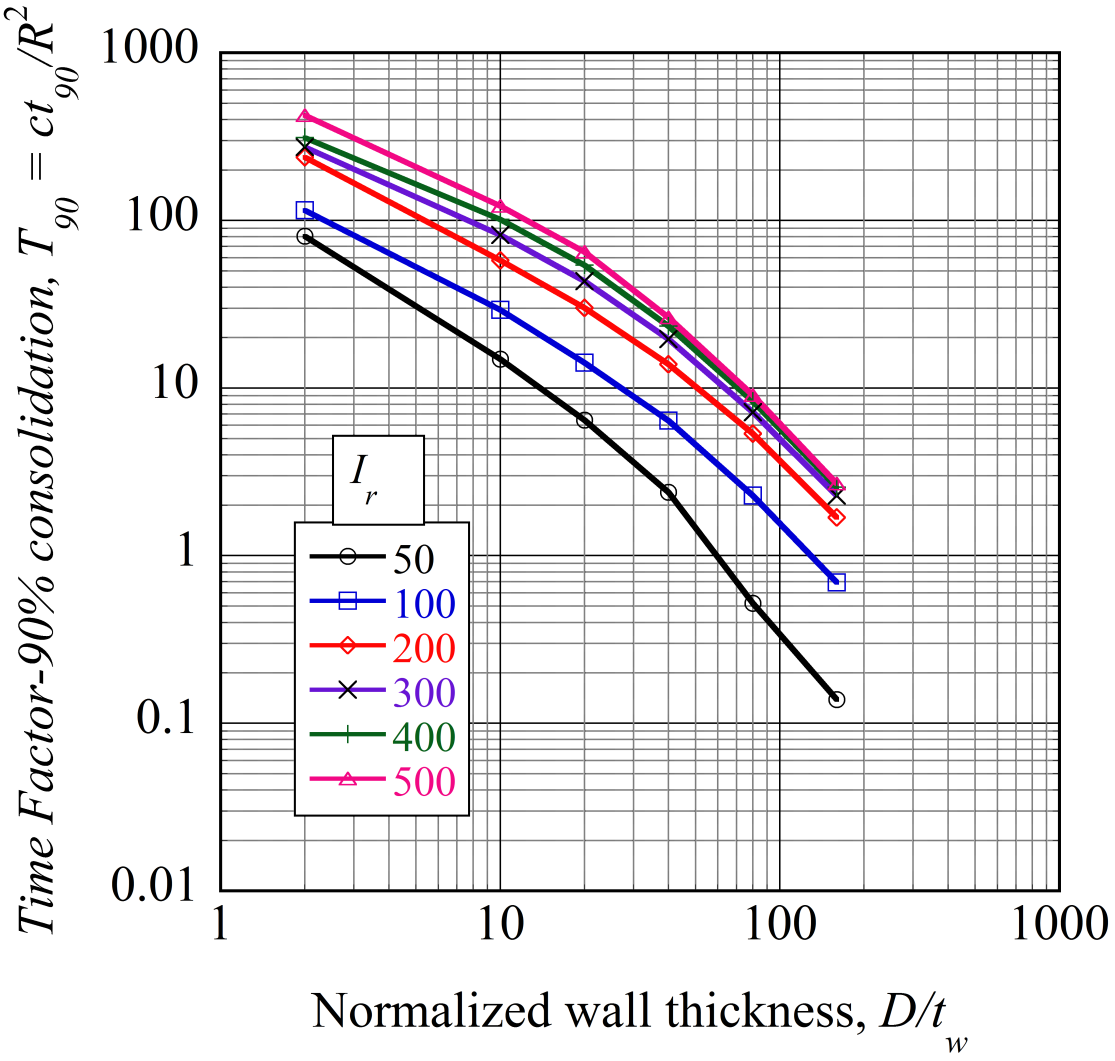


Figure 6.6: Design Guide: Predicted times to 90% consolidation

the consolidation curves for different rigidity indices, this is especially true over a range $I_r$ = 200 to 500, which corresponds to either over-consolidated or relatively stiff clays. However, the normalization is not very effective over a wider range of rigidity indices, $I_r$, specifically less than 100.

A second series of consolidation curves are presented in Fig. 6.8. For this sensitivity

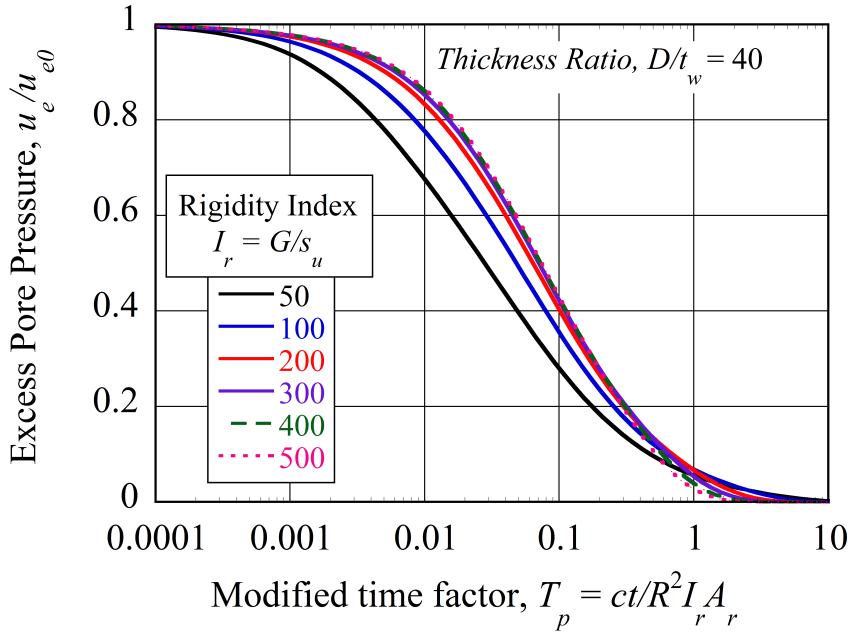


Figure 6.7: Pore pressure dissipation vs modified time factor $T_p$: Effect of $I_r$

study, rigidity index was kept constant while the normalized wall thickness was varied over a range of 2 to 160, where $D/t_w = 2$ corresponds to a solid (or plugged) pile. Once more, the normalization is only partially effective and brings together curves over a range $D/t_w = 2$ to 40, which correspond to relatively thick tubular piles. However, when thinner walls are considered, for example $D/t_w = 80$ to 160, the normalization clearly stops working.

Overall, normalizing based on a radius of the zone of plastic yielding ($R_p$) could be said to be somewhat useful. However it cannot be reasonably taken to extremes, particularly to thin-walled piles (i.e. high thickness ratios, $D/t_w$) and very soft clays (i.e. low rigidity indices, $I_r$).

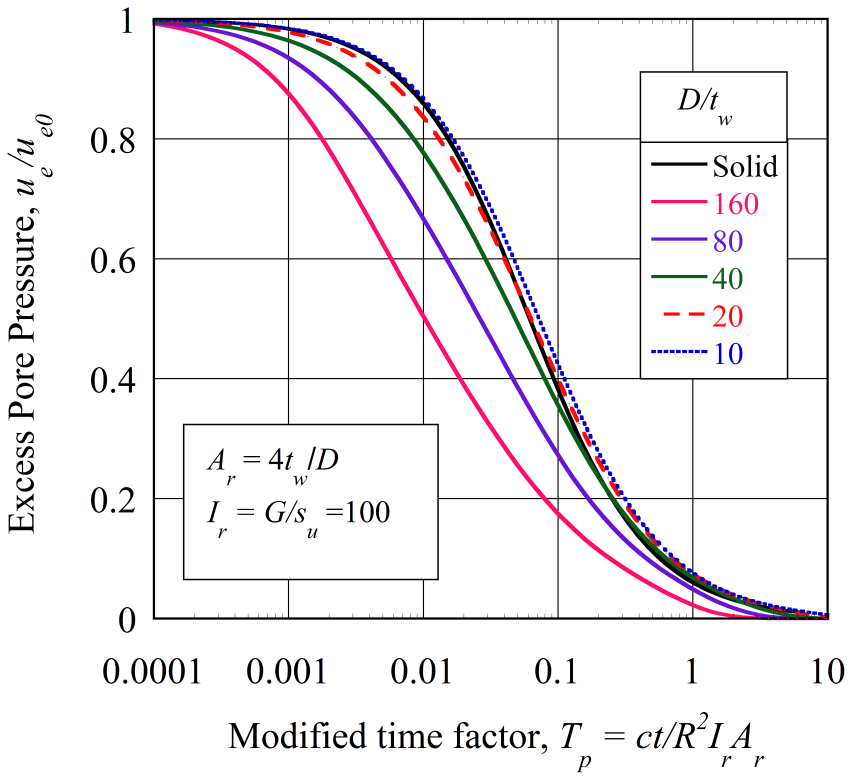


Figure 6.8: Pore pressure dissipation vs modified time factor $T_p$: Effect of $D/t_w$

## 6.4 Model Validation

### 6.4.1 Comparison and calibration to field data

Bogard and Matlock (1990) derived an empirical expression for degree of consolidation around a probe in terms of the time to 50% consolidation $t_{50}$, which was based on pore pressure measurements on instrumented probes:

$$U = (t/t_{50})/(1.1 + t/t_{50}) \tag{6.22}$$

In this dissertation, the degree of consolidation is defined in terms of the normalized excess pore pressure at the pile boundary $U = 1 - u_e/u_{e0}$. Excellent agreement has been

found between the strain path solutions (plotted as red circles) and the empirical expression (continuous black line) for the case of a solid pile, as it is shown in Fig. 6.9. For open-ended piles, relatively small deviations are observed between strain path solutions and Bogard's empirical equation (Bogard and Matlock, 1990). Deviations seem to increase somewhat if thin-walled piles are used. Nevertheless, Eq. 6.22 resembles very well the shape of the consolidation curve for both solid and open-ended piles.

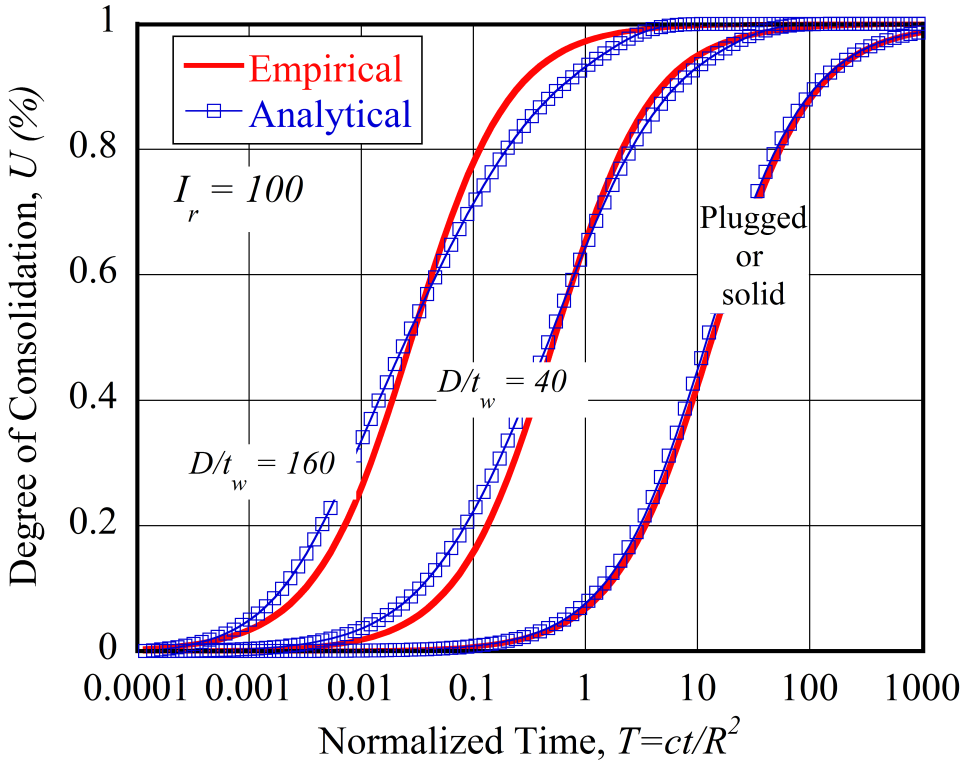


Figure 6.9: Strain Path comparison to empirical dissipation curves

In a later study, Bogard (2001) presented times to 50% consolidation following the installation of solid piles from a several sites in the Gulf of Mexico (GoM). After normalizing by pile diameter, his data indicated times in a range of about $t_{50}/D^2$ = 68-100 m$^2$/day. In terms of pile radius this indicates an average of about $t_{50}/R^2$ = 340 m$^2$/day. Figure 6.7

gives a non-dimensional time factor in the range $T_{50}$ = 5 to 10 when assuming rigidity indices in the range of $I_r$ = 100 to 200.

Applying this to Bogard's data produces an apparent coefficient of consolidation for the soil in the range of 0.015 to 0.029 $m^2$/day (Aubeny and Grajales, 2015). Sites considered in Bogard's study (Bogard, 2001) had liquid limits (LL) ranging in general between 70 and 100. By comparing these coefficients of consolidation and liquid limits to the empirical correlations presented in NAVFAC (1986) it can be concluded that the derived $c$ values are consistent with pore pressure dissipation in a reloading mode (See Fig. 2.19). This finding is consistent with the notion presented by (Levadeux and Baligh, 1986): the rate of recovery following undrained penetration largely involves reloading of the soil and,thus, the coefficient of consolidation corresponding to conditions of reloading is more adequate to characterize the process (Aubeny and Grajales, 2015).

Data on the effects of wall thickness on setup times for driven piles was presented by Bogard and Matlock (1990) and Bogard (2001) for Gulf of Mexico sites. Their data show considerable scatter, thus only the trend line of the ratio of the time to 50% consolidation for an open-ended pile to 50% consolidation for a solid pile, $t_{50}/t_{50-solid}$ is presented in Fig. 6.10. Overall, the consolidation time for a pile with wall thickness $D/t_w$ = 24 is about half that of a solid pile, while the consolidation time for a pile with wall thickness $D/t_w$ = 40 is about one-fifth that of a solid pile (Aubeny and Grajales, 2015).

in Fig. 6.10, analytical strain path predictions have been superimposed over the empirical trend line (red). SPM predictions clearly under-predict the rate of excess pore pres-

sure dissipation (Aubeny and Grajales, 2015). Given the uncertainties in the variables affecting the penetration and setup process, the source of the discrepancies between measurement and prediction is uncertain and subject to debate.

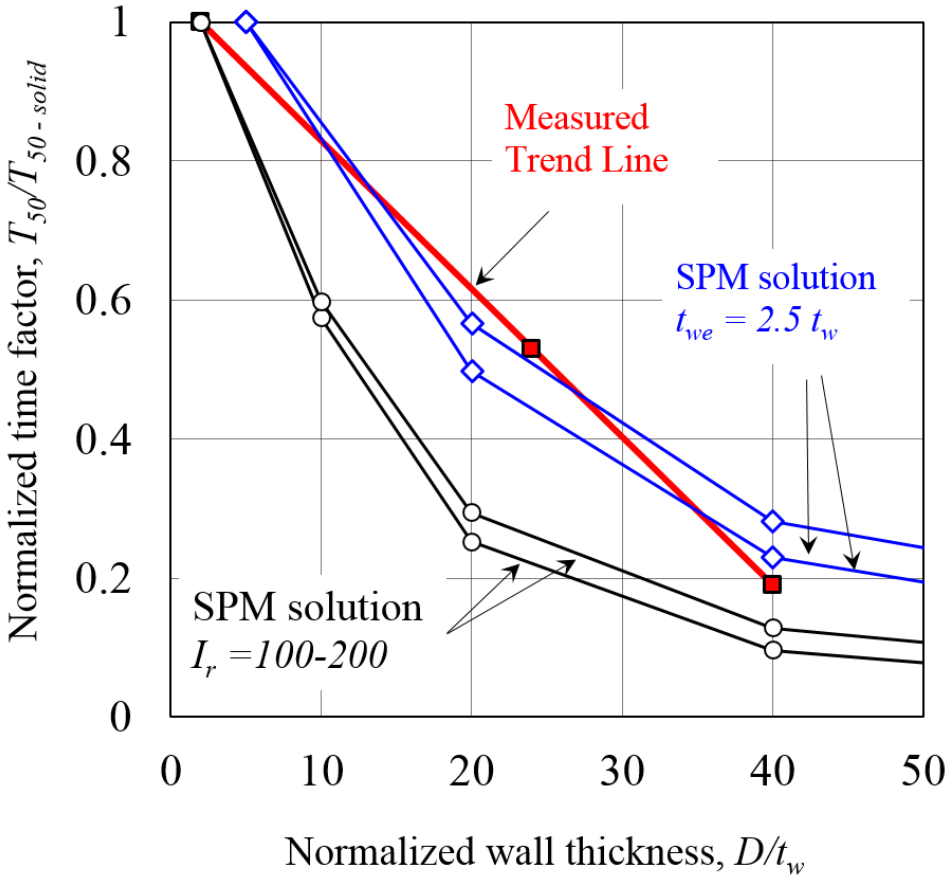


Figure 6.10: Comparison to dissipation times for driven piles

However, the most likely cause is that the strain path analysis under-predicts the amount of soil moving into the interior of the pile (Aubeny and Grajales, 2015). Frictional resistance on the inner pile wall allows less soil to "flow" inside the pile; therefore the additional soil volume pushed outside the pile produces an increase of disturbance in this region. A simple approach to simulating this 'partial plugging' effect is to increase the

effective wall thickness of the pile. After trial and error, an effective wall thickness 2.5 times the physical wall thickness, $t_{weff} = 2.5t_w$, was found to produce a reasonable match between the SPM solutions and the field data Aubeny and Grajales (2015).

The comparisons presented in the previous paragraphs focused on relatively thick-walled piles and probes installed by driving and jacking. At the other end of the current state of practice are relatively thin-walled caissons installed by suction. Jeanjean (2006) presented an extensive compilation of setup characteristics for caissons from various Gulf of Mexico sites. Strictly speaking, his study investigated the increase in adhesion $\alpha$ over time following installation of suction caissons. the time-dependent increase in $\alpha$ can be taken as a proxy for degree of consolidation, at least for the purpose of a first order assessment, keeping in mind however that thixotropy could also contribute to the setup phenomenon.

Jeanjean (2006) proposed 6.23 in order to relate the adhesion factor ($\alpha$) to the pore pressure dissipation at a given time:

$$\alpha_t = \alpha_0 + \frac{\left(1 - \frac{u_t}{u_0}\right)}{0.9} \cdot (\alpha_{90} - \alpha_0) \tag{6.23}$$

where $\alpha_0$ is the adhesion factor at a time of 0.01 days, $\alpha_{90}$ is the adhesion factor after 90% consolidation has occurred, $\alpha_t$ is the adhesion factor at a time $t$ and $u_t/u_0$ corresponds to the normalized pore pressure as function of time (Aubeny and Grajales, 2015).

Strain path analyses have been performed for two representative caisson geometries from his study with diameters $D$ = 3.66 and 5.49 m. Both caissons had a wall thickness of

$t_w$ = 0.0381 m. The SPM analyses were developed using a rigidity index $I_r$ = 100 and a coefficient of consolidation $c$ = 0.022 m$^2$/day, according to the above presented discussion. After obtaining pore pressures ($u_t/u0$) from SPM analyses, Eq. 6.23 was used to calculate equivalent adhesion factors $\alpha$.

Andersen and Joostad (2002) have suggested adhesion factor $\alpha_{90}$ = 0.65 with a sensitivity of 3 for cases when no field data is available. However for this dissertation an adhesion factor $\alpha_{90}$ = 0.75 has been selected in order to be consistent with recommendations and calculations given by Jeanjean (2006). An initial adhesion factor $\alpha_0$ has been assumed to be the inverse of the sensitivity or 0.33.

Results presented by Jeanjean (2006) indicate that 90% setup occurred after about 70-80 days. The normalized wall thicknesses for the caissons considered in his study were in the range $D/t_w$ = 96-144. Corresponding SPM analyses for the previously described caissons are presented in Figure 6.11. The SPM predictions indicate that wall thickness is the dominant factor controlling the rate of consolidation: the curves predicted analytically are very similar despite the differences in diameter. The predicted time to 90% consolidation is approximately 100 days, which is more than that indicated from the field data. These predictions are in contrast to the case described above for driven piles, where the strain path analyses predicted lower consolidation times (Aubeny and Grajales, 2015).

Given the uncertainty in the coefficient of consolidation and rigidity index, the differences between predictions and measurements are not completely reliable. However, a plausible cause of the over-estimation in the setup time could be related to the fact that

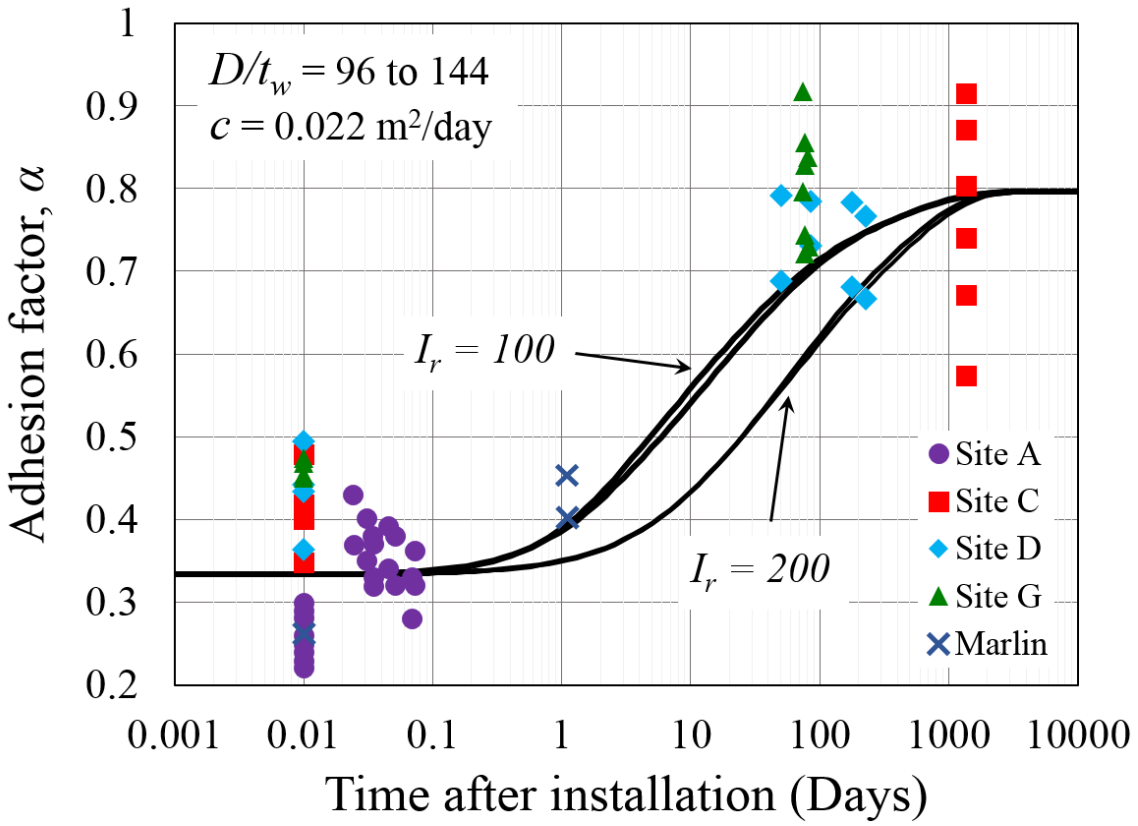


Figure 6.11: Comparison to dissipation times for suction caissons

caissons were at least partially installed by suction. Therefore, instead of partial plugging pushing soil outside the caisson, suction installation draws more soil inside the caisson than would normally occur, producing a reduction on the size of the outer zone of disturbance (Aubeny and Grajales, 2015).

To sum up, strain path estimates of setup time based seem to produce realistic but possibly somewhat high estimates of setup time for suction caisson installations. The fact that suction installation may draw more soil inside the caisson, thereby reducing the exterior zone of disturbance, could be leading to the slight tendency to over-estimate setup time (Aubeny and Grajales, 2015). In contrast, for the case of driven piles, the SPM based sim-

ulations unmistakably under-predict setup time. A plausible cause of this discrepancy is partial plugging of the pile, with soil near the inner surface of the pile being dragged downward such that the effective wall thickness is substantially greater than the actual thickness. In the case of the Gulf of Mexico pile installations using an effective wall thickness $t_{weff}$ = 2.5 tw produced a reasonable match between analytical predictions and measurements. However, it is necessary to emphasize that this is a purely empirical adjustment that should not necessarily be extrapolated to other soil and site conditions.

### 6.4.2 Comparison to data from geotechnical centrifuge tests

Cao et al. (2002a,b) developed centrifuge tests to investigate the distribution and dissipation of excess pore pressures following the installation of suction caissons in normally consolidated and slightly over-consolidated clays (Aubeny and Grajales, 2015). A sketch of their test setup is presented in Fig. 6.12.

Their soil testing bed was made of fine kaolin clay with a reported liquid limit (LL) of 69% and a plasticity index (PI) of 31 (Cao et al., 2002a). The coefficient of virgin consolidation was given as 0.1 $mm^2$/sec (0.00864 $m^2$/day).

They performed eight sets of tests, however reported data corresponds to tests SAT06 and SAT08 (Cao et al., 2002b), which were both conducted on normally consolidated clay. Both tests were conducted at a centrifuge acceleration equivalent to one hundred times gravity (100g). Their model caisson corresponded to a prototype caisson with diameter 5.17 m, wall thickness of 65 mm ($D/t_w \approx 80$) and a submerged weight of 500kN (Cao et al., 2002b).

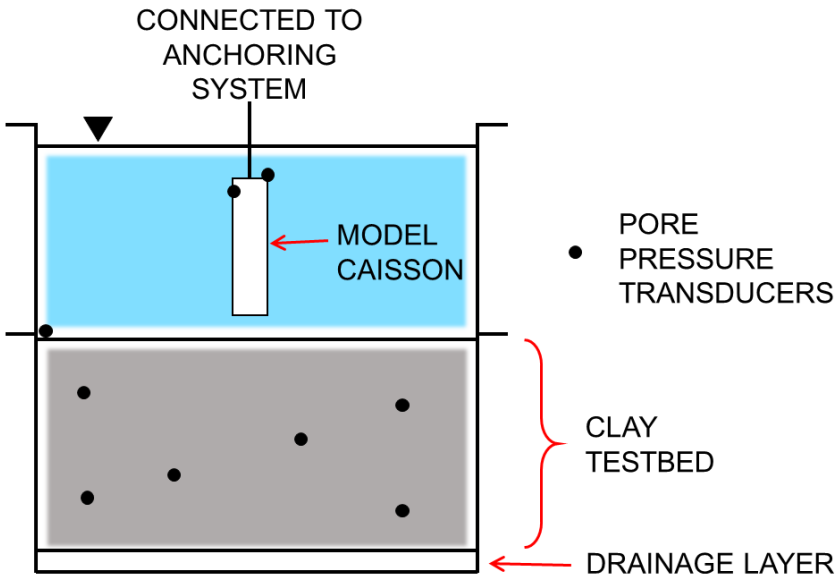


Figure 6.12: Schematic of testing bucket and placement of pore pressure sensors (Cao et al., 2002b)

Cao et al. (2002b) compared their data to cavity expansion solutions and recommended a rigidity index ($I_r$) of 150, which they assumed based on data presented by Hjortnaes-Pedersen and Bezuijen (1992). However, for reasons discussed in previous sections, rigidity indices of 100 and 200 are being considered for this dissertation.

Figure 6.13 presents results from strain path predictions plotted against Cao et al. (2002b) data for tests SAT06 and SAT08. A Somewhat reasonable agreement has been found.

During initial stages of consolidation ($U < 50\%$), SPM predictions for rigidity indices of 100 and 200 bound data from both tests. During final stages, recorded pore pressures seem to correlate better to a rigidity index of 100. The high amount of noise present in Cao et al. (2002b) data set makes uncertain the selection of $t_{90}$ (time to 90% consolidation),

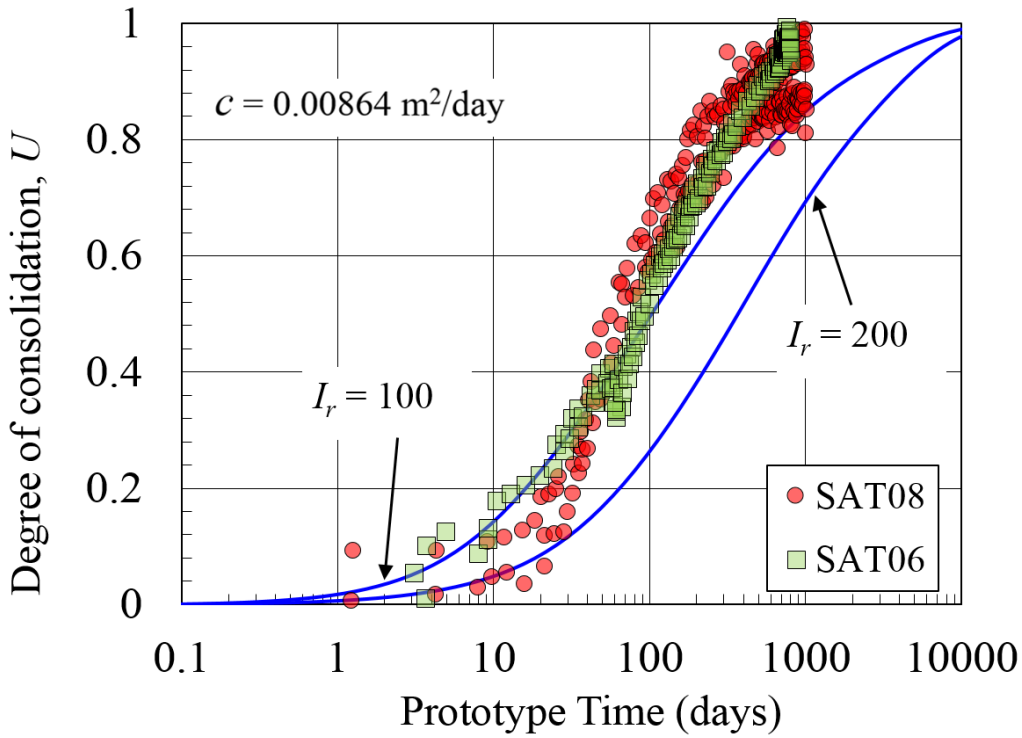


Figure 6.13: Comparison of SPM predictions to geotechnical centrifuge data. (Cao et al., 2002b)

which could range anywhere from 350 to 800 days. Cao et al. (2002b) reported a measured dissipation time to 90% consolidation of 442 days for SAT06 and 510 days for SAT08. Compared to these values, strain path predictions are considered to be somewhat high: dissipation times are overestimated, with $t_{90} \approx 1000$ days. On the other hand, a womewhat better agreement is observed for $t_{50}$ (time to 50% consolidation). Centrifuge data shows pore pressures ranging from 50 to 70 days for SAT08 and 80 to 90 days for SAT06, whilst according to strain path predictions for a rigidity index $I_r = 100$, $t_{50}$ is approximately 100 days.

### 6.4.3 Comparison to laboratory data

Olson et al. (2003) conducted a series of 1g laboratory tests to investigate the re-consolidation of soil around suction caissons during and after their installation in clay. Their model caisson consisted of a 100mm diameter aluminum pipe with a wall thickness of 0.81mm (diameter to thickness ratio, $D/t_w \approx 125$). The aspect ratio ($L_f/D$) was approximately 9, value that corresponds to a relatively long caisson.

Olson et al. (2003) placed pore pressure transducers at different locations both inside and outside the caisson wall to measure pore water pressures (Fig. 6.14). For the requirements of this dissertation, measurements recorded by a transducer located at mid-depth outside the caisson wall are going to be used (Sensor O1 in Fig. 6.14). Two different installation procedures were considered: (1) dead weight penetration and (2) penetration by both dead weight and suction. A sketch of sensor placement as well as pore pressure recordings is presented in Figure 6.14.

Their soil test bed was designed to be a normally consolidated soil deposit prepared using kaolinite slurry (Pedersen, 2001). Liquid limit (LL) ranged from 54 to 58% and the plasticity index (PI) was reported to be 24 (Aubeny and Grajales, 2015). According to data presented by Pedersen (2001) the coefficient of consolidation ranged from 0.01 $ft^2$/day to 0.04 $ft^2$/day (0.0009 $m^2$/day to 0.004 $m^2$/day).

Their pore pressure versus time measurements seem to indicate no (or even a slight) increase in pore pressure at initial testing times (approximately 0 to 1 hr). The cause of this is not clear. However one reason could be the actual two-dimensional nature of pore

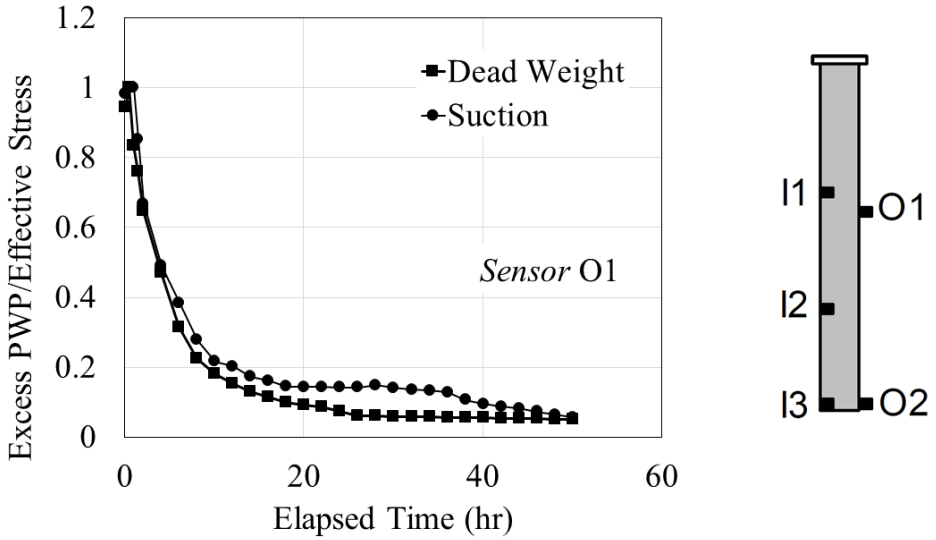


Figure 6.14: Pore pressure dissipations measured with different sensors (Olson et al., 2003)

water dissipation around a penetrating element, which produces elevated pore pressures at the pile tip to migrate upward along the shaft.

For the purpose of performing a comparison between analytical predictions against laboratory measurements, the origin of the time scale for pore water pressure dissipation ($t_0$) has been taken as the time at which the pore pressure data set reaches its peak value. For example, in the case of dead weight installation $t_0$ was assumed to be 0.6 hr ($\approx$ 40min) whilst for suction installation a value of 1 hour was selected.

Strain path analyses were performed according to the previously discussed parameters. As mentioned in Chapter 2 of this dissertation, rigidity indices ($I_r$) were assumed to range from 100 to 200. Comparisons between laboratory data (Olson et al., 2003) and strain path predictions (Aubeny and Grajales, 2015) are presented in Fig. 6.15. For each

rigidity index, upper and lower bounds are plotted (not to be confused with plasticity methods). For example, for the case of $I_r$ = 100, the lower bound corresponds to a consolidation coefficient of 0.01 ft$^2$/day whilst the upper bound corresponds to 0.04 ft$^2$/day. Overall, the analytical predictions seemed to provide a relatively good representation of the data (Aubeny and Grajales, 2015).

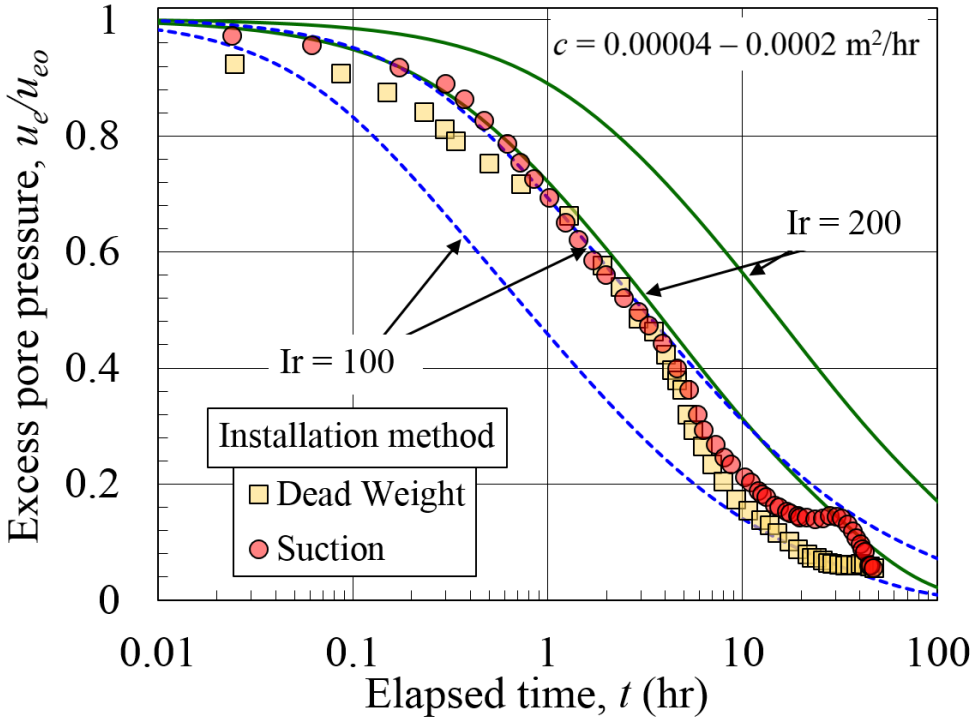


Figure 6.15: Comparison of SPM predictions to laboratory model test data

Experimental readings seem to show that dissipation of pore pressures is not substantially influenced by the installation mode (i.e. dead weight vs suction installation). During the final stages of the consolidation process (this is, $U$ = 80 to 90%), recorded datapoints for both installation methods is in very good agreement with strain path predictions for $I_r$ = 100.

When comparing predictions of normalized time at 50% and 90% consolidation ($T_{50}$ and $T_{90}$ respectively) from both experiments against those shown previously in Fig. 6.5 and 6.6, it is observed that they are also within the expected range of values. As an illustrative example: if the lowest coefficient of consolidation is used, for dead weight penetration $T_{50} \approx 0.2$ and $T_{90} \approx 1.6$ while for suction penetration $T_{50} \approx 0.2$ and $T_{90} \approx 3.2$.

# 7 SUMMARY AND CONCLUSIONS

## 7.1 Finite Element Model

A three-dimensional finite element model has been created using the software ABAQUS. The model has been successfully calibrated by using rigorous solutions (Randolph and Houlsby, 1984) and validated by comparisons to both centrifuge and laboratory data (Murali, 2015; Beemer, 2015) . Although in this study the model was utilized only to model the pile or caisson as a rigid body, it has capabilities to accommodate different pile materials and account for elastic effects.

In order to construct the mesh, a systematic tool was developed using Matlab. This tool allows the user to change the geometry, material properties, contact properties and boundary conditions in a quick way, without having to make a different code for each variation needed. In addition, the mesh generator provides a significant advantage when developing parametric studies, since the 'model generation' stage is reduced to around 5 minutes per model. This tool will be readily available to future students and can be used to model any type of vertically installed solid or tubular member (e.g. piles, caissons, skirts, conductors).

## 7.2 Capacity of laterally loaded piles and caisson

### 7.2.1 Upper bound analysis of laterally loaded piles in clay

A bimodal three dimensional plastic limit analysis method has been presented. The method combines the traditional collapse mechanism presented by Murff and Hamilton (1993) with a scoop failure mechanism inspired by previous publications by Randolph and House (2002). The new mechanism seems to perform significantly better for caissons of very short aspect ratio: $L_f/D \approx 1.5$.

The scoop mechanism geometry more closely matches the collapse mechanism predicted by FE and also provides improved numerical estimates of collapse loads. However, both mechanisms still tend to over-estimate collapse load, for caisson aspect ratios in the range of 2 to 4. For aspect ratios in this range, a reduction coefficient has been developed to better calibrate the PLA predictions to finite element analyses (Equation 4.15). The reduction takes the form of a power function and depends on the aspect ratio. One advantage of this approach is that while it enables the method to be used for short piles and caissons,it does not alter the predicted capacities for long slender piles, for which the original PLA model is believed to provide accurate results.

### 7.2.2 Simplified upper bound method

A disadvantage of the three dimensional failure mechanism is the fact that relatively high programming skills are required in order to code it. The method can not be easily implemented in a traditional spreadsheet. Furthermore, running time is significantly affected by complexities related to optimization parameters, which need to be selected with care.

For this reason the original Murff-Hamilton simplified approach has been modified. The newly developed approach relies on selection of soil resistance distributions based on finite element results. Finite element soil distributions were found to be in disagreement with previously published empirical functions by Murff and Hamilton (1993). The discrepancy was mostly affecting results for caissons with short aspect ratios (i.e. less than 4).

In order to minimize the changes to the current expression for soil resistance distributions, presented in Eq.4.16 (Murff and Hamilton, 1993), it was decided to make modifications to the variable $\eta$ which is a function of the normalized strength gradient ($\rho = s_{u0}/kD$). Usage of a parabolic equation with adequate fitting parameters produced a very good agreement with bearing capacity profiles obtained from finite element predictions for both the case of constant strength profile (Fig. 4.12) and for a wide range of normalized strength gradients, as presented in Fig. 4.13.

Finally, comparisons in terms of total capacity between finite element, 3-D Upper bound and Simplified upper bound, show very good agreement with predicted capacities for long piles, with the simplified method given slightly lower estimates. Capacities for short caissons have been significantly improved in both 3-D Upper bound and Simplified upper bound methods, however once more, results obtained through the simplified equations are somewhat more conservative.

While this last fact might possibly raise some criticism, the advantages of simplicity and accessibility for routine design use are believed to offset the disadvantage of some

level of conservatism in capacities at small aspect ratios.

## 7.3 Capacity of laterally loaded piles and caissons in stratified soils

The existent upper bound PLA code has been modified in order to accommodate non-linear soil profiles, specifically the case where a relatively stiff 'crust' overlays a stratum of soft cohesive soil.. Results show that there is significant influence associated with the presence of crusts on top of soft soil strata.

Lateral bearing capacity is somewhat affected by the presence of a crust. Behavior could be divided into to categories: (1) diameters shorter than the crust depth and (2) diameters larger than the crust depth. For case 1, small diameters reach higher capacities with lower aspect ratios. The opposite happens for case 2, as larger diameter piles can bear more horizontal load at shorter aspect ratios.

A series of parametric studies were developed, to assess the effect of pile diameter and soil strength. Conclusions from this chapter are important for the prediction of capacity of piles and caissons and for computation of p-y curves.

The original empirical fit initially developed by Murff and Hamilton (1993) does not seems to be adequate for modeling the behavior of laterally loaded piles in non-linear soils and specially for cases in which the crust's strength profile exhibits a relatively irregular shape (i.e. triangular or trapezoidal) such as the average and low crusts.

For cases where the crust has a relatively constant strength (i.e. high crust), the depth of the crust seems to control the vertical extent of the failure wedge. A simplified

approach has been proposed to calculate bearing capacities $N_{ps}$ for the cases in which pile diameter ($D$) is less than the crust thickness ($D < H_{crust}$) is to utilize the original empirical function, but modifying the strength profile as per profiles 'Empirical-B'. However, the limit pressure should be calculated as $p_u = N_{ps} s_u D$, without modifying the original strength profile of the soil with crust.

This practical approach should be limited for piles with diameters less than the crust thickness ($H_{crust}$). For typical crust profiles, the proposed simplification is limited to pile diameters less than 2.44 m (96 in).

## 7.4 Strain Path Solution of Setup Time Around Piles in Clay

An analysis of setup time following pile or caisson installation is conducted in terms of a strain path analysis using the ring source solution proposed by Chin (1986) for analysis of open ended pile penetration. The analytical approach used herein implicitly assumes that setup occurs primarily due to dissipation of excess pore pressures during the pile installation process; possible interactions with thixotropic effects are not considered. The analysis utilizes an elastic perfectly plastic model of soil behavior and an uncoupled analysis of consolidation to simulate conditions sufficiently far above the pile tip to be unaffected by end effects.

A series of parametric studies investigate the effects of relative wall thickness and soil rigidity index. Wall thickness ratios ranging from $D/t_w = 2$ (i.e., a solid or plugged pile) to 160 are considered, which is broadly representative of the range of piles and suction

caissons seen in practice. A range of rigidity indices $I_r$ ranging from 50 to 500 is considered in the parametric study, which may be considered representative of several normally to over-consolidated clays.

The strain path predictions are compared to laboratory data for suction caissons in a kaolinite slurry test bed and to field data for driven piles and suction caissons at various Gulf of Mexico sites. The following items can be highlighted from obtained results (Aubeny and Grajales, 2015):

- Setup time is strongly influenced by pile wall thickness, as seen in Figures 6.4, 6.5 and 6.6 , with setup times varying by 3 orders of magnitude over a wall thickness range $D/t_w$ = 2 to 160. On the other hand, rigidity index $I_r$ over a range $I_r$ = 50-500 can influence setup times by 1-2 orders of magnitude. In this case thin-walled piles are more sensitive to $I_r$ than solid piles.
- Definition of the time scale in terms of the zone of plastic yielding (Eqs.6.20 and 6.21) reduces significantly the width of the band of predicted consolidation curves for various wall thicknesses and rigidity indices (Fig. 6.7 and 6.8). However, it does not produce a band of consolidation curves sufficiently narrow for practical prediction of setup time. Towards this end, the most suitable framework for setup time prediction is in terms of a time factor defined by Eq. 16 together with predictions for specific values of $D/t_w$ and $I_r$ (Fig. 6.4 through 6.7).
- Comparison of strain path predictions to data derived from pore pressure decay measurements from various Gulf of Mexico sites support the notion (Levadeux and Ba-

ligh, 1986) that the coefficient of consolidation corresponding to reloading conditions is the most suitable choice for $c$ in Eq. 6.19. Furthermore, comparison to laboratory experimental data (Fig. 6.14 and 6.15) suggests that strain path predictions provide reasonable estimates of consolidation time around a caisson in normally consolidated clay. Nevertheless, care must be taken when using the method because, analytical predictions are highly sensitive to the selected value of coefficient of consolidation $c$.

- The 'simple open ended pile' solution (Eqs. 6.1 and 6.2) cannot strictly simulate the effects of inner wall resistance or suction installation, which at the same time inhibit or enhance the amount of soil going inside the pile relative to that predicted by the simple pile solution. These effects are most severe for driven piles. A way of mitigating this limitation is by using an empirical effective wall thickness $t_{we}$, depending on the conditions of installation, when using Figure 6.4 through 6.6 for pore pressure dissipation predictions.

## 7.5 Future Studies

Following this study several research topics can be explored, some of which are mentioned below:

### 7.5.1 Occurrence of gaps behind laterally loaded piles

Although this topic has been somewhat mentioned in this study, more research is required. Current FE codes do not seem to be able to model the gap in an appropriate way:

they show that gaps extend all the way to the bottom of the pile when a lateral translational displacement is applied. Furthermore, there is no clear evidence of gapping for monotonic loading, in field conditions. However many authors disagree with this fact.

### 7.5.2 Permanent deformations of piles and caissons

Accepted practice for deep foundations is to model the pile as an elastic beam-column with the soil continuum modeled as discrete, uncoupled, non-linear springs (p-y curves). The resulting pile-spring model is used to simulate a compliant foundation in the structural analysis of the superstructure as well as to design the pile itself. Guidelines for constructing p-y curves (lateral springs) and t-z curves (axial springs) have been developed empirically from load test data corresponding to certain types of soil conditions, for monotonic and cyclic loading (Matlock (1970) Reese et al. (1975)).

In recent years, more authors have presented studies about the implementation of the p-y method developed by Matlock Matlock (1970) to the design of large diameter foundations and caissons. However, it has been shown that when comparing FEM results with those obtained with the p-y method, the latter tends to underestimate capacity and overestimate deformations. In addition to the previously mentioned studies, Gerolymos and Gazetas (2006b) and Gerolymos and Gazetas (2006a) have suggested the use of Winkler models in order to simulate the soil stiffness for suction caissons and large diameter piles.

### 7.5.3 Performance of laterally loaded piles in non-linear soil profiles

This item probably represents one of the newest finding of this research. Work needed could include experimental modeling and numerical simulations in order to be able

to generate equivalent p-y curves that could effectively capture the influence of an irregular soil profile, particularly those cases in which a stiff stratum is either on top of the soil mas or within the soil mass.

# REFERENCES


Andersen, K. and Joostad, H. (2002). ``Shear strength along outside wall of suction anchors in clay after installation." *Proceedings of 12th ISOPE Conference, Kyushu, Japan*.

Andersen, K., Murff, J., Randolph, M., Clukey, E., Erbrich, C., Jostad, H., Hansen, B., Aubeny, C., Sharma, P., and Supachawarote, C. (2005). ``Suction anchors for deepwater applications." *Keynote. Proceedings of the International Symposium on Frontiers in Offshore Geotechnics, Perth, Western Australia.* (September).

Andresen, L., Jostad, H., and Andersen, K. (2011). ``Finite element analyses applied in design of foundations and anchors for offshore structures." *International Journal of Geomechanics*, 11(6), 417--430.

Aubeny, C. (1992). ``Rational interpretation of in situ tests in cohesive soils." Ph.D. Dissertation, Massachusetts Institute of Technology, Cambridge, Massachusetts, USA.

Aubeny, C. and Grajales, F. (2015). ``Strain path analysis of setup time around piles and caissons." *Proceedings of the ASME2015 34 Int. Conf Ocean, Offshore and Arctic Engr, OMAE2015*.

Aubeny, C., Han, S., and Murff, J. (2003). ``Inclined load capacity of suction caissons." *Int. J. Numer. Anal. Meth. Geomech.*, 27, 1235--1254.

Aubeny, C., Moon, S., and Murff, J. (2001a). ``Lateral undrained resistance of suction caisson anchors." *Intl. J. Offshore and Polar Engineering*, 11 (3), 211--219.

Aubeny, C. and Murff, J. (2005). ``Simplified limit solutions for the capacity of suction

anchors under undrained conditions." *Ocean Engineering*, 32, 864--877.

Aubeny, C., Murff, J., and Roesset, J. (2001b). ``Geotechnical issues in deep and ultra deep waters." *International Journal of Geomechanics*, 1(2), 225--247.

Aubeny, C., Whittle, A., and Ladd (2000). ``Effects of disturbance on undrained strengths interpreted from pressuremeter tests." *Journal of Geotechnical and Geoenvironmental Engineering*, (126), 1133--1144.

Azzouz, A., Baligh, M., and Whittle, A. (1990). ``Shaft resistance of piles in clay." *ASCE Journal of Geotechnical Engineering*, (116), 202--221.

Baligh, M. (1985). ``The strain path method." *Journal of Geotechnical Engineering, ASCE*, (111), 1108--1136.

Baligh, M. (1986). ``Fundamental of deep penetration I: Shear stresses." *Geotechnique*, 36(4), 471--485.

Baligh, M., Azzouz, A., and Chin, C. (1987). ``Disturbances due to ideal tube sampling." *Journal of Geotechnical Engineering, American Society of Civil Engineers*, (113), 739--757.

Beemer, R., Murali, M., Aubeny, C., and Biscontin, G. (2016). ``Rotational behavior of squat monopiles in soft clay from centrifuge experiments." *GeoChicago2016*.

Beemer, R. D. (2015). ``Global stiffness of offshore monopile and its behaviour under cyclic conditions." Ph.D. Dissertation, Texas A&M University, College Station, Texas, USA.

Bennett, R., Ransom, B., Kastner, M., Baerwald, R., Hulbert, M., Sawyer, W., H., O., and

M., L. (1999). ``Early diagenesis: impact of organic matter on mass physical properties and processes, california continental margin.." *Marine Geology*, (159), 7--34.

Bogard, D. (2001). ``Effective stress and axial pile capacity: Lessons learned from empire.." *Offshore Technology Conference, OTC-13059*.

Bogard, D. and Matlock, H. (1990). ``Application of model pile tests to axial design." *Offshore Technology Conference, OTC-6376*.

Bohlke, B. and Bennett, R. (1980). ``Mississippi prodelta crusts: a clay fabric and geotechnical analysis.." *Marine Geotechnology*, (4), 55--82.

Boylan, N., Long, M., Ward, D., Barwise, A., and B., G. (2007). ``Full-flow penetrometer testing in bothkennar clay." *Proceedings of the 6th International Offshore Site Investigation and Geotechnics Conference: Confronting New Challenges and Sharing Knowledge*, 177--186.

Bransby, M. F. and Randolph, M. (1998). ``Combined loading of skirted foundations." *Géotechnique*, 48 (5), 637--655.

Broms, B. B. (1964). ``Lateral resistance of piles in cohesive soils." *Journal of the Soil Mechanics and Foundations Division*, 90, 27--63.

Calladine, C. (2000). *Plasticity for Engineers*. Horwood Publishing, Chichester, England.

Cao, J., Phillips, R., Popescu, R., Al-Khafaji, Z., and Audilbert, J. (2002a). ``Penetration resistance of suction caissons in clay." *Proceedings of 12th ISOPE Conference*, 800--806.

Cao, J., Phillips, R., Popescu, R., Audilbert, J., and Al-Khafaji, Z. (2002b). ``Excess pore pressures induced by installation of suction caissons in NC clays." *Society of Underwater*

*Technology, SUT-OSIG-02-405*.

Carter, J., Randolph, M., and Wroth, C. (1979). ``Stress and pore pressure changes in clay during and after the expansion of a cylindrical cavity." *International Journal for Numerical and Analytical Methods in Geomechanics*, (3), 305--322.

Cassidy, M. (2012). ``Experimental observations of the penetration of spudcan footings in silt." *Geotechnique*, 62(8), 727--732.

Cassidy, M. and Byrne, B. (2001). ``Drum centrifuge model tests comparing the performance of sspudcan and caissons in kaolin clay." *Report No. Report No. OUEL 2248/01*, University of Oxford.

Chakrabarti, S. K. (2005). *Handbook of Offshore Engineering*. Elsevier Science, London, UK

Chen, W.-F. (2008). *Limit Analysis and Soil Plasticity*. J. Ross Publishing, Florida, USA

Chi, C.-M. (2010). ``Plastic limit analysis of offshore foundation and anchor." Ph.D. Dissertation, Texas A&M University, College Station, Texas, USA.

Chin, C.-T. (1986). ``Open-ended pile penetration in saturated clays." Ph.D. Dissertation, Massachusetts Institute of Technology, Cambridge, Massachusetts, USA.

Clukey, E., Aubeny, C., and Murff, J. (2004). ``Comparison of analytical and centrifuge model tests for suction caissons subjected to combined loads." *Journal for Offshore Mechanics and Arctic Engineering, ASME*, 126 No. 4, 364--367.

Colliat, J.-L., Dendani, H., Puech, A., and Nauroy, J.-F. (2011). ``Gulf of guinea deepwater sediments: geotechnical properties, design issues and installation experiences."

*Frontiers in Offshore Geotechnics II*, S. Gourvenec and White, eds., London, Taylor & Francis, 59--86.

Davisson, M. and Gill, H. (1963). ``Laterally loaded piles in a layered soil system." *Journal of the Soil Mechanics and Foundations Division, ASCE*, (89), 63--94.

Dean, E. R., James, R., Schofield, A. N., Tan, F., and Tsukamoto, Y. (1992). ``The bearing capacity of conical footings on sand in relation to the behaviour of spudcan footing of jackups." *Proceedings of the Wroth Memorial Symposium 'Predictive soil mechanics'*, 230--253.

Doyle, E. (1973). ``Soil-wave tank studies of marine soil instability.." *Offshore Technology Conference, OTC-1901*.

Doyle, E., McClelland, B., and G., F. (1971). ``Wire-line vane probe for deep penetration measurements of ocean sediment strength." *Offshore Technology Conference, OTC-1327-MS*.

Ehlers, C., Chen, J., Roberts, H., and Lee, Y. (2005). ``The origin of near-seafloor 'crust zones' in deepwater." *Proceedings of the International Symposium on Frontiers in Offshore Geotechnics (ISFOG)*, 927--933.

Elgamal, A., Dobry, R., and Van Laak, P. (1991). ``Design, construction and operation of 100 g-ton centrifuge at rpi." *Centrifuge*, Boulder, CO, 27--34.

Foott, R., R. and Ladd, C. (1981). ``Undrained settlement of plastic and organic clays." *Journal of the Geotechnical Eng Division, ASCE*, 107(107), 1079--1094 Proc. Paper 16421.

Georgiadis, M. (1983). ``Development of p-y curves for layered soils." *Proceedings of the Conference on Geotechnical Practice in Offshore Engineering*, 536--545.

Gerolymos, N. and Gazetas, G. (2006a). ``Development of winkler model for static and dynamic response of caisson foundations with soil and interface nonlinearities." *Soil Dynamics and Earthquake Engineering*, 26, 363--376.

Gerolymos, N. and Gazetas, G. (2006b). ``Winkler model for lateral response of rigid caisson foundations in linear soil." *Soil Dynamics and Earthquake Engineering*, 26, 347--361.

Gerwick, B. C. (2007). *Construction of Marine and Offshore Structures*. 3rd edition, CRC Press, Florida, USA.

Goodman, L., Lee, C., and Walker, F. (1961). ``The feasibility of vacuum anchorage in soil." *Geotechnique*, (11), 356--359.

Gourvenec, S. (2007). ``Failure envelopes for offshore shallow foundations under general loading." *Géotechnique*, 57 (9), 715--727.

Gourvenec, S. (2008). ``Effect of embedment on the undrained capacity of shallow foundations under general loading." *Geotechnique*, 58(3), 177--185.

Grajales, F., Beemer, R. D., Murali, M., Aubeny, C., and Biscontin, G. (2015). ``Response of short monopiles for offshore wind turbine foundations: virgin and post-cyclic capacity.." *Proceedings of the 68th Canadian Geotechnical Conference, Quebec, CA*.

Hamilton, J., Phillips, R., Dunnavant, T., and Murff, J. (1991). ``Centrifuge study of laterally loaded piles in soft clay." *Proc Int Conf Centrifuge 1991, ISSMFE*.

Han, S.-W. (2002). ``The capacity of suction caisson in isotropic and anisotropic cohesive soils under general loading conditions." Ph.D. Dissertation, Texas A&M University, College Station, Texas, USA.

Hill, R. (1950). *The Mathematical Theory of Plasticity*. Oxford University Press Inc., New York, USA.

Hjortnaes-Pedersen, A. and Bezuijen, A. (1992). ``Offshore skirt penetration in clay in the geocentrifuge." *BOSS 92, 6th International Conference on the Behavior of Offshore Structures*, Vol. 1, 528.

Hopper, J. (1980). ``Crustal layers in mississippi delta mudflows." *Proceedings of the Offshore Technology Conference*.

Houlsby, G. T. and Martin, C. M. (1992). ``Modelling of the behaviour of foundations of jack up units on clay.." *Proceedings of the Wroth Memorial Symposium 'Predictive soil mechanics'*, 339--358.

Jeanjean, P. (2006). ``Setup characteristics for suction anchors in gulf of mexico clays: Experience from field installation and retrieval." *Offshore Technology Conference, OTC-18005-MS*.

Jeanjean, P. (2017). Personal communication. January 2017.

Jeanjean, P., Campbell, K., and Kalsnes, B. (1998). ``Use of integrated study to characterize the marlin deepwater site." *SUT Offshore Site Investigation and Foundation Behaviour, Paper OSIFB-98-139*.

Kavvadas, M. (1982). ``Non-linear consolidation around driven piles in clays." Ph.D. Dis-

sertation, Massachusetts Institute of Technology, Cambridge, Massachusetts, USA.

Kay, S. and Palix, E. (2011). ``Caisson capacity in clay: VHM resistance envelope - Part 2: VHM envelope equation and design procedures." *Frontiers in Offshore Geotechnics II*, Taylor & Francis Group, London.

Khadilkar, B., Chandrasekaran, V., and Rizvi, I. (1973). ``Analysis of laterally loaded piles in two-layered soils." *Proceedings of the eight international conference on soil mechanics and foundation engineering*, Vol. 21, 155--158.

Kuchemann, D. and Weber, J. (1953). *Aerodynamics of Propulsion*. 1st edition. McGraw Hill. New York, USA

Kuo, M. (2011). ``Deep ocean clay crust: behaviour and biological origin." Ph.D. Dissertation, University of Cambridge, Cambridge, UK.

Kuo, M. and Bolton, M. (2009). ``Soil characterization of deep sea west african clays: Is biology a source of mechanical strength?." *Proceedings of the Nineteenth International Offshore and Polar Engineering Conference (ISOPE)*, 488--494.

Kuo, M. and Bolton, M. (2013). ``The nature and origin of deep ocean clay crust from the gulf of guinea." *Geotechnique*, (63), 500--509.

Kuo, M., Bolton, M., Hill, A., and Rattley, M. (2011). ``New evidence for the origin and behaviour of deep ocean 'crusts'." *Proceedings of the 2nd International Symposium on Frontiers in Offshore Geotechnics*, 365--370.

Lau, B. (2015). ``Cyclic behaviour of monopile foundations for offshore wind turbines in clay." Ph.D. Dissertation, University of Cambridge, Cambridge, UK.

Levadeux, J.-N. and Baligh (1986). ``Consolidation after undrained piezocone penetration. i: Prediction." *Journal of Geotechnical Engineering, American Society of Civil Engineers*, (112), 707--726.

Liedtke, E., Jeanjean, P., and Humphrey, G. (2006). ``Geotechnical site investigation for the mad dog spar anchors." *Offshore Technology Conference, OTC-17862*.

Low, H., Randolph, M., Rutherford, C., B., B., and Brooks, J. (2008). ``Characterization of near seabed surface sediment." *Offshore Technology Conference, OTC-19149*.

Maholtra, S. (2009). ``Design considerations for offshore wind turbine foundations in the united states." *Proceedings of the Nineteenth International Offshore and Polar Engineering Conference*.

Martin, C. M. (1994). ``Physical and numerical modelling of offshore foundations under combined load." Ph.D. Dissertation, University of Oxford, Oxford, UK.

Martin, C. M. (2001). ``Vertical bearing capacity of skirted circular foundations on tresca soil." *Proc. 15th Int. Conference on Soil Mechanics and Geotechnical Engineering, Istanbul*, 743--746.

Martin, C. M. and Randolph, M. F. (2006). ``Upper bound analysis of lateral pile capacity in cohesive soil.." *Geotechnique*, 56(2), 141--145.

Matlock, H. (1970). ``Correlations for design of laterally loaded piles in soft clay." *Offshore Technology Conference, OTC-1204*

McCave, I. (1984). ``Erosion, transport and deposition of fine-grained marine sediments." *Fine-Grained Sediments: Deep-Water Processes and Facies. Geological Society Special*

*Publications*, (15), 35--69.

Murali, M. (2011). ``Characterisation of gulf of mexico clay." M.S. Thesis, Texas A&M University, Texas A&M University.

Murali, M. (2015). ``Characterization of soft clays and the response of soil-foundations systems for offshore applications." Ph.D. Dissertation, Texas A&M University, College Station, Texas, USA.

Murali, M., Grajales, F., Beemer, R., Biscontin, G., and Aubeny, C. (2015). ``Centrifuge and numerical modeling of monopiles for offshore wind towers in clay." *Proceedings of the 34rd International Conference on Ocean, Offshore and Arctic Engineering (OMAE2015-41332)*.

Murff, J. (2002). ``Notes on Geomechanics (CVEN-651). Texas A&M University, College Station, Texas, USA.

Murff, J. and Hamilton, J. (1993). ``P-ultimate for undrained analysis of laterally loaded piles.." *ASCE Journal of Geotechnical Engineering*, 119 (1), 91--107.

Murff, J. D. (1994). ``Limit analysis of multi footing foundation systems." *Proc. 8th International conference of computational methods and advanced geomechanics.*, 223--244.

Naik, T. and Peyrot, A. (1976). ``Analysis and design of laterally loaded piles and caissons in a layered soil system." *Methods of Structural Analysis, Proceedings of the National Structural Engineering Conference, ASCE*, (2), 589--606.

NAVFAC (1986). *Soil Mechanics: Foundations and Earth Structures Design Manual*.

Olson, R., Rauch, A., Luke, A., Maniar, D., Tassoulas, J., and Mecham, E. (2003). ``Soil

reconsolidation following the installation of suction caissons." *Offshore Technology Conference, OTC-15263*.

Palix, E., Chan, N., Yangrui, Z., and Haijing, W. (2013). ``Liwan 3-1: How deep water sediments from south china sea compare with gulf of guinea sediments." *Offshore Technology Conference, OTC-24010*.

Pedersen, R. (2001). ``Model offshore soil deposit: Design, preparation and characterization." M.S. thesis, The University of Texas at Austin, Austin, Texas, USA.

Peuchen, J. (2000). ``Deepwater cone penetration tests." *Offshore Technology Conference, OTC-12094*.

Prager, W. (1959). *An Introduction to Plasticity*. Addison-Wesley Publishing Co., Massachusetts, USA

Puech, A., Colliat, J.-L., Nauroy, J.-F., and Meunier, J. (2005). ``Some geotechnical specispecific of gulf of guinea deepwater sediments." *Proceedings of the International Symposium on Frontiers in Offshore Geotechnics (ISFOG)*, 1047--1053.

Randall, R. E. (2010). *Elements of Ocean Engineering*. The Society of Naval Architects and Marine Engineers, 2nd edition. USA.

Randolph, M. (2003). ``Science and empiricism in pile foundation design." *Geotechnique*, (53), 847--875.

Randolph, M. and Gourvenec, S. (2011). *Offshore Geotechnical Engineering*. SPON Press, Taylor and Francis Group, New York, USA.

Randolph, M., O'Neil, M., and Stewart, D. (1998). ``Performance of suction anchors in

fine-grained calcareous soil." *Offshore Technology Conference, OTC-8831*.

Randolph, M. and Wroth, C. (1979). ``An analytical solution for the consolidation around a driven pile." *International Journal for Numerical and Analytical Methods in Geomechanics*, (3), 217--229.

Randolph, M. F. and Houlsby, G. T. (1984). ``The limiting pressure on a circular pile loaded laterally in cohesive soil." *Géotechnique*, 34(4), 613--623.

Randolph, M. F. and House, A. (2002). ``Analysis of suction caisson capacity in clay." *Offshore Technology Conference, OTC-14236*.

Rani, S. and Prashant, A. (2015). ``Estimation of the linear spring constant for a laterally loaded monopile embedded in nonlinear soil." *International Journal of Geomechanics, ASCE*, (15), 04014090.

Reese, L. C., Cox, W. R., , and Koop, F. (1975). ``Field testing and analysis of laterally loaded piles in stiff clay." *Offshore Technology Conference, OTC-2312*.

Roberts, H., Cratsley, D., and Whelan, T. (1976). ``Stability of mississippi delta sediments as evaluated by analysis of structural features in sediment borings." *Offshore Technology Conference, OTC-2425-MS*.

Schneider, J. and Senders, M. (2010). ``Foundation design: A comparisson of oil and gas platforms with offshore wind turbines." *Marine Technology Society Journal*, Vol. 44, No.1, 32--51.

Schroeder, K., Andersen, K., and Tjok, K.-M. (2006). ``Laboratory testing and detailed geotechnical design of the mad dog anchors." *Offshore Technology Conference, OTC-*

*17949*.

Schroeder, K. and Resseguier, S. (2015). ``Comparison of dnv and api design codes for design of suction anchors." *Frontiers in Offshore Geotechnics III*, 1387--1391.

Sharma, P. (2004). ``Ultimate capacity of suction caisson in normally and lightly overconsolidated clays." M.S. thesis, Texas A&M University, College Station, Texas, USA.

Shi, H. (2005). ``Numerical simulation and predictive models of undrained penetration in soft soils.." Ph.D. Dissertation, Texas A&M University, College Station, Texas, USA.

Sills, G. (1975). ``Some conditions under which biot equations of consolidation reduce to terzaghi equation." *Geotechnique*, (25), 129--132.

SIMULIA (2012). *ABAQUS/Standard V6.12 Users Manual*.

Smithsonian (2016). Ocean portal: Foraminifera, https://ocean.si.edu/slideshow/foraminifera

Soderberg, L. (1962). ``Consolidation theory applied to time effects." *Geotechnique*, (12), 217--225.

Stewart, D. P. and Randolph, M. F. (1991). ``A new site investigation tool for the centrifuge." *Proc. Int. Conf. On Centrifuge Modelling, Balkema, Rotterdam, Netherlands*, 531--538.

Sukumaran, B. and McCarron, W. (1999). ``Total and effective stress analysis of suction caissons for gulf of mexico conditions." *Analysis, Design Construction and Testing of Deep Foundations, ASCE Geotechnical Special Publication*, 88, 247--260.

Tan, F. (1990). ``Centrifuge and theoretical modelling of conical footings on sand." Ph.D.

Dissertation, University of Cambridge, Cambridge, UK.

Ubilla, J., Abdoun, T., and Zimmie, T. (2006). ``Application of in-flight robot in centrifuge modeling of laterally loaded stiff pile foundations." *6th ICPMG'06*, Taylor and Francis, eds., Hong Kong, 259--264.

Vasquez, L., Maniar, D., and Tassoulas, J. (2010). ``Installation and axial pullout of suction caissons: Numerical modelling." *Journal of Geotechnical and Geoenvironmental Engineering*, (136), 1137--1147.

Vesic, A. (1972). ``Expansion of cavities in infinite soil mass." *ASCE J. Geotech. Engng*, 98(3), 265--290.

Villalobos, F. A., Byrne, B. W., and Houlsby, G. (2009). ``An experimental study of the drained capacity of suction caisson foundations under monotonic loading for offshore applications." *Soils and Foundations*, 49, No 3, 477--488.

Yang, M. (2008). ``Undrained behavior of plate anchors subjected to general loading." Ph.D. Dissertation, Texas A&M University, College Station, Texas, USA.

Yang, Z. and Jeremic, B. (2005). ``Study of soil layering effects on lateral loading behavior of piles." *Journal of Geotechnical and Geoenvironmental Engineering, ASCE*, (131), 762--770.

Yetniger, A., Tjelta, T., Yang, S., Lunne, T., Colliat-Dangus, J.-L., and Longuet, A. (2012). ``Seafloor based drilling and sample quality at soft clay sites." *Society of Underwater Technology (SUT-OSIG-12-75)*, 659--666.

Young, A., Bryant, W., Slowey, N., Brand, J., and Gartner, S. (2003). ``Age dating of past

slope failures of the sigsbee escarpment within Atlantis and Mad Dog developments." *Offshore Technology Conference, OTC-15204*.

Yu, H. (2000). *Cavity Expansion Methods in Geomechanics*. Kluwer Academic Publishers, The Netherlands.

Yu, H. (2006). *Plasticity and Geotechnics*. Springer, New York, USA.

Yu, J., Huang, M., and Zhang, C. (2015). ``Three-dimensional upper-bound analysis for ultimate bearing capacity of laterally loaded rigid pile in undrained clay." *Canadian Geotechnical Journal*, (52), 1775--1790.

Zhang, C., White, D., and Randolph, M. (2011). ``Centrifuge modeling of the cyclic lateral response of a rigid pile in soft clay." *Journal of Geotechnical and Geoenvironmental Engineering*, 137(7), 717--729.

Zhang, L., Minghua, Z., and Zou, X. (2015). ``Behavior of laterally loaded piles in multi-layered soils." *International Journal of Geomechanics, ASCE*, (15) Technical Note.

Zhang, Y. (2015). ``Finite element analysis of elastic behavior of suction caisson." Ph.D. Dissertation, Texas A&M University, College Station, Texas, USA.

Zhu, B., Sun, Y., Chen, R., Guo, W., and Yang, Y. (2015). ``Experimental and analytical models of laterally loaded rigid monopiles with hardening p-y curves." *Journal of Waterway, Port, Coastal and Ocean Engineering (ASCE)*, , 10.1061/(ASCE)WW.1943-5460.0000310 , 04015007.

# APPENDIX A

# MESH GENERATION CODE

```
%Mesh generator for suction caisson
%Created by: Francisco Grajales & Dr. Charles Aubeny
%Flexible bottom boundary
%this version allows slippage/gaps at soil-pile interface
%column of cubes at centerline to avoid wedge elements
clear all
clc
%caisson or pile dimensions/features
D=5; %Diameter
t=.05; %Thickness
L=10; %Length
zpad=-.0001; %Depth of load attachment (padeye)
Ltotal=3*L;  %total depth of mesh
topcap=0;    %rigid topcap: 1=yes, 0=no
padstiff=0; %padeye stiffener: 1=yes, 0=no
%elment size controls
nelz=L; %number of elements within depth of pile
nelztotal=3*L;  %total number elements in z direction
nelrad_in=7;
nelrad_out=20;
neltheta=48; %pick even mulitple of 6
ncore=neltheta/8; %cube elements in center half-core
dcore=0.5;  %core element dimension (prior to adjusting)
rc=1.3;     %adjustment ratio of core elements
aspect=2.5;
%loading
nstep=1; %=40
%loadinc=0.5;
cloadinc=10000;
%Total Displacement
disptot=3;
%Total Rotation
rottot=0;
%soil properties
su0=2; %Strength at mudline
```

```
k=1.6; %Strength gradient
gamma=7; %Soil Density
alpha_out=1;     %adhesion on outer pile surface
alpha_in=1;      %adhesion on inner pile surface
slip_out=1; %slippage/gap at outer interface; 0=no; 1=yes
slip_in=1; %slippage/gap at inner interface; 0=no; 1=yes
su_rf=0.025;      %reduction factor for soil at tip
%printing summary of inputs
fid=fopen('SpecialRun6.txt','w');
fprintf(fid,'============ S U M M A R Y O F I N P U T S...
 ===========\r\n\r\n\r\n');
fprintf(fid,'I) CAISSON PROPERTIES\r\n\r\n');
fprintf(fid,'Diameter = %u\r\n',D);
fprintf(fid,'Length = %u\r\n',L);
fprintf(fid,'Wall thickness = %u\r\n',t);
fprintf(fid,'Padeye location = %u\r\n',zpad);
fprintf(fid,'Padeye stiffener (yes=1; no=0) = %u\r\n',...
padstiff);
fprintf(fid,'\r\nII) MESH PROPERTIES\r\n\r\n');
fprintf(fid,'Total depth of the mesh = %u\r\n',Ltotal);
fprintf(fid,'Number caisson elements ,...
 vertical direction = %u\r\n',nelz);
fprintf(fid,'Number of elements in vertical...
 direction = %u\r\n',nelztotal);
fprintf(fid,'Number of elements in the radial direction ,...
 inside the pile = %u\r\n',nelrad_in);
fprintf(fid,'Number of elements in the radial direction ,...
 outside the pile = %u\r\n',nelrad_out);
fprintf(fid,'Number of elements in the angular...
 direction = %u\r\n',neltheta);
fprintf(fid,'Number of cube elements in the center...
 half core = %u\r\n',ncore);
fprintf(fid,'Core element dimension = %u\r\n',dcore);
fprintf(fid,'Adjustment ratio of core...
 elements = %u\r\n',rc);
fprintf(fid,'Aspect ratio = %u\r\n',aspect);
fprintf(fid,'\r\nIII) SOIL PROPERTIES\r\n\r\n');
fprintf(fid,'Soil unit weight (gamma) = %u\r\n',gamma);
fprintf(fid,'Soil undrained shear strength is...
 characterized by a linear\r\n');
fprintf(fid,'relationship of the type...
 Su(z) = Su0 + k*z\r\n');
```

```
fprintf(fid,'Su0 = %u\r\n',su0);
fprintf(fid,'k = %u\r\n',k);
fprintf(fid,'Adhesion on outer...
 pile surface = %u\r\n',alpha_out);
fprintf(fid,'Adhesion on inner...
 pile surface = %u\r\n',alpha_in);
fprintf(fid,'slippage/gapping at outer...
 soil-pile interface;...
 (0=no; 1=yes) = %u\r\n',slip_out);
fprintf(fid,'slippage/gapping at inner...
 soil-pile interface;...
 (0=no; 1=yes) = %u\r\n',slip_in);
fclose(fid);
%CREATE JOB FILE
fid=fopen('SpecialRun6.job','w');
fprintf(fid,'#BSUB -J SpecialRun6\n');
fprintf(fid,'#BSUB -L /bin/bash\n');
fprintf(fid,'#BSUB -W 16:00\n');
fprintf(fid,'#BSUB -n 1\n');
fprintf(fid,'#BSUB -R "span[ptile=1]"\n');
fprintf(fid,'#BSUB -R "select[nxt]"\n');
fprintf(fid,'#BSUB -R "rusage[mem=16000]"\n');
fprintf(fid,'#BSUB -M 16000\n');
fprintf(fid,'#BSUB -o stdout1.%%J\n');
fprintf(fid,'#BSUB -u fran09.supercomputer@gmail.com\n');
fprintf(fid,'#BSUB -B -N\n');
fprintf(fid,'cd $SCRATCH/CALIBRATION\n');
fprintf(fid,'module load ABAQUS/6.12.1-linux-x86_64\n');
fprintf(fid,'abaqus memory="16gb"...
 job=SpecialRun6 input=SpecialRun6.inp\n');
fclose(fid);
%preprocess
nnode_in=(nelztotal+1)+(nelztotal+1)*nelrad_in*neltheta;
nnode_shell=2*(nelz+1)*neltheta;
nnode_middle=2*(nelztotal-nelz)*neltheta;
nnode_out=(nelztotal+1)*(nelrad_out+1)*neltheta;
delz=L/nelz;
delr0=delz/aspect;
deltheta=2*pi/neltheta;
nnode_total=nnode_in+nnode_out;
%initialize nodal arrays
node(1:nnode_total)=0;  %all nodes
```

```
x(1:nnode_total)=0;      %x-coordinates of nodes
y(1:nnode_total)=0;      %y-coordinates of nodes
z(1:nnode_total)=0;      %z-coordinates of nodes
%For nodes between core and inner shell nodes
inner_soil_surface((nelz+1)*(neltheta))=0;
%For nodes between core and inner "middle" nodes
inner_soil_surface2((nelztotal-nelz+1)*(neltheta))=0;
%For nodes outside shell nodes
outer_soil_surface((nelz+1)*(neltheta))=0;
%For nodes outside "middle" nodes
outer_soil_surface2((nelztotal-nelz+1)*(neltheta))=0;
%For nodes forming the caisson shell
%inner shell nodes
shell_in((nelz+1)*(neltheta))=0;
%outer shell nodes
shell_out((nelz+1)*(neltheta))=0;
x_shell_in((nelz+1)*(neltheta))=0; %inner shell coordinates
y_shell_in((nelz+1)*(neltheta))=0;
z_shell_in((nelz+1)*(neltheta))=0;
x_shell_out((nelz+1)*(neltheta))=0; %outer shell coordinates
y_shell_out((nelz+1)*(neltheta))=0;
z_shell_out((nelz+1)*(neltheta))=0;
%For nodes located right below the caisson
%shell to the bottom of mesh
%inner shell nodes
shell2_in((nelztotal-nelz+1)*(neltheta))=0;
%outer shell nodes
shell2_out((nelztotal-nelz+1)*(neltheta))=0;
%inner shell coordinates
x_shell2_in((nelztotal-nelz+1)*(neltheta))=0;
y_shell2_in((nelztotal-nelz+1)*(neltheta))=0;
z_shell2_in((nelztotal-nelz+1)*(neltheta))=0;
%outer shell coordinates
x_shell2_out((nelztotal-nelz+1)*(neltheta))=0;
y_shell2_out((nelztotal-nelz+1)*(neltheta))=0;
z_shell2_out((nelztotal-nelz+1)*(neltheta))=0;
%For nodes forming the bottom of the mesh
bottom(1:1+(3+nelrad_in+nelrad_out)*neltheta)=0;
%For nodes forming the top of the caisson
inner_top(neltheta*nelrad_in)=0;
%For nodes forming the far ends (infinite elements)
far(neltheta*(nelztotal+1))=0;
```

```
%Not sure about nelztotal in this three next counters
inner_circum(nelz+1,neltheta)=0;
outer_circum(nelz+1,neltheta)=0;
inner_circum2(nelztotal-nelz+1,neltheta)=0;
outer_circum2(nelztotal-nelz+1,neltheta)=0;
core_matrix(2*ncore+1,2*ncore+1,nelztotal+1)=0;
%iniialize element arrays
iel(nelz*neltheta*(nelrad_in+nelrad_out),9)=0;%all elements
elshell(1:nelz*neltheta)=0;                  %shell elements
elmiddle(1:neltheta*(nelztotal-nelz))=0;
%inner soil elements
ellayin(1:nelz,1:nelrad_in-1,neltheta)=0;
%outer soil elements
ellayout(1:nelz,1:nelrad_out,neltheta)=0;
%%%%%%%%%%%%%%%%%%  NODES  %%%%%%%%%%%%
nnode=0;
nbottom=0;
if topcap==1
topcontrol=1;
else
topcontrol=0;
end
%create inner soil nodes in radial segments
r0=dcore*ncore*sqrt(2);     %radius of core
delr=(D/2-t-r0)/(nelrad_in-ncore);
n_inner_soil_surface=0;
n_inner_soil_surface2=0;
n_inner_shell_surface=0;
n_inner_shell_surface2=0;
n_inner_circum=0; n_inner_circum2=0;
ninner_top=0;
ncoresurfB=0;
ninner_pile=0;
for jj=ncore:nelrad_in;
for ii=1:nelztotal+1
%         n_inner_circum(ii)=0;
%         n_inner_circum2(ii)=0;
nnode=nnode+1;
node(nnode)=10000*ii+100*jj;
rad=r0+delr*(jj-ncore);
x(nnode)=rad;
y(nnode)=0;
```

```
z(nnode)=-delz*(ii-1);
if ii==nelztotal+1 && jj<nelrad_in
nbottom=nbottom+1;
bottom(nbottom)=node(nnode);
end
if ii==topcontrol && jj<nelrad_in
ninner_top=ninner_top+1;
inner_top(ninner_top)=node(nnode);
end
if jj==ncore
if ii>topcontrol
ncoresurfB=ncoresurfB+1;
coresurfB(ncoresurfB)=node(nnode);
end
%adjust surface of core to octagon shape
x(nnode)=ncore*dcore*rc;
y(nnode)=0;
end
if jj==nelrad_in
if ii<=nelz+1; %For nodes located in the pile
%record inner soil surface
n_inner_soil_surface=n_inner_soil_surface+1;
inner_soil_surface(n_inner_soil_surface)=node(nnode);
%create inner shell surface
n_inner_shell_surface=n_inner_shell_surface+1;
ndum=n_inner_shell_surface;
shell_in(ndum)=node(nnode)+1000000;
x_shell_in(ndum)=x(nnode);
y_shell_in(ndum)=y(nnode);
z_shell_in(ndum)=z(nnode);
%                 if ii==nelztotal+1
%                     nbottom=nbottom+1;
%                     bottom(nbottom)=shell_in(ndum);
%                 end
n_inner_circum=ii;%n_inner_circum+1;
inner_circum(n_inner_circum,1)=node(nnode);
%store inner nodes on pile shell
if ii==topcontrol
ninner_pile=ninner_pile+1;
inner_pile(ninner_pile)=node(nnode)+1000000;
end
elseif ii>=nelz+1; %For nodes located right below the pile
```

```
%record inner soil surface
n_inner_soil_surface2=n_inner_soil_surface2+1;
inner_soil_surface2(n_inner_soil_surface2)=node(nnode);
%create inner shell surface
n_inner_shell_surface2=n_inner_shell_surface2+1;
ndum=n_inner_shell_surface2;
shell2_in(ndum)=node(nnode)+1000000;
x_shell2_in(ndum)=x(nnode);
y_shell2_in(ndum)=y(nnode);
z_shell2_in(ndum)=z(nnode);
if ii==nelztotal+1
nbottom=nbottom+1;
bottom(nbottom)=shell2_in(ndum);
end
n_inner_circum2=ii-(nelz+1);%n_inner_circum2+1;
inner_circum2(n_inner_circum2,1)=node(nnode);
end
end
for kk=1:neltheta-1
theta=kk*deltheta;
nnode=nnode+1;
node(nnode)=node(nnode-1)+1;
x(nnode)=rad*cos(theta);
y(nnode)=rad*sin(theta);
z(nnode)=-delz*(ii-1);
if ii==nelztotal+1 && jj < nelrad_in
nbottom=nbottom+1;
bottom(nbottom)=node(nnode);
end
if ii==topcontrol && jj < nelrad_in
ninner_top=ninner_top+1;
inner_top(ninner_top)=node(nnode);
end
if jj==ncore
if ii>topcontrol
ncoresurfB=ncoresurfB+1;
coresurfB(ncoresurfB)=node(nnode);
end
%adjust surface of core to octagon shape
if kk<=ncore
mm=ncore;
nn=kk;
```

```
signx=1;
signy=1;
end
if kk>ncore && kk<=2*ncore
mm=2*ncore-kk;
nn=ncore;
signx=1;
signy=1;
end
if kk>2*ncore && kk<=3*ncore
mm=kk-2*ncore;
nn=ncore;
signx=-1;
signy=1;
end
if kk>3*ncore && kk<=4*ncore
mm=ncore;
nn=4*ncore-kk;
signx=-1;
signy=1;
end
if kk>4*ncore && kk<=5*ncore
mm=ncore;
nn=kk-4*ncore;
signx=-1;
signy=-1;
end
if kk>5*ncore && kk<=6*ncore
mm=6*ncore-kk;
nn=ncore;
signx=-1;
signy=-1;
end
if kk>6*ncore && kk<=7*ncore
mm=kk-6*ncore;
nn=ncore;
signx=1;
signy=-1;
end
if kk>7*ncore && kk<=8*ncore-1
mm=ncore;
nn=8*ncore-kk;
```

```
signx=1;
signy=-1;
end
x(nnode)=signx*mm*dcore*(rc-(rc-1)*nn/ncore);
y(nnode)=signy*nn*dcore*(rc-(rc-1)*mm/ncore);
end
if jj==nelrad_in
if ii<=nelz+1; %For nodes located in the pile
%record inner soil surface
n_inner_soil_surface=n_inner_soil_surface+1;
inner_soil_surface(n_inner_soil_surface)=node(nnode);
%create inner shell surface
n_inner_shell_surface=n_inner_shell_surface+1;
ndum=n_inner_shell_surface;
shell_in(ndum)=node(nnode)+1000000;
x_shell_in(ndum)=x(nnode);
y_shell_in(ndum)=y(nnode);
z_shell_in(ndum)=z(nnode);
n_inner_circum=ii;%n_inner_circum+1;
inner_circum(n_inner_circum,kk+1)=node(nnode);
%store inner nodes on pile shell
if ii==topcontrol
ninner_pile=ninner_pile+1;
inner_pile(ninner_pile)=node(nnode)+1000000;
end
elseif ii>=nelz+1; %For nodes located right below the pile
%record inner soil surface
n_inner_soil_surface2=n_inner_soil_surface2+1;
inner_soil_surface2(n_inner_soil_surface2)=node(nnode);
%create inner shell surface
n_inner_shell_surface2=n_inner_shell_surface2+1;
ndum=n_inner_shell_surface2;
shell2_in(ndum)=node(nnode)+1000000;
x_shell2_in(ndum)=x(nnode);
y_shell2_in(ndum)=y(nnode);
z_shell2_in(ndum)=z(nnode);
if ii==nelztotal+1
nbottom=nbottom+1;
bottom(nbottom)=shell2_in(ndum);
end
n_inner_circum2=ii-(nelz+1);%n_inner_circum2+1;
inner_circum2(n_inner_circum2,kk+1)=node(nnode);
```

```
end
end
end
end
end
%Create soil nodes outside of pile
rad=D/2;
n_outer_soil_surface=0;
n_outer_soil_surface2=0;
n_outer_shell_surface=0;
n_outer_shell_surface2=0;
n_outer_circum=0;
n_outer_circum2=0;
nfar=0;
nnodei=0;
n_inf_bot=0;
for jj=1:nelrad_out+1;
for ii=1:nelztotal+1
nnode=nnode+1;
node(nnode)=10000*ii+100*(jj+nelrad_in);
x(nnode)=rad;
y(nnode)=0;
z(nnode)=-delz*(ii-1);
if ii==nelztotal+1 && jj > 1
nbottom=nbottom+1;
bottom(nbottom)=node(nnode);
end
if jj==nelrad_out+1
nfar=nfar+1;
far(nfar)=node(nnode);
end
if jj==nelrad_out+1 %infinite nodes
nnodei=nnodei+1;
nodei(nnodei)=node(nnode)+100;
xi(nnodei)=2*x(nnode);
yi(nnodei)=2*y(nnode);
zi(nnodei)=z(nnode);
%record bottom nodes in infinite elements
if ii==nelztotal+1
n_inf_bot=n_inf_bot+1;
inf_bot(n_inf_bot)=node(nnode);
n_inf_bot=n_inf_bot+1;
```

```
inf_bot(n_inf_bot)=nodei(nnodei);
end
end
if jj==1
if ii<=nelz+1;%Nodes forming the pile
%record outer soil surface
n_outer_soil_surface=n_outer_soil_surface+1;
outer_soil_surface(n_outer_soil_surface)=node(nnode);
%create outer shell surface
n_outer_shell_surface=n_outer_shell_surface+1;
ndum=n_outer_shell_surface;
shell_out(ndum)=node(nnode)+1000000;
x_shell_out(ndum)=x(nnode);
y_shell_out(ndum)=y(nnode);
z_shell_out(ndum)=z(nnode);
if z_shell_out(ndum) <= zpad &&...
 z_shell_out(ndum-neltheta) > zpad
padmid=shell_out(ndum);
padtop=padmid-10000;
padbot=padmid+10000;
end
n_outer_circum=ii;%n_outer_circum+1;
outer_circum(n_outer_circum,1)=node(nnode);
elseif ii>=nelz+1; %Soil nodes below pile
%record outer soil surface
n_outer_soil_surface2=n_outer_soil_surface2+1;
outer_soil_surface2(n_outer_soil_surface2)=node(nnode);
%create outer shell surface
n_outer_shell_surface2=n_outer_shell_surface2+1;
ndum=n_outer_shell_surface2;
shell2_out(ndum)=node(nnode)+1000000;
x_shell2_out(ndum)=x(nnode);
y_shell2_out(ndum)=y(nnode);
z_shell2_out(ndum)=z(nnode);
if ii==nelztotal+1
nbottom=nbottom+1;
bottom(nbottom)=shell2_out(ndum);
end
n_outer_circum2=ii-(nelz+1);%n_outer_circum2+1;
outer_circum2(n_outer_circum2,1)=node(nnode);
end
end
```

```
for kk=1:neltheta-1
theta=kk*deltheta;
nnode=nnode+1;
node(nnode)=node(nnode-1)+1;
x(nnode)=rad*cos(theta);
y(nnode)=rad*sin(theta);
z(nnode)=-delz*(ii-1);
if ii==nelztotal+1 && jj > 1
nbottom=nbottom+1;
bottom(nbottom)=node(nnode);
end
if jj==nelrad_out+1
nfar=nfar+1;
far(nfar)=node(nnode);
end
if jj==nelrad_out+1 %infinite nodes
nnodei=nnodei+1;
nodei(nnodei)=node(nnode)+100;
xi(nnodei)=2*x(nnode);
yi(nnodei)=2*y(nnode);
zi(nnodei)=z(nnode);
%record bottom nodes in infinite elements
if ii==nelztotal+1
n_inf_bot=n_inf_bot+1;
inf_bot(n_inf_bot)=node(nnode);
n_inf_bot=n_inf_bot+1;
inf_bot(n_inf_bot)=nodei(nnodei);
end
end
if jj==1
if ii<=nelz+1;%Nodes forming the pile
%record outer soil surface
n_outer_soil_surface=n_outer_soil_surface+1;
outer_soil_surface(n_outer_soil_surface)=node(nnode);
%create outer shell surface
n_outer_shell_surface=n_outer_shell_surface+1;
ndum=n_outer_shell_surface;
shell_out(ndum)=node(nnode)+1000000;
x_shell_out(ndum)=x(nnode);
y_shell_out(ndum)=y(nnode);
z_shell_out(ndum)=z(nnode);
n_outer_circum=ii;%n_outer_circum+1;
```

```
outer_circum(n_outer_circum,kk+1)=node(nnode);
elseif ii>=nelz+1; %Soil nodes below pile
%record outer soil surface
n_outer_soil_surface2=n_outer_soil_surface2+1;
outer_soil_surface2(n_outer_soil_surface2)=node(nnode);
%create outer shell surface
n_outer_shell_surface2=n_outer_shell_surface2+1;
ndum=n_outer_shell_surface2;
shell2_out(ndum)=node(nnode)+1000000;
x_shell2_out(ndum)=x(nnode);
y_shell2_out(ndum)=y(nnode);
z_shell2_out(ndum)=z(nnode);
if ii==nelztotal+1
nbottom=nbottom+1;
bottom(nbottom)=shell2_out(ndum);
end
n_outer_circum2=ii-(nelz+1);%n_outer_circum2+1;
outer_circum2(n_outer_circum2,kk+1)=node(nnode);
end
end
end
end
delr=6.28*rad/(neltheta-3.14);
if delr<delr0
delr=delr0;
end
rad=rad+delr;
end
%create core nodes
nnode_core=0;
nstart=2000000;
ngrid=2*ncore+1;
ncoretop=0;
ncoresurfA=0;
for ii=1:nelztotal+1
for mx=1:ngrid
for ny=1:ngrid
nnode_core=nnode_core+1;
node_core(nnode_core)=nnode_core+nstart;
mm=mx-ncore-1;
nn=ny-ncore-1;
x_core(nnode_core)=mm*dcore*(rc-(rc-1)*abs(nn)/ncore);
```

```
y_core(nnode_core)=nn*dcore*(rc-(rc-1)*abs(mm)/ncore);
z_core(nnode_core)=-(ii-1)*delz;
core_matrix(mx,ny,ii)=nnode_core+nstart;
if mx==1 || mx==ngrid || ny==1 || ny==ngrid
if ii>topcontrol
ncoresurfA=ncoresurfA+1;  %surface of inner core
coresurfA(ncoresurfA)=nnode_core+nstart;
end
end
if ii==topcontrol
ncoretop=ncoretop+1;
coretop(ncoretop)=nnode_core+nstart;
end
if ii==nelztotal+1
nbottom=nbottom+1;
bottom(nbottom)=node_core(nnode_core);
end
end
end
end
%%%%%%%%%%%%%%% ELEMENTS  %%%%%%%%%%
% % on centerline
nel=0;
nelbot=0;
nmast=0;
mast(1:nelz*neltheta)=0;
% inner elements
for jj=ncore+1:nelrad_in
for ii=1:nelztotal
for kk=1:neltheta
n1=(ii+1)*10000+100*(jj-1)+kk-1;
n2=n1+100;
n5=n1-10000;
n6=n5+100;
if kk<neltheta
n3=n2+1;
n4=n1+1;
n7=n6+1;
n8=n5+1;
else
n3=n2-neltheta+1;
n4=n1-neltheta+1;
```

```
n7=n6-neltheta+1;
n8=n5-neltheta+1;
end
nel=nel+1;
iel(nel,1)=nel;
iel(nel,2)=n1;
iel(nel,3)=n2;
iel(nel,4)=n3;
iel(nel,5)=n4;
iel(nel,6)=n5;
iel(nel,7)=n6;
iel(nel,8)=n7;
iel(nel,9)=n8;
ellayin(ii,jj-ncore,kk)=nel;
%record bottom elements
if ii==nelztotal
nelbot=nelbot+1;
elbot(nelbot)=nel;
end
%record elements of inner octagonal surface
if jj==ncore+1
nmast=nmast+1;
mast(nmast)=nel;
end
end
end
end
% outer elements
nstart=10000+(nelrad_in+1)*100;
for jj=1:nelrad_out
for ii=1:nelztotal
for kk=1:neltheta
n1=nstart+(ii)*10000+100*(jj-1)+kk-1;
n2=n1+100;
n5=n1-10000;
n6=n5+100;
if kk<neltheta
n3=n2+1;
n4=n1+1;
n7=n6+1;
n8=n5+1;
else
```

```
n3=n2-neltheta+1;
n4=n1-neltheta+1;
n7=n6-neltheta+1;
n8=n5-neltheta+1;
end
nel=nel+1;
iel(nel,1)=nel;
iel(nel,2)=n1;
iel(nel,3)=n2;
iel(nel,4)=n3;
iel(nel,5)=n4;
iel(nel,6)=n5;
iel(nel,7)=n6;
iel(nel,8)=n7;
iel(nel,9)=n8;
ellayout(ii,jj,kk)=nel;
if ii==nelztotal;
nelbot=nelbot+1;
elbot(nelbot)=nel;
end
end
end
end
% shell elements
nstart=shell_in(1)+10000;
nelshell=0;
for ii=1:nelz
for kk=1:neltheta
n1=nstart+(ii-1)*10000+kk-1;
n2=n1+100;
n5=n1-10000;
n6=n5+100;
if kk<neltheta
n3=n2+1;
n4=n1+1;
n7=n6+1;
n8=n5+1;
else
n3=n2-neltheta+1;
n4=n1-neltheta+1;
n7=n6-neltheta+1;
n8=n5-neltheta+1;
```

```
end
nel=nel+1;
nelshell=nelshell+1;
iel(nel,1)=nel;
iel(nel,2)=n1;
iel(nel,3)=n2;
iel(nel,4)=n3;
iel(nel,5)=n4;
iel(nel,6)=n5;
iel(nel,7)=n6;
iel(nel,8)=n7;
iel(nel,9)=n8;
elshell(nelshell)=nel;
if ii==nelztotal
nelbot=nelbot+1;
elbot(nelbot)=nel;
end
end
end
nelmiddle=0;
nstart=shell2_in(1);%+10000;
for ii=1:(nelztotal-nelz);
for kk=1:neltheta;
n1=nstart+(ii-1)*10000+kk-1;
n2=n1+100;
n5=n1-10000;
n6=n5+100;
if kk<neltheta
n3=n2+1;
n4=n1+1;
n7=n6+1;
n8=n5+1;
else
n3=n2-neltheta+1;
n4=n1-neltheta+1;
n7=n6-neltheta+1;
n8=n5-neltheta+1;
end
nel=nel+1;
nelmiddle=nelmiddle+1;
iel(nel,1)=nel;
iel(nel,2)=n1;
```

```
iel(nel,3)=n2;
iel(nel,4)=n3;
iel(nel,5)=n4;
iel(nel,6)=n5;
iel(nel,7)=n6;
iel(nel,8)=n7;
iel(nel,9)=n8;
elmiddle(nelmiddle)=nel;
if ii==nelztotal;
nelbot=nelbot+1;
elbot(nelbot)=nel;
end
end
end
% infinite elements
nstart=far(1);
nelinf=0;
for ii=1:nelztotal
for kk=1:neltheta
n1=nstart+ii*10000+kk-1;
n2=n1+1;
n3=n2-10000;
n4=n3-1;
n5=n1+100;
n6=n2+100;
n7=n3+100;
n8=n4+100;
if kk==neltheta
n2=n2-neltheta;
n3=n3-neltheta;
n6=n6-neltheta;
n7=n7-neltheta;
end
nel=nel+1;
nelinf=nelinf+1;
iel(nel,1)=nel;
iel(nel,2)=n1;
iel(nel,3)=n2;
iel(nel,4)=n3;
iel(nel,5)=n4;
iel(nel,6)=n5;
iel(nel,7)=n6;
```

```
iel(nel,8)=n7;
iel(nel,9)=n8;
elinf(ii,kk)=nel;
end
end
%core elements
nelcore=0;
corestart=2000000;
ncorebot=0;
for ii=1:nelztotal;
for mx=1:2*ncore
for ny=1:2*ncore
n1=core_matrix(mx,  ny,  ii+1);
n2=core_matrix(mx+1,ny,  ii+1);
n3=core_matrix(mx+1,ny+1,ii+1);
n4=core_matrix(mx,  ny+1,ii+1);
n5=core_matrix(mx,  ny,  ii);
n6=core_matrix(mx+1,ny,  ii);
n7=core_matrix(mx+1,ny+1,ii);
n8=core_matrix(mx,  ny+1,ii);
nelcore=nelcore+1;
elcore(nelcore,1)=nelcore+corestart;
elcore(nelcore,2)=n1;
elcore(nelcore,3)=n2;
elcore(nelcore,4)=n3;
elcore(nelcore,5)=n4;
elcore(nelcore,6)=n5;
elcore(nelcore,7)=n6;
elcore(nelcore,8)=n7;
elcore(nelcore,9)=n8;
if ii==nelztotal;
ncorebot=ncorebot+1;
corebot(ncorebot)=nelcore+corestart;
end
end
end
end
%%%%%%%%%%%%%%%%%%%%%%%%%%%%%%%%%%%%%%%%
%%% CREATE ABAQUS INPUT FILE %%%%%%%%%
%%%%%%%%%%%%%%%%%%%%%%%%%%%%%%%%%%%%%%%%
fid=fopen('SpecialRun6.inp','w');      %open output file
```

```
%PRINTING HEADING OF THE INPUT FILE
fprintf(fid,'*HEADING\n NEES WIND:CAPACITY AND...
 PERFORMANCE OF FOUNDATIONS FOR OFFSHORE WIND TURBINES\n');
fprintf(fid,' 3D ANALYSIS OF A LATERALLY LOADED...
 PILE USING ELASTIC-PERFECTLY PLASTIC MATERIAL MODEL\n');
fprintf(fid,' PRINCIPAL INVESTIGATOR(S): DR.GIOVANNA...
 BISCONTIN, DR.CHARLES AUBENY\n STUDENT:...
  FRANCISCO GRAJALES\n DATE:\n');
fprintf(fid,' ZACHRY DEPARTMENT OF CIVIL...
 ENGINEERING, TEXAS A&M UNIVERSITY\n');
fprintf(fid,'**-------------------------...
--------\n');
%%%%%%%%%%%%%%%%%%%%%%%%% NODES %%%%%%%%%%
%print all node definitions: soil and pile%%%
%soil
fprintf(fid,'*NODE, NSET=LOADINGNODE\r\n');
fprintf(fid,'989898,0,0,0\r\n');
fprintf(fid,'*NODE, NSET=SOIL\r\n');
for ijk=1:nnode
fprintf(fid,'%u,%f,%f,%f\r\n',...
node(ijk),x(ijk),y(ijk),z(ijk));
end
%pile
fprintf(fid,'*NODE, NSET=PILE\r\n');
for ijk=1:nnode_shell/2
fprintf(fid,'%u,%f,%f,%f\r\n',...
shell_in(ijk),x_shell_in(ijk),...
y_shell_in(ijk),z_shell_in(ijk));
end
for ijk=1:nnode_shell/2
fprintf(fid,'%u,%f,%f,%f\r\n',...
shell_out(ijk),x_shell_out(ijk),...
y_shell_out(ijk),z_shell_out(ijk));
end
%Inner Pile
fprintf(fid,'*NSET, NSET=PILEIN\r\n');
for ijk=1:nnode_shell/2
if ijk<nnode_shell/2;
fprintf(fid,'%u,\r\n',shell_in(ijk));
elseif ijk==nnode_shell/2;
fprintf(fid,'%u\r\n',shell_in(ijk));
end
```

```
end
%Outer Pile
fprintf(fid,'*NSET,␣NSET=PILEOUT\r\n');
for ijk=1:nnode_shell/2
if ijk<nnode_shell/2;
fprintf(fid,'%u,\r\n',shell_out(ijk));
elseif ijk==nnode_shell/2;
fprintf(fid,'%u\r\n',shell_out(ijk));
end
end
%Inner Pile Rings
dumdum1=0;
dumdum2=0;
for ijk=1:(nelz+1);
dumdum1=dumdum1+1;
fprintf(fid,'*NSET,␣NSET=PILEIN-%u\r\n',dumdum1);
for kji=1:neltheta;
dumdum2=dumdum2+1;
if kji<neltheta;
fprintf(fid,'%u,\r\n',shell_in(dumdum2));
elseif kji==neltheta;
fprintf(fid,'%u\r\n',shell_in(dumdum2));
end
end
end
%Outer Pile Rings
dumdum1=0;
dumdum2=0;
for ijk=1:(nelz+1);
dumdum1=dumdum1+1;
fprintf(fid,'*NSET,␣NSET=PILEOUT-%u\r\n',dumdum1);
for kji=1:neltheta;
dumdum2=dumdum2+1;
if kji<neltheta;
fprintf(fid,'%u,\r\n',shell_out(dumdum2));
elseif kji==neltheta;
fprintf(fid,'%u\r\n',shell_out(dumdum2));
end
end
end
%Middle
fprintf(fid,'*NODE,␣NSET=N_MIDDLE\r\n');
```

```
for ijk=1:nnode_middle/2
fprintf(fid,'%u,%f,%f,%f\r\n',...
shell2_in(ijk),x_shell2_in(ijk),...
y_shell2_in(ijk),z_shell2_in(ijk));
end
for ijk=1:nnode_middle/2
fprintf(fid,'%u,%f,%f,%f\r\n',...
shell2_out(ijk),x_shell2_out(ijk),...
y_shell2_out(ijk),z_shell2_out(ijk));
end
%infinite
fprintf(fid,'*NODE,␣NSET=INFINITE\r\n');
for ijk=1:nnodei
fprintf(fid,'%u,%f,%f,%f\r\n',...
nodei(ijk),xi(ijk),yi(ijk),zi(ijk));
end
%core nodes
fprintf(fid,'*NODE,␣NSET=CORE\r\n');
for ijk=1:nnode_core
fprintf(fid,'%u,%f,%f,%f\r\n',...
node_core(ijk),x_core(ijk),y_core(ijk),z_core(ijk));
end
%print bottom layer node set
last=mod(nbottom,6);
tmp=bottom;
fprintf(fid,'*NSET,␣NSET=BOTTOM\r\n');
for i=1:6:nbottom-last
fprintf(fid,'%u,%u,%u,%u,%u,%u\r\n',...
tmp(i),tmp(i+1),tmp(i+2),tmp(i+3),tmp(i+4),tmp(i+5));
end
i1=nbottom-last+1;
i2=nbottom-last+2;
i3=nbottom-last+3;
i4=nbottom-last+4;
i5=nbottom-last+5;
if last==1
fprintf(fid,'%u\r\n',tmp(i1));
elseif last==2
fprintf(fid,'%u,%u\r\n',tmp(i1),tmp(i2));
elseif last==3
fprintf(fid,'%u,%u,%u\r\n',tmp(i1),tmp(i2),tmp(i3));
elseif last==4
```

```
fprintf(fid,'%u,%u,%u,%u\r\n',...
tmp(i1),tmp(i2),tmp(i3),tmp(i4));
elseif last==5
fprintf(fid,'%u,%u,%u,%u,%u\r\n',...
tmp(i1),tmp(i2),tmp(i3),tmp(i4),tmp(i5));
end
%print inner soil surface node set
last=mod(n_inner_soil_surface,6);
tmp=inner_soil_surface;
fprintf(fid,'*NSET,␣NSET=INNER_SOIL_SURFACE\r\n');
for i=1:6:n_inner_soil_surface-last
fprintf(fid,'%u,%u,%u,%u,%u,%u\r\n',...
tmp(i),tmp(i+1),tmp(i+2),tmp(i+3),tmp(i+4),tmp(i+5));
end
i1=n_inner_soil_surface-last+1;
i2=n_inner_soil_surface-last+2;
i3=n_inner_soil_surface-last+3;
i4=n_inner_soil_surface-last+4;
i5=n_inner_soil_surface-last+5;
if last==1
fprintf(fid,'%u\r\n',tmp(i1));
elseif last==2
fprintf(fid,'%u,%u\r\n',tmp(i1),tmp(i2));
elseif last==3
fprintf(fid,'%u,%u,%u\r\n',tmp(i1),tmp(i2),tmp(i3));
elseif last==4
fprintf(fid,'%u,%u,%u,%u\r\n',...
tmp(i1),tmp(i2),tmp(i3),tmp(i4));
elseif last==5
fprintf(fid,'%u,%u,%u,%u,%u\r\n',...
tmp(i1),tmp(i2),tmp(i3),tmp(i4),tmp(i5));
end
%print outer soil surface node set
last=mod(n_outer_soil_surface,6);
tmp=outer_soil_surface;
fprintf(fid,'*NSET,␣NSET=OUTER_SOIL_SURFACE\r\n');
for i=1:6:n_outer_soil_surface-last
fprintf(fid,'%u,%u,%u,%u,%u,%u\r\n',...
tmp(i),tmp(i+1),tmp(i+2),tmp(i+3),tmp(i+4),tmp(i+5));
end
i1=n_outer_soil_surface-last+1;
i2=n_outer_soil_surface-last+2;
```

```
i3=n_outer_soil_surface-last+3;
i4=n_outer_soil_surface-last+4;
i5=n_outer_soil_surface-last+5;
if last==1
fprintf(fid,'%u\r\n',tmp(i1));
elseif last==2
fprintf(fid,'%u,%u\r\n',tmp(i1),tmp(i2));
elseif last==3
fprintf(fid,'%u,%u,%u\r\n',tmp(i1),tmp(i2),tmp(i3));
elseif last==4
fprintf(fid,'%u,%u,%u,%u\r\n',...
tmp(i1),tmp(i2),tmp(i3),tmp(i4));
elseif last==5
fprintf(fid,'%u,%u,%u,%u,%u\r\n',...
tmp(i1),tmp(i2),tmp(i3),tmp(i4),tmp(i5));
end
%print inner pile surface node set
last=mod(n_inner_shell_surface,6);
tmp=shell_in;
fprintf(fid,'*NSET,␣NSET=INNER_SHELL_SURFACE\r\n');
for i=1:6:n_inner_shell_surface-last
fprintf(fid,'%u,%u,%u,%u,%u,%u\r\n',...
tmp(i),tmp(i+1),tmp(i+2),tmp(i+3),tmp(i+4),tmp(i+5));
end
i1=n_inner_shell_surface-last+1;
i2=n_inner_shell_surface-last+2;
i3=n_inner_shell_surface-last+3;
i4=n_inner_shell_surface-last+4;
i5=n_inner_shell_surface-last+5;
if last==1
fprintf(fid,'%u\r\n',tmp(i1));
elseif last==2
fprintf(fid,'%u,%u\r\n',tmp(i1),tmp(i2));
elseif last==3
fprintf(fid,'%u,%u,%u\r\n',tmp(i1),tmp(i2),tmp(i3));
elseif last==4
fprintf(fid,'%u,%u,%u,%u\r\n',...
tmp(i1),tmp(i2),tmp(i3),tmp(i4));
elseif last==5
fprintf(fid,'%u,%u,%u,%u,%u\r\n',...
tmp(i1),tmp(i2),tmp(i3),tmp(i4),tmp(i5));
end
```

```
%print outer pile surface node set
last=mod(n_outer_shell_surface,6);
tmp=shell_out;
fprintf(fid,'*NSET,␣NSET=OUTER_SHELL_SURFACE\r\n');
for i=1:6:n_outer_shell_surface-last
fprintf(fid,'%u,%u,%u,%u,%u,%u\r\n',...
tmp(i),tmp(i+1),tmp(i+2),tmp(i+3),tmp(i+4),tmp(i+5));
end
i1=n_outer_shell_surface-last+1;
i2=n_outer_shell_surface-last+2;
i3=n_outer_shell_surface-last+3;
i4=n_outer_shell_surface-last+4;
i5=n_outer_shell_surface-last+5;
if last==1
fprintf(fid,'%u\r\n',tmp(i1));
elseif last==2
fprintf(fid,'%u,%u\r\n',tmp(i1),tmp(i2));
elseif last==3
fprintf(fid,'%u,%u,%u\r\n',tmp(i1),tmp(i2),tmp(i3));
elseif last==4
fprintf(fid,'%u,%u,%u,%u\r\n',...
tmp(i1),tmp(i2),tmp(i3),tmp(i4));
elseif last==5
fprintf(fid,'%u,%u,%u,%u,%u\r\n',...
tmp(i1),tmp(i2),tmp(i3),tmp(i4),tmp(i5));
end
%print inner top soil boundary node set (outside of core)
if topcap==1
last=mod(ninner_top,6);
tmp=inner_top;
fprintf(fid,'*NSET,␣NSET=INNER_TOP_SOIL\r\n');
for i=1:6:ninner_top-last
fprintf(fid,'%u,%u,%u,%u,%u,%u\r\n',...
tmp(i),tmp(i+1),tmp(i+2),tmp(i+3),tmp(i+4),tmp(i+5));
end
i1=ninner_top-last+1;
i2=ninner_top-last+2;
i3=ninner_top-last+3;
i4=ninner_top-last+4;
i5=ninner_top-last+5;
if last==1
fprintf(fid,'%u\r\n',tmp(i1));
```

```
elseif last==2
fprintf(fid,'%u,%u\r\n',tmp(i1),tmp(i2));
elseif last==3
fprintf(fid,'%u,%u,%u\r\n',tmp(i1),tmp(i2),tmp(i3));
elseif last==4
fprintf(fid,'%u,%u,%u,%u\r\n',...
tmp(i1),tmp(i2),tmp(i3),tmp(i4));
elseif last==5
fprintf(fid,'%u,%u,%u,%u,%u\r\n',...
tmp(i1),tmp(i2),tmp(i3),tmp(i4),tmp(i5));
end
end
%print top nodes on core outer surface
if topcap==1
fprintf(fid,'*NSET,␣NSET=CORETOP\r\n');
tmp=coretop;
for kk=1:ncoretop
fprintf(fid,'%u\r\n',tmp(kk));
end
end
%print far field node set
last=mod(nfar,6);
tmp=far;
fprintf(fid,'*NSET,␣NSET=FAR\r\n');
for i=1:6:nfar-last
fprintf(fid,'%u,%u,%u,%u,%u,%u\r\n',...
tmp(i),tmp(i+1),tmp(i+2),tmp(i+3),tmp(i+4),tmp(i+5));
end
i1=nfar-last+1;
i2=nfar-last+2;
i3=nfar-last+3;
i4=nfar-last+4;
i5=nfar-last+5;
if last==1
fprintf(fid,'%u\r\n',tmp(i1));
elseif last==2
fprintf(fid,'%u,%u\r\n',tmp(i1),tmp(i2));
elseif last==3
fprintf(fid,'%u,%u,%u\r\n',tmp(i1),tmp(i2),tmp(i3));
elseif last==4
fprintf(fid,'%u,%u,%u,%u\r\n',...
tmp(i1),tmp(i2),tmp(i3),tmp(i4));
```

```
elseif last==5
fprintf(fid,'%u,%u,%u,%u,%u\r\n',...
tmp(i1),tmp(i2),tmp(i3),tmp(i4),tmp(i5));
end
%print inner soil boundary nodes by layer
%(assume neltheta even mulitple of 6)
for ii=1:nelz+1
fprintf(fid,'*NSET,␣NSET=INNERLAYER%u\r\n',ii);
tmp(1:neltheta)=inner_circum(ii,1:neltheta);
for kk=1:6:neltheta
fprintf(fid,'%u,%u,%u,%u,%u,%u\r\n',...
tmp(kk),tmp(kk+1),tmp(kk+2),tmp(kk+3),tmp(kk+4),tmp(kk+5));
end
end
for ii=1:nelztotal-nelz
fprintf(fid,'*NSET,␣NSET=INNERLAYERbot%u\r\n',ii);
tmp(1:neltheta)=inner_circum2(ii,1:neltheta);
for kk=1:6:neltheta
fprintf(fid,'%u,%u,%u,%u,%u,%u\r\n',...
tmp(kk),tmp(kk+1),tmp(kk+2),tmp(kk+3),tmp(kk+4),tmp(kk+5));
end
end
%print outer soil boundary nodes by layer
%(assume neltheta even mulitple of 6)
for ii=1:nelz+1
fprintf(fid,'*NSET,␣NSET=OUTERLAYER%u\r\n',ii);
tmp(1:neltheta)=outer_circum(ii,1:neltheta);
for kk=1:6:neltheta
fprintf(fid,'%u,%u,%u,%u,%u,%u\r\n',...
tmp(kk),tmp(kk+1),tmp(kk+2),tmp(kk+3),tmp(kk+4),tmp(kk+5));
end
end
for ii=1:nelztotal-nelz
fprintf(fid,'*NSET,␣NSET=OUTERLAYERbot%u\r\n',ii);
tmp(1:neltheta)=outer_circum2(ii,1:neltheta);
for kk=1:6:neltheta
fprintf(fid,'%u,%u,%u,%u,%u,%u\r\n',...
tmp(kk),tmp(kk+1),tmp(kk+2),tmp(kk+3),tmp(kk+4),tmp(kk+5));
end
end
%print infinite element nodes on bottom boundary
%(assume neltheta even mulitple of 6)
```

```
fprintf(fid,'*NSET,␣NSET=BOTTOM_INFINITE\r\n');
tmp=inf_bot;
for kk=1:6:2*neltheta
fprintf(fid,'%u,%u,%u,%u,%u,%u\r\n',...
tmp(kk),tmp(kk+1),tmp(kk+2),tmp(kk+3),tmp(kk+4),tmp(kk+5));
end
%print nodes at surface of inner core (slave nodes)
fprintf(fid,'*NSET,␣NSET=CORE_SLAVE\r\n');
tmp=coresurfA;
for i=1:6:ncoresurfA
fprintf(fid,'%u,%u,%u,%u,%u,%u\r\n',...
tmp(i),tmp(i+1),tmp(i+2),tmp(i+3),tmp(i+4),tmp(i+5));
end
%print nodes at top inner surface of pile
if topcap==1
fprintf(fid,'*NSET,␣NSET=PILETOP\r\n');
tmp=inner_pile;
for i=1:6:neltheta
fprintf(fid,'%u,%u,%u,%u,%u,%u\r\n',...
tmp(i),tmp(i+1),tmp(i+2),tmp(i+3),tmp(i+4),tmp(i+5));
end
end
%print set of padeye nodes (load control)
fprintf(fid,'*NSET,␣NSET=PADEYE\r\n');
fprintf(fid,'%u,%u,%u\r\n',padtop,padmid,padbot);
%padeye (displacement control)
% pad=5000000;
% xpad=1000;
% ypad=0;
% fprintf(fid,'*NODE, NSET=PADEYE\r\n');
% fprintf(fid,'%u,%u,%u,%u\r\n',pad,xpad,ypad,zpad);
%%%%%%%%%%%%%%%%%%%%%%%%% ELEMENTS %%%%
%print inner soil elements layer by layer
for ii=1:nelztotal
fprintf(fid,'*ELEMENT,...
␣TYPE=C3D8,ELSET=INNERLAYER%u\r\n',ii);
for jj=1:nelrad_in-ncore
for kk=1:neltheta
el=ellayin(ii,jj,kk);
id=iel(el,1);
n1=iel(el,2);
n2=iel(el,3);
```

```
n3=iel(el,4);
n4=iel(el,5);
n5=iel(el,6);
n6=iel(el,7);
n7=iel(el,8);
n8=iel(el,9);
fprintf(fid,'%u,%u,%u,%u,%u,%u,%u,%u,%u\r\n',...
id,n1,n2,n3,n4,n5,n6,n7,n8);
%Evaluate if nodes belong to the ring of elements located
%immediately close to the wall
if jj==(nelrad_in-ncore) && ii<=(nelz+2);
soil_in_r(ii,kk)=id;
%This should define an extra ring of
%soil right below the caisson tip
end
end
end
end
%print outer elements layer by layer
for ii=1:nelztotal
fprintf(fid,'*ELEMENT,␣TYPE=C3D8,...
ELSET=OUTERLAYER%u\r\n',ii);
for jj=1:nelrad_out
for kk=1:neltheta;
el=ellayout(ii,jj,kk);
id=iel(el,1);
n1=iel(el,2);
n2=iel(el,3);
n3=iel(el,4);
n4=iel(el,5);
n5=iel(el,6);
n6=iel(el,7);
n7=iel(el,8);
n8=iel(el,9);
fprintf(fid,'%u,%u,%u,%u,%u,%u,%u,%u,%u\r\n',...
id,n1,n2,n3,n4,n5,n6,n7,n8);
%Evaluate if nodes belong to the 'ring' of elements located
%immediately close to the wall,...
 store elem number in an array
if jj==1 && ii<=(nelz+2);
%This should define an extra ring of
%soil right below the caisson tip
```

```
soil_r(ii,kk)=id;
end
if jj==2 && ii<=(nelz+2);
soil_r2(ii,kk)=id;
end
end
end
end
%print 'soil-rings' stored in array soil_r;
for ii=1:(nelz+2);
fprintf(fid,'*ELSET,␣ELSET=SOILCIRC%u\r\n',ii);
for jj=1:neltheta;
fprintf(fid,'%u\r\n',soil_r(ii,jj));
end
end
for ii=1:(nelz+2);
fprintf(fid,'*ELSET,␣ELSET=SOILCIRCOUT%u\r\n',ii);
for jj=1:neltheta;
fprintf(fid,'%u\r\n',soil_r2(ii,jj));
end
end
%print 'soil-rings' stored in array soil_in_r;
for ii=1:(nelz+2);
fprintf(fid,'*ELSET,␣ELSET=SOILCIRCIN%u\r\n',ii);
for jj=1:neltheta;
fprintf(fid,'%u\r\n',soil_in_r(ii,jj));
end
end
%print core elements layer by layer
nelplane=(2*ncore)^2;
for ii=1:nelztotal
fprintf(fid,'*ELEMENT,␣TYPE=C3D8,ELSET=CORE%u\r\n',ii);
for mm=1:nelplane
el=nelplane*(ii-1)+mm;
id=elcore(el,1);
n1=elcore(el,2);
n2=elcore(el,3);
n3=elcore(el,4);
n4=elcore(el,5);
n5=elcore(el,6);
n6=elcore(el,7);
n7=elcore(el,8);
```

```
n8=elcore(el,9);
fprintf(fid,'%u,%u,%u,%u,%u,%u,%u,%u,%u\r\n',...
id,n1,n2,n3,n4,n5,n6,n7,n8);
end
end
%print infinite elements layer by layer
for ii=1:nelztotal
fprintf(fid,'*ELEMENT,␣TYPE=CIN3D8,ELSET=ILAYER%u\r\n',ii);
for kk=1:neltheta
el=elinf(ii,kk);
id=iel(el,1);
n1=iel(el,2);
n2=iel(el,3);
n3=iel(el,4);
n4=iel(el,5);
n5=iel(el,6);
n6=iel(el,7);
n7=iel(el,8);
n8=iel(el,9);
fprintf(fid,'%u,%u,%u,%u,%u,%u,%u,%u,%u\r\n',...
id,n1,n2,n3,n4,n5,n6,n7,n8);
end
end
%print shell elements layer by layer
fprintf(fid,'*ELEMENT,␣TYPE=C3D8I,ELSET=PILE\r\n');
for ijk=1:nelshell
el=elshell(ijk);
id=iel(el,1);
n1=iel(el,2);
n2=iel(el,3);
n3=iel(el,4);
n4=iel(el,5);
n5=iel(el,6);
n6=iel(el,7);
n7=iel(el,8);
n8=iel(el,9);
fprintf(fid,'%u,%u,%u,%u,%u,%u,%u,%u,%u\r\n',...
id,n1,n2,n3,n4,n5,n6,n7,n8);
end
%print pile element rings
dumdum3=0;
for ii=1:nelz;
```

```
fprintf(fid,'*ELSET,␣ELSET=PILERING-%u\r\n',ii);
for jj=1:neltheta;
dumdum3=dumdum3+1;
if jj<neltheta;
fprintf(fid,'%u,\r\n',elshell(dumdum3));
elseif jj==neltheta;
fprintf(fid,'%u\r\n',elshell(dumdum3));
end
end
end
%print 'middle' soil elements layer by layer
countf=0;
for ijk=(nelz+1):nelztotal;
fprintf(fid,'*ELEMENT,␣TYPE=C3D8,ELSET=MIDDLE%u\r\n',ijk);
for kk=1:neltheta
countf=countf+1;
el=elmiddle(countf);
id=iel(el,1);
n1=iel(el,2);
n2=iel(el,3);
n3=iel(el,4);
n4=iel(el,5);
n5=iel(el,6);
n6=iel(el,7);
n7=iel(el,8);
n8=iel(el,9);
fprintf(fid,'%u,%u,%u,%u,%u,%u,%u,%u,%u\r\n',...
id,n1,n2,n3,n4,n5,n6,n7,n8);
end
end
%Combine inner and outer soil layers
%into single element sets
for ii=1:nelztotal;
if ii<=nelz;
fprintf(fid,'*ELSET,ELSET=LAYER%u\r\n',ii);
fprintf(fid,'CORE%u,INNERLAYER%u,...
OUTERLAYER%u\r\n',ii,ii,ii);
elseif ii>nelz;
fprintf(fid,'*ELSET,ELSET=LAYER%u\r\n',ii);
fprintf(fid,'CORE%u,INNERLAYER%u,...
OUTERLAYER%u,MIDDLE%u\r\n',ii,ii,ii,ii);
end
```

```
end
%ADDED SEPTEMBER 29, 2014
%NEED TO MODIFY
z1=nelz; z2=nelz+1;
fprintf(fid,'*ELSET,ELSET=SOILTIP\r\n');
fprintf(fid,'SOILCIRC%u,SOILCIRCIN%u,\r\n',z1,z1);
fprintf(fid,'SOILCIRC%u,SOILCIRCIN%u,\r\n',z2,z2);
fprintf(fid,'MIDDLE%u\r\n',z2);
%ADDED  SEPTEMBER 29, 2014
fprintf(fid,'*ELSET,ELSET=CYLINDER\r\n');
fprintf(fid,'PILE\r\n');
for ii=1:nelz;
fprintf(fid,'CORE%u,INNERLAYER%u\r\n',ii,ii);
end
%print bottom element set
last=mod(nelbot,6);
tmp=elbot;
fprintf(fid,'*ELSET,␣ELSET=ELBOT\r\n');
for i=1:6:nelbot-last
fprintf(fid,'%u,%u,%u,%u,%u,%u\r\n',...
tmp(i),tmp(i+1),tmp(i+2),tmp(i+3),tmp(i+4),tmp(i+5));
end
i1=nelbot-last+1;
i2=nelbot-last+2;
i3=nelbot-last+3;
i4=nelbot-last+4;
i5=nelbot-last+5;
if last==1
fprintf(fid,'%u\r\n',tmp(i1));
elseif last==2
fprintf(fid,'%u,%u\r\n',tmp(i1),tmp(i2));
elseif last==3
fprintf(fid,'%u,%u,%u\r\n',tmp(i1),tmp(i2),tmp(i3));
elseif last==4
fprintf(fid,'%u,%u,%u,%u\r\n',...
tmp(i1),tmp(i2),tmp(i3),tmp(i4));
elseif last==5
fprintf(fid,'%u,%u,%u,%u,%u\r\n',...
tmp(i1),tmp(i2),tmp(i3),tmp(i4),tmp(i5));
end
%print elements at surface of inner core (master elements)
fprintf(fid,'*ELSET,␣ELSET=CORE_MASTER\r\n');
```

```
tmp=mast;
for i=1:6:nmast
fprintf(fid,'%u,%u,%u,%u,%u,%u\r\n',...
tmp(i),tmp(i+1),tmp(i+2),tmp(i+3),tmp(i+4),tmp(i+5));
end
%print elements at bottom of inner core (master elements)
fprintf(fid,'*ELSET,␣ELSET=COREBOT\r\n');
tmp=corebot;
for i=1:6:ncorebot
fprintf(fid,'%u,%u,%u,%u,%u,%u\r\n',...
tmp(i),tmp(i+1),tmp(i+2),tmp(i+3),tmp(i+4),tmp(i+5));
end
%%%%%%%%%%%%%%%%%%%%%%%%% MATERIAL %%%%
% Solid section declaration
% pile
fprintf(fid,'*SOLID␣SECTION,ELSET=PILE,MATERIAL=PILE\r\n');
% soil
for ii=1:nelztotal;
fprintf(fid,'*SOLID␣SECTION,ELSET=LAYER%u,...
MATERIAL=LAYER%u\r\n',ii,ii);
end
% infinite
for ii=1:nelztotal;
fprintf(fid,'*SOLID␣SECTION,ELSET=ILAYER%u,...
MATERIAL=ILAYER%u\r\n',ii,ii);
end
%Tip Elements (almost no shear strength)
fprintf(fid,'*SOLID␣SECTION,␣ELSET=SOILTIP,...
MATERIAL=WEAKSOIL\r\n');
%Elements in contact with the wall
for ii=1:nelztotal;
fprintf(fid,'*SOLID␣SECTION,ELSET=SOILCIRC%u,...
MATERIAL=SOILCIRC%u\r\n',ii,ii);
end
%material properties definition
% pile
fprintf(fid,'*MATERIAL,NAME=PILE\r\n');
fprintf(fid,'*ELASTIC,TYPE=ISOTROPIC\r\n');
fprintf(fid,'1E+12,0.3,0.0\r\n');
% soil
for ii=1:nelztotal;
su=su0+k*(ii-0.5)*delz;
```

```
E=150*su;
mu=0.49;
fprintf(fid,'*MATERIAL,NAME=LAYER%u\r\n',ii);
fprintf(fid,'*ELASTIC,TYPE=ISOTROPIC\r\n');
fprintf(fid,'%u,%u,0.0\r\n',E,mu);
fprintf(fid,'*MOHR␣COULOMB\r\n');
fprintf(fid,'0.0␣␣␣,0.0\r\n');
fprintf(fid,'*MOHR␣COULOMB␣HARDENING\r\n');
fprintf(fid,'%u\r\n',su);
end
% soil in contact
for ii=1:nelztotal;
su=alpha_out*(su0+k*(ii-0.5)*delz);
E=150*su;
mu=0.49;
fprintf(fid,'*MATERIAL,NAME=SOILCIRC%u\r\n',ii);
fprintf(fid,'*ELASTIC,TYPE=ISOTROPIC\r\n');
fprintf(fid,'%u,%u,0.0\r\n',E,mu);
fprintf(fid,'*MOHR␣COULOMB\r\n');
fprintf(fid,'0.0␣␣␣,0.0\r\n');
fprintf(fid,'*MOHR␣COULOMB␣HARDENING\r\n');
fprintf(fid,'%u\r\n',su);
end
% infinite
for ii=1:nelztotal;
su=su0+k*(ii-0.5)*delz;
E=150*su;
mu=0.49;
fprintf(fid,'*MATERIAL,NAME=ILAYER%u\r\n',ii);
fprintf(fid,'*ELASTIC,TYPE=ISOTROPIC\r\n');
fprintf(fid,'%u,%u,0.0\r\n',E,mu);
end
%Weak soil
fprintf(fid,'*MATERIAL,NAME=WEAKSOIL\r\n');
fprintf(fid,'*ELASTIC,␣TYPE=ISOTROPIC\r\n');
su_r=su_rf*(su0+k*(L)); mu=0.49;
E=150*su_r;
fprintf(fid,'%u,%u,0.0\r\n',E,mu);
fprintf(fid,'*MOHR␣COULOMB\r\n');
fprintf(fid,'0.0␣␣␣,0.0\r\n');
fprintf(fid,'*MOHR␣COULOMB␣HARDENING\r\n');
fprintf(fid,'%u\r\n',su_r);
```

```
% %%%%%%%%%%%%%%%%% INITIAL CONDITIONS %%%%
sigze=-gamma*100;
fprintf(fid,'*INITIAL␣CONDITIONS,...
TYPE=STRESS,GEOSTATIC\r\n');
fprintf(fid,'PILE,0.0,0.0,%u,-100.0,0.55,0.55\r\n',sigze);
for ii=1:nelztotal;
fprintf(fid,'LAYER%u,0.0,0.0,%u,...
-100.0,0.55,0.55\r\n',ii,sigze);
end
for ii=1:nelztotal;
fprintf(fid,'ILAYER%u,0.0,0.0,%u,...
-100.0,0.55,0.55\r\n',ii,sigze);
end
%%%%%%%%%%%%%%%%%%% RIGID PADEYE STIFFENER %%
if padstiff==1
fprintf(fid,'*KINEMATIC␣COUPLING,REF␣NODE=%u\r\n',padtop);
fprintf(fid,'%u,1,3\r\n',padtop+neltheta/2);
fprintf(fid,'*KINEMATIC␣COUPLING,REF␣NODE=%u\r\n',padmid);
fprintf(fid,'%u,1,3\r\n',padmid+neltheta/2);
fprintf(fid,'*KINEMATIC␣COUPLING,REF␣NODE=%u\r\n',padbot);
fprintf(fid,'%u,1,3\r\n',padbot+neltheta/2);
end
%%%%%%%%%%%%%%%%%%% CONSTRAINT EQUATION %%
% ratio=(zpad-zpad2)/(zpad1-zpad2);
% A1=ratio;
% A2=1-ratio;
% DOF=1;
% load=-1;
% fprintf(fid,'*EQUATION\r\n');
% fprintf(fid,'3\r\n');
% fprintf(fid,'%u,%u,%u\r\n',pad1,DOF,A1);
% fprintf(fid,'%u,%u,%u\r\n',pad2,DOF,A2);
% fprintf(fid,'%u,%u,%u\r\n',pad,DOF,load);
%%%%%%%% TIE INNER CORE ELEMENTS TO MESH %%%
fprintf(fid,'*SURFACE,TYPE=ELEMENT,NAME=CORE_MASTER\r\n');
fprintf(fid,'CORE_MASTER,S6\r\n');
fprintf(fid,'*SURFACE,TYPE=NODE,NAME=CORE_SLAVE\r\n');
fprintf(fid,'CORE_SLAVE\r\n');
fprintf(fid,'*TIE,NAME=CORE\r\n');
fprintf(fid,'CORE_SLAVE,CORE_MASTER\r\n');
%%%%%%%%%%%%%%%%%%%% RIGID TOP CAP %%
if topcap==1
```

```
fprintf(fid,'*NSET,NSET=CAP\r\n');
fprintf(fid,'INNER_TOP_SOIL,CORETOP,PILETOP\r\n');
fprintf(fid,'*NODE,NSET=NODE_999\r\n');
fprintf(fid,'999,0.0,0.0,0.0\r\n');
fprintf(fid,'*RIGID␣BODY,PIN␣NSET=CAP,REFNODE=999\r\n');
end
%%%%%%%%%%%%%%%% SURFACE DEFINITIONS %
%nomenclature
% NODE sets defining soil surfaces: INNERLAYERn, OUTERLAYERn
% ELEMENT sets defining pile:
%PILE (S6=inner surface, S4=outer surface))
% SURFACE names for soils: SLINn, SLOUTn
% SURFACE names for pile: PILEIN, PILEOUT
% INTERACTION names: SOILINn, SOILOUTn
% n=soil layer number
%define surfaces as needed for slip boundaries
%inner surface
if slip_in==1
%pile
fprintf(fid,'*SURFACE,TYPE=ELEMENT,NAME=PILEIN\r\n');
fprintf(fid,'PILE,S6\r\n');
%soil
for ii=1:nelz+1
fprintf(fid,'*SURFACE,TYPE=NODE,NAME=SLIN%u\r\n',ii);
fprintf(fid,'INNERLAYER%u\r\n',ii);
end
%soil below pile
for ii=1:nelztotal-nelz;
fprintf(fid,'*SURFACE,TYPE=NODE,NAME=SLINbot2%u\r\n',ii);
fprintf(fid,'INNERLAYERbot%u\r\n',ii);
end
end
%outer surface
if slip_out==1
%pile
fprintf(fid,'*SURFACE,TYPE=ELEMENT,NAME=PILEOUT\r\n');
fprintf(fid,'PILE,S4\r\n');
%soil around pile
for ii=1:nelz+1
fprintf(fid,'*SURFACE,TYPE=NODE,NAME=SLOUT%u\r\n',ii);
fprintf(fid,'OUTERLAYER%u\r\n',ii);
end
```

```
%soil below pile
for ii=1:nelztotal-nelz;
fprintf(fid,'*SURFACE,TYPE=NODE,NAME=SLOUTbot2%u\r\n',ii);
fprintf(fid,'OUTERLAYERbot%u\r\n',ii);
end
end
%%%%%%%%%%%%%%%%%%%% CONTACT PAIRS %%%%
%define contacts between surfaces
%inner pile boundary and inner soil
if slip_in==1
for ii=1:nelz+1
fprintf(fid,'*CONTACT␣PAIR,INTERACTION=SOILIN%u,...
ADJUST=INNERLAYER%u,SMALL␣SLIDING\r\n',ii,ii);
fprintf(fid,'SLIN%u,PILEIN\r\n',ii);
end
end
%outer pile boundary and inner soil
if slip_out==1
for ii=1:nelz+1
fprintf(fid,'*CONTACT␣PAIR,INTERACTION=SOILOUT%u,...
ADJUST=OUTERLAYER%u,SMALL␣SLIDING\r\n',ii,ii);
fprintf(fid,'SLOUT%u,PILEOUT\r\n',ii);
end
end
%%%%%%%%%%%%%%%%%% SURFACE INTERACTIONS %%%
%inner pile boundary and inner soil
if slip_in==1
for ii=1:nelz+1
su=su0+k*ii*delz;
taumax=alpha_in*su;
fprintf(fid,'*SURFACE␣INTERACTION,␣NAME=SOILIN%u\r\n',ii);
fprintf(fid,'*FRICTION,␣TAUMAX=%u\r\n',taumax);
fprintf(fid,'1,\r\n');
end
end
%outer pile boundary and outer soil
if slip_out==1
for ii=1:nelz+1
su=su0+k*ii*delz;
taumax=alpha_out*su;
fprintf(fid,'*SURFACE␣INTERACTION,␣NAME=SOILOUT%u\r\n',ii);
fprintf(fid,'*FRICTION,␣TAUMAX=%u\r\n',taumax);
```

```
fprintf(fid,'1,\r\n');
end
end
%%%%%%%%%%%%%%%%%%%% COUPLING %%%
if slip_in==0
for ijk=1:n_inner_soil_surface
slave=inner_soil_surface(ijk);
master=slave+1000000;
fprintf(fid,'*KINEMATIC␣COUPLING,REF␣NODE=%u\r\n',master);
fprintf(fid,'%u,1,3\r\n',slave);
end
end
if slip_out==0
for ijk=1:n_outer_soil_surface
slave=outer_soil_surface(ijk);
master=slave+1000000;
fprintf(fid,'*KINEMATIC␣COUPLING,REF␣NODE=%u\r\n',master);
fprintf(fid,'%u,1,3\r\n',slave);
end
end
for ijk=1:n_outer_soil_surface2
slave=outer_soil_surface2(ijk);
master=slave+1000000;
fprintf(fid,'*KINEMATIC␣COUPLING,REF␣NODE=%u\r\n',master);
fprintf(fid,'%u,1,3\r\n',slave);
end
for ijk=1:n_inner_soil_surface2
slave=inner_soil_surface2(ijk);
master=slave+1000000;
fprintf(fid,'*KINEMATIC␣COUPLING,REF␣NODE=%u\r\n',master);
fprintf(fid,'%u,1,3\r\n',slave);
end
%%%%%%% CREATING RIGID BODY %%%%%%%%%%%
fprintf(fid,'**\r\n');
fprintf(fid,'*RIGID␣BODY,...
␣TIE␣NSET=PILE,␣REF␣NODE=LOADINGNODE\r\n');
fprintf(fid,'**\r\n');
%%%%%%%%% BOUNDARY CONDITIONS %%%%%%%%%%%%%%
botcl=nelz(1)*10000;
% fprintf(fid,'*NSET,NSET=BOTCL\r\n');
% fprintf(fid,'%u\r\n',botcl);
fprintf(fid,'*BOUNDARY\r\n');
```

```
fprintf(fid,'BOTTOM_INFINITE,3,3,0.0\r\n');
fprintf(fid,'BOTTOM,3,3,0.0\r\n');
%%%%%%%%%%%%%%%%%%%% LOADING %%%
fprintf(fid,'*RESTART,WRITE,FREQ=1000\r\n');
pbottom=gamma*L;
%GEOSTATIC
fprintf(fid,'*STEP\r\n');
fprintf(fid,'*GEOSTATIC\r\n');
fprintf(fid,'*DLOAD\r\n');
fprintf(fid,'PILE,BZ,-%u\r\n',gamma);
for ii=1:nelztotal;
fprintf(fid,'LAYER%u,BZ,-%u\r\n',ii,gamma);
end
% fprintf(fid,'*DLOAD\r\n');
% fprintf(fid,'ELBOT,P1,%u\r\n',pbottom);
% fprintf(fid,'COREBOT,P1,%u\r\n',pbottom);
fprintf(fid,'*OUTPUT,FIELD,FREQ=1000\r\n');
fprintf(fid,'*ELEMENT␣OUTPUT\r\n');
fprintf(fid,'S,␣NFORC\r\n');
fprintf(fid,'*NODE␣OUTPUT\r\n');
fprintf(fid,'U\r\n');
fprintf(fid,'RF\r\n');
fprintf(fid,'*END␣STEP\r\n');
% %
% %GENERAL LOADING
% for step=1:nstep
% fprintf(fid,'*STEP\r\n');
% fprintf(fid,'*STATIC\r\n');
% fprintf(fid,'0.05,1.0,0.01\r\n');
% fprintf(fid,'*BOUNDARY, TYPE=DISPLACEMENT\r\n');
% fprintf(fid,'PADEYE,1, 1, 0.1\r\n');
% fprintf(fid,'*OUTPUT,FIELD,FREQ=99\r\n');
% fprintf(fid,'*ELEMENT OUTPUT\r\n');
% fprintf(fid,'S\r\n');
% fprintf(fid,'*NODE OUTPUT\r\n');
% fprintf(fid,'U\r\n');
% fprintf(fid,'RF\r\n');
% fprintf(fid,'*END STEP\r\n');
% end
dispstep=0;
rotstep=0;
%GENERAL DISPLACEMENT
```

```
for step=1:nstep
fprintf(fid,'*STEP, NAME=LOADING-%u, INC=1000\r\n',step);
fprintf(fid,'*STATIC\r\n');
fprintf(fid,'0.05,1.0,0.01\r\n');
fprintf(fid,'*BOUNDARY, TYPE=DISPLACEMENT\r\n');
if disptot>0;
dispstep=dispstep+disptot/nstep;
fprintf(fid,'LOADINGNODE, 1, 1, %u\r\n',dispstep);
end
if rottot>0;
rotstep=rotstep+rottot/nstep;
fprintf(fid,'LOADINGNODE, 5, 5, %u\r\n',rotstep);
end
if step==nstep;
fprintf(fid,'**********************\r\n');
fprintf(fid,'** .DAT PRINT OUTPUT\r\n');
fprintf(fid,'**********************\r\n');
fprintf(fid,'*NODE PRINT, FREQ=1,NSET=LOADINGNODE\r\n');
fprintf(fid,'U,\r\nRF\r\n');
end
fprintf(fid,'**********************\r\n');
fprintf(fid,'** .ODB FIELD OUTPUT\r\n');
fprintf(fid,'**********************\r\n');
fprintf(fid,'*OUTPUT,FIELD,FREQUENCY=1\r\n');
fprintf(fid,'*ELEMENT OUTPUT\r\n');
fprintf(fid,'S, E, PE, NFORC\r\n');
fprintf(fid,'*NODE OUTPUT\r\n');
fprintf(fid,'U\r\n');
fprintf(fid,'RF\r\n');
fprintf(fid,'*END STEP\r\n');
fprintf(fid,'**\r\n**\r\n');
end
fclose(fid);
```

# APPENDIX B

# MURFF-HAMILTON FUNCTION

```
function [FMH]=murff_hamilton_check(opt,var)
%Rename fixed variables
R=var(1);
Lf=var(2);
tw=var(3);
sum=var(4);
k=var(5);
eta=var(6);
v0=var(7);
lap=var(8);
Li=var(9);
gamma=var(10);
cas=var(11);
suc=var(12);
if cas==1;
L0=var(13);
end
%Rename opt variables
if cas==2;
L0=opt(1);
z0=opt(2);
r0=opt(3);
alpha=opt(4);
else
z0=opt(1);
r0=opt(2);
alpha=opt(3);
end
%Additional variable(s)
inc=100; %Spatial discretization for integration
cc=z0/L0;
%Lateral Bearing Factor from [RH1984]
%plane strain solution
if eta==0;
Np_RH=9.14;
```

```
elseif eta==1;
Np_RH=11.94;
else
Np_RH=9.14+(11.94-9.14)*eta;
end
%COMPUTE DISSIPATION TERMS (INTERNAL WORK)
%==================== Compute D1dot ====================
%Reference: [MH1993, P104, Eq27]
%spatial discretization
dr=(r0-R)/inc;
dtheta=pi/2/inc;
dztarget=z0/inc;
%perform triple integration for D1dot
D1dot=0;
for ii=1:inc
r=R+dr*(ii-1+0.5);
zmax=z0*(r0-r)/(r0-R);
incz=round(zmax/dztarget);
dz=zmax/incz;
for jj=1:incz
z=dz*(jj-1+0.5);
su=sum+k*z;          %soil strength
for kk=1:inc
theta=dtheta*(kk-1+0.5);
%g and its derivatives
g=v0*(alpha-1)*R^alpha/(r^(1+alpha))*cos(theta);
dgdr=-(R^alpha*v0*cos(theta)*(alpha-1)*...
(alpha+1))/r^(alpha+2);
dgdtheta=-(R^alpha*v0*sin(theta)*...
(alpha - 1))/r^(alpha + 1);
%h and its derivatives
h=v0*z0*cos(theta)*(R/r)^alpha*(r0-r)/(r0-R)*(-1/(r0-r)...
+cc/(r0-R)+(((1-alpha)/r)*(1-0.5*cc*(r0-r)/(r0-R))));
dhdr=(v0*z0*cos(theta)*(R/r)^alpha*(1/(r - r0) ...
- cc/(R - r0) + (((cc*(r - r0))/(2*(R - r0)) - 1)*...
(alpha - 1))/r))/(R - r0) - (v0*z0*cos(theta)*(R/r)...
^alpha*(r - r0)*(1/(r - r0)^2 + (((cc*(r - r0))/...
(2*(R - r0)) - 1)*(alpha - 1))/r^2 - (cc*(alpha - 1))/...
(2*r*(R - r0))))/(R - r0) - (R*alpha*v0*z0*cos(theta)*...
(R/r)^(alpha - 1)*(r - r0)*(1/(r - r0) - cc/(R - r0) + ...
(((cc*(r - r0))/(2*(R - r0)) - 1)*(alpha - 1))/r))/...
(r^2*(R - r0));
```

```
dhdtheta=-(v0*z0*sin(theta)*(R/r)^alpha*(r - r0)*...
(1/(r - r0) - cc/(R - r0) + (((cc*(r - r0))/...
(2*(R - r0)) - 1)*(alpha - 1))/r))/(R - r0);
%radial velocity and its derivatives (dvrdz=0)
vr=v0*(R/r)^alpha*(1-cc*z/z0)*cos(theta);
dvrdr=(R*alpha*v0*cos(theta)*((cc*z)/z0 - 1)*...
(R/r)^(alpha - 1))/r^2;
dvrdtheta=v0*sin(theta)*((cc*z)/z0 - 1)*(R/r)^alpha;
dvrdz=-(cc*v0*cos(theta)*(R/r)^alpha)/z0;
%vertical velocity and its derivatives
vz=g*(z-cc*z^2/(2*z0))+h;
dvzdr=dgdr*(z-cc*z^2/(2*z0))+dhdr;
dvzdz=g*(1-cc*z/z0);
dvzdtheta=dgdtheta*(z-cc*z^2/2/z0)+dhdtheta;
%strain rates
errdot=dvrdr;
ettdot=vr/r;
ezzdot=dvzdz;
ertdot=1/2*(dvrdtheta/r);
etzdot=1/2*(dvzdtheta/r);
ezrdot=1/2*(dvzdr+dvrdz);
%energy dissipation per unit volume
sumsquare=errdot^2+ettdot^2+ezzdot^2;
sumsquare=sumsquare+2*(ertdot^2+etzdot^2+ezrdot^2);
E1dot=su*sqrt(2*sumsquare);
D1dot=D1dot+E1dot*r*dtheta*dz*dr;
end
end
end
D1dot=2*D1dot;
%==================== Compute D2dot ====================
%Reference: [MH1993, P105, Eq32]
%Spatial Discretization
D2dot=0;
dz=z0/inc;
%Perform Integration
for jj=1:inc
z=dz*(jj-1+0.5);
%Soil Strength
su=sum+k*z;
%Integration
denom=(r0-z/z0*(r0-R))^(alpha-1);
```

```
D2dot=D2dot+(su*R^alpha*(1-cc*z/z0)/denom)*dz;
end
C1=2*v0*sqrt(1+(z0/(r0-R))^2)*sqrt(1+((R-r0)/z0)^2);
%Compute Dissipation
D2dot=C1*D2dot;
%==================== Compute D3dot ====================
%Reference: [MH1993, P105, Eq36]
%Spatial Discretization
dz=z0/inc; dtheta=pi/2/inc;
%Initialize D3dot
D3dot=0;
%Perform double integration
for ii=1:inc;
z=dz*(ii-1+0.5);
%Soil Strength
su=sum+k*z;
for jj=1:inc;
theta=dtheta*(jj-1+0.5);
%Compute circumferential slip velocity (vc)
%vc=v0*sin(theta);
%CORRECTION FOR CIRCUMFERENTIAL SLIP VELOCITY (vc)
vc=v0*(1-cc*z/z0)*sin(theta);
%Compute vertical slip [MH1993, Eq21, 22 & 25]
%Get g
g=v0*(alpha-1)*R^alpha/(r^(1+alpha))*cos(theta);
%Get h
h=v0*z0*cos(theta)*(R/r)^alpha*(r0-r)/...
(r0-R)*(-1/(r0-r)+cc/(r0-R)+(((1-alpha)/r)*...
(1-0.5*cc*(r0-r)/(r0-R))));
%Vertical Slip
vz=g*(z-cc*z^2/(2*z0))+h;
%Perform Integration
D3dot=D3dot+eta*su*R*sqrt(vc^2+vz^2)*dtheta*dz;
end
end
D3dot=2*D3dot;
%============= Compute D4dot and D5dot  ===
%Note: D5dot is dependent on
%whether the center of rotation (herein defined
%by 'cc' falls withing the length of
%the pile or outside (below or above)
%the pile.
```

```
%Reference: [MH1993 P105 Eq37 to 40]
%Initialize D4dot
D4dot=0;
D5dot=0;
if (L0)<abs(Lf);
%In cases in which the center of
%rotation is contained within the
%length of the pile, the next two
%integrals are required in order to
%compute D4dot and D5dot
%Integration limits for D4dot
zp_a=0; zp_b=(z0/cc)-z0;
%Spatial discretization
dzp=(zp_b-zp_a)/inc;
%Perform integration
for ii=1:inc;
z=z0+dzp*(ii-1+0.5);
%Soil Strength
su=sum+k*z;
zp=(z0/cc)-z;
D4dot=D4dot+v0*zp*(cc/z0)*su*Np_RH*R*dzp;
end
D4dot=2*D4dot;
%Integration limits for D5dot
zp_c=0; zp_d=Lf-(z0/cc);
%Spatial discretization
dzp=(zp_d-zp_c)/inc;
%Perform integration
for ii=1:inc;
z=z0/cc+dzp*(ii-1+0.5);
%Soil Strength
su=sum+k*z;
zp=z-(z0/cc);
D5dot=D5dot+v0*zp*(cc/z0)*su*Np_RH*R*dzp;
end
D5dot=2*D5dot;
elseif (L0)>abs(Lf);
%In cases in which the center of
%rotation falls outside the length of
%the pile (i.e. either above or below
%the pile), then the term D5dot is
%neglected and D4dot is computed as follows
```

```
%Integration limits for D4dot
zp_a=(z0/cc)-Lf; zp_b=(z0/cc)-z0;
%Spatial discretization
dzp=(zp_b-zp_a)/inc;
%Perform integration
for ii=1:inc;
z=z0+dzp*(ii-1+0.5);
%Soil Strength
su=sum+k*z;
zp=(z0/cc)-z;
%          %Soil Strength
%          su=sum+k*((z0/cc)-zp);
D4dot=D4dot+v0*zp*(cc/z0)*su*Np_RH*R*dzp;
end
D4dot=2*D4dot;
end
%NOTE: Dissipation term for the
%formation of a plastic hinge has not been
%included in this version of the program.
%This program is mainly developed
%to be applied to large diameter piles
%and caissons. If the program is
%going to be modified in order to
%include the plastic hinge, then the term
%needs to be added.
%====== Compute D6dot (Tip Resistance)  ==
%Reference: [MH1993 P106 Eq43]
R1=abs(Lf-L0);
R2=sqrt(R1^2+R^2);
%double integration
%inc=150;
wmax=asin(R/R2);
dw=wmax/inc;
dphi=2*pi/inc;
D6dot=0;
for i=1:inc;
phi=dphi*(i-1)+dphi/2;
for j=1:inc;
w=dw*(i-1)+dw/2;
if z0/cc<Lf
z_loc=(z0/cc)+R2*cos(w);
else
```

```
z_loc=(z0/cc)-R2*cos(w);
end
su=sum+k*(z_loc);
f=sqrt(cos(w)^2+sin(w)^2*sin(phi)^2)*sin(w);
D6dot=D6dot+f*su*dw*dphi;
end
end
D6dot=v0*R2^3*cc*D6dot/z0;
%WORK DONE BY SOIL WEIGHT IN A GRAVITATIONAL FIELD
%==================== Compute W1dot ====================
%Reference: [MH1993, P106, Eq42]
%spatial discretization
dr=(r0-R)/inc;
dtheta=pi/2/inc;
dztarget=z0/inc;
%Perform triple integration for W1dot
W1dot=0;
for ii=1:inc
r=R+dr*(ii-1+0.5);
zmax=z0*(r0-r)/(r0-R);
incz=round(zmax/dztarget);
dz=zmax/incz;
for jj=1:incz
z=dz*(jj-1+0.5);
su=sum+k*z;          %soil strength
for kk=1:inc
theta=dtheta*(kk-1+0.5);
%Compute vertical slip [MH1993, Eq21, 22 & 25]
%Get g
g=v0*(alpha-1)*R^alpha/(r^(1+alpha))*cos(theta);
%Get h
h=v0*z0*cos(theta)*(R/r)^alpha*(r0-r)/(r0-R)*...
(-1/(r0-r)+cc/(r0-R)+(((1-alpha)/r)*...
(1-0.5*cc*(r0-r)/(r0-R))));
%Vertical Slip
%vz=g*(z)+h;
vz=g*(z-cc*z^2/(2*z0))+h;
W1dot=W1dot+vz*gamma*r*dtheta*dz*dr;
end
end
end
W1dot=2*W1dot;
```

```
%These next lines should go after
%all the possible cases that exist
suavg=(sum+(sum+k*Lf))/2;
if suc==2;
D1dot=2*D1dot;
D2dot=2*D2dot;
D3dot=2*D3dot;
W1dot=0;
end
if cas==2
vi=v0*abs(L0-Li)/L0;
FMH=(D1dot+D2dot+D3dot+D4dot+D5dot+D6dot-W1dot)/vi;
elseif cas==1
FMH=(D1dot+D2dot+D3dot+D4dot+D5dot+D6dot-W1dot)/v0;
end
FMH
NMH=FMH/(2*R*Lf*suavg)
disp('D1dot␣D2dot␣D3dot␣D4dot␣D5dot␣D6dot␣W1dot');
Dissip=[D1dot D2dot D3dot D4dot D5dot D6dot W1dot]
if cas==1
disp('z0␣␣␣␣r0␣␣␣␣alpha');
optimization_var=[z0 r0 alpha]
elseif cas==2
%disp('L0   z0    r0    alpha');
optimization_var=[L0 z0 r0 alpha];
end
```